

AD-A274 057



AFIT/GE/ENG/93D-34

①

SDTIC  
ELECTE  
DEC 23 1993  
A

DESIGN OF A SUBSONIC ENVELOPE FLIGHT  
CONTROL SYSTEM FOR THE VISTA F-16 USING  
QUANTITATIVE FEEDBACK THEORY

THESIS  
Odell R. Reynolds  
First Lieutenant, USAF

AFIT/GE/ENG/93D-34

93-30930

Approved for public release; Distribution Unlimited

93 12 22 043

The views expressed in this thesis are those of the author and do not reflect the official policy or position of the Department of Defense or the U. S. Government.

Accession For	
NTIS	CRAM
DTIC	14w
Unannounced	
Justification	
By	
Distribution/	
Availability	
Dist	Avail and/or Special
A-1	

DTIC QUALITY INSPECTED 3

**AFIT/GE/ENG/93D-34**

**DESIGN OF A SUBSONIC ENVELOPE FLIGHT CONTROL SYSTEM FOR  
THE VISTA F-16 USING QUANTITATIVE FEEDBACK THEORY**

**THESIS**

**Presented to the Faculty of the Graduate School of Engineering  
of the Air Force Institute of Technology**

**Air University**

**In Partial Fulfillment of the  
Requirements for the Degree of  
Master of Science in Electrical Engineering**

**Odell R. Reynolds, B.S. Electrical and Electronics Engineering  
First Lieutenant, USAF**

**December, 1993**

**Approved for public release; Distribution Unlimited**

### *Acknowledgements*

I would like to thank my advisor, Dr. Meir Pachter, for his eternal patience and guidance throughout the ordeal that was my thesis. Without his help, I would not have achieved the level of flight control understanding that was necessary to complete this undertaking.

However, the greatest of thanks must go to Richard Sating, for without the assistance of his CAD package, I would have been forced to do my thesis in ICECAP. Along the same lines, I would like to thank the helpful people of Matlab for creating such a friendly, effective program, putting Matrix<sub>X</sub> out of its misery.

I would like to thank my fellow classmates for providing endless hours of help: to Mark for taking point on all the homework, to Vince for his endless knowledge of Matlab and L<sup>A</sup>T<sub>E</sub>X, to Chip for correcting all my stupid mistakes, and to Neil for providing the never ending supplies of Canadian debriefing sauce. Thanks must also be extended to my GnC classmates for continually dragging me away from my academic endeavors. Special thanks to Chip for relentlessly pointing out the few sunny days that graced our stay in Dayton, and to Pat and Neil for finally letting me beat them in raquetball and golf.

Finally, thanks must be extended to my wife Stacey, who didn't divorce me even though I spent the first two months of our marriage buried away in the AFIT computer labs. I'm sure my stressed out attitude was not the easiest to deal with as I tried to finish my masters thesis.

Odell R. Reynolds

## *Table of Contents*

	<b>Page</b>
Acknowledgements . . . . .	ii
List of Figures . . . . .	viii
List of Tables . . . . .	xiv
Abstract . . . . .	xv
 I. Introduction . . . . .	 1-1
1.1 Background . . . . .	1-2
1.2 Potential of QFT . . . . .	1-4
1.3 Assumptions . . . . .	1-5
1.4 Scope . . . . .	1-7
1.5 Standards . . . . .	1-7
1.6 Methodology . . . . .	1-8
1.7 Conclusion . . . . .	1-8
 II. Identification of Aircraft Models . . . . .	 2-1
2.1 Introduction . . . . .	2-1
2.2 Modelling . . . . .	2-1
2.3 Longitudinal Channel . . . . .	2-2
2.3.1 Actuator Model . . . . .	2-3
2.3.2 Inner Loop Model . . . . .	2-4
2.3.3 Outer Loop Model . . . . .	2-5
2.4 Lateral/Directional Channel . . . . .	2-9
2.4.1 Yaw Damper Model . . . . .	2-9
2.4.2 Final Lateral Design Model . . . . .	2-10

	Page
III. Compensator Design Information . . . . .	3-1
3.1 Introduction . . . . .	3-1
3.2 QFT Overview . . . . .	3-1
3.2.1 MISO QFT Design . . . . .	3-2
3.2.2 MIMO QFT Design . . . . .	3-4
3.2.3 Summary . . . . .	3-6
3.3 Thesis Innovation . . . . .	3-7
3.4 Time Period of Interest . . . . .	3-8
3.5 Determination of the Design Envelope's Left Boundary . . .	3-8
3.6 Disturbance Model for Inner Loop . . . . .	3-10
3.7 Chapter Summary . . . . .	3-13
IV. Longitudinal Compensator Design . . . . .	4-1
4.1 Introduction . . . . .	4-1
4.2 Flying Qualities Specifications . . . . .	4-1
4.2.1 Frequency Domain Performance Specifications . . .	4-1
4.2.2 Time Domain Performance Specifications . . . . .	4-2
4.2.3 Additional Frequency Domain Specifications . . . .	4-4
4.3 Inner Loop Design . . . . .	4-5
4.3.1 Bounds . . . . .	4-5
4.3.2 Compensator Design . . . . .	4-5
4.3.3 Results of the Inner Loop Design . . . . .	4-8
4.4 Outer Loop $N_z$ Command Design . . . . .	4-9
4.4.1 Bounds . . . . .	4-9
4.4.2 Compensator Design . . . . .	4-15
4.4.3 Results of the $N_z$ Design . . . . .	4-17
4.5 Outer Loop $\alpha$ Command Design . . . . .	4-21
4.5.1 Bounds . . . . .	4-21

	Page
4.5.2 Compensator Design . . . . .	4-21
4.5.3 Results of the $\alpha$ Design . . . . .	4-22
4.6 $C^*$ Outer Loop Design . . . . .	4-24
4.6.1 Bounds . . . . .	4-26
4.6.2 Redesign of the Inner Loop . . . . .	4-26
4.6.3 Outer Loop Design . . . . .	4-28
4.6.4 Results of the $C^*$ Design . . . . .	4-28
4.6.5 Redesign of the $\alpha$ Loop . . . . .	4-30
4.7 Chapter Summary . . . . .	4-34
V. Useful Insights Gained From the Longitudinal Design . . . . .	5-1
5.1 Introduction . . . . .	5-1
5.2 Description of the Initial Design . . . . .	5-1
5.2.1 Inner Loop Design . . . . .	5-1
5.2.2 Outer Loop $N_z$ Command Design . . . . .	5-1
5.2.3 Outer Loop $\alpha$ Command Design . . . . .	5-4
5.3 Problems with the Initial Design . . . . .	5-6
5.3.1 Control Surface Requirements . . . . .	5-6
5.3.2 Bandwidth of the Compensator . . . . .	5-7
5.4 Results of Modifying Tracking Bounds . . . . .	5-8
5.5 Useful Lessons of Initial Design . . . . .	5-9
5.5.1 Nominal Plant Choice . . . . .	5-9
5.5.2 Control Surface Requirements . . . . .	5-10
5.5.3 Actuator Model . . . . .	5-11
VI. Lateral/Directional Compensator Design . . . . .	6-1
6.1 Flying Qualities Specifications . . . . .	6-1
6.1.1 Frequency Domain Specifications . . . . .	6-1

	<b>Page</b>
6.1.2 Additional Time Domain Specifications . . . . .	6-2
6.2 Lateral Design Bounds . . . . .	6-3
6.3 Initial Lateral Design Attempt . . . . .	6-3
6.3.1 Weighting Matrix . . . . .	6-3
6.3.2 Compensator Design . . . . .	6-4
6.4 Implementation of a Yaw Damper . . . . .	6-5
6.4.1 Yaw Damper Design . . . . .	6-5
6.4.2 Results of Yaw Damper Implementation . . . . .	6-6
6.5 Second Lateral Design Attempt . . . . .	6-8
6.5.1 Weighting Matrix . . . . .	6-8
6.5.2 Compensator Design . . . . .	6-8
6.5.3 Time Domain Results . . . . .	6-9
6.6 Final Body Axis Design . . . . .	6-11
6.6.1 Compensator Design . . . . .	6-11
6.6.2 Time Domain and Specification Results . . . . .	6-11
6.7 Stability Axis Roll Rate Design . . . . .	6-14
6.7.1 Compensator Design . . . . .	6-14
6.7.2 Time Domain and Flying Qualities Results . . . . .	6-16
6.8 Chapter Summary . . . . .	6-16
 VII. Conclusions and Recommendations . . . . .	 7-1
7.1 Longitudinal Channel . . . . .	7-1
7.2 Lateral/Directional Channel . . . . .	7-3
7.3 Summary . . . . .	7-3
7.4 Recommendations . . . . .	7-4
 Appendix A. Robust Control Attack on Nonlinearity . . . . .	 A-1
 Appendix B. Plant Information . . . . .	 B-1



	<b>Page</b>
<b>Appendix C.     Compensator Design Information . . . . .</b>	<b>C-1</b>
<b>Appendix D.     Bound Plots . . . . .</b>	<b>D-1</b>
<b>Appendix E.     QFT CAD Package Results . . . . .</b>	<b>E-1</b>
<b>Appendix F.     Flying Qualities Results . . . . .</b>	<b>F-1</b>
<b>Bibliography . . . . .</b>	<b>BIB-1</b>
<b>Vita . . . . .</b>	<b>VITA-1</b>

# *List of Figures*

Figure	Page
1.1. Typical F-16 Subsonic Flight Envelope with Nominal Operating Points	1-3
1.2. Typical QFT Design Template . . . . .	1-4
2.1. Comparison of First and Fourth Order Actuator Models . . . . .	2-4
2.2. Axes Relation for Pilot Station Acceleration . . . . .	2-7
2.3. Modified System for $N_z$ Output Addition . . . . .	2-8
2.4. Feedback Control System Used for Longitudinal Outer Loop Plants . .	2-8
2.5. System Used for Final Lateral Design Plants . . . . .	2-11
3.1. Feedback Control Structure for MISO QFT Design . . . . .	3-2
3.2. Bode Plots of $T_{RL}$ and $T_{RU}$ . . . . .	3-3
3.3. Feedback Control Structure for MIMO QFT Design . . . . .	3-5
3.4. Equivalent MISO Loops for MIMO QFT Design . . . . .	3-6
3.5. Dual Loop Control System . . . . .	3-7
3.6. Left Edge Poles for 15,000 ft . . . . .	3-10
3.7. Trim Elevator Values for the Envelope of Interest . . . . .	3-11
3.8. Block Diagram Showing the Disturbance Plant . . . . .	3-12
4.1. Dual Loop Control System . . . . .	4-1
4.2. Short Period Natural Frequency Specifications . . . . .	4-2
4.3. Second Order Model Pitch Rate Response to a Step Command . . . .	4-3
4.4. Representative Nichols Chart Showing Phase and Gain Margins . . . .	4-4
4.5. Inner Loop Stability Bounds . . . . .	4-5
4.6. Inner Loop Disturbance Bounds (-30 dB) . . . . .	4-6
4.7. Pitch Rate Feedback Inner Loop Bode Plots (top) and Templates . . .	4-7
4.8. Loop Shaping for the Longitudinal Inner Loop . . . . .	4-8

Figure	Page
4.9. Stability Plots for the Longitudinal $N_z$ Inner Loop . . . . .	4-9
4.10. $N_z$ Loop Bode Plots Without (top) and With Inner Compensator . .	4-10
4.11. $N_z$ Loop Templates Without (top) and With Inner Compensator . . .	4-11
4.12. Alpha Loop Bode Plots Without (top) and With Inner Compensator .	4-12
4.13. Alpha Loop Templates Without (top) and With Inner Compensator .	4-13
4.14. Modified $N_z$ Loop Tracking Bounds . . . . .	4-15
4.15. $N_z$ Outer Loop Stability Bounds . . . . .	4-16
4.16. $N_z$ Outer Loop Tracking Bounds . . . . .	4-16
4.17. Final Loop Shaping for the Outer Loop $N_z$ Design . . . . .	4-17
4.18. Cutoff Frequency Verification for the Longitudinal $N_z$ Design . . . . .	4-18
4.19. Stability Margin Verification for the Longitudinal $N_z$ Design . . . . .	4-18
4.20. $N_z$ and Elevator Time Responses to a Step Input . . . . .	4-19
4.21. Time Domain Specification Results for the $N_z$ Design . . . . .	4-20
4.22. Outer $\alpha$ Loop Tracking Bounds . . . . .	4-22
4.23. Stability Verification for the Longitudinal $\alpha$ Design . . . . .	4-23
4.24. $\alpha$ and Elevator Time Response to a $1^\circ$ Step Input . . . . .	4-24
4.25. Time Domain Specification Results for the $\alpha$ Design . . . . .	4-25
4.26. $C^*/\delta_{cmd}$ Bode Plots before Inner Loop Redesign . . . . .	4-26
4.27. Inner Loop Disturbance Responses . . . . .	4-27
4.28. Stability Margin Verification for the Longitudinal $C^*$ Design . . . . .	4-28
4.29. $N_z$ Time Response with First Order Prefilter (left) and Zero Added (right) . . . . .	4-29
4.30. $N_z$ and Elevator Time Response to Step Input for the $C^*$ Design . . .	4-30
4.31. Time Domain Specification Results for the $C^*$ Design . . . . .	4-31
4.32. $\alpha$ and Elevator Time Response to Step Input for the $C^*$ Design . . . .	4-32
4.33. Time Domain Specification Results for the $C^*$ $\alpha$ Design . . . . .	4-33
5.1. Original $N_z$ Outer Loop Tracking Bounds . . . . .	5-2

Figure	Page
5.2. Initial $N_z$ Loop Shaping . . . . .	5-3
5.3. $N_z$ Time Response to a Step Input . . . . .	5-4
5.4. $\omega_{nsp}$ Results from Second Order Time Response Conversion . . . . .	5-5
5.5. Elevator Response to Step Command . . . . .	5-6
5.6. Open Loop Bode Plots for the Initial $N_z$ Design . . . . .	5-7
5.7. Modified $N_z$ Loop Tracking Bounds . . . . .	5-8
5.8. $N_z$ and Elevator Time Response to a Step Input . . . . .	5-9
5.9. $\omega_{sp}$ Results from Time Response Matching . . . . .	5-10
5.10. Initial Design (left) and Effect of Fourth Actuator Order Model (right)	5-11
6.1. Lateral/Directional System . . . . .	6-1
6.2. Initial (2,2) Loop Shaping . . . . .	6-5
6.3. Yaw Damper Loop Shaping . . . . .	6-6
6.4. Channel (2,2) Bode Plots Before (top) and After (bottom) Yaw Damper Implementation . . . . .	6-7
6.5. Plant #1 (left) and Plant #5 (right) Time Responses with Interconnects	6-9
6.6. Actuator Time Responses for High $\bar{q}$ Plant with Interconnects . . . .	6-10
6.7. Plant #5 Time Response without Interconnects . . . . .	6-10
6.8. Comparison of Third (solid) and Second (dotted) Order Compensator Time Responses . . . . .	6-12
6.9. Time Responses for Step Commands to $p$ and $\beta$ . . . . .	6-13
6.10. Off Diagonal Responses for Step Commands to $p$ (left) and $\beta$ (right) .	6-14
6.11. Graphical Interpretation of the Lower Order System Matching . . . .	6-15
6.12. Time Responses for Step Commands to $p$ (left) and $\beta$ (right) . . . . .	6-16
6.13. Off Diagonal Responses for Step Commands to $p$ (left) and $\beta$ (right) .	6-17
6.14. Graphical Interpretation of Lower Order Bode Plot Matching . . . . .	6-18
7.1. Recommended FCS for the Longitudinal Channel . . . . .	7-3
7.2. Recommended FCS for the Lateral Channel . . . . .	7-4

Figure	Page
A.1. Open Loop Nonlinear System . . . . .	A-1
A.2. Nonlinear System with State Feedback . . . . .	A-2
A.3. Nonlinear State Feedback System with Trim Input . . . . .	A-3
A.4. Linear State Feedback System . . . . .	A-3
A.5. Nonlinear State Feedback System with Linear Control Law . . . . .	A-4
A.6. Commonly Used Nonlinear State Feedback System with Linear Control Law . . . . .	A-5
A.7. Nonlinear State Feedback System with Linear Control Law and Disturbance . . . . .	A-5
C.1. Longitudinal Outer Loop $C^*$ Bode Plots . . . . .	C-2
C.2. Longitudinal Outer Loop $C^*$ Templates . . . . .	C-2
C.3. Longitudinal Outer Loop $C^* \alpha$ Bode Plots . . . . .	C-3
C.4. Longitudinal Outer Loop $C^* \alpha$ Templates . . . . .	C-3
C.5. Bare Plant Bode Plots for the Body Axis Design . . . . .	C-4
C.6. Body Axis $P_e$ Bode Plots without Interconnects . . . . .	C-4
C.7. Body Axis $q_{ii}$ Bode Plots without Interconnects . . . . .	C-5
C.8. Body Axis (2,2) Templates without Interconnects . . . . .	C-5
C.9. Body Axis (1,1) Templates without Interconnects . . . . .	C-6
C.10. Body Axis $P_e$ Bode Plots with Interconnects . . . . .	C-6
C.11. Body Axis $q_{ii}$ Bode Plots with Interconnects . . . . .	C-7
C.12. Body Axis (2,2) Templates with Interconnects . . . . .	C-7
C.13. Body Axis (1,1) Templates with Interconnects . . . . .	C-8
C.14. Bare Plant Bode Plots for the Stability Axis Design . . . . .	C-8
C.15. Stability Axis $P_e$ Bode Plots . . . . .	C-9
C.16. Stability Axis $q_{ii}$ Bode Plots without . . . . .	C-9
C.17. Stability Axis (2,2) Templates . . . . .	C-10
C.18. Stability Axis (1,1) Templates . . . . .	C-10

Figure	Page
D.1. Alpha Outer Loop Stability Bounds . . . . .	D-2
D.2. Alpha Outer Loop Tracking Bounds . . . . .	D-2
D.3. Initial $N_z$ Outer Loop Tracking Bounds with Low Nominal Plant . . .	D-3
D.4. Final $N_z$ Outer Loop Tracking Bounds . . . . .	D-3
D.5. Final $C^*$ Outer Loop Stability Bounds . . . . .	D-4
D.6. Final $\alpha$ Outer Loop Stability Bounds . . . . .	D-4
D.7. Body Axis (2,2) Stability Bounds with Interconnects . . . . .	D-5
D.8. Body Axis (1,1) Stability Bounds with Interconnects . . . . .	D-5
D.9. Body Axis (2,2) Stability Bounds without Interconnects . . . . .	D-6
D.10. Body Axis (1,1) Stability Bounds without Interconnects . . . . .	D-6
D.11. Stability Axis (2,2) Stability Bounds without Interconnects . . . . .	D-7
D.12. Stability Axis (1,1) Stability Bounds without Interconnects . . . . .	D-7
E.1. Representative Nichols Chart Showing Phase and Gain Margins . . . .	E-1
E.2. Cutoff Frequency Verification for the Longitudinal $N_z$ Inner Loop . .	E-2
E.3. Loop Shaping for the Longitudinal $\alpha$ Design . . . . .	E-2
E.4. Cutoff Frequency Verification for the Longitudinal $\alpha$ Design . . . . .	E-3
E.5. Loop Shaping for the Redesigned $C^*$ Inner Loop . . . . .	E-3
E.6. Cutoff Frequency Verification for the Redesigned $C^*$ Inner Loop . . .	E-4
E.7. Stability Verification for the Redesigned $C^*$ Inner Loop . . . . .	E-4
E.8. Loop Shaping for the Longitudinal $C^*$ Design . . . . .	E-5
E.9. Cutoff Frequency Verification for the Longitudinal $C^*$ Design . . . . .	E-5
E.10. Loop Shaping for the Longitudinal $C^* \alpha$ Design . . . . .	E-6
E.11. Cutoff Frequency Verification for the Longitudinal $C^* \alpha$ Design . . . .	E-6
E.12. Stability Verification for the Longitudinal $C^* \alpha$ Design . . . . .	E-7
E.13. Initial (2,2) Loop Shaping with Yaw Damper . . . . .	E-8
E.14. Cutoff Frequency Verification for Initial Body Axis (2,2) Design . . .	E-8
E.15. Stability Verification for Initial Body Axis (2,2) Design . . . . .	E-9

Figure	Page
E.16. Initial (1,1) Loop Shaping with Yaw Damper . . . . .	E-9
E.17. Cutoff Frequency Verification for Initial Body Axis (1,1) Design . . .	E-10
E.18. Stability Verification for Initial Body Axis (1,1) Design . . . . .	E-10
E.19. Stability Plots for Initial Body Axis (2,2) Design Without Interconnects	E-11
E.20. Final (2,2) Loop Shaping with Yaw Damper . . . . .	E-11
E.21. Cutoff Frequency Verification for Final Body Axis (2,2) Design . . . .	E-12
E.22. Stability Verification for Final Body Axis (2,2) Design . . . . .	E-12
E.23. Third Order (1,1) Loop Shaping with Yaw Damper . . . . .	E-13
E.24. Cutoff Frequency Verification for Third Order Body Axis (1,1) Design	E-13
E.25. Stability Verification for Third Order Body Axis (1,1) Design . . . . .	E-14
E.26. Final (1,1) Loop Shaping with Yaw Damper . . . . .	E-14
E.27. Cutoff Frequency Verification for Final Body Axis (1,1) Design . . . .	E-15
E.28. Stability Verification for Final Body Axis (1,1) Design . . . . .	E-15
E.29. Stability Axis (2,2) Loop Shaping . . . . .	E-16
E.30. Cutoff Frequency Verification for Stability Axis (2,2) Design . . . . .	E-16
E.31. Stability Verification for Stability Axis (2,2) Design . . . . .	E-17
E.32. Stability Axis (1,1) Loop Shaping . . . . .	E-17
E.33. Cutoff Frequency Verification for Stability Axis (1,1) Design . . . . .	E-18
E.34. Stability Verification for Stability Axis (1,1) Design . . . . .	E-18
F.1. Second Order Model Pitch Rate Response to Step Controller Deflection	F-1

### *List of Tables*

Table	Page
2.1. Configuration Information Common to All Linearized Plants . . . . .	2-2
2.2. Description of Aircraft States and Inputs . . . . .	2-3
3.1. Left Edge Poles and Zeros for 15,000 ft . . . . .	3-9
3.2. Mach Numbers for High Alpha Dynamic Regions . . . . .	3-11
4.1. Flying Qualities Specifications for the Longitudinal Channel . . . . .	4-4
6.1. Frequency Domain Lateral/Directional Specifications . . . . .	6-2
B.1. Plant Parameters . . . . .	B-2
B.2. $\dot{u}$ Longitudinal Stability Derivatives . . . . .	B-3
B.3. $\dot{\alpha}$ Longitudinal Stability Derivatives . . . . .	B-4
B.4. $\dot{q}$ Longitudinal Stability Derivatives . . . . .	B-5
B.5. $\dot{\beta}$ Lateral Stability Derivatives . . . . .	B-6
B.6. $\dot{\phi}$ and $\dot{p}$ Lateral Stability Derivatives . . . . .	B-7
B.7. $\dot{r}$ Lateral Stability Derivatives . . . . .	B-8
F.1. Results of Time Domain $q$ Analysis for the $N_z$ Control Design . . . . .	F-2
F.2. Results of Time Domain $q$ Analysis for the First $\alpha$ Control Design . . . . .	F-3
F.3. Results of Time Domain $q$ Analysis for the $C^*$ Control Design . . . . .	F-4
F.4. Results of Time Domain $q$ Analysis for the Second $\alpha$ Control Design . . . . .	F-5
F.5. Specification Terms for the Body Axis Design . . . . .	F-6
F.6. Additional Terms for the Body Axis Design . . . . .	F-7
F.7. Specification Terms for the Stability Axis Design . . . . .	F-8
F.8. Additional Terms for the Stability Axis Design . . . . .	F-9



*Abstract*

A controlled plant's characteristics can vary widely throughout its operational envelope. This is a major problem in nominal plant-based control system design. Hence, gain scheduling is often used for full envelope design. In this paper, it is proposed to address the plant's variability using robust control design concepts. In particular, the frequency domain based Quantitative Feedback Theory Multiple-Input Multiple-Output robust control design method is employed for the synthesis of a full envelope flight control system for an F-16 derivative. Compensators for the aircraft's pitch and lateral directional channels are designed, and the designs are validated using linear simulations.

# DESIGN OF A SUBSONIC ENVELOPE FLIGHT CONTROL SYSTEM FOR THE VISTA F-16 USING QUANTITATIVE FEEDBACK THEORY

## *I. Introduction*

The objective of this thesis is to demonstrate the benefits of using Quantitative Feedback Theory (QFT) to design a full subsonic envelope Flight Control System (FCS) for the VISTA F-16. The methods currently used to design full envelope flight control systems have severe limitations. These limitations arise from the fact that these methods involve: (1) numerous flight condition point designs and/or the requirement for complex gain scheduling, including smooth transitions between design points, and (2) many flight test/redesign iterations may be required. The QFT robust FCS design technique has the potential to significantly reduce or eliminate these time consuming and therefore expensive iterations.

QFT has the unique feature of being able to determine if the specifications are achievable early in the design process. If the specifications can be met, the complexity of the compensator, including the amount of scheduling needed, can be determined early in the design process, giving the designer the option of changing the control hardware or software. If the specifications are not achievable, a trade off may be attempted in order to achieve an acceptable FCS design.

The aircraft to be used for this FCS design is the Variable Inflight Stability Test Aircraft (VISTA), an F-16 derivative with a programmable FCS used for testing different flight control systems. The VISTA is chosen because its flight data are readily available for constructing the models used in FCS design. Additionally, there is a full nonlinear VISTA computer simulation available for testing the final FCS design. If the simulation is successful, the actual aircraft's variable FCS can be modified for flight testing.

The initial portion of this thesis involves using the applicable military specifications to determine the specifications that the FCS must meet. Then a set of linear time-invariant

(LTI) models are developed which cover the subsonic flight envelope at normal operations. Finally, a robust FCS is designed using gain scheduling only where necessary to meet specifications.

### *1.1 Background*

In the never-ending quest for the ultimate weapon, designers are continually striving to increase the capabilities of the next generation of fighter aircraft. They are expanding the operational flight envelopes of these aircraft and designing them to be increasingly agile in those envelopes. More and more, this increased performance drive results in an inherently unstable aircraft that requires a feedback flight control system just to stabilize the aircraft and keep it airborne. However, today's FCS needs to do more than keep the aircraft in the air; it must also fly the aircraft in a manner that allows the pilot to concentrate more on the mission than controlling the aircraft. To ensure successful mission completion, the USAF has developed a set of flying quality specifications that fighter aircraft must meet.

The F-16 is a modern fighter aircraft, and the large size of its flight envelope and the nonlinear nature of its dynamics have highlighted several problems with current FCS design methods. Because no technique has been sufficiently developed to design nonlinear controllers, nonlinear systems must be linearized around specific operating points in order to design effective controllers. In FCS design, these operating points correspond to particular flight conditions throughout the flight envelope.

Some current design techniques use an iteration, or gain scheduling, method for compensator or controller design. For example, a particular flight condition (FC) is chosen for a digital FCS such as 20,000 ft at Mach 0.9 of Fig. 1.1, and a compensator  $G(s) = K_i G_i(s)$  is designed to meet the specifications at that point, where  $K_i$  is the gain for the compensator  $G_i(s)$ . Then the designer must test the system at points around FC #1 to determine the region in which the compensator continues to meet the specifications (region A). This procedure is repeated for FC #2, whose valid region is, hopefully, distinct from the region associated with FC #1. In gain scheduling, an attempt is made to keep the same  $G_i$  and only modify  $K_i$ . Then only  $K_i$  is scheduled, with  $G_i$  remaining fixed to hopefully satisfy the specifications for the entire region. If straight  $K_i$  scheduling is not sufficient,

then  $G_i$  needs to be modified and scheduled as well. This procedure is repeated until the entire envelope is covered by the scheduled compensator regions, and then some method of transitioning smoothly between the regions must be developed; a highly nontrivial task. Next, the total FCS must be tested to see if it actually meets the specifications, particularly around the edges of the different regions. If it does not, further  $K_i$  or  $G_i$  scheduling is required for the problem region, and the method of transitioning must be modified to include the new region or modify the existing ones. This process of designing and testing is repeated until satisfactory performance over the entire envelope is achieved.

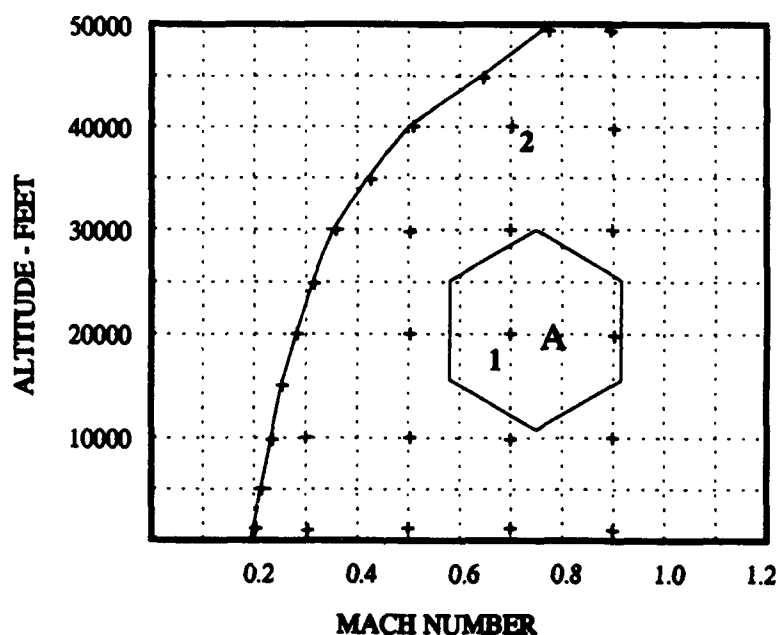


Figure 1.1 Typical F-16 Subsonic Flight Envelope with Nominal Operating Points

Unfortunately, significant guesswork is involved in choosing the starting points for the compensator designs because, up until now, there has been no way to visualize how the different regions of the flight envelope can relate to each other and, therefore, no way to choose the optimal starting point. This iteration method has proven to be an expensive, time consuming process and promises to become more so as the envelopes of today's fighter aircraft continue to expand.

## 1.2 Potential of QFT

Quantitative Feedback Theory for robust FCS design has the potential to alleviate or eliminate the majority of guesswork involved in designing flight control systems that involve structured plant parameter uncertainty. Early in the QFT design process, the designer transfers the LTI models that represent various distinct flight conditions onto a set of frequency domain representation templates. These templates indicate whether the design will be achievable, and if not, where gain scheduling will be necessary. The relative size of the templates indicates whether or not the design can be achieved to meet specifications; the higher and wider the template is, the more difficult the design will be. In addition, similar flight conditions tend to group together inside the template, indicating to the designer the optimal places to break up the template if the need for gain scheduling arises.

Figure 1.2 is a picture of a typical QFT template. On this template, each of the flight conditions marked in Fig. 1.1 is represented by an  $\times$ . As one can clearly see, there is a grouping of flight conditions on the lower right side. If specifications cannot be met using the entire template, the template can be split into two templates which are significantly smaller. If the left template is still too large, the designer can cut it in half again and see easily which flight conditions fall into each template. This clustering of flight conditions indicates where to schedule the gains if the need arises.

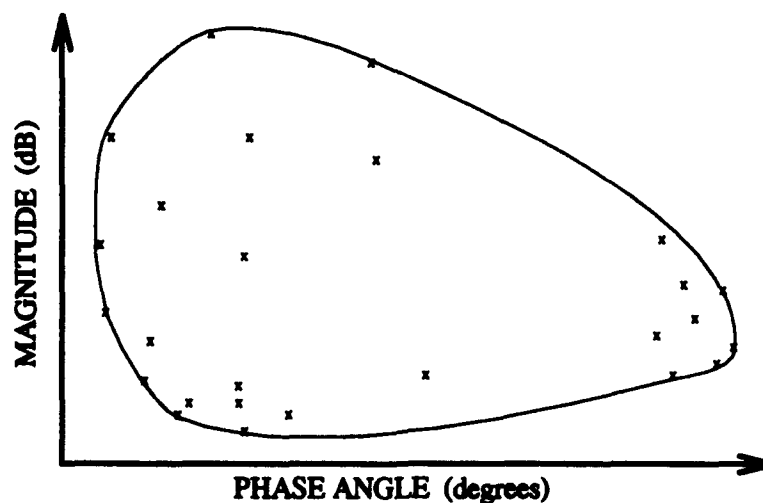


Figure 1.2 Typical QFT Design Template

QFT has been applied to compensators and controllers in the past. The majority of the work has been done here at AFIT by MS students. Several flight control systems have been designed for the Lambda URV [7], a small remotely piloted aircraft maintained at the Control Systems Development Branch of Wright Laboratory (WL/FIGS), Wright-Patterson AFB, Ohio. This aircraft is used to test new flight control systems without risk to a human pilot. QFT designs have also been produced for automatically controlling large aircraft during refueling [17], controlling aircraft during high angle-of-attack ( $\alpha$ ) maneuvers [14], and aircraft with battle damage and/or failed control systems or surfaces [11]. However, due to the time and cost constraints of flight testing these designs, the majority of this work has been restricted to paper design. Two exceptions were the full envelope Lambda designs, which have been implemented and successfully flight tested.

The primary difficulty in implementing the past designs has been the lack of CAD software and accurate flight data. The original Lambda controller could not be implemented because of inaccuracies in the model data, but as more accurate data became available, the FCS was modified and eventually flown in the fall of 1992. Another URV QFT flight control system was implemented and successfully flight tested in the summer of 1993. These successes indicate that QFT is a viable tool for designing flight control systems, assuming the information used for the design is correct.

### *1.3 Assumptions*

As stated above, the primary problem with previous QFT designs has been the inaccuracy of the flight data obtained. For this thesis, the problem is solved through the use of the Simulation/Rapid-Prototyping Facility (SRF) for the F-16 VISTA, a non-realtime aircraft simulation computer package maintained at WL/FIGS. This package is used to provide the data needed for generating the models used in the FCS design, and it is assumed that this data is accurate. If it is not valid data for the true VISTA, then the FCS designed will probably not be implementable on the actual aircraft, but it is still valid for the SRF simulation.

This design uses the linearized equations of motion for an aircraft trimmed in straight and level flight, rigorously developed in Nelson's textbook [9]. These equations use the

body axes for a reference, where the  $x$ -axis is out of the aircraft nose, making the initial perturbation in  $\alpha$  zero, the  $y$ -axis is along the right wing, and the  $z$ -axis is out the bottom of the aircraft. These equations are similar to Blakelock's stability axes equations, barring a coordinate transformation, and the assumptions governing the derivation of these equations include [2]:

1. The  $x$ - and  $z$ -axes lie in the plane of symmetry of the aircraft, and the  $xy$  and  $yz$  products of inertia are equal to zero, which is true for both the body and stability coordinate systems.
2. The mass of the aircraft remains constant, which can be assumed because the period of analysis is small, and no stores are being dropped.
3. The aircraft is a rigid body, which can be assumed as long as none of the bending modes are excited.
4. The earth is an inertial reference frame and the atmosphere is fixed with respect to the earth (no wind), which is assumed because the gyros and accelerometers used for control systems are incapable of sensing the rotations and accelerations due to the rotation of the earth.
5. The perturbations in the states and angles are assumed small enough to make the products of the variations small in comparison to the variations themselves, and to make the small angle assumptions valid, including  $\sin \alpha \approx \alpha$ .
6. Quasisteady flow over the surfaces is assumed, allowing derivatives with respect to velocity rates of changes and unsteady aerodynamics to be neglected.

These equations also assume that the longitudinal (pitch) channel can be decoupled from the lateral (roll/yaw) channel. This is not a very limiting assumption, because over the majority of the flight envelope, the coupling terms in these equations are negligible. This assumption degrades the performance of the FCS in regions, such as high  $\alpha$  flight, where the decoupling assumption is not valid. However, in this thesis, high  $\alpha$  flight is not considered.

Finally, simulations to test the performance of the FCS are run only for short time periods ( $\approx 5\text{sec}$ ) because the interest for this thesis lies in the transient response. An

aircraft with cruise capabilities is still needed, but that is the function of an autopilot. Additionally, while maneuvering, the pilot is controlling the throttle with unmodelled lead and is also continually changing the control commands, i.e., no single command is maintained for an overly long time period. Finally, there are limitations in the numerical accuracy of any digital computer attempting to simulate nonlinear dynamics for an extended time [12].

#### *1.4 Scope*

The flight control systems for the Lambda were successful, but the flight envelopes for both designs were very small as compared to the F-16's. Previous theses and past designers' experiences have demonstrated that a single FCS for both the subsonic and supersonic regions is virtually impossible to design due to the tremendous variations in an aircraft's dynamics as it approaches and passes the sound barrier [12]. For this reason, this thesis deals only with the portion of the flight envelope below Mach 0.9. Additionally, due to time constraints, this thesis is restricted to an analog design.

There are also large variations in these dynamics when the aircraft is loaded with fuel or weapons or when it extends its flaps or landing gear. Due to time limitations, this thesis deals only with straight and level trimmed flight, full tanks, and wingtip AIM-9L stores. However, robustness to additional parameter variability is expected because of "high gain" effects.

#### *1.5 Standards*

To determine the flying qualities of an aircraft, test pilots fly the aircraft through a series of tasks and rate it on a scale of 1 to 10, 1 being best. Aircraft with an average rating of 1 through 3 are considered to have Level 1 flying qualities and are clearly adequate for the mission. Level 2 flying qualities are assigned to aircraft with ratings of 4 and 5, indicating some minor to moderate deficiencies which do not overly interfere with mission completion. Level 3 flying qualities are assigned to those aircraft which are virtually uncontrollable [11]. To compare its performance to the systems presently in existence, the FCS developed in



this thesis is designed to perform with Level 1 flying qualities as defined in Mil-Std 1797A [4].

### 1.6 Methodology

First, Level 1 flying qualities are determined from Mil-Std 1797A. A performance baseline is established using normal acceleration ( $N_z$ ) or  $\alpha$ , roll rate, and sideslip angle as the controlled variables. Next, the SRF is used to extract a set of 40 LTI models which are representative of the entire subsonic VISTA F-16 flight envelope at straight and level, trimmed, unloaded flight.

A single FCS is then designed to control the aircraft at those flight conditions. This FCS consists of two channels, a longitudinal channel to control  $N_z$  ( $g$  force) or  $\alpha$  using the elevator as a control surface, and a lateral channel to control roll rate ( $p$ ) and sideslip angle ( $\beta$ ) using the ailerons, differential elevator, and rudder as control surfaces. In the longitudinal channel, an initial inner loop QFT design using pitch rate feedback is performed to stabilize the aircraft over the entire flight envelope. This closure decreases the size of the templates used for the outer loop QFT design, making the final design specifications easier to achieve. The second loop feeds back a combination of  $q$  and  $N_z$ , or  $\alpha$  in an attempt to meet the specifications determined in the initial phase of this thesis. The lateral channel FCS attempts to minimize the cross-coupling between the rolling and yawing motion of the aircraft. If the pilot wants the aircraft to roll, it should not yaw, and conversely, if the pilot wants to yaw the aircraft, it should not roll. In this design, QFT uses  $p$  and  $\beta$  feedback to meet the specifications necessary for lateral/directional Level 1 flying qualities.

The primary goal of the FCS design is to meet Level 1 flying qualities with the minimum amount of complexity and gain scheduling necessary.

### 1.7 Conclusion

This thesis is intended to demonstrate the advantages of the QFT designed robust compensator for a full envelope flight control system. QFT has the potential to eliminate the time-consuming and expensive procedures currently used to design high performance,

gain scheduled flight control systems. Chapter II discusses the modelling techniques used in this thesis. Chapter III outlines some of the innovations and theories behind the design. Chapters IV and VI explain the longitudinal and lateral designs, respectively, and chapter V elaborates on some useful insights gained during the longitudinal design process. Finally, chapter VII contains the conclusions and recommendations arrived at during this thesis.

## *II. Identification of Aircraft Models*

### *2.1 Introduction*

The equations describing the motion of an aircraft in flight are nonlinear, but no method for designing nonlinear compensators has been sufficiently developed. Therefore, to design a full envelope FCS, one develops a set of linearized models that describe the aircraft's dynamics about each of its expected flight conditions. The perturbation equations of motion developed in Nelson [9] are used in this FCS design.

For this thesis, the aircraft's weight, center of gravity location, and stores configuration are assumed fixed. This assumption is not valid for long periods of time, but because of the high gain associated with robust compensator or controller design, it is expected that the FCS designed here will exhibit robustness with respect to additional parameter variations not considered here.

### *2.2 Modelling*

The Simulation/Rapid-Prototyping Facility (SRF) [16] is used to extract the linear time-invariant (LTI) plant models required for the compensator design. The SRF is a nonlinear computer simulation package maintained at WL/FIGS. Information about the desired flight condition is input to the SRF, and the SRF then trims the aircraft and outputs an LTI model. The "constant" throttle input setting is used, and all other SRF input parameters, except altitude and Mach, are set to default values. These settings correspond to trimmed, straight and level flight, with wings empty, gear up, and wingtip AIM-9L stores. Altitude and Mach are varied to extract the 40 different plants used in the FCS design. Table 2.1 contains the data that are constant for all 40 flight conditions and Table B.1 contains the altitude and Mach information.

Table 2.1 Configuration Information Common to All Linearized Plants

Load Factor	1.0 <i>g</i>	Weight	24,892.6 <i>lbs</i>
IXX	9466.0 <i>slugs - ft<sup>2</sup></i>	IYY	59021.0 <i>slugs - ft<sup>2</sup></i>
IZZ	66065.0 <i>slugs - ft<sup>2</sup></i>	IXZ	385.0 <i>slugs - ft<sup>2</sup></i>
Mean Aerodynamic Chord	11.32 <i>ft</i>	Surface Area	300 <i>ft<sup>2</sup></i>
Wing Span	30 <i>ft</i>		

The SRF outputs an **A** and **B** matrix of the form

$$\mathbf{A} = \begin{bmatrix} 0 & 0 & 0 & 1 & 0 & 0 & 0 & 0 \\ X_\theta & X_u & X_\alpha & X_q & 0 & 0 & 0 & 0 \\ Z_\theta & Z_u & Z_\alpha & Z_q & 0 & 0 & 0 & 0 \\ M_\theta & M_u & M_\alpha & M_q & 0 & 0 & 0 & 0 \\ 0 & 0 & 0 & 0 & 0 & 0 & 1 & \phi_r \\ 0 & 0 & 0 & 0 & Y_\phi & Y_\beta & Y_p & Y_r \\ 0 & 0 & 0 & 0 & 0 & L_\beta & L_p & L_r \\ 0 & 0 & 0 & 0 & 0 & N_\beta & N_p & N_r \end{bmatrix} \quad \mathbf{B} = \begin{bmatrix} 0 & 0 & 0 & 0 & 0 \\ X_{\delta_e} & 0 & X_{\delta_r} & 0 & 0 \\ Z_{\delta_e} & 0 & Z_{\delta_r} & 0 & 0 \\ M_{\delta_e} & 0 & M_{\delta_r} & 0 & 0 \\ 0 & 0 & 0 & 0 & 0 \\ 0 & Y_{\delta_{a1}} & 0 & Y_{\delta_a} & Y_{\delta_r} \\ 0 & L_{\delta_{a1}} & 0 & L_{\delta_a} & L_{\delta_r} \\ 0 & N_{\delta_{a1}} & 0 & N_{\delta_a} & N_{\delta_r} \end{bmatrix} \quad (2.1)$$

for each flight condition. These matrices are used in the state space equations of motion

$$\dot{\mathbf{x}} = \mathbf{Ax} + \mathbf{Bu} \quad \mathbf{y} = \mathbf{Cx} + \mathbf{Du} \quad (2.2)$$

where the state  $\mathbf{x} = [\theta \ u \ \alpha \ q \ \phi \ \beta \ p \ r]^T$  and input  $\mathbf{u} = [\delta_e \ \delta_{a1} \ \delta_a \ \delta_r]^T$  are perturbation values whose descriptions are given in Table 2.2.

As can be seen in Eq. (2.1), the SRF given cross coupling terms in the **A** and **B** matrices are zero, indicating that the equations of motion can be split into a longitudinal and lateral channel. Component values for each of the 40 **A** and **B** matrices are contained in Appendix B.

### 2.3 Longitudinal Channel

The longitudinal states are  $\theta$ ,  $u$ ,  $\alpha$ , and  $q$  and the control inputs are  $\delta_e$  and  $\delta_r$ . A mathematical model for  $N_z$  is developed, and  $N_z$  is added as a fifth output. The

Table 2.2 Description of Aircraft States and Inputs

Variable	Description	Units
$\theta$	pitch angle	degrees
$u$	body axial velocity	ft/sec
$\alpha$	angle of attack	degrees
$q$	body axis pitch rate	deg/sec
$\phi$	Euler roll angle	degrees
$\beta$	sideslip angle	degrees
$p$	body axis roll rate	deg/sec
$r$	body axis yaw rate	deg/sec
$\delta_e$	elevator deflection	degrees
$\delta_{dt}$	differential elevator deflection	degrees
$\delta_f$	flap deflection	degrees
$\delta_a$	aileron deflection	degrees
$\delta_r$	rudder deflection	degrees

longitudinal FCS uses  $q$  and  $N_z$  or  $\alpha$  measurements to control a  $\delta_{e_{cmd}}$ . The flaperons are not used in this FCS design, because they are currently scheduled with  $\alpha$  and are not used for maneuvering, except possibly to act in concert with the elevator to reduce the nonminimum phase effects at the center of gravity [15].

For the longitudinal channel FCS design, the flight envelope is partitioned into two regions: those flight conditions with dynamic pressure ( $\bar{q}$ ) below 130 psf, and those with  $\bar{q}$  above 130 psf. This partition is not a limitation of the QFT design method, but rather it is used for flying qualities. In the low  $\bar{q}$  region,  $\alpha$  is controlled, and in the high  $\bar{q}$  region, normal acceleration at the pilot station ( $N_z$ ) is controlled, making the relevant transfer functions minimum phase. Furthermore, this flight envelope partitioning makes physical sense because the aircraft is incapable of responding with high  $N_z$  at low dynamic pressure, and the pilot/human operator is incapable of distinguishing between small variations in  $N_z$ .

**2.3.1 Actuator Model.** For simplicity, the actuator dynamical model used in the initial design is the commonly used approximation given by the equation

$$\frac{\delta_e(s)}{\delta_{e_{cmd}}(s)} = \frac{20}{s + 20} \quad (2.3)$$

This approximation may be adequate for individual point designs, but it creates significant problems when used for relatively high bandwidth (QFT) robust control design. The primary problem is illustrated in Fig 2.1, where the first-order approximation of Eq. (2.3) is shown as dashed lines while the full fourth-order model

$$\frac{\delta_e(s)}{\delta_{e_{cmd}}(s)} = \frac{(20.2)(71.4)^2(144.8)}{(s + 20.2)(s^2 + 2(0.736)(71.4)s + 71.4^2)(s + 144.8)} \quad (2.4)$$

is shown as solid lines [15]. The magnitude plots of the two models are similar, but the fourth-order model adds approximately  $50^\circ$  of phase lag to the system at 30 rad/sec and even more at higher frequencies. This proves to be a significant problem in QFT robust compensator design and is discussed further in section 5.5.3.

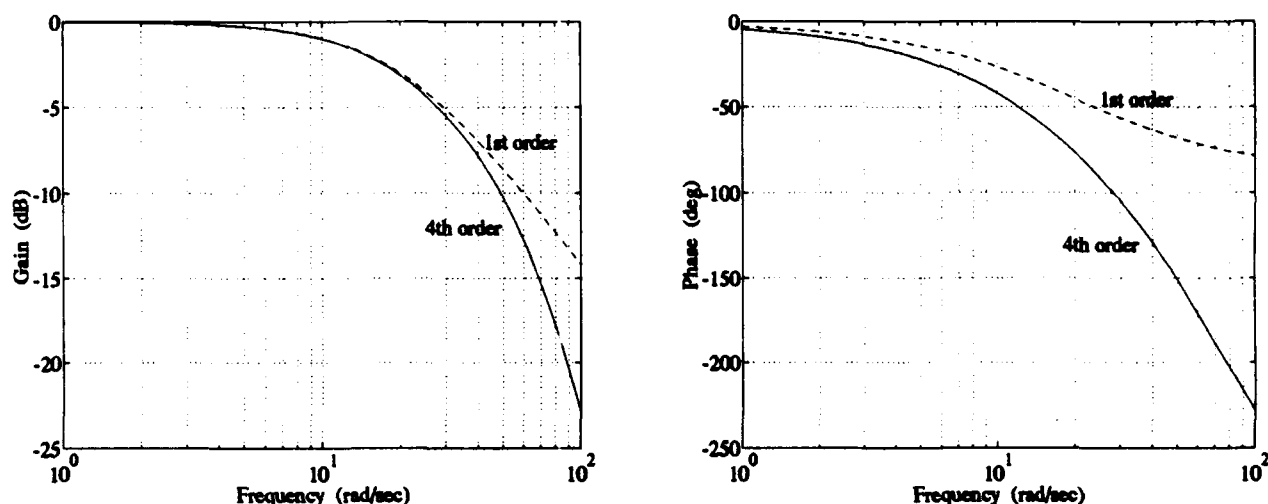


Figure 2.1 Comparison of First and Fourth Order Actuator Models

**2.3.2 Inner Loop Model.** The inner loop design uses pitch rate ( $q$ ) as a feedback variable to control elevator command ( $\delta_{e_{cmd}}$ ). This means that the output matrices are  $C = [0 \ 0 \ 0 \ 1]$  and  $D = [0]$ . The longitudinal **A** matrix consists of the upper left quadrant of the **A** matrix in Eq. (2.1), and the longitudinal **B** matrix is composed of the

top half of the first column of the **B** matrix in the same equation.

$$\mathbf{A}_{long} = \begin{bmatrix} 0 & 0 & 0 & 1 \\ X_\theta & X_u & X_\alpha & X_q \\ Z_\theta & Z_u & Z_\alpha & Z_q \\ M_\theta & M_u & M_\alpha & M_q \end{bmatrix} \quad \mathbf{B}_{long} = \begin{bmatrix} 0 \\ X_{\delta_e} \\ Z_{\delta_e} \\ M_{\delta_e} \end{bmatrix} \quad \begin{aligned} \mathbf{C}_{long} &= \begin{bmatrix} 0 & 0 & 0 & 1 \end{bmatrix} \\ \mathbf{D}_{long} &= \begin{bmatrix} 0 \end{bmatrix} \end{aligned} \quad (2.5)$$

These state space models are input into the MIMO QFT CAD package and converted to the  $q/\delta_{e_{cmd}}$  s-domain transfer functions used for the QFT design. There is no need for input or sensor weighting matrices because there is only one input and one output signal. Additionally, a measurement of the  $q$  state is available for feedback.

**2.3.3 Outer Loop Model.** The outer loop of the longitudinal channel uses  $N_z$  or  $\alpha$  as a feedback variable to  $q$  command. Although a measurement of  $N_z$  is available, it still must be mathematically implemented into the state space model for compensator design. To accomplish this, an equation for  $N_z$  is derived.

**Normal Acceleration at the Pilot Station.** The equation describing  $N_z$  is derived by finding the velocity of the pilot station and differentiating it in the center of gravity (cg) reference frame affixed to the body axis (Fig. 2.2). The derivative of a vector given in one reference frame with respect to a second reference frame is given by

$$\frac{D\bar{V}}{Dt} = \frac{d\bar{V}}{dt} + \bar{\omega} \times \bar{V} \quad (2.6)$$

The velocity of the pilot station is found through the equation

$$\bar{V}_p = \bar{V}_{cg} + \bar{V}_{p/cg} + \bar{\omega}_{p/cg} \times \bar{r}_{p/cg} \quad (2.7)$$

where  $\bar{V}_{cg}$  is the velocity of the cg of the aircraft,  $\bar{V}_{p/cg}$  is the velocity of the pilot station with respect to the cg,  $\bar{\omega}_{p/cg}$  is the rotation of the pilot station reference frame with respect

to the cg reference frame, and  $\bar{r}_{p/cg}$  is the distance from the cg to the pilot station.

$$\bar{V}_{cg} = \begin{bmatrix} U \\ 0 \\ W \end{bmatrix} \quad \bar{V}_{p/cg} = 0 \quad \bar{\omega}_{p/cg} = \begin{bmatrix} 0 \\ q \\ 0 \end{bmatrix} \quad \bar{r}_{p/cg} = \begin{bmatrix} l \\ 0 \\ -h \end{bmatrix} \quad (2.8)$$

Hence,

$$\dot{\bar{V}}_p = \begin{bmatrix} \dot{U} - qh \\ 0 \\ \dot{W} - ql \end{bmatrix} \quad (2.9)$$

Reapplying Eq. (2.6) yields

$$\bar{A}_p = \dot{\bar{V}}_p + \bar{\omega} \times \bar{V}_p = \begin{bmatrix} \dot{U} - qh + qW - q^2l \\ 0 \\ \dot{W} - ql - qU + q^2h \end{bmatrix} \quad (2.10)$$

The required component of  $\bar{A}_p$  is in the  $z$  body axis direction. In line with the small perturbations hypothesis,  $q$  and  $h$  are assumed small, and the nonlinear  $q^2h$  term is neglected, yielding

$$A_{pz} = U(\dot{W}/U - q) - ql \quad (2.11)$$

However,  $\dot{W}/U$  is approximately equal to  $\dot{\alpha}$ . Since  $q$ ,  $\dot{\alpha}$ , and  $ql$  are in  $deg/sec$ , a conversion factor of

$$\left( \frac{1}{32.2} \frac{g}{ft/sec^2} \right) \left( \frac{\pi}{180} \frac{rad}{deg} \right) \quad (2.12)$$

is added to yield the final equation for normal acceleration at the pilot station in  $g$ 's:

$$N_z = \left( \frac{\pi}{5796} \frac{g}{deg \ ft/sec^2} \right) [U(\dot{\alpha} - q) - l_z \dot{q}] \quad (2.13)$$

where  $U$  is the trim velocity and  $l_z$  is the distance from the aircraft center of gravity to the pilot station (13.95 ft) [11].



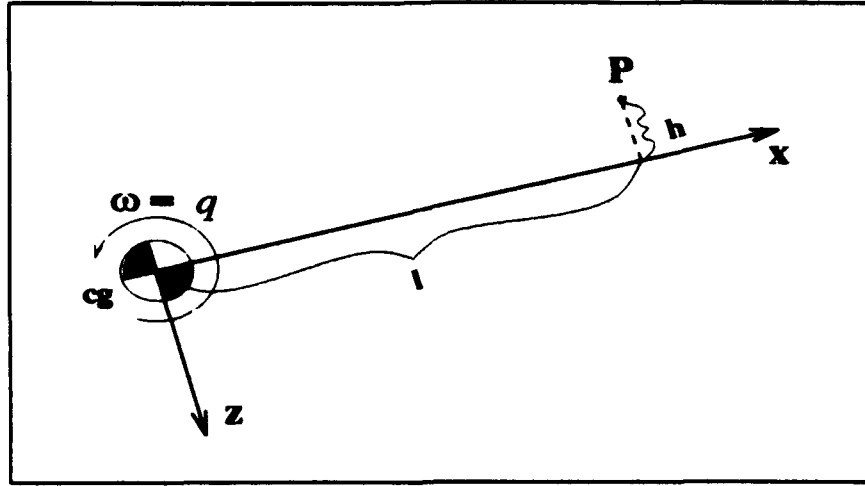


Figure 2.2 Axes Relation for Pilot Station Acceleration

$N_z$  Addition. To input the model into the QFT CAD package, the additional output ( $N_z$ ) is added to the state space model in two steps. From Eq. (2.2),  $\dot{\alpha}$  and  $\dot{q}$  are added to the original model by modifying the C and D matrices as follows

$$C_{new} = \begin{bmatrix} I_4 \\ A_{long} \end{bmatrix} \quad D_{new} = \begin{bmatrix} 0 \\ B_{long} \end{bmatrix} \quad (2.14)$$

The output of this augmented system is then

$$y = [\theta \ u \ \alpha \ q \ \dot{\theta} \ \dot{u} \ \dot{\alpha} \ \dot{q}]^T \quad (2.15)$$

Matlab [8] is then used to form the linear model of the system shown in Fig. 2.3 where  $K$  is the conversion constant in Eq. (2.12). This results in a four state model with  $y = [\theta \ u \ \alpha \ q \ N_z]^T$ .

The state space model formed above is then implemented in the "Aircraft" block in the system in Fig. 2.4, and Matlab is used to form the state space model for input into the QFT CAD package as the bare plants for the outer loop design.

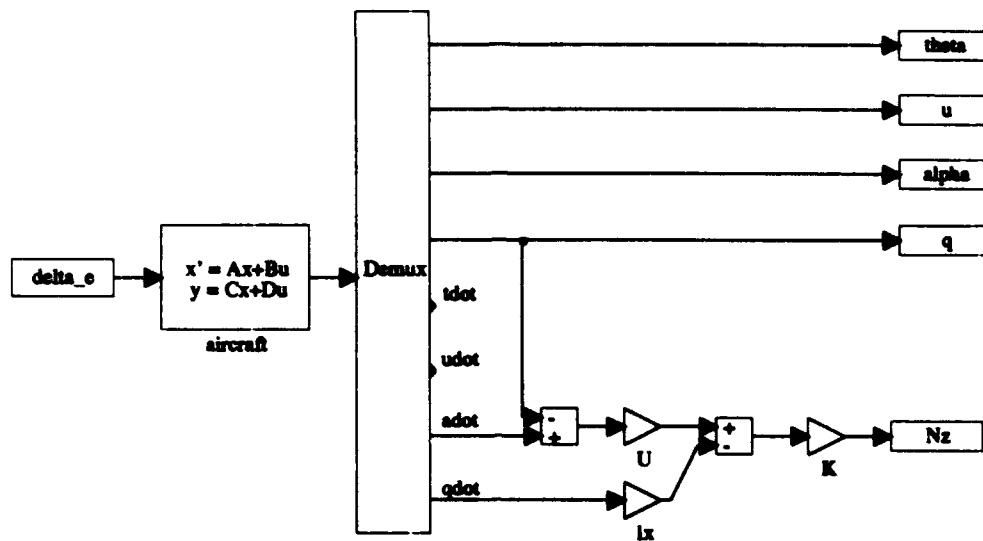


Figure 2.3 Modified System for  $N$ , Output Addition

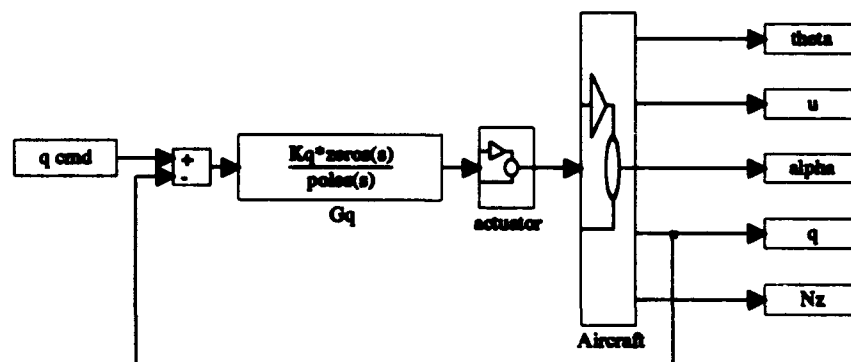


Figure 2.4 Feedback Control System Used for Longitudinal Outer Loop Plants

## 2.4 Lateral/Directional Channel

The lateral/directional portion of the equations of motion describe the rolling and yawing motion of the aircraft. The four states of the lateral channel are  $\phi$ ,  $\beta$ ,  $p$ , and  $r$ . This portion of the thesis involves a MIMO design, using stability axis roll rate ( $p_{stab}$ ) and sideslip angle ( $\beta$ ) as controlled variables and the differential tail, ailerons, and rudder as control surfaces.

There are three control signals available for the lateral directional FCS channel, but the current VISTA coupling of the differential tail and aileron commands is used. This creates a  $2 \times 2$  MIMO plant, where the primary inputs are "generalized" aileron and rudder, and the controlled outputs are  $p_{stab}$  and  $\beta$ . Stability axis roll rate is desired, rather than  $x$  body axis roll rate, because it produces a velocity vector roll. Therefore, an axes rotation is used to convert body axis roll and yaw rate to stability axis roll rate as follows:

$$p_{stab} = p_{body} \cos(\alpha) + r_{body} \sin(\alpha) \quad (2.16)$$

If a roll is commanded, yaw rate is required to produce a coordinated turn, while sideslip angle is not desired. Although yaw rate is a faster variable, sideslip angle is the controlled variable of choice because the QFT design technique permits the designer to try to minimize or eliminate the cross-coupling between the two commands as required.

**2.4.1 Yaw Damper Model.** The yaw damper in the lateral design uses yaw rate ( $r$ ) as a feedback variable to control the rudder command ( $\delta_{r_{cmd}}$ ). The **A** matrix for this portion of the design consists of the lower right quadrant of the **A** matrix in Eq. (2.1), and the **B** matrix is made up of the bottom half of the second, fourth, and fifth columns of the **B** matrix in that equation. **C** is set equal to a  $4 \times 4$  identity matrix to provide access to

all the states, and the **D** matrix is a  $4 \times 3$  array of zeros.

$$\begin{aligned} \mathbf{A}_{lat} &= \begin{bmatrix} 0 & 0 & 1 & \phi_r \\ Y_\phi & Y_\beta & Y_p & Y_r \\ 0 & L_\beta & L_p & L_r \\ 0 & N_\beta & N_p & N_r \end{bmatrix} & \mathbf{B}_{lat} &= \begin{bmatrix} 0 & 0 & 0 \\ Y_{\delta_{lat}} & Y_{\delta_a} & Y_{\delta_r} \\ L_{\delta_{lat}} & L_{\delta_a} & L_{\delta_r} \\ N_{\delta_{lat}} & N_{\delta_a} & N_{\delta_r} \end{bmatrix} & \mathbf{C}_{lat} &= \begin{bmatrix} \mathbf{I}_4 \end{bmatrix} \\ & & & & \mathbf{D}_{lat} &= \begin{bmatrix} \mathbf{0} \end{bmatrix} \end{aligned} \quad (2.17)$$

These state space models are input into the QFT CAD package and converted to the  $r/\delta_{r_{cmd}}$  transfer functions used for QFT design. This is accomplished through the use of input and sensor weighting matrices to convert  $r$  to the single output and  $\delta_{r_{cmd}}$  to the single input. Finally, the models used for the actuators are the fourth-order models given by

$$\frac{\delta_{dt}(s)}{\delta_{dt_{cmd}}(s)} = \frac{\delta_a(s)}{\delta_{a_{cmd}}(s)} = \frac{\delta_r(s)}{\delta_{r_{cmd}}(s)} = \frac{(20.2)(71.4)^2(144.8)}{(s + 20.2)(s^2 + 2(0.736)(71.4)s + 71.4^2)(s + 144.8)} \quad (2.18)$$

**2.4.2 Final Lateral Design Model.** The final portion of this design uses  $p_{lat}$  and  $\beta$  as feedback variables to command  $\delta_{dt_{cmd}}$ ,  $\delta_{a_{cmd}}$ , and  $\delta_{r_{cmd}}$ . The **A**, **B**, **C**, and **D** matrices in Eq. (2.17) are implemented in the "Aircraft" block in Fig. 2.5 and Matlab is then used to form a linear model of the system for implementation as the bare plants in the final MIMO design.

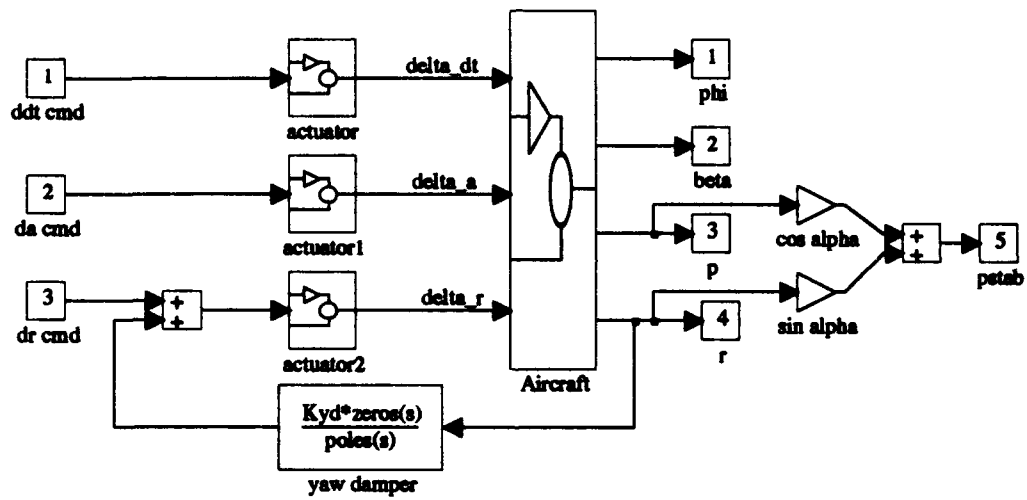


Figure 2.5 System Used for Final Lateral Design Plants

### *III. Compensator Design Information*

#### *3.1 Introduction*

This chapter discusses the QFT robust compensator design technique, with a few innovative additions, along with the other investigations of this thesis. It is assumed that the reader is somewhat familiar with the design technique, thus, only a short overview of QFT is presented. This is followed by a discussion of how QFT is innovatively applied to the longitudinal compensator design. Next, it discusses how the simulation time and the left boundary of the flight envelope are chosen. Finally, the theory behind the inner-loop disturbance bound is applied to the longitudinal design.

#### *3.2 QFT Overview*

If the transfer function of a system is precisely known, then a prefilter can be inserted to cancel out the undesired poles, assuming perfect cancellation, and to include the desired ones, thereby obtaining the specified performance. Additionally, if the disturbance is also known, then a signal equal to the disturbance can be subtracted from the input signal to cancel out its effects. However, all real world plants have some degree of variation, perfect cancellation is not achievable, and the disturbances are seldom known [5].

Robust control refers to the design of a compensator that causes the output of a system to follow some desired input in a specified manner regardless of reasonable system parameter variation or unwanted and unmeasurable disturbances. QFT is a robust compensator design technique that uses feedback of measurable states to illicit a desired response from a system even in the face of quantified, structured plant modelling uncertainty and disturbance signals. It was developed by Professor Isaac Horowitz in the early seventies, and modifications and improvements continue to be made today [3].

QFT uses unity feedback, a cascade compensator, and a prefilter to reduce the variation of the plant output due to plant parameter variations and disturbances. The technique naturally takes into account quantitative information on the plant's variability, the disturbance amplitude and attenuation requirements, and the robust performance requirements [6]. The cascade compensator is designed to insure that the robustness and disturbance

rejection requirements can be met, and the prefilter is then used to tailor the response to meet the required performance specifications.

**3.2.1 MISO QFT Design.** MISO QFT design is based on a system like the one shown in Fig. 3.1. Usually, the output  $C$  is required to track the input  $R$  with some set of performance requirements, and to reject the disturbance input  $D$  with some set of attenuation requirements. To apply the QFT method, one must synthesize a desired control ratio relating the output to each of the inputs. For Fig. 3.1, the control ratios are

$$T_R(s) = \frac{C(s)}{R(s)} = \frac{F(s)G(s)P(s)}{1 + G(s)P(s)} = \frac{F(s)L(s)}{1 + L(s)} \quad (3.1)$$

and

$$T_D(s) = \frac{D(s)}{R(s)} = \frac{P_D(s)}{1 + G(s)P(s)} = \frac{P_D(s)}{1 + L(s)} \quad (3.2)$$

where  $L(s) = G(s)P(s)$  is the loop transmission function [6].

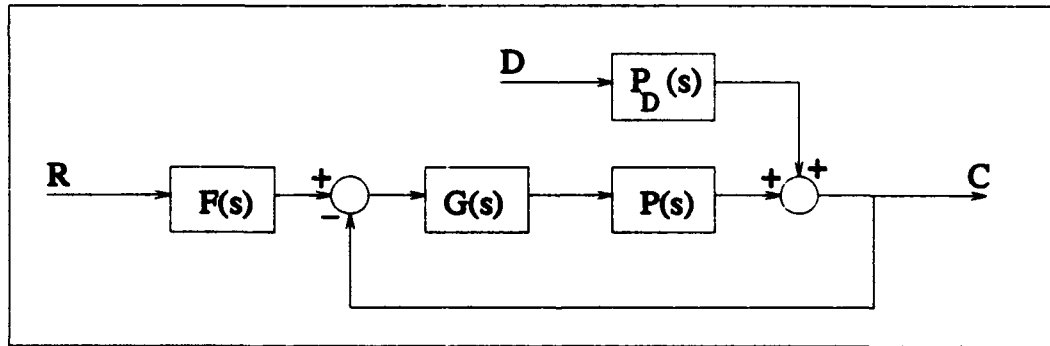


Figure 3.1 Feedback Control Structure for MISO QFT Design

For the tracking performance portion of the design, a range of allowable control ratios are determined. This range is usually based on satisfying some set of time response requirements from which the upper ( $T_{Ru}$ ) and lower ( $T_{Rl}$ ) control ratios are synthesized. These control ratios are then represented in the frequency domain, forming the upper and lower tracking bounds as shown in Fig. 3.2. For the disturbance attenuation portion of the design, only an upper bound ( $T_{Du}$ ) needs to be synthesized, and this bound is also

transferred to the frequency domain.  $T_{DU}$  is often just set equal to a constant magnitude that the disturbance output time response must remain below.

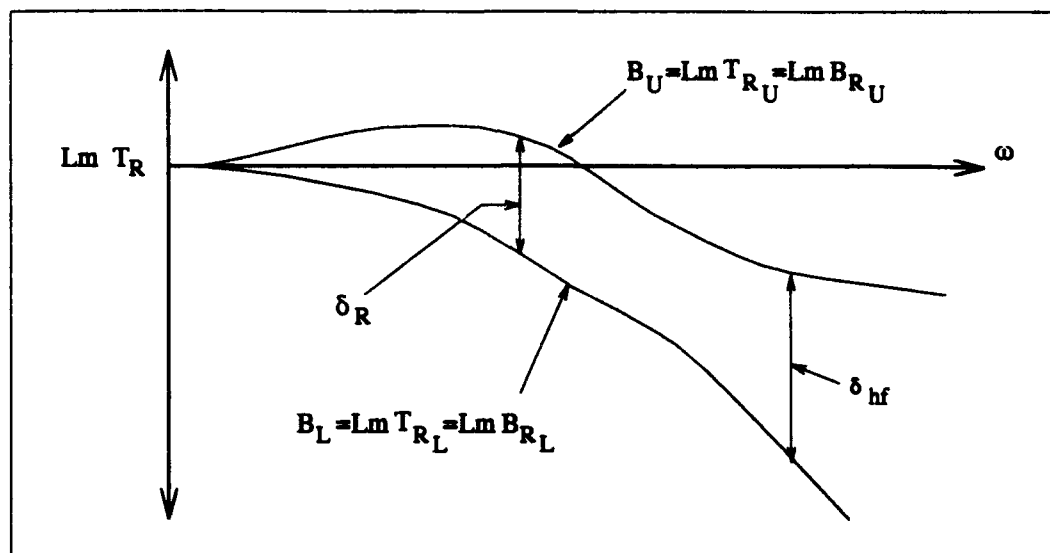


Figure 3.2 Bode Plots of  $T_{RL}$  and  $T_{RU}$

To design a QFT compensator for a nonlinear system, the nonlinear plant is trimmed at a number of operating conditions, and linear models are extracted for each condition. Each of the linear models is defined as a separate plant  $P_i(s)$ , which when taken as a whole, form the set  $\mathcal{P}(s)$ . An assumption here is that there are sufficient  $P_i(s) \in \mathcal{P}(s)$  to adequately represent the structured uncertainty of the nonlinear plant.  $\mathcal{P}(s)$  is then used to synthesize a set of templates that represent the parameter uncertainty in  $P_i(j\omega_i)$  on the Nichols chart. A nominal plant  $P_o$  is picked from  $\mathcal{P}(s)$  based on frequency requirements or designer preference.

Next, a set of bounds for each  $\omega_i$  are constructed based on the stability, tracking, and disturbance rejection requirements of the closed-loop system. The stability bounds  $B_S(j\omega_i)$  are synthesized from the relation between the template size and the required phase margin angle  $\gamma$  of the system and guarantee that the loop transmissions will remain outside the stability contour. In some cases, the closed-loop log magnitude peak  $M_L$  is used since it is related to  $\gamma$ . The tracking bounds  $B_R(j\omega_i)$  are synthesized from the relation between template size and  $\delta_R(j\omega_i) = B_U(j\omega_i) - B_L(j\omega_i)$ . These bounds are used in the



loop transmission synthesis procedure to guarantee that each  $T_{R_i}$  will lie between  $B_U$  and  $B_L$ . The disturbance bounds  $B_D(j\omega_i)$  are synthesized from the relation between template size and the magnitude of  $T_D(j\omega_i)$ . These bounds are also used in the loop transmission synthesis procedure to guarantee that each  $T_{D_i}$  will fall below  $Lm T_{D_U}$ . As stated above, all the bounds are related to template size; the larger the templates are, the more stringent the bounds become. The optimal bounds  $B_O(j\omega_i)$  are then formed based on the suboptimal bounds  $B_R(j\omega_i)$  and  $B_D(j\omega_i)$ . The point on each suboptimal bound, for a given frequency, having the largest dB value on the Nichols chart is chosen as a point on  $B_O(j\omega_i)$ .

The loop shaping then proceeds using  $L_o(s) = G(s)P_o(s)$ . Note that the initial loop transmission used to start the loop shaping process is  $L_o = P_o$ , and then  $G(s)$  is modified until the  $Lm L_o(j\omega_i)$  lies on or above each  $B_O(j\omega_i)$ . This insures that the closed-loop system can meet each of the frequency domain requirements.  $F(s)$  is then synthesized so that each  $T_{R_i}$  falls between  $B_U$  and  $B_L$ .

**3.2.2 MIMO QFT Design.** The QFT design technique for an  $m \times m$  MIMO system is based on the fact that a MIMO system can be rigorously transformed into a set of equivalent  $m^2$  MISO problems. If each of the MISO loops are successfully designed, the solution is guaranteed to work for the original MIMO plant [6]. The MIMO design is based on a system such as the one in Fig. 3.3 where

$$\mathbf{F} = \begin{bmatrix} f_{11} & f_{12} \\ f_{21} & f_{22} \end{bmatrix} \quad \mathbf{G} = \begin{bmatrix} g_1 & 0 \\ 0 & g_2 \end{bmatrix} \quad \mathbf{P} = \begin{bmatrix} p_{11} & p_{12} \\ p_{21} & p_{22} \end{bmatrix} \quad (3.3)$$

To convert the MIMO system into its MISO equivalents, the inverse of  $\mathbf{P}$

$$\mathbf{P}^{-1} = \begin{bmatrix} p_{11}^* & p_{12}^* \\ p_{21}^* & p_{22}^* \end{bmatrix} \quad (3.4)$$

is obtained and then converted into  $\mathbf{Q}$  as shown in Eq. 3.5

$$\mathbf{Q} = \begin{bmatrix} q_{11} & q_{12} \\ q_{21} & q_{22} \end{bmatrix} = \begin{bmatrix} 1/p_{11}^* & 1/p_{12}^* \\ 1/p_{21}^* & 1/p_{22}^* \end{bmatrix} \quad (3.5)$$

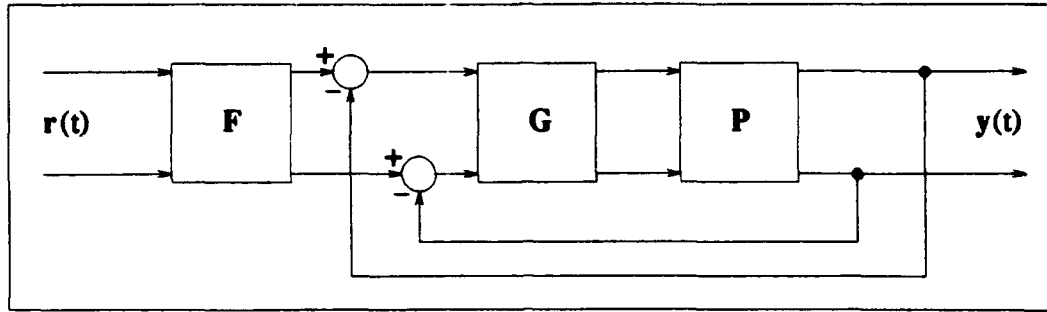


Figure 3.3 Feedback Control Structure for MIMO QFT Design

Once these conversions are accomplished, the entire system can be represented by the MISO loops shown in Fig. 3.4. The control ratio of each diagonal MISO loop is given by

$$t_{ii} = \frac{f_{ii}g_iq_{ii} + d_{ii}q_{ii}}{1 + g_iq_{ii}} = t_{r,ii} + t_{d,ii} \quad (3.6)$$

$$t_{r,ii} = \frac{f_{ii}g_iq_{ii}}{1 + g_iq_{ii}} \quad t_{d,ii} = \frac{d_{ii}q_{ii}}{1 + g_iq_{ii}} \quad (3.7)$$

and the off-diagonal control ratios are given by

$$t_{ij} = t_{d,ij} = \frac{d_{ij}q_{ii}}{1 + g_iq_{ii}} \quad i \neq j \quad (3.8)$$

since  $f_{ij}$   $i \neq j$  is set equal to zero for most MIMO QFT design. The disturbance input for  $i = j$  and  $i \neq j$  is given by

$$d_{ij} = - \sum_{k \neq i} \left[ \frac{t_{kj}}{q_{ik}} \right] \quad (3.9)$$

and represents the cross-coupling disturbance between the channels. Each of the diagonal loops are designed in the same manner as for the MISO case. The design utilizes the tracking bounds resulting from the  $t_{r,ii}$  performance specifications and the cross-coupling disturbance bounds resulting from the disturbance rejection specifications and the  $t_{d,ii}$  and  $t_{ij}$  transfer functions. If all the bounds are not violated, the solution is guaranteed to work for the MIMO system.

There are two methods of design available for the MIMO case. Method 1 designs each of the loops separately to achieve the specifications. Method 2 uses the information

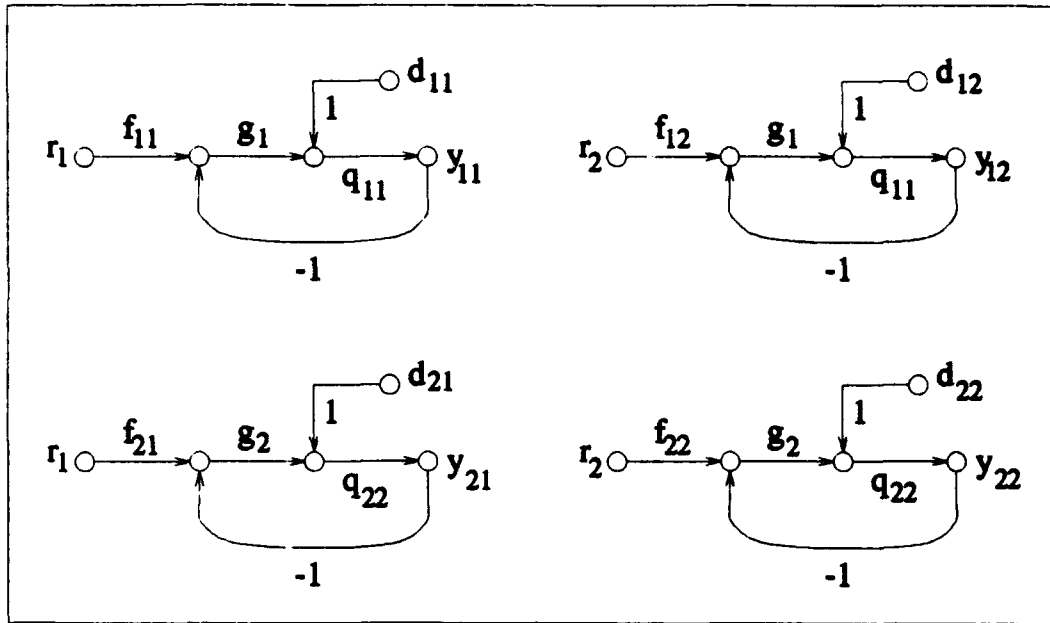


Figure 3.4 Equivalent MISO Loops for MIMO QFT Design

gained from the prior loop designs to recompute the  $\mathbf{Q}$  matrices. Method 2 allows less over-design, but requires a higher bandwidth system. Method 2 is also required when restrictions, such as a diagonal  $\mathbf{P}$  matrix, are not satisfied. Since the MIMO design in this thesis satisfies all the requirements for Method 1, and because high bandwidth systems are being designed, Method 1 is the design choice. For further information on the different design methods, the reader is referred to the references [6].

**3.2.3 Summary.** QFT is a transparent frequency domain design technique because tradeoffs between compensator complexity and system performance are readily visualized. The loop shaping is done on the Nichols chart which displays phase/gain margins and stability/performance bounds along with their relation to the closed loop performance. During the loop shaping process with the MIMO QFT CAD package, modifying the poles and zeros of the compensator produces immediately visible results, enabling the designer to choose between compensator complexity (order) and system performance [5].

Finally, multiple-input multiple-output (MIMO) plants are mathematically decomposed into their multiple-input single-output (MISO) counterparts, where the coupling

between the channels is treated in the same manner as a disturbance [6]. Virtually any system can be converted into a set of LTI MISO plants that can be controlled using a QFT designed controller. Fortunately, a MIMO QFT CAD package has been developed at AFIT which greatly facilitates the QFT design process [13].

### 3.3 Thesis Innovation

This thesis employs a dual loop QFT design in the longitudinal channel. Designers in the past have successfully used multiple loop closures to design compensators, but they have used other methods, such as root locus, whereas this thesis uses the QFT robust compensator design technique for both loops. The resulting system is shown in Fig. 3.5.

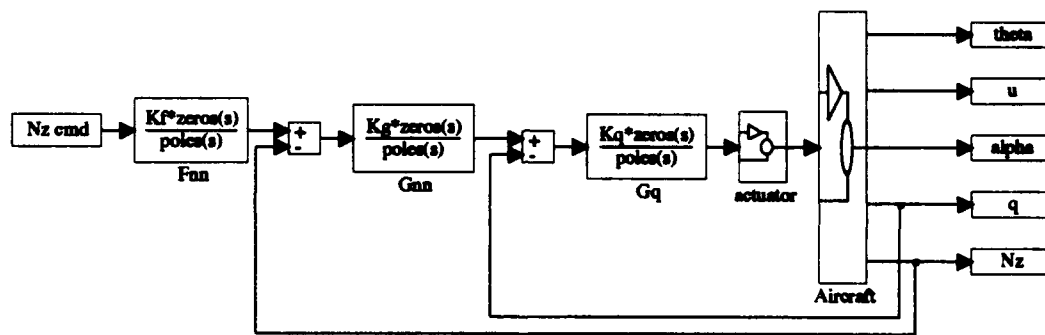


Figure 3.5 Dual Loop Control System

The stated objective of the inner loop design is to stabilize the aircraft, but the primary goal of this design is to decrease the size of the templates used in the outer loop design, enabling a full envelope FCS design with no gain scheduling. In Trosen's thesis, a wing leveler was used to successfully decrease the size of the templates used in the final design, but this thesis uses QFT to design the inner loop, allowing the designer to visualize the effect of the compensator on all the plants.

Pitch rate is chosen as the inner loop feedback variable because it is the fastest (highest bandwidth) state in the longitudinal channel, and therefore should be the most effective state for outer-loop variable control.

### *3.4 Time Period of Interest*

Because this is a FCS design and not an autopilot, the time horizon of interest is chosen as approximately five seconds. This time period applies primarily to the Short Period mode and not to the Phugoid. The Phugoid poles are affected by inputs to the throttle, which are provided by the pilot with a large amount of unmodelled lead before a desired maneuver. It is beyond the scope of this thesis to model this, and the primary effects are in the long period (Phugoid) dynamics. Additionally, the speed in the linear models is unconstrained, resulting in aircraft velocity quickly changing to unrealistic values during linear simulations, sometimes even causing the plane to fly "backwards". Obviously, the linear simulation is no longer valid at this point. The model is also not accurate for long time periods because the aircraft would change trim conditions. Each of the design models is linearized about a particular trim condition, and if the aircraft moves to another flight condition during the maneuver, a different model is applicable. Finally, in the nonlinear SRF simulation, maneuvers with time horizons greater than 10 seconds are suspect, because the "nonlinear trim" condition has been observed to drift. For all these reasons, it is not constructive to simulate for more than a short period of time.

### *3.5 Determination of the Design Envelope's Left Boundary*

The left boundary of the applicable flight envelope is determined by examining the  $q/\delta_{c_{m,d}}$  Bode plots, because there are several regions with qualitatively different dynamics. When one performs a constant altitude, increasing Mach number scan of the envelope, a speed is located before which the SRF will not initialize. At higher speeds, a number of different characteristic regions are observed. Region 1 contains plants with the expected real-stable/unstable Short Period mode and complex-stable Phugoid mode. In region 2, the Short Period mode becomes complex-stable and the Phugoid becomes real-stable/unstable. Region 3 plants retain the complex-stable Short Period, but the Phugoid becomes complex-unstable. Then there is a region similar to the first, where the Short Period poles move toward the origin and the Phugoid poles are complex-stable. The fifth region has the same pole structure as the fourth, but one of the zeros is nonminimum phase. Finally, in the

sixth region, the Short Period poles jump back away from the origin and remain there for the entire subsonic portion of the flight envelope.

This dynamic behavior is observed at 15, 25, 30, and 35 thousand feet when a 0.01 Mach increment is used, and it is assumed that the behavior is also present at the other altitudes and could be observed if smaller Mach increments are used. Table 3.1 contains the poles and zeros of the plants generated by scanning the left edge of the envelope at 15,000 feet, and Fig. 3.6 is a scatter diagram of those poles, showing the different regions.

Table 3.1 Left Edge Poles and Zeros for 15,000 ft

Plant	Short Period Poles		Phugoid Poles		Zeros		
1	-1.15	0.58	-0.099-0.19j	-0.099+0.19j	-0.29	-0.012	0
2	-0.40-0.38j	-0.40+0.38j	0.18	-0.12	-0.24	-0.035	0
3	-0.38-0.91j	-0.38+0.91j	0.006-0.11j	0.006+0.11j	-0.27	-0.019	0
4	-0.87	0.32	-0.171-0.21j	-0.171+0.21j	-0.44	-0.021	0
5	-0.82	0.30	-0.191-0.19j	-0.191+0.19j	-0.45	-0.011	0
6	-0.71	0.27	-0.238-0.15j	-0.238+0.15j	-0.45	0.0003	0
7	-1.36	0.55	-0.064-0.19j	-0.064+0.19j	-0.46	-0.014	0
8	-1.36	0.54	-0.065-0.18j	-0.065+0.18j	-0.47	-0.008	0
9	-1.40	0.54	-0.063-0.18j	-0.063+0.18j	-0.48	-0.001	0

The  $q/\delta_{cmd}$  transfer function Bode plots for each of the regions have their own characteristic shape. At low frequencies, the Bode plots for plants in regions two and five are 180° out of phase with those residing in the heart of the envelope and 360° out of phase with each other. This is caused by the unstable Phugoid poles in combination with the stable Short Period poles in region two and the nonminimum phase zero in region five. Table 3.2 contains the speed at each altitude where each of the shifts begin and end for 0.01 increments. These 180° and 360° phase shifts can adversely affect the QFT robust compensator design method by creating extremely wide templates, so the problematic "boundary layer" is eliminated from the design envelope, with the loss of approximately 0.05 Mach. Additionally, there is some question as to the validity of the model at the extreme left side (higher alpha region) of the envelope, where stronger inter-channel cross-coupling presumably occurs. This question arises because the cross-coupling terms in the SRF generated linearized model are zero. Because this is a full envelope design, and it is

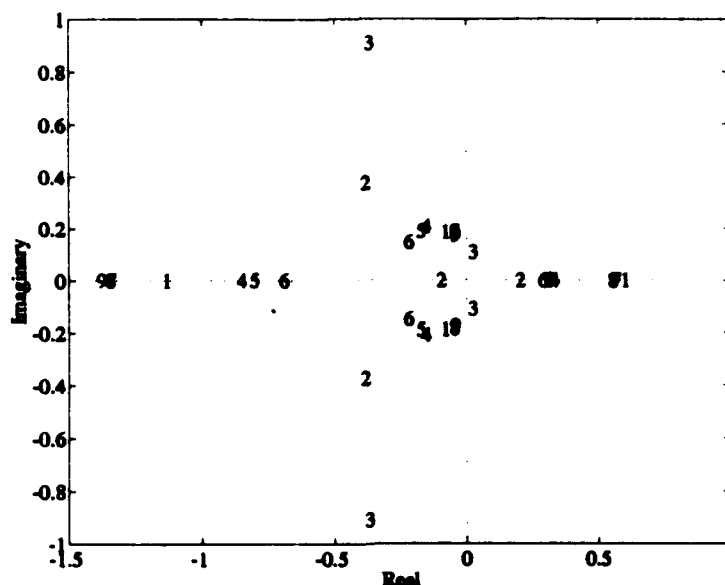


Figure 3.6 Left Edge Poles for 15,000 ft

imperative in FCS design to use valid plant models, the boundary layer discussed above is ignored for the remainder of this thesis.

### 3.6 Disturbance Model for Inner Loop

As explained in Appendix A, the disturbance rejection required for the linear control of nonlinear plants is equal to the trim input to the plant. For the longitudinal channel, this corresponds to the elevator trim angle. The elevator trim changes as the aircraft moves around to different flight conditions/trim states in the flight envelope, and the compensator command must include this trim in addition to actual perturbation inputs. Figure 3.7 shows the elevator trim values for the flight envelope of interest.

Because the trim input enters before the plant, to implement it into the QFT CAD package, the plant itself is entered as the disturbance plant as shown in Fig. 3.8 ( $P = P_D$ ). Disturbance bounds for every frequency are generated, but not all are needed for this type of disturbance. All the bounds would be needed if the disturbance were actually a step, but it is not. It actually appears over a period of time, as the aircraft moves from one

Table 3.2 Mach Numbers for High Alpha Dynamic Regions

Altitude	Initialized	1st Shift	Return	2nd Shift	Return
1,000	0.19	0.21	0.22		0.24
5,000	0.21	0.22	0.23		0.26
10,000	0.23	0.25	0.26		0.28
15,000	0.25	0.27	0.28	0.30	0.31
20,000	0.28	0.30	0.31		0.34
25,000	0.31	0.33	0.35	0.37	0.38
30,000	0.35	0.36	0.39	0.41	0.42
35,000	0.42	0.42	0.44	0.46	0.47
40,000	0.50			0.52	0.53
45,000	0.64			0.69	0.70
50,000	0.77			0.77	0.78

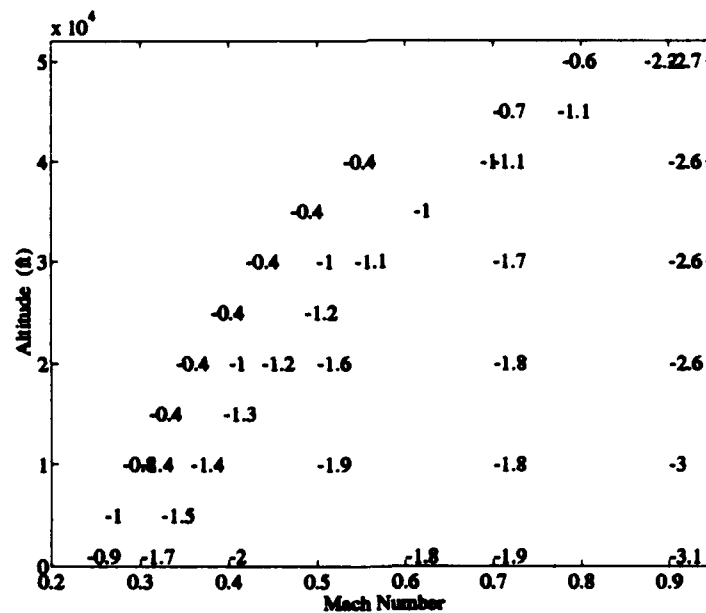


Figure 3.7 Trim Elevator Values for the Envelope of Interest



flight condition to another. Even at 1000 ft/sec, it takes 10 seconds to move up or down one level in Fig. 3.7, and the greatest trim change for this type of move is 0.7 degrees.

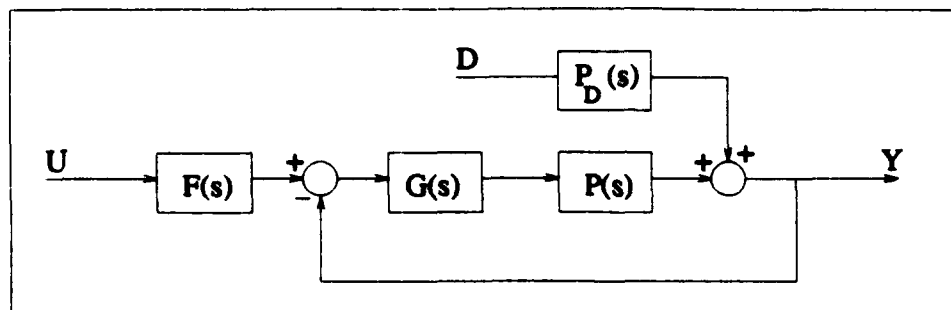


Figure 3.8 Block Diagram Showing the Disturbance Plant

It is not precisely known how fast the aircraft can change Mach number and altitude in combination, because this would require an examination of minimum time to climb maneuvers, etc. However, any change requires a number of seconds. The maximum trim change between any adjacent flight conditions is 1.6 degrees: a decrease from Mach 0.9 to Mach 0.8 at 50,000 feet. If 10 seconds is used as a typical value for the time required for this change, then the disturbance can be represented by a sinusoid with a 1.6 degree magnitude and a 40 sec time period (0.157 rad/sec). If it takes longer than ten seconds to change flight conditions, the error would occur at a lower frequency, and changes between any other flight conditions would correspond to a smaller trim elevator change.

Figure 4.7 shows the Bode plots for the  $q/\delta_{cmd}$  transfer functions. At a frequency of 0.157 rad/sec, these transfer functions have a maximum magnitude of 40 dB, which corresponds to a pitch rate error of 100 deg/sec for every degree of elevator error. If 30 dB of disturbance rejection is added to the system, it would reduce this error to 0.032 deg/sec per degree of elevator error in the steady state. However, transient effects based on the poles of the system will also be seen, and the initial response is expected to rise above this value. However, even doubling the 0.032 value results in a negligible disturbance response.

### ***3.7 Chapter Summary***

QFT is the primary design technique applied in this thesis, but it is applied in innovative ways. A dual loop closure is used in the longitudinal channel to reduce the size of the outer loop design templates. Disturbance bounds are used in the inner loop to insure that the linear compensator controls the nonlinear plant in the face of trim changes. These innovations lead to some interesting results. Additionally, the left edge of the flight envelope is modified because of the dynamics discovered there, but robustness to additional parametric variation is expected because of the extremely robust nature of the outer loop angle-of-attack design. Finally, the linear simulation time period is rather short because of the nature of piloted aircraft flight.

## IV. Longitudinal Compensator Design

### 4.1 Introduction

In chapter II it is shown that, due to decoupling, the longitudinal channel is strictly a SISO system (Fig. 4.1). Therefore, the longitudinal channel is designed by using MISO QFT techniques to perform a dual loop closure. The inner loop uses pitch rate ( $q$ ) as a feedback, and the outer loop uses either angle of attack ( $\alpha$ ) or normal acceleration at the pilot station ( $N_z$ ) as the controlled variable. The control surface used in this design is the horizontal tail. This chapter contains the specifications for the longitudinal channel and a description of each of the designs and its results.

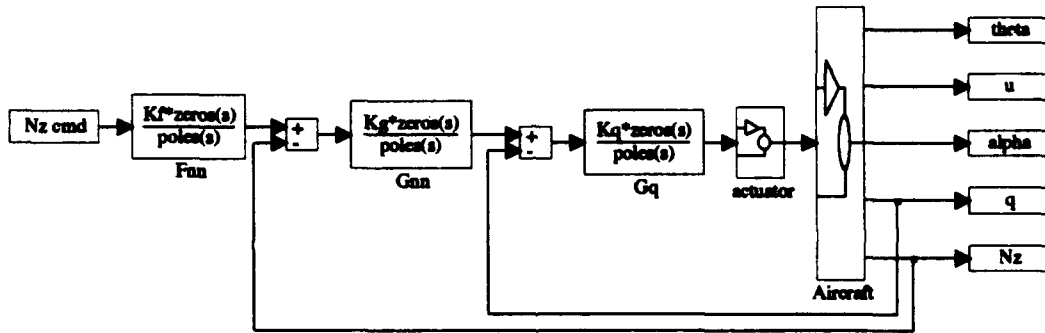


Figure 4.1 Dual Loop Control System

### 4.2 Flying Qualities Specifications

Mil-Std 1797A is used to define the longitudinal design specifications. The specifications are given in both frequency domain and time domain formats.

**4.2.1 Frequency Domain Performance Specifications.** In the frequency domain, the specifications are based on the  $\bar{q}$  dependent ratio

$$\frac{N_z}{\alpha} \approx \frac{\bar{q} S a}{mg} \quad g's/rad \quad (4.1)$$

where  $\bar{q}$  is the dynamic pressure,  $S$  is the surface area of the wing,  $a$  is the lift curve slope in  $rad^{-1}$  and  $mg$  is the weight of the aircraft. The system specifications are based on

simultaneously matching the Bode plots of the final system to those of the fourth order systems

$$\frac{n'(s)}{\delta_{stk}(s)} = \frac{K_n s(s + 1/T_{h1}) \exp^{-\tau_n s}}{(s^2 + 2\zeta_p \omega_p s + \omega_p^2)(s^2 + 2\zeta_{sp} \omega_{sp} s + \omega_{sp}^2)} \quad (4.2)$$

and

$$\frac{q(s)}{\delta_{stk}(s)} = \frac{K_\theta(s + 1/T_{\theta1})(s + 1/T_{\theta2}) \exp^{-\tau_\theta s}}{(s^2 + 2\zeta_p \omega_p s + \omega_p^2)(s^2 + 2\zeta_{sp} \omega_{sp} s + \omega_{sp}^2)} \quad (4.3)$$

where  $n'$  is the normal acceleration of the center of gravity of the aircraft. For category A flight phases, fighter aircraft Level 1 flying qualities require that the Control Anticipation Parameter (CAP) given by

$$CAP = \frac{\omega_{sp}^2}{(N_z/\alpha)} \quad (4.4)$$

be between 0.28 and 3.6 (Fig. 4.2). The short period damping ( $\zeta_{sp}$ ) must be between 0.35 and 1.30, the short period natural frequency ( $\omega_{sp}$ ) must be greater than 1.0, and the allowable equivalent time delay ( $\tau_\theta$ ) must be less than 0.1 seconds.

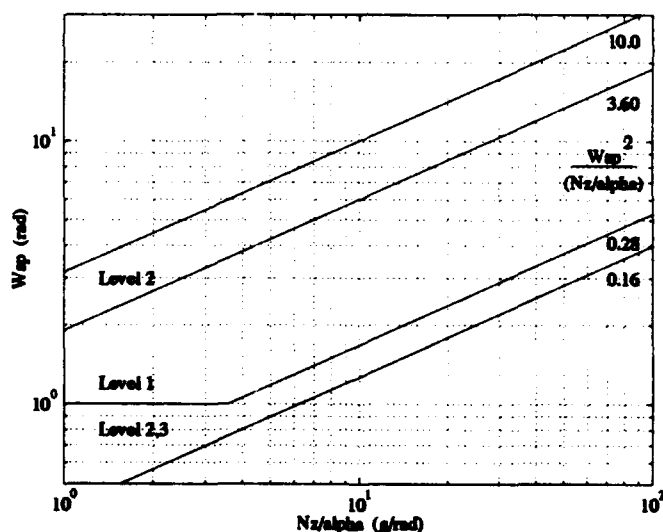


Figure 4.2 Short Period Natural Frequency Specifications

**4.2.2 Time Domain Performance Specifications.** The time domain specifications are based on the  $q$  response to a step input command calculated from the two-degree-of-freedom model, which is determined by constraining the speed ( $\dot{u} = 0$ ). Mathematically, this is accomplished by taking the Short Period approximation of the fourth-order aircraft

model. The time domain specifications are based around two straight lines drawn on the  $q$  response (Fig. 4.3):

1. A straight horizontal line drawn through the steady state  $q$ .
2. A straight line drawn tangent to the  $q$  response at its point of maximum slope.

The specifications are obtained from the following time definitions measured from the instant that the step input is applied:

1.  $t_1 \equiv$  the time at which line 2 intersects the time axis.
2.  $t_2 \equiv$  the time at which line 2 intersects line 1.

and the following magnitude definitions:

1.  $\Delta q_1 \equiv$  the difference between the maximum  $q$  and the steady state  $q$ .
2.  $\Delta q_2 \equiv$  the difference between the steady state  $q$  and the first minimum in  $q$ .

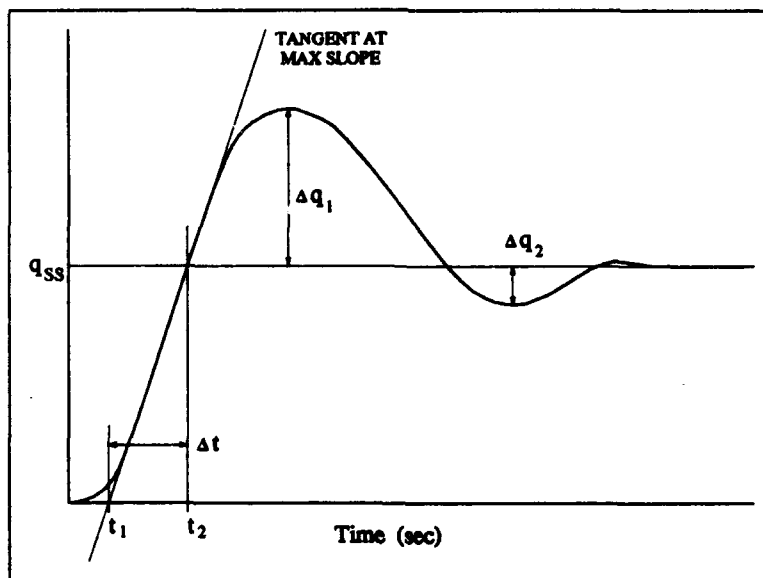


Figure 4.3 Second Order Model Pitch Rate Response to a Step Command

Table 4.1 contains the time domain specifications for flying qualities in nonterminal flight phases where  $t_1$  is the equivalent time delay,  $\Delta q_2/\Delta q_1$  is the transient peak ratio,  $\Delta t = t_2 - t_1$  is the effective rise time, and  $V_T$  is the true airspeed (ft/sec).

Table 4.1 Flying Qualities Specifications for the Longitudinal Channel

Parameter	Level 1	Level 2	Level 3
$t_1$ max	0.12 sec	0.17 sec	0.21 sec
$\Delta q_2/\Delta q_1$ max	0.30	0.60	0.85
$\Delta t$ max	$500/V_T$ sec	$1600/V_T$ sec	undefined
$\Delta t$ min	$9/V_T$ sec	$3.2/V_T$ sec	undefined

4.2.3 *Additional Frequency Domain Specifications.* The additional frequency domain specifications are obtained by examining a Nichols or Bode representation of the open loop system. Figure 4.4 portrays a representative Nichols chart plot.

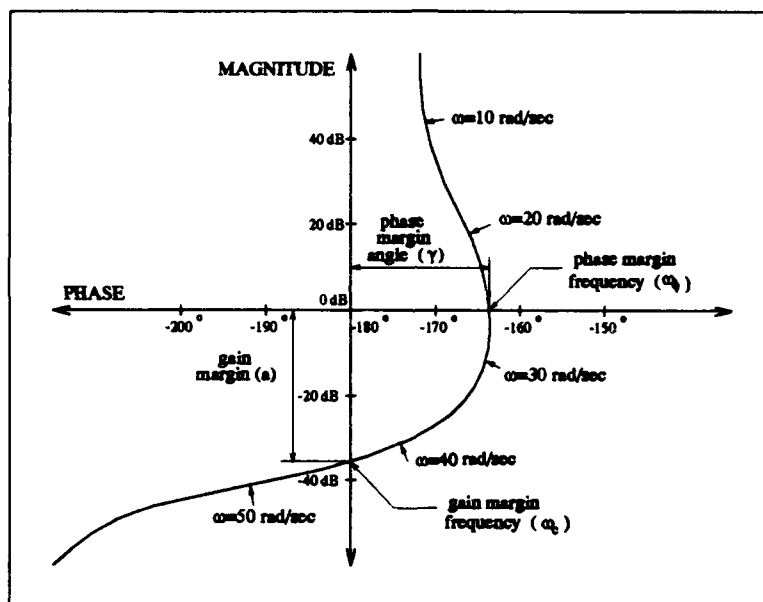


Figure 4.4 Representative Nichols Chart Showing Phase and Gain Margins

Stability margin requirements apply to the phase margin angle ( $\gamma$ ), and the gain margin ( $a$ ). For the F-16,  $a$  must be greater than 6 dB, and  $\gamma$  must be greater than  $30^\circ$  [1]. For the longitudinal channel, the open loop system is obtained by breaking the outer loop in Fig 4.1 and removing the prefilter. In addition,  $\omega_\phi$ , sometimes referred to as the cutoff frequency, should be less than 30 rad/sec to prevent deleterious interaction with the bending modes of the aircraft.

**4.3.1 Bounds.** As discussed in section 3.3, the inner loop uses QFT to robustly stabilize the aircraft with  $q$  as the feedback variable. Therefore, stability bounds for a minimal  $10^\circ$  phase margin angle are generated just to insure stability and are shown in Fig. 4.5. Additionally, disturbance bounds for a 30 dB rejection are generated in an attempt to meet the 0.157 rad/sec bound as discussed in section 3.6, and these bounds are shown Fig. 4.6



4-5

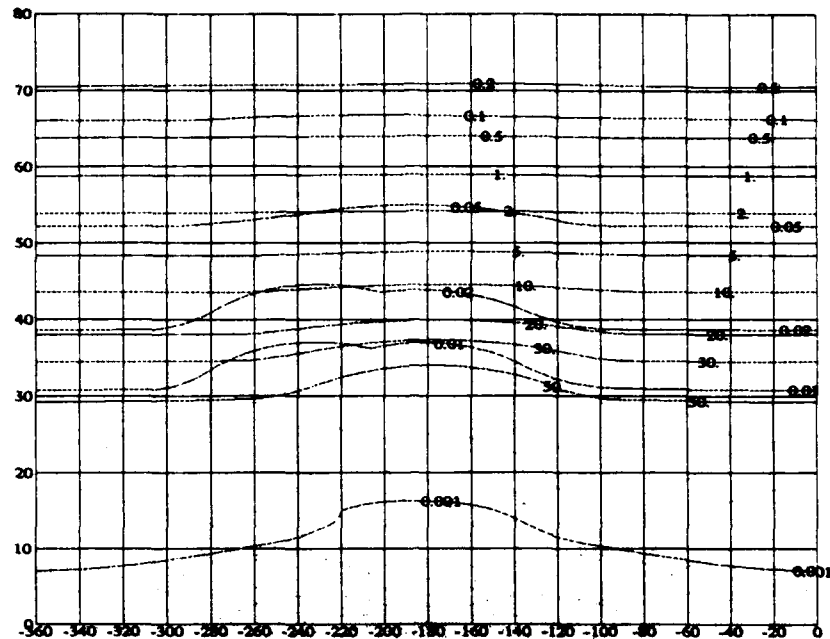


Figure 4.6 Inner Loop Disturbance Bounds (-30 dB)

Plant #5 is chosen as the nominal plant because it is on the top of the templates in the cutoff frequency ( $\omega_\phi$ ) region. This enables one to design with the nominal loop and be assured that the  $\omega_\phi$  of the other plants is less than that of the nominal plant. After one integrator is added to increase the low frequency disturbance rejection, two zeros are needed to pull the nominal loop to the right of the stability bounds. A second, high frequency pole is added to make the compensator equal order.

It is discovered through various iterations of inner loop design that higher gain is the most effective at decreasing the size of the outer loop templates. Using a  $\gamma = 1^\circ$  stability bound allows the highest gain to be implemented, but this small  $\gamma$  results in a pair of highly underdamped poles in the outer loop transfer functions, causing an undesirable resonance in the Bode plots. A final stability bound of  $\gamma = 10^\circ$  is chosen as a reference. The gain and zeros are adjusted for the highest gain in order to decrease the template size, while maintaining a reasonable phase margin angle to prevent the resonance. The maximum allowable  $\omega_\phi = 30$  rad/sec is also utilized to allow the greatest gain. As shown in the loop shaping of Fig. 4.8, the disturbance bounds are met below 0.2 rad/sec with the inner loop



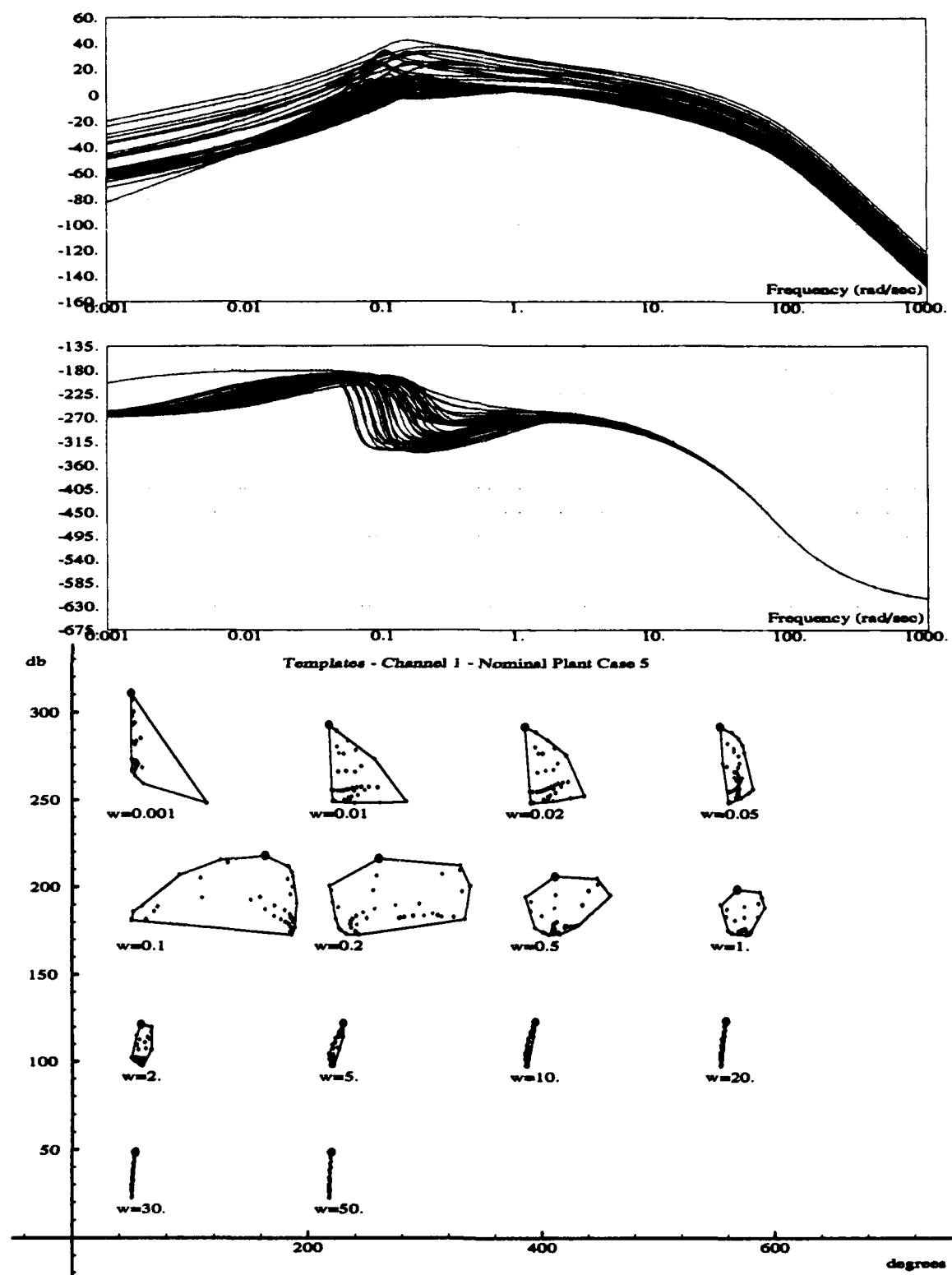


Figure 4.7 Pitch Rate Feedback Inner Loop Bode Plots (top) and Templates

compensator given by

$$G_q(s) = \frac{-3.1(s+13)(s+17)}{s(s+100)} \quad (4.5)$$

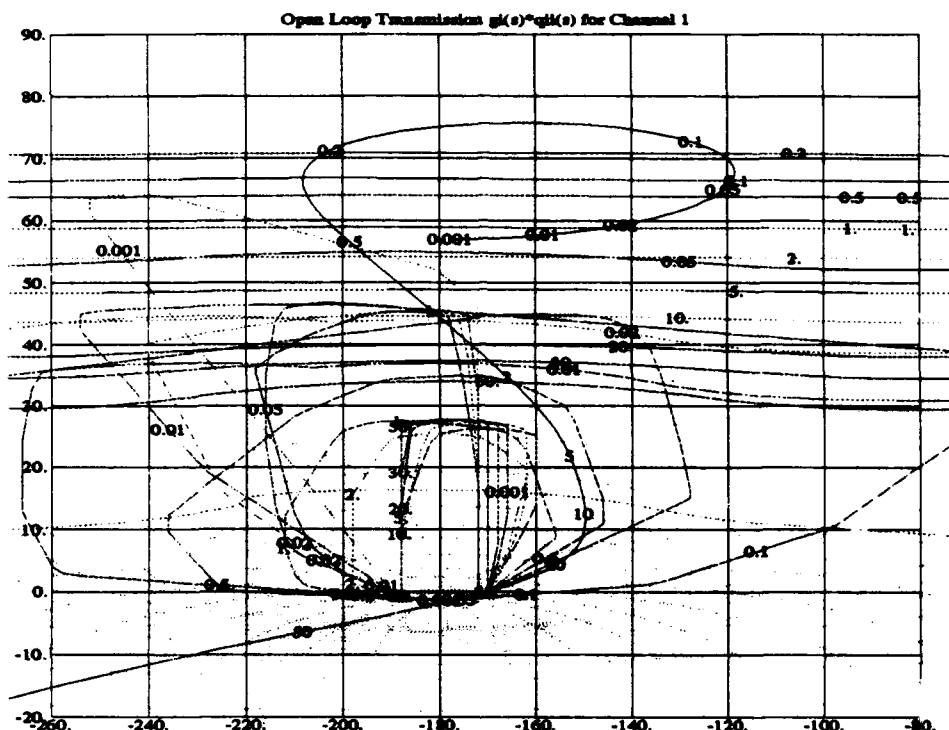


Figure 4.8 Loop Shaping for the Longitudinal Inner Loop

The Nichols chart stability diagram for this design is shown in Fig. 4.9. All of the plants are stable except the "exceptional" plant corresponding to 30,000 ft, Mach 0.5, which begins approximately -13 dB below the stability point (0 dB, -180°) and crosses the 0 dB line around -105°. This plant can be stabilized by adding another integrator to the compensator, but the size of the outer loop templates is not significantly reduced. Therefore, in the interest of minimizing the order of the compensator, Eq. (4.5) is retained. Furthermore, in this thesis a FCS is being designed, not an autopilot, and the proximity of the unstable pole to the origin (0.0016) places its dynamics outside the time period of interest ( $\approx 5$  sec) as discussed in section 3.4.

**4.3.3 Results of the Inner Loop Design.** Because there are no tracking bounds in this portion of the design, there is no prefilter needed. However, the inner loop design is

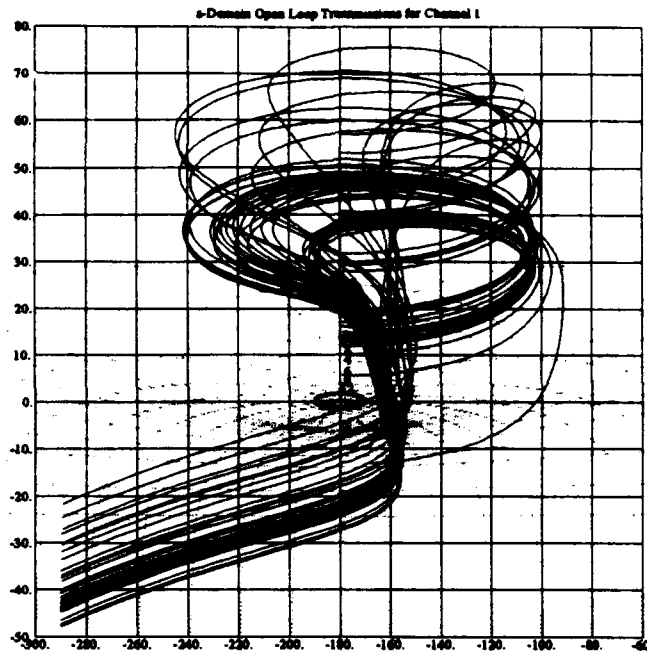


Figure 4.9 Stability Plots for the Longitudinal  $N_z$  Inner Loop

successful in reducing the size of the outer loop templates. For the  $N_z$  outer loop design, the maximum height of the templates is cut in half (Fig. 4.11), and one large excursion in phase is eliminated (Fig. 4.10). Note the dB scales are not identical. The remaining magnitude and phase excursions are caused by the underdamped zeros (anti-resonance) in the  $N_z/\delta_{cmd}$  transfer function, over which the inner loop design has no control.

The inner loop also reduces the height of the  $\alpha$  portion templates by approximately one half (Fig. 4.13). However, the phase portion of this design introduces an additional problem. The low frequency portions of the phase plots for some plants are  $180^\circ$  out of phase with the other plants (Fig. 4.12). This is caused by the nonminimum phase characteristics of some of the plants. There is also an anti-resonance present in this portion of the design, but again, the inner loop has no control over  $\alpha/\delta_{cmd}$  transfer function zeros.

#### 4.4 Outer Loop $N_z$ Command Design

**4.4.1 Bounds.** Because QFT tracking bounds are based on a frequency domain format, the frequency domain flying qualities specifications are used to determine those

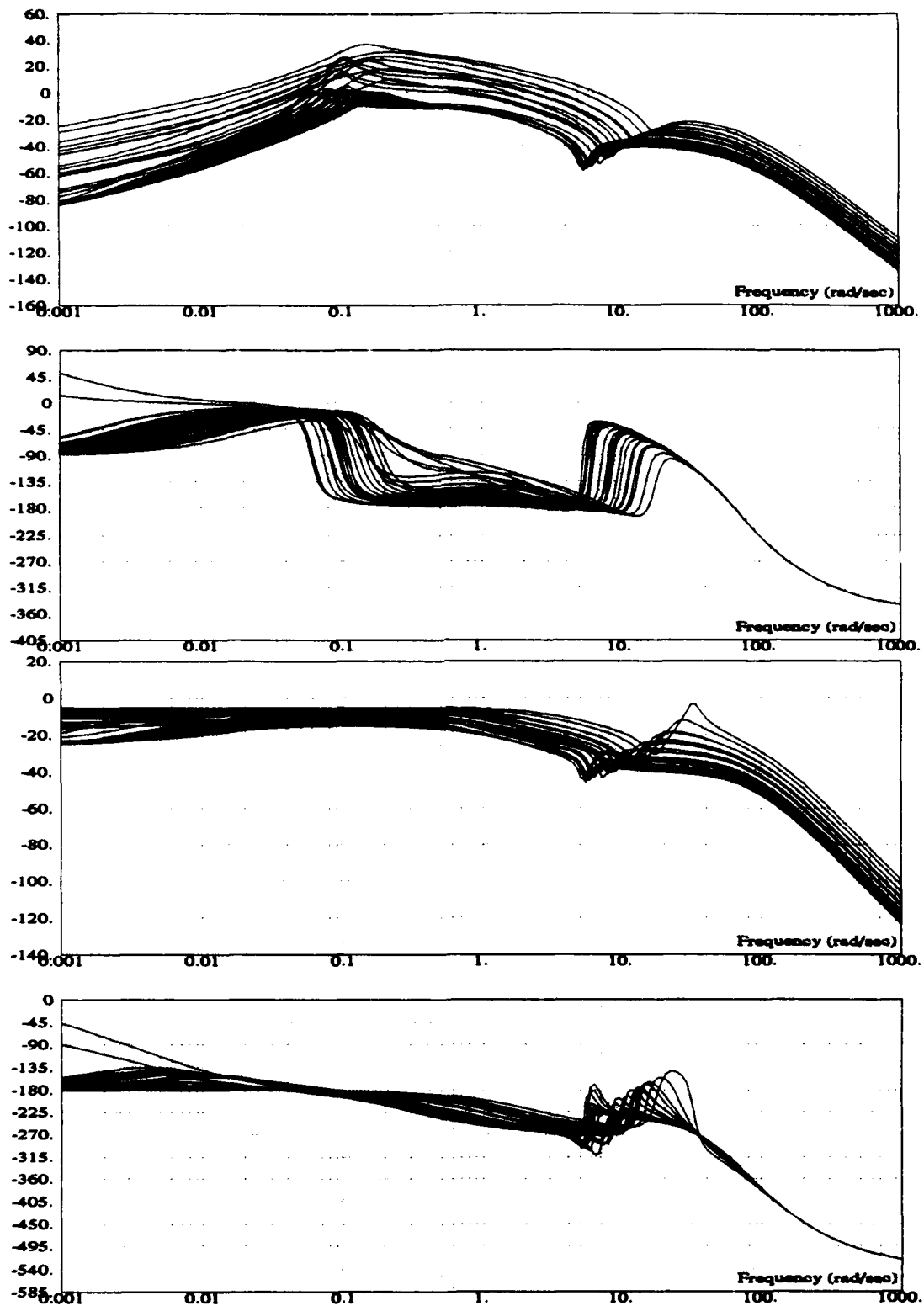


Figure 4.10  $N$ , Loop Bode Plots Without (top) and With Inner Compensator

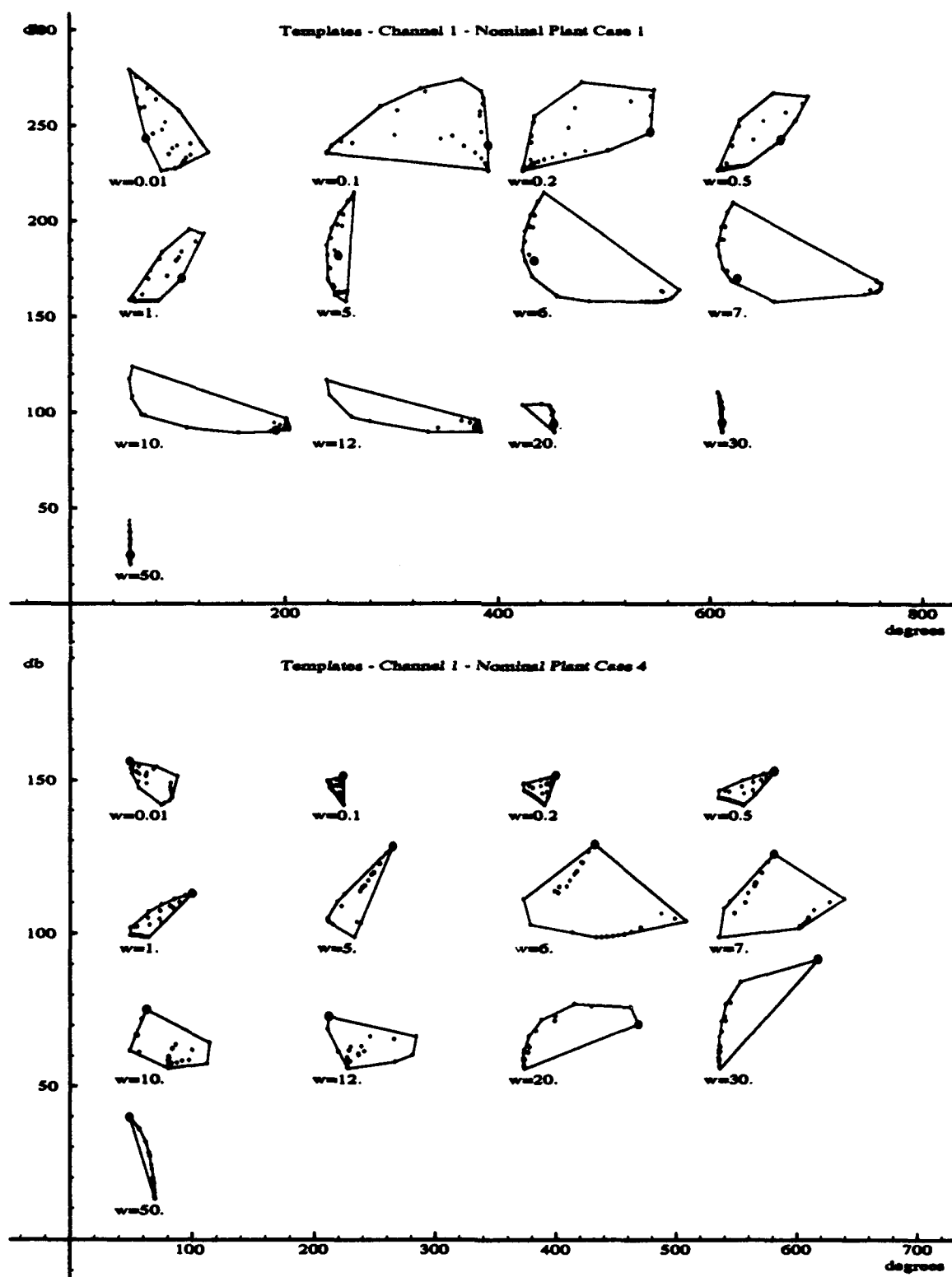


Figure 4.11  $N_z$  Loop Templates Without (top) and With Inner Compensator

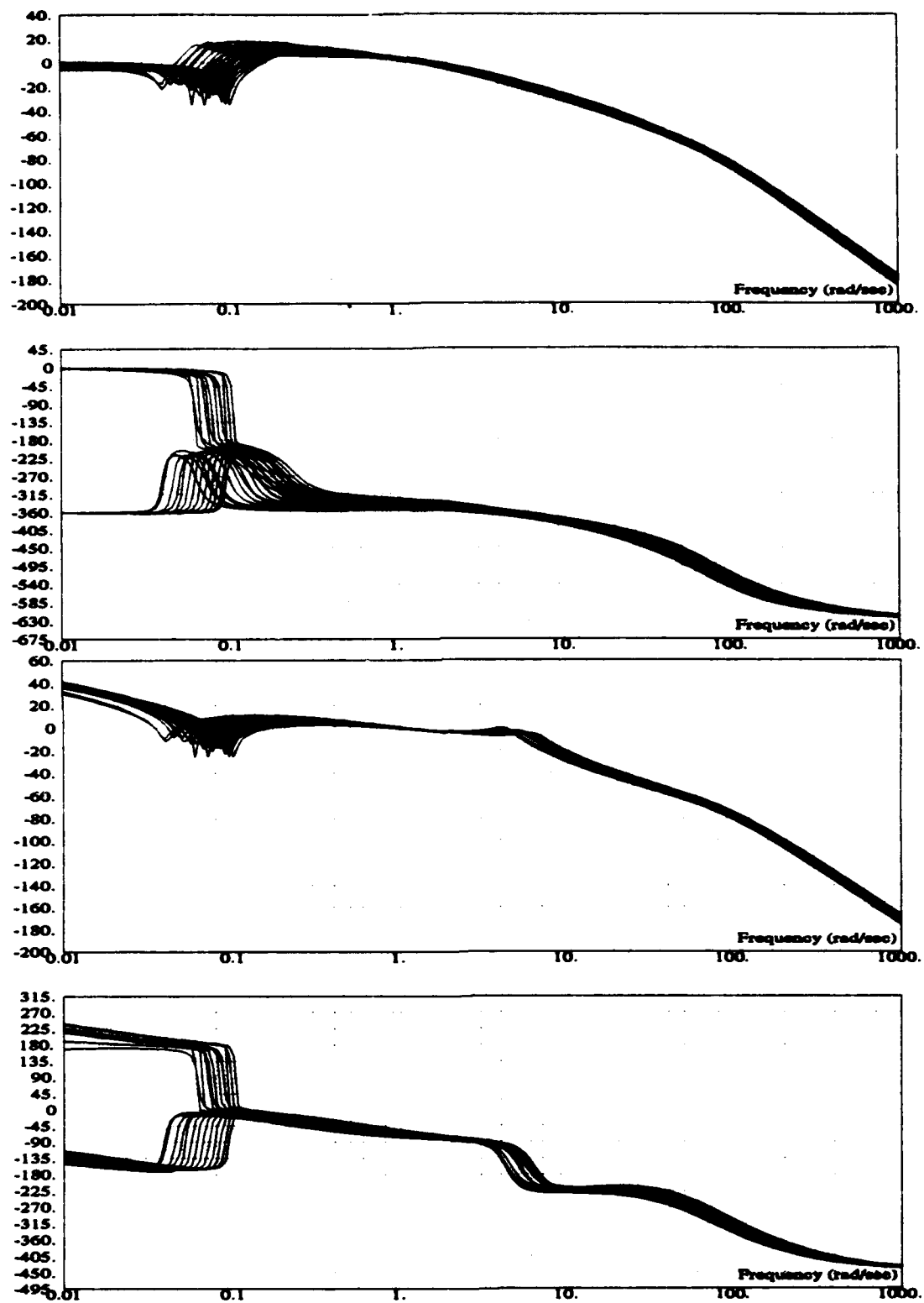


Figure 4.12 Alpha Loop Bode Plots Without (top) and With Inner Compensator

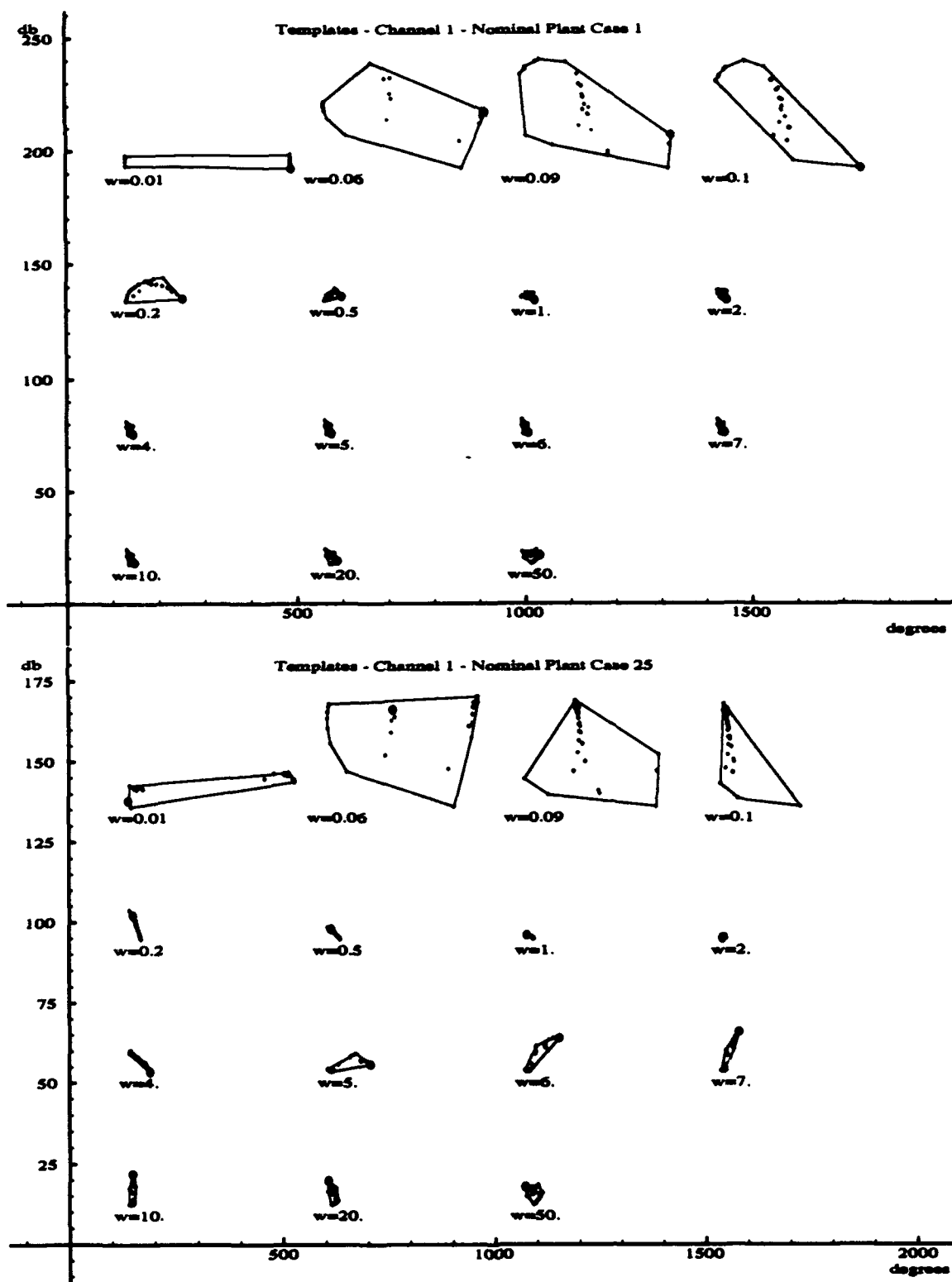


Figure 4.13 Alpha Loop Templates Without (top) and With Inner Compensator

bounds. For the  $N_z$  controlled flight,  $N_z/\alpha$  varies between 5.4 and 76.1. As shown in Fig. 4.2, the maximum  $\omega_{np}$  allowed at 5.4 is 4.41 rad/sec and the minimum  $\omega_{np}$  allowed at 76.1 is 4.62 rad/sec, which indicates that there is no range of  $\omega_{np}$  for the  $N_z$  flight envelope. This lack of valid  $\omega_{np}$  illustrates a limitation of full envelope robust FCS design. The specifications are not constant over the entire envelope, but rather change at each flight condition. The original designs use an  $\omega_{np}$  of 4.5 rad/sec for both the upper and lower tracking bounds, but the natural frequency of the low  $\bar{q}$  aircraft responses is lower than those of the high. Therefore, the upper bound starts with an  $\omega_{np}$  of 4.5 rad/sec and a  $\zeta = 0.35$ , and a zero is added at  $-9$ . The natural frequency and damping of the original poles is modified slightly to match the same Bode plot peak as before.

$$T_{RU}(s) = \frac{2.0544s + 18.49}{s^2 + 3.182s + 18.49} = \frac{2.0544(s + 9)}{s + 1.591 \pm j3.995} \quad (4.6)$$

Although the lower bound's natural frequency should be set to 4.5 rad/sec, it is lowered to 2.5 rad/sec as discussed in section 5.4, and the additional pole is moved to  $-6$ . This change makes the magnitude difference between the upper and lower bounds much greater than before. The final lower tracking bound is

$$T_{RL}(s) = \frac{37.5}{s^3 + 12s^2 + 42.25s + 37.5} = \frac{37.5}{(s + 1.342)(s + 4.658)(s + 6)} \quad (4.7)$$

The Bode plots of these bounds are shown in Fig. 4.14. The original second order bounds are shown as dotted lines while the bounds modified for use with QFT are solid. The  $-12$  dB line is also shown, indicating that the tracking bounds need be met only at frequencies below 15 rad/sec. In addition, a conservative stability bound corresponding to a  $45^\circ$  phase margin angle is used to insure that the final design meets the required  $\gamma = 30^\circ$ . This large phase margin angle is not needed for the stability requirements, but the early designs using  $\gamma = 35^\circ$  have very large overshoots. Disturbance bounds are not required in the remaining longitudinal designs because the trim change disturbance is addressed in the inner loop, and there are no further disturbance rejection requirements.



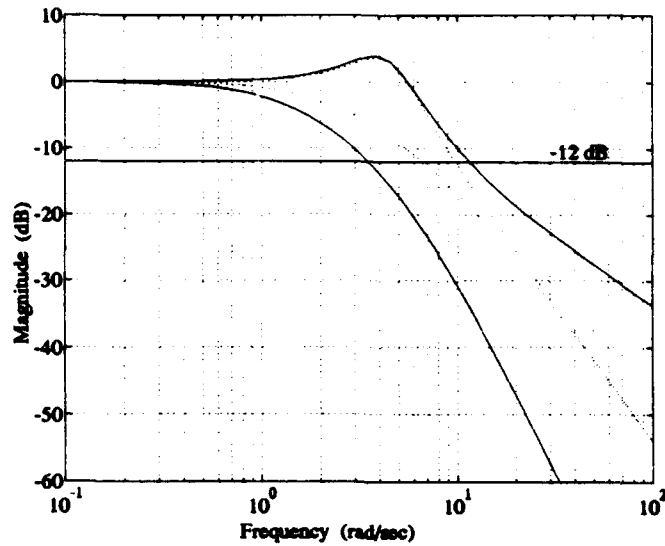


Figure 4.14 Modified  $N$ , Loop Tracking Bounds

**4.4.2 Compensator Design.** The Nichols chart stability and tracking bounds are shown in Figs. 4.15 and 4.16 respectively. As shown in the loop shaping of Fig. 4.17, the primary difficulties in this portion of the design are meeting the 6 rad/sec tracking bound while remaining outside the 30 rad/sec stability bound. Initial attempts to accomplish this are unsuccessful, so the plant corresponding to 1,000 ft, Mach 0.9 is removed to reduce the size of the 30 rad/sec stability bound. A successful system with an  $\omega_\phi < 30$  rad/sec for all but the problem plant is designed, and the problem plant is then returned in an attempt to stabilize it as much as possible. When the previous compensator is tuned, the problem plant attains the required  $30^\circ$  phase margin angle, and all the plants meet the tracking bounds above 0.1 rad/sec. However, in order to meet the tracking specifications while maintaining stability, it is necessary to violate the  $\omega_\phi$  requirement for two of the plants: 1,000 ft, Mach 0.9 and 10,000 ft, Mach 0.9 with cutoff frequencies of approximately 40 and 60 rad/sec respectively. The final compensator is

$$G_n(s) = \frac{-30(s + 1.61 \pm j1.643)(s + 21 \pm j36.373)}{s(s + 4.9 \pm j4.999)(s + 100)} \quad (4.8)$$

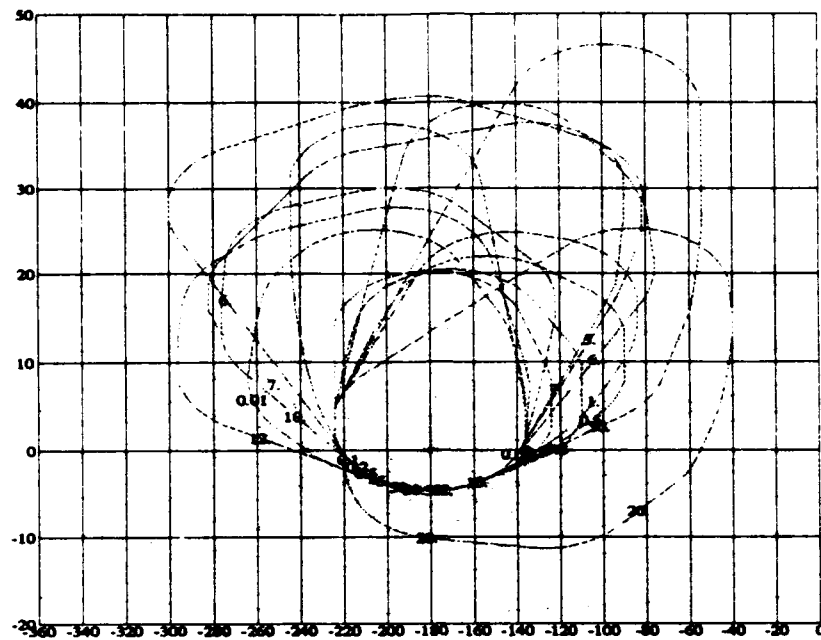


Figure 4.15  $N_z$  Outer Loop Stability Bounds

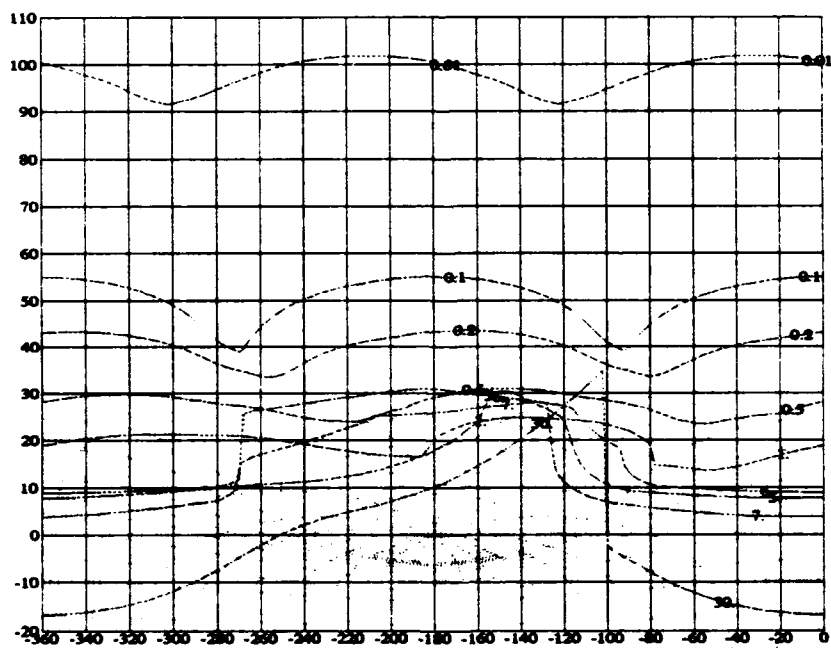


Figure 4.16  $N_z$  Outer Loop Tracking Bounds

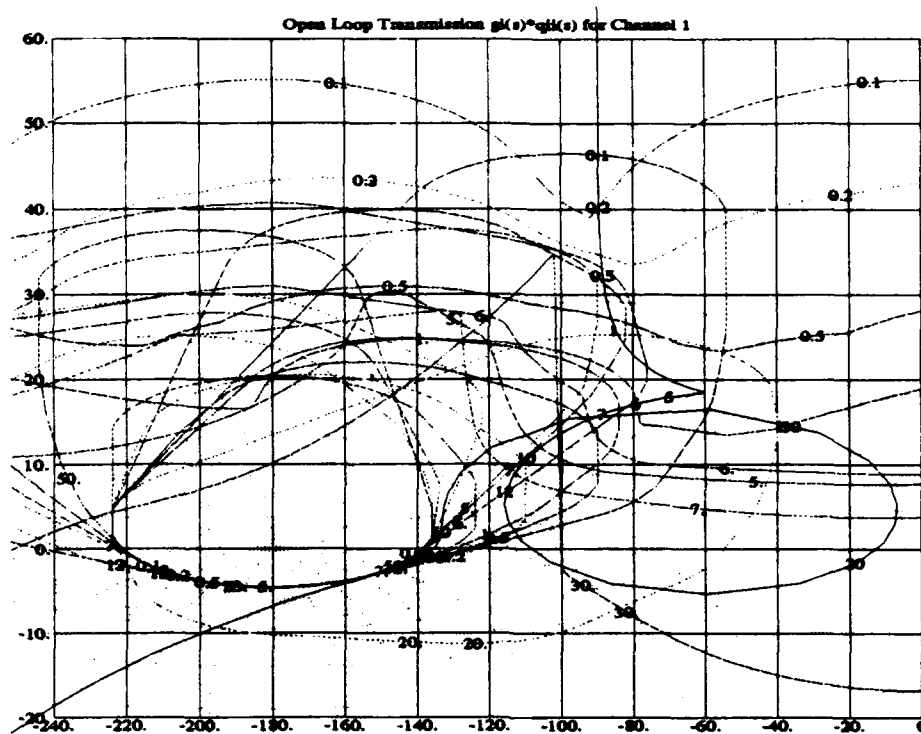


Figure 4.17 Final Loop Shaping for the Outer Loop  $N_z$  Design

The Bode plots of the open loop transfer functions are contained in Fig. 4.18, verifying that the  $\omega_\phi$ 's are below 30 rad/sec for all but two of the plants. Figure 4.19 contains the  $\gamma > 30^\circ$  and  $a > 6$  dB verification.

**4.4.3 Results of the  $N_z$  Design.** A starting point for the prefilter design is obtained using the QFT CAD package, but the prefilter is tuned through time domain simulations until an acceptable time response is achieved. The final prefilter is

$$F_n(s) = \frac{2}{s + 2} \quad (4.9)$$

The  $N_z$  time responses to a step command of 1  $g$  are shown in Fig. 4.20. It is a relatively overdamped system for the high  $\bar{q}$  plants, but the low  $\bar{q}$  plants have some overshoot. However, the elevator responses hint that a pair of highly underdamped poles are present in the design, and this poses a problem in meeting the specifications.

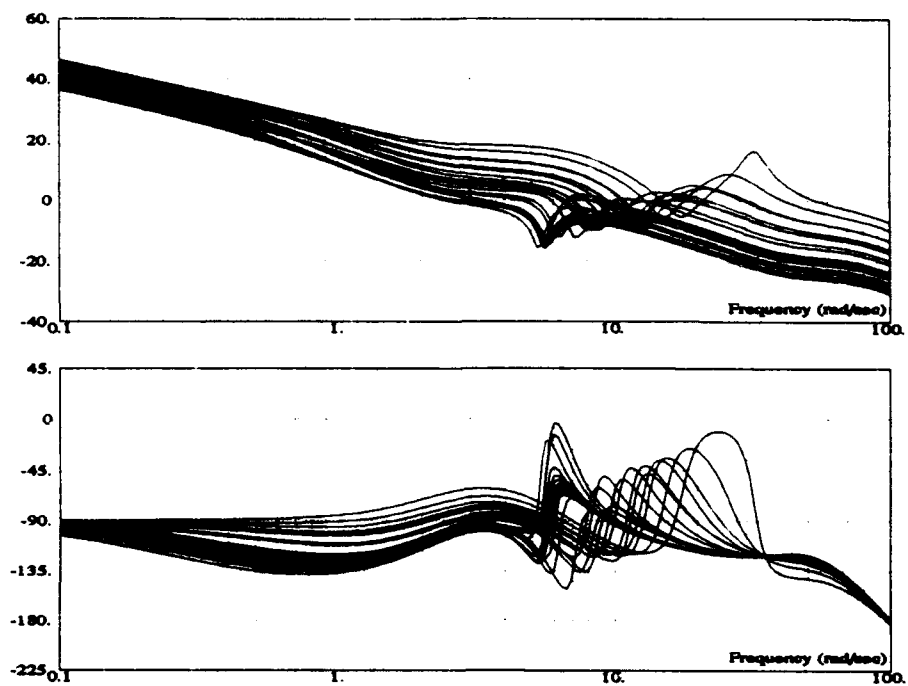


Figure 4.18 Cutoff Frequency Verification for the Longitudinal  $N_z$  Design

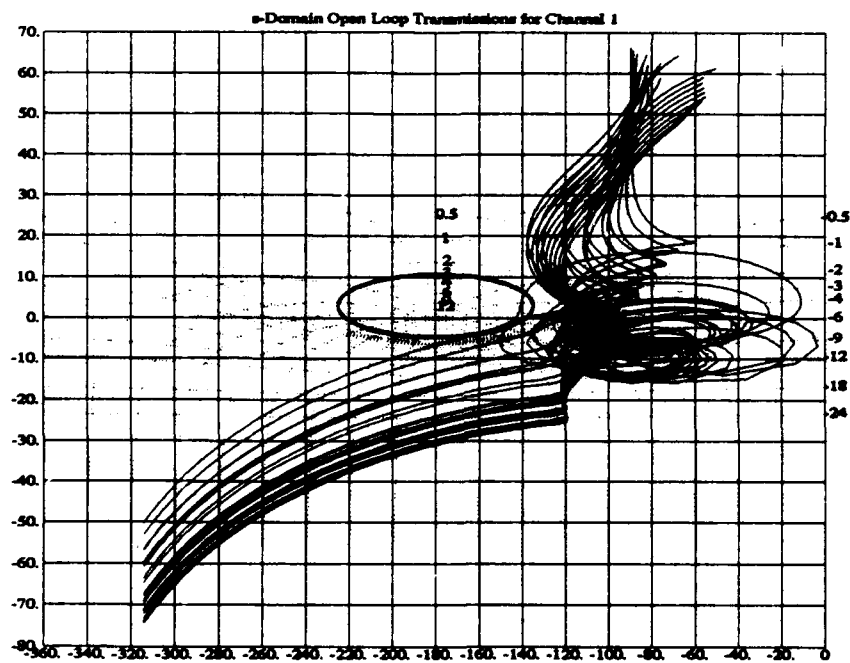


Figure 4.19 Stability Margin Verification for the Longitudinal  $N_z$  Design

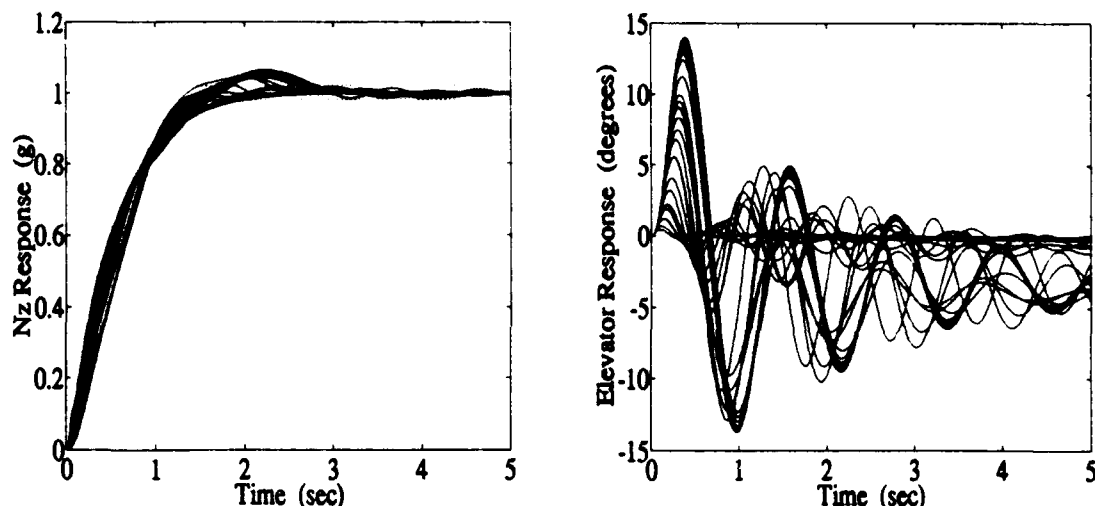


Figure 4.20  $N_z$  and Elevator Time Responses to a Step Input

Initially, an attempt is made to match the  $q/N_{z_{cmd}}$  Bode plots to the fourth order system of Eq. (4.3). This is unsuccessful because the lower order system is given with reference to a step elevator command. A step elevator command does not result in a steady state  $q$ , but a step command to  $N_z$  does. For this reason, the Bode plot matching is not accurate, and the time domain specifications are used for analysis, with the results displayed in Fig. 4.21

The time domain flying qualities specifications are not even close to satisfied. Most of the plants have Level 2 flying qualities, and some are even Level 3 or worse in the effective time delay and transient peak ratio specifications. A zero could be added to  $F_n$  to decrease the effective time delay, but that would require more elevator authority, and the elevator is already saturating at maximum sustainable  $g$ 's. Another pole could be added to  $F_n$  to decrease the transient peak ratio, but this would increase the effective time delay. Any attempt to fix one problem by modifying  $F_n$  only results in making another worse. These results do not mean QFT failed, because the longitudinal flying qualities specifications apply to the  $q$  response, while the QFT design uses  $N_z$  as a control variable. If the  $N_z/N_{z_{cmd}}$  transfer functions are matched to the lower order system in Eq. (4.2), which is where the bounds originated, the time delays, short period natural frequencies, and short period dampings are all within the frequency domain specifications for Level 1

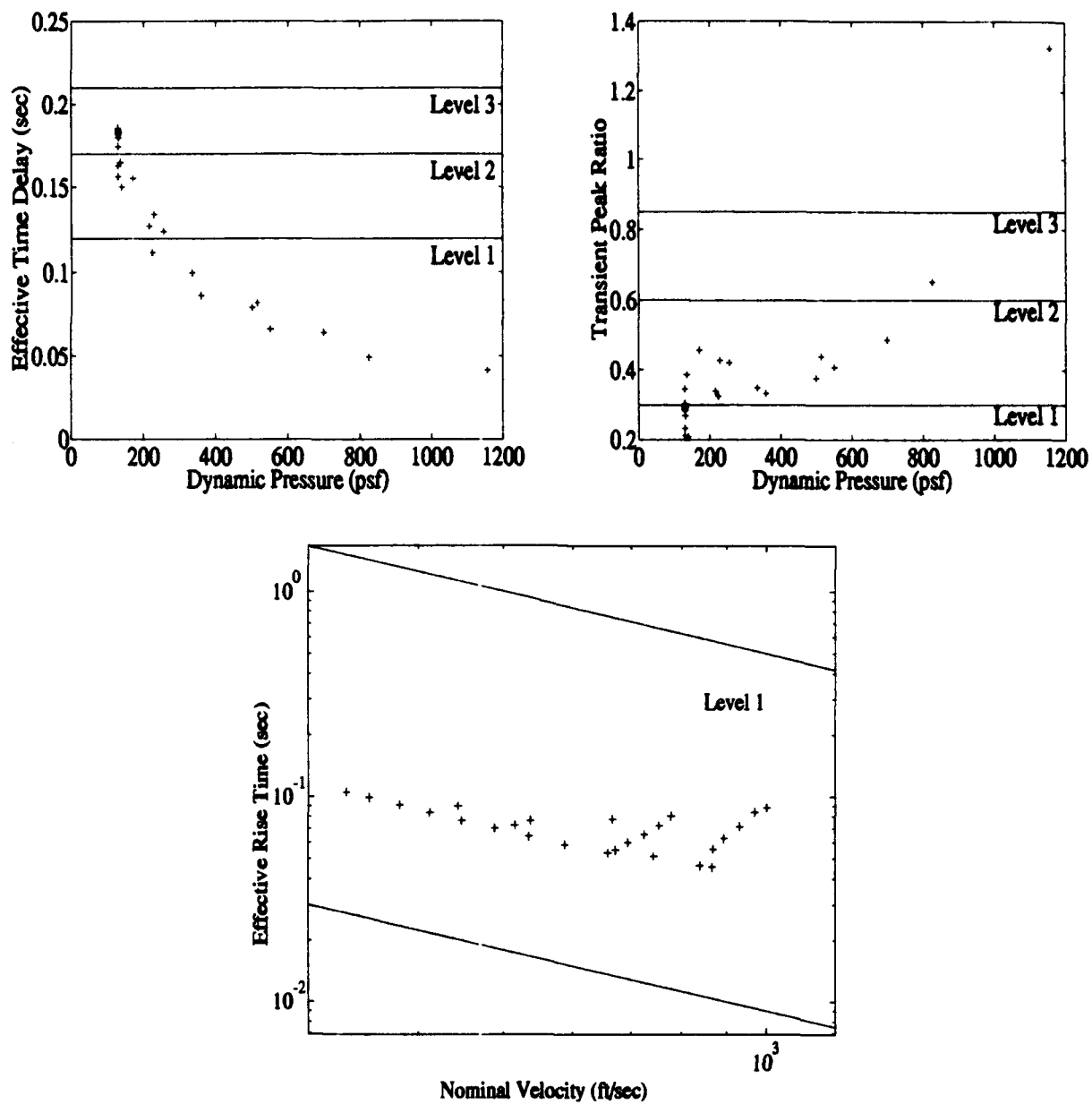


Figure 4.21 Time Domain Specification Results for the  $N_s$  Design

flying qualities. Therefore QFT does what it is designed to do. It is a shortcoming of the flying qualities specifications that they are not based on the desired control variable.

#### 4.5 Outer Loop $\alpha$ Command Design

**4.5.1 Bounds.** For the  $\alpha$  controlled flight ( $\bar{q} < 130 \text{ psf}$ ),  $N_z/\alpha$  varies between 3.49 and 7.62, so from Fig. 4.2 an  $\omega_{sp}$  between 1.46 and 3.54 is required, and a  $\zeta_{sp}$  between 0.35 and 1.3 is used to meet specifications for all flight conditions. The upper bound starts with an  $\omega_{sp}$  of 3.54 and a  $\zeta_{sp}$  of 0.35, and it is then modified by adding a zero at a  $-3$  and adjusting the natural frequency and damping to maintain the height of the peak of the Bode plot in the given  $\omega_{sp}$  range. The final chosen upper bound is

$$T_{RU}(s) = \frac{1.6133s + 4.84}{s^2 + 1.76s + 4.84} = \frac{1.6133(s + 3)}{(s + 0.88 \pm j2.02)} \quad (4.10)$$

For the lower bound,  $\zeta_{sp} = 1.30$  and  $\omega_{sp} = 1.46$  are used, and a pole is added at  $-10$ . This results in a transfer function of

$$T_{RL}(s) = \frac{22.5}{s^3 + 13.9s^2 + 41.25s + 22.5} = \frac{22.5}{(s + 0.704)(s + 3.196)(s + 10)} \quad (4.11)$$

These bounds are shown in Fig. 4.22. The original second order bounds are shown as dotted lines while the bounds modified for use with QFT are solid. Additionally, the  $-12 \text{ dB}$  line is shown, indicating that the tracking bounds need only be met at frequencies less than  $7 \text{ rad/sec}$ . As in the  $N_z$  design, a conservative stability bound of  $\gamma = 45^\circ$  is used.

**4.5.2 Compensator Design.** The Nichols chart stability and tracking bounds are similar to the previous designs, so they are shown in Figures D.1 and D.2 respectively. Plant case 25 is chosen as the nominal plant, because it is on the top of the templates in the cutoff frequency region. The tracking bounds are not very restrictive at higher frequencies, but the low frequency tracking bounds are very high due to the  $180^\circ$  phase shifts in the  $\alpha/\delta_e$  transfer functions at these frequencies. This causes the tracking bounds to be violated below  $0.2 \text{ rad/sec}$ . All the high frequency bounds can be met with a second order compensator, but then the low frequency stability bounds are violated. To alleviate

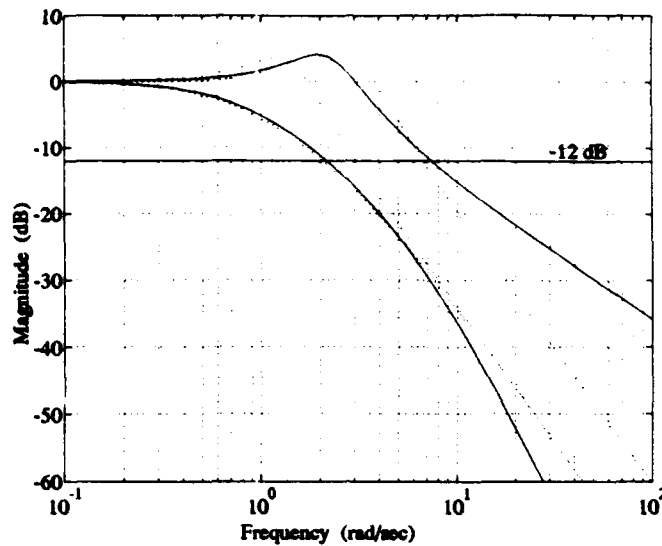


Figure 4.22 Outer  $\alpha$  Loop Tracking Bounds

this, an integrator is added to increase the low frequency loop transmission magnitudes. Three zeros are then needed to pull the loop outside all the stability bounds. Finally, two poles are added at  $-100$  to make an equal order compensator of

$$G_a(s) = \frac{2300(s + 0.4)(s + 2.7)(s + 10)}{s(s + 100)(s + 100)} \quad (4.12)$$

The loop shaping is similar to the previous designs and is shown in Fig. E.3. The Nichols chart stability plots for the closed loop systems are shown in Fig. 4.23, but their appearance is not correct. The plants on the right side of the plot appear to be completely stable, but they are not. This instability is caused by the presence of nonminimum phase zeros in the low speed plants. The time constants associated with these unstable poles are so high that their dynamics are outside the time period of interest. Additionally, each of the poles lies almost directly on top of its corresponding nonminimum phase zero, making the time domain contribution of these poles extremely negligible.

**4.5.3 Results of the  $\alpha$  Design.** As before, the QFT CAD package is used to find a starting point for the prefilter, and the prefilter is adjusted until an acceptable time



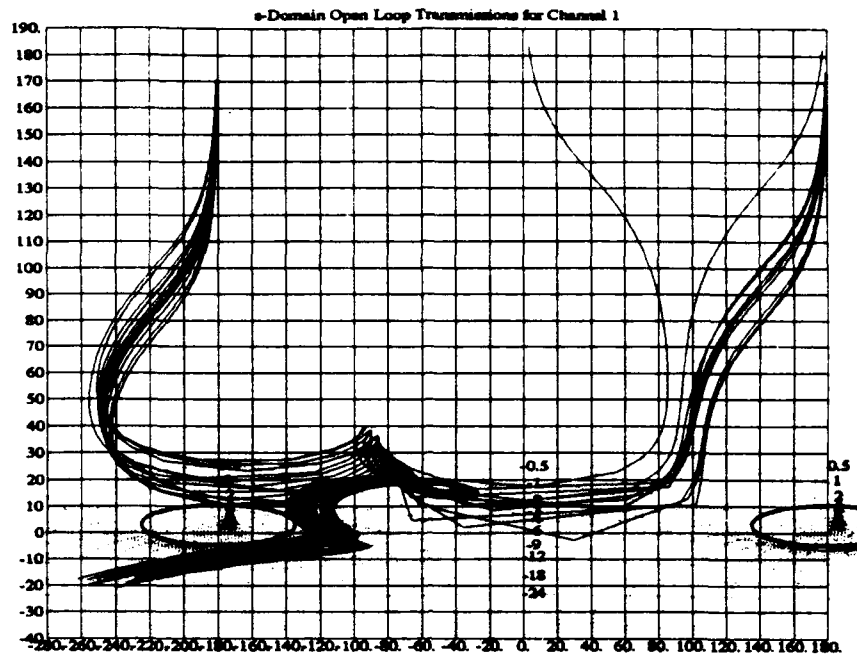


Figure 4.23 Stability Verification for the Longitudinal  $\alpha$  Design

response is achieved. The final prefilter is

$$F_a(s) \frac{4}{s + 1.4 \pm j1.428} \quad (4.13)$$

The time responses of  $\alpha$  to a step command of  $1^\circ$  for each plant are shown in Fig. 4.24. It is an underdamped system with a minor overshoot, caused by the selection of the prefilter poles as slightly underdamped. Virtually any response can be achieved just by modifying the prefilter because of the robustness that is present in the system, as evidenced by the tight grouping of the  $\alpha$  responses.

The time responses of the elevator to the same  $1^\circ$  step input are also shown in Fig. 4.24. A one degree change in  $\alpha$  requires a maximum of  $1.2^\circ$  of elevator deflection. If the maximum elevator deflection is approximately  $21^\circ$ , then this control system allows a step command of  $17.5^\circ$ . Any higher step command is not allowed because of actuator saturations. A faster  $\alpha$  response can be produced with a first order prefilter, but the initial elevator requirements are much larger, further limiting the possible step  $\alpha$  commands.

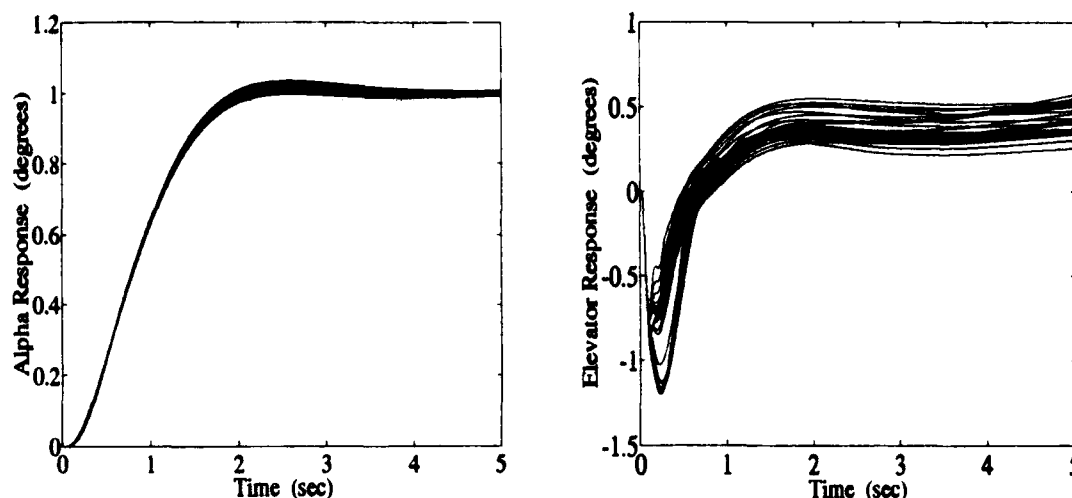


Figure 4.24  $\alpha$  and Elevator Time Response to a  $1^\circ$  Step Input

As in the  $N_z$  design, the time domain specifications on the  $q$  response are used to determine if the system meets flying qualities requirements, and these results are shown in Fig. 4.25. All of the specifications are easily met, with none of the resonance problems present the  $N_z$  design.

#### 4.6 $C^*$ Outer Loop Design

An insight can be gained from the  $N_z$  design by examining the transient peak ratio results in Fig. 4.21. This time domain specification is based on the frequency domain  $\zeta_p$  specification. If one plots the final  $q/N_{zcmd}$  transfer functions, a resonance is noticed that can readily be seen in the elevator time responses. The reason this resonance is not present in the  $N_z$  time responses is the cancellation of these closed loop resonant poles by the highly underdamped zeros present in the  $N_z/\delta_e$  transfer functions.

A solution to this resonance problem can be found in state feedback theory, where another state is added to the controlled variable to move the design zeros away from the low  $\zeta$  positions of the  $N_z$  design. There is also a flight control theory that suggests the pilot does not fly  $N_z$ , but rather a combination of  $N_z$  and  $q$  called  $C^*$ . From these theories, it is decided to mix a portion of  $q$  into the control ratio to remove the anti-resonance. It also makes sense to add  $q$  since the flying qualities specifications are  $q$  based. Because positive

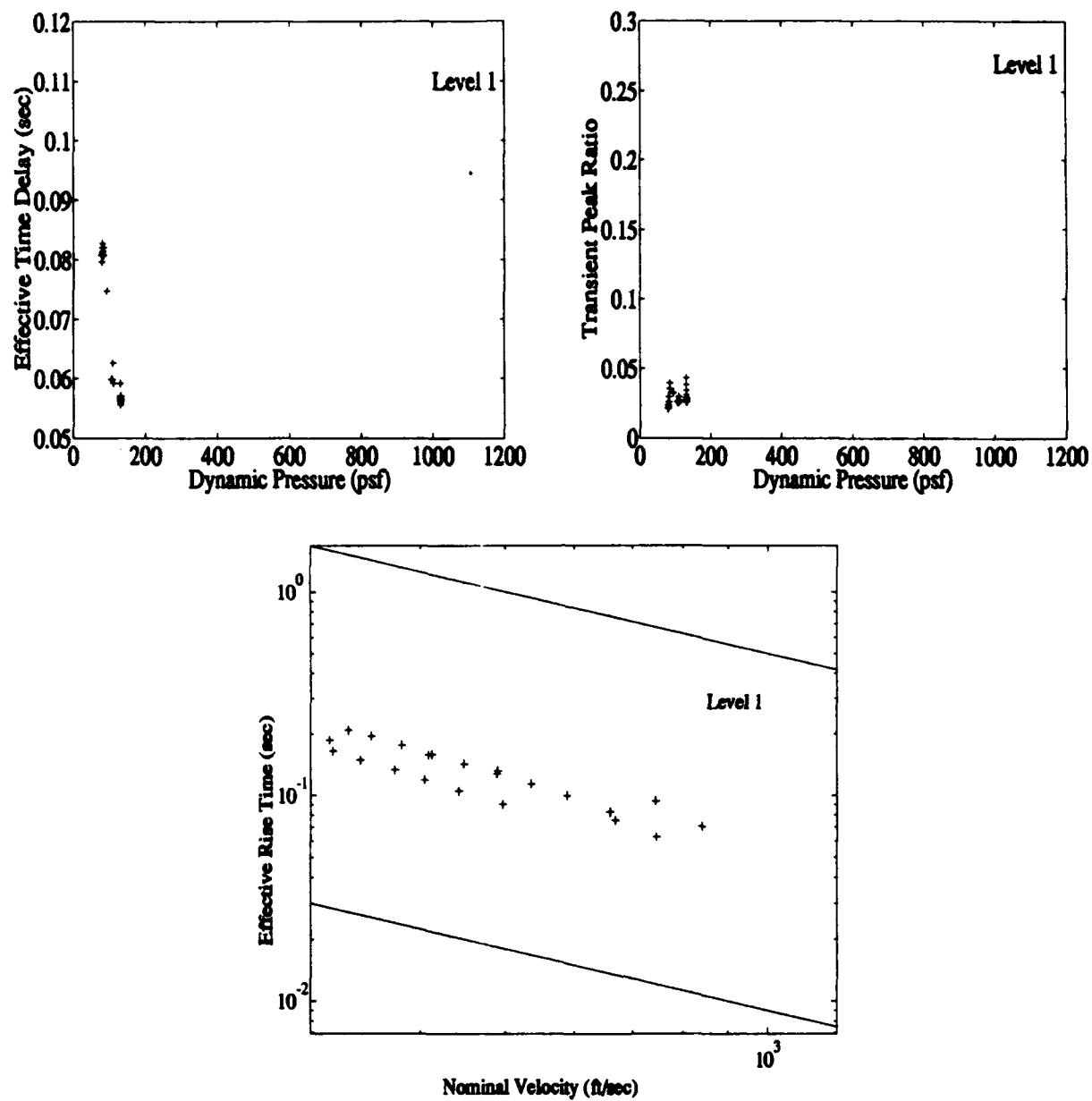


Figure 4.25 Time Domain Specification Results for the  $\alpha$  Design

$q$  is in the opposite direction of positive  $N_z$ , negative  $q$  is added to the control variable. Through experimentation, the following control variable is obtained.

$$C^* = N_z - 0.1q \quad (4.14)$$

Figure 4.26 demonstrates that the  $C^*$  variable succeeds in greatly reducing the anti-resonance present in the  $N_z$  Bode plots of Fig. 4.10.

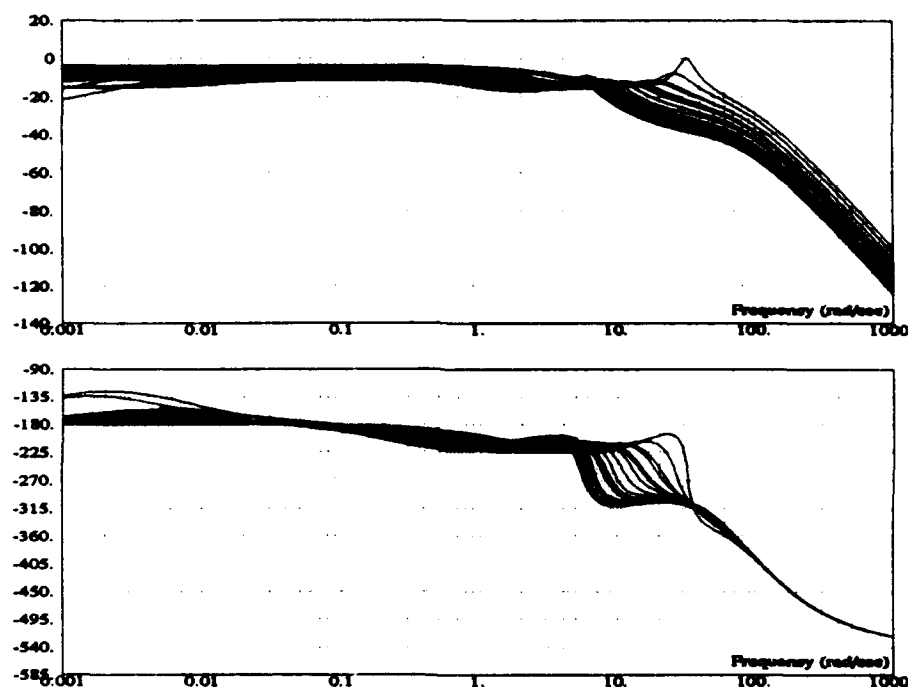


Figure 4.26  $C^*/\delta_{\epsilon_{cmd}}$  Bode Plots before Inner Loop Redesign

**4.6.1 Bounds.** There are no flying qualities specifications for  $C^*$ . Therefore, because the  $N_z$  design illustrates the ineffectiveness of applying tracking bounds to a variable that is not related to the specifications, the only bounds used in this design are the stability bounds. These are set to a conservative phase margin angle of  $35^\circ$  to insure the required  $\gamma = 30^\circ$  is met.

**4.6.2 Redesign of the Inner Loop.** When an initial outer loop design is attempted with  $C^*$ , it is discovered that the primary limitation in the design is the height of plant #4 (1,000 ft Mach 0.9) on the template. This peak at 30 rad/sec can readily be seen in the

$N_z/\delta_{e_{cmd}}$  Bode plots of Fig. 4.10. This resonance is present even when  $C^*$  is used (Fig. 4.26) and is caused by the proximity of the open loop transmission to the stability point on the Nichols chart in the inner loop design. To try to alleviate this problem, the stability bound in the inner design is increased to achieve a  $\gamma = 15^\circ$ , and the  $G_q(s)$  zeros and gain are modified to move the transmission away from the stability point while still meeting the 30 rad/sec phase margin frequency. The 0.157 disturbance bound is only slightly violated, but the outside disturbance bounds in the QFT CAD package are believed conservative [12]. The loop shaping is shown in Fig. E.5 for the new inner loop compensator given by

$$G_{qc}(s) = \frac{-2.36(s + 14)(s + 15)}{s(s + 100)} \quad (4.15)$$

The disturbance rejection of the system is as predicted. Figure 4.27 shows both the frequency and time domain responses. The frequency domain response indicates that the -30 dB requirement is met for all frequencies below 0.157 rad/sec as shown by the loop shaping. The time domain responses show a response higher than 0.032, but that is due to the initial transient related to the position of the closed loop poles. If the simulation is run out another cycle, the response remains below  $\pm 0.032$ .

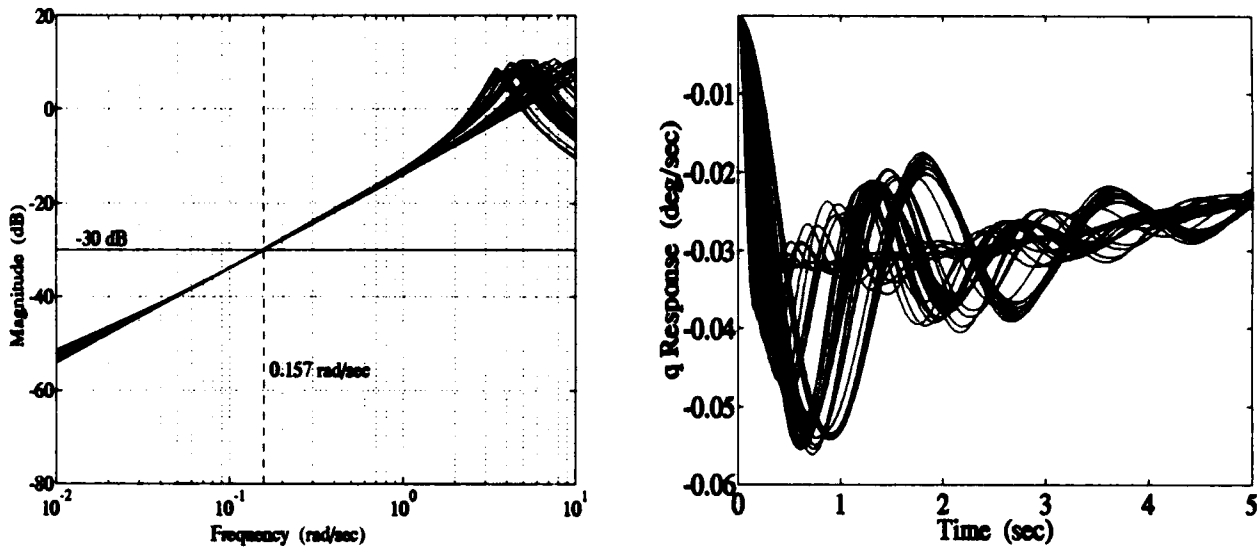


Figure 4.27 Inner Loop Disturbance Responses

**4.6.3 Outer Loop Design.** When the inner loop is redesigned, the templates in the 30 rad/sec range decrease in size, and the design is then relatively easy to accomplish. A PI compensator is all that is required to meet all the stability bounds. The  $\omega_\phi = 30$  rad/sec requirement is only violated for one plant (1,000 ft Mach 0.9), and it is still less than 40 rad/sec. This is a marked improvement over the  $N_z$  design, both in compensator complexity and system bandwidth. The loop shaping is shown in Fig. E.8 for the outer loop compensator given by

$$G_c(s) = \frac{-4(s+3)}{s} \quad (4.16)$$

The design is successful in meeting the  $a$  and  $\gamma$  requirements as shown in Fig. 4.28, and Fig. E.9 contains the  $\omega_\phi$  verification.

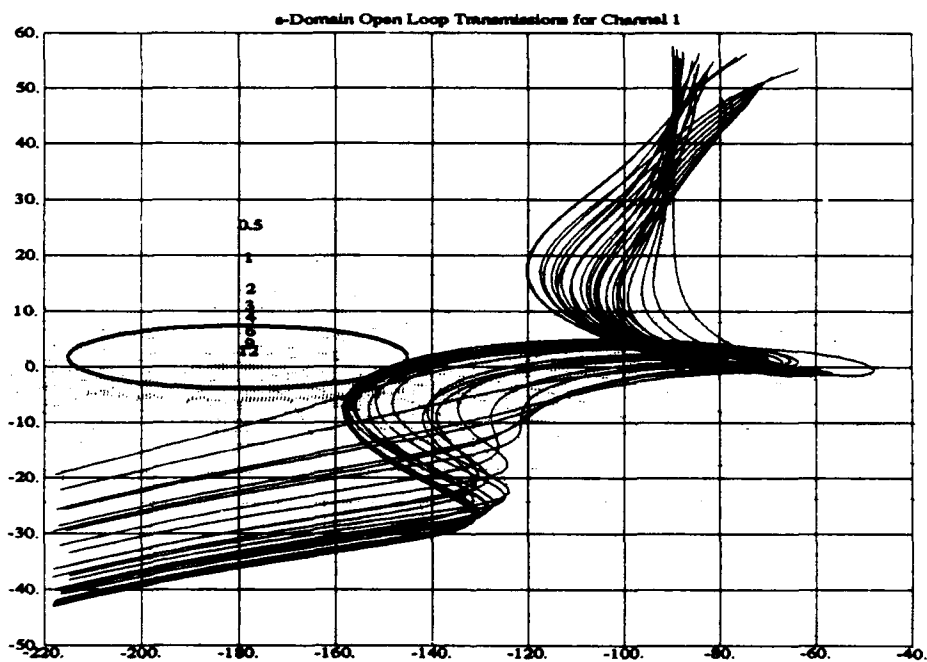


Figure 4.28 Stability Margin Verification for the Longitudinal  $C^*$  Design

**4.6.4 Results of the  $C^*$  Design.** Although  $C^*$  is fed back to the compensator,  $N_z$  still remains the desired output variable. Because of this, the QFT CAD prefilter program cannot be used. When a first order prefilter is inserted to examine the time responses and specification results, several points are noticed:

1. The effective time delay of the low  $\bar{q}$  plants is too long.
2. The final  $N_z$  value is not equal to the commanded  $N_z$  (Fig. 4.29).
3. The elevator requirements are much less than the  $N_z$  design.
4. There is a "waver" in the initial  $N_z$  response of plant #4.

The effective time delay can be reduced by decreasing the time constant of the prefilter pole or by adding a zero. While there is plenty of elevator authority to spare, it is discovered that for the same increase in elevator requirements, adding a zero has a much greater effect on decreasing the effective time delay than decreasing the time constant. The final value of  $N_z$  is not equal to the commanded  $N_z$  because the feedback variable is  $C^*$ , which contains a component of  $q$ . This is remedied by increasing the gain of the prefilter to cancel out the "average" effect of  $q$ . When the zero is added and the gain is increased, all the effective time delays fall within Level 1 flying qualities specifications. However, the "waver" spreads to additional plants and increases in severity as shown in Fig. 4.29.

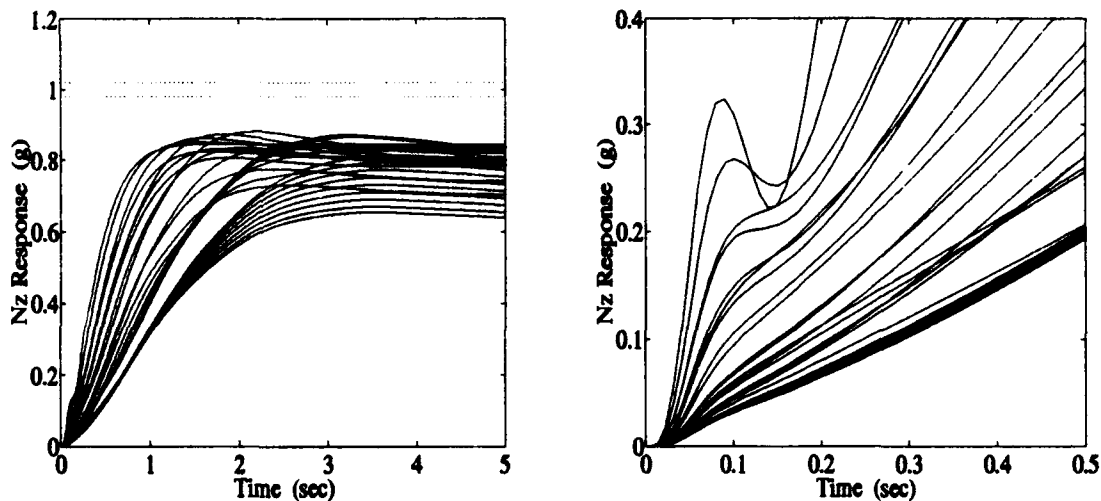


Figure 4.29  $N_z$  Time Response with First Order Prefilter (left) and Zero Added (right)

The prefilter is then scheduled on  $\bar{q}$  to eliminate the "waver" while still maintaining Level 1 time delays. To accomplish this, a "switching" scheme is implemented where the original first order prefilter is retained for those plants with a  $\bar{q}$  above 400 psf, and an additional first order lead network is added for those below 400 psf. The gains in both are

adjusted so the final  $N_z$  value is close to that commanded. The  $\bar{q} > 400$  psf prefilter is given by

$$F_c(s) = \frac{6.1}{s + 5} \quad (4.17)$$

while the  $\bar{q} < 400$  psf prefilter is

$$F_c(s) = \left( \frac{8.32(s + 10)}{(s + 80)} \right) \left( \frac{6.1}{(s + 5)} \right) \quad (4.18)$$

The  $N_z$  and elevator time responses are shown in Fig 4.30. The final  $N_z$  values are not exactly correct, but the prefilter gains are adjusted so they are closer where the higher  $N_z$  commands are physically possible. Furthermore, the elevator requirements for this design are much less than those of the straight  $N_z$  design, allowing much higher command accelerations.

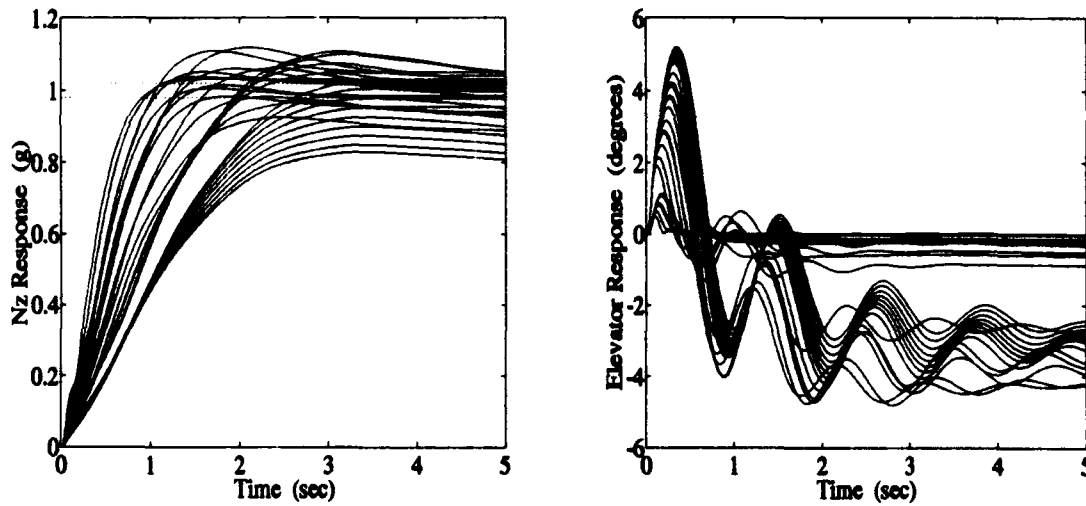


Figure 4.30  $N_z$  and Elevator Time Response to Step Input for the  $C^*$  Design

The time domain flying qualities specifications are used in this portion of the design as well because this is still basically an acceleration command design. Figure 4.31 shows that Level 1 flying qualities are met for all plant cases.

**4.6.5 Redesign of the  $\alpha$  Loop.** A new  $\alpha$  loop design is now undertaken based on the modification of the inner loop compensator. Because the tracking bounds are not



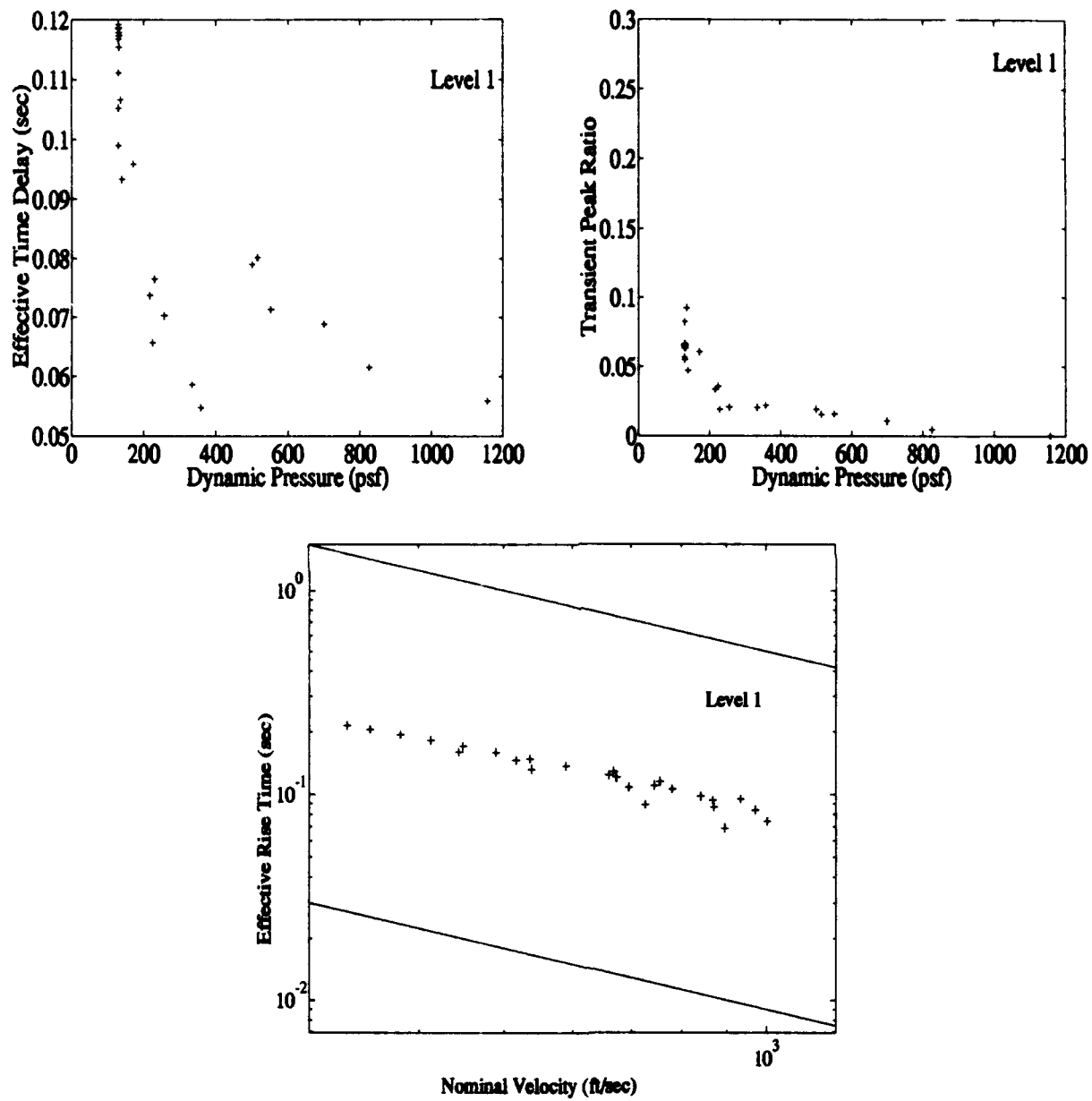


Figure 4.31 Time Domain Specification Results for the  $C^*$  Design

restrictive, only the stability bound of  $\gamma = 35^\circ$  is used in this redesign. Because the redesigned inner loop causes only a minor change in the  $\alpha$  loop, the outer loop redesign consists of minor modifications to the previous  $\alpha$  compensator. The new compensator is given by

$$G_a(s) = \frac{3100(s + 0.6)(s + 4)(s + 10)}{s(s + 100)(s + 100)} \quad (4.19)$$

The  $\omega_\phi$  and stability margin verification plots are similar to the previous design and are shown in Figs. E.11 and E.12. The damping of the prefilter poles is increased slightly to offset the use of a lower value of  $\gamma$  in this design, with the result:

$$F_a(s) = \frac{4}{s + 1.6 \pm j1.2} \quad (4.20)$$

The  $\alpha$  and elevator time responses are shown in Fig. 4.32. Again, there is a high degree of robustness, evidenced by the tight grouping of the  $\alpha$  responses. The elevator requirements are slightly higher than those of the initial  $\alpha$  design, cutting the allowable step  $\alpha$  command to approximately  $16^\circ$ . The specification results are similar to the previous design in that they all meet Level 1 flying qualities (Fig. 4.33).

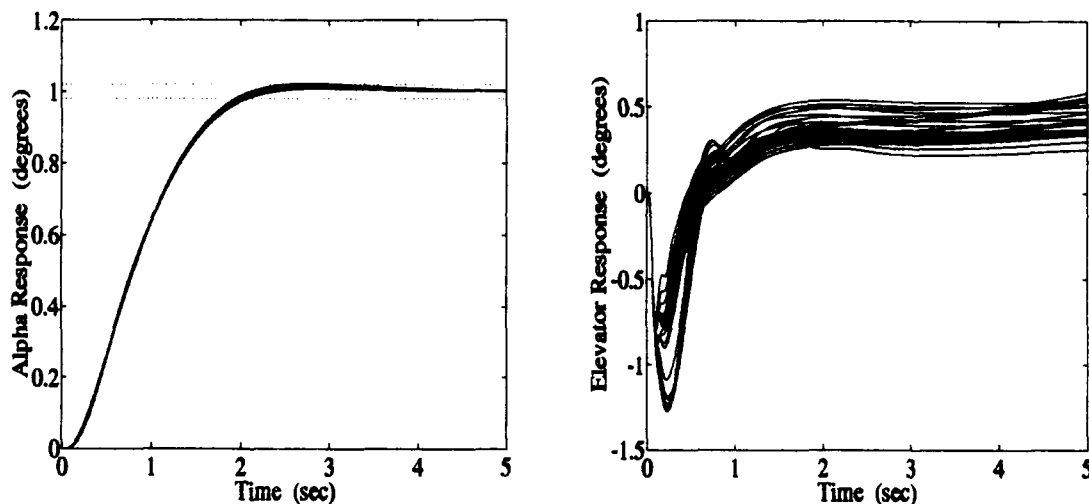


Figure 4.32  $\alpha$  and Elevator Time Response to Step Input for the  $C^*$  Design

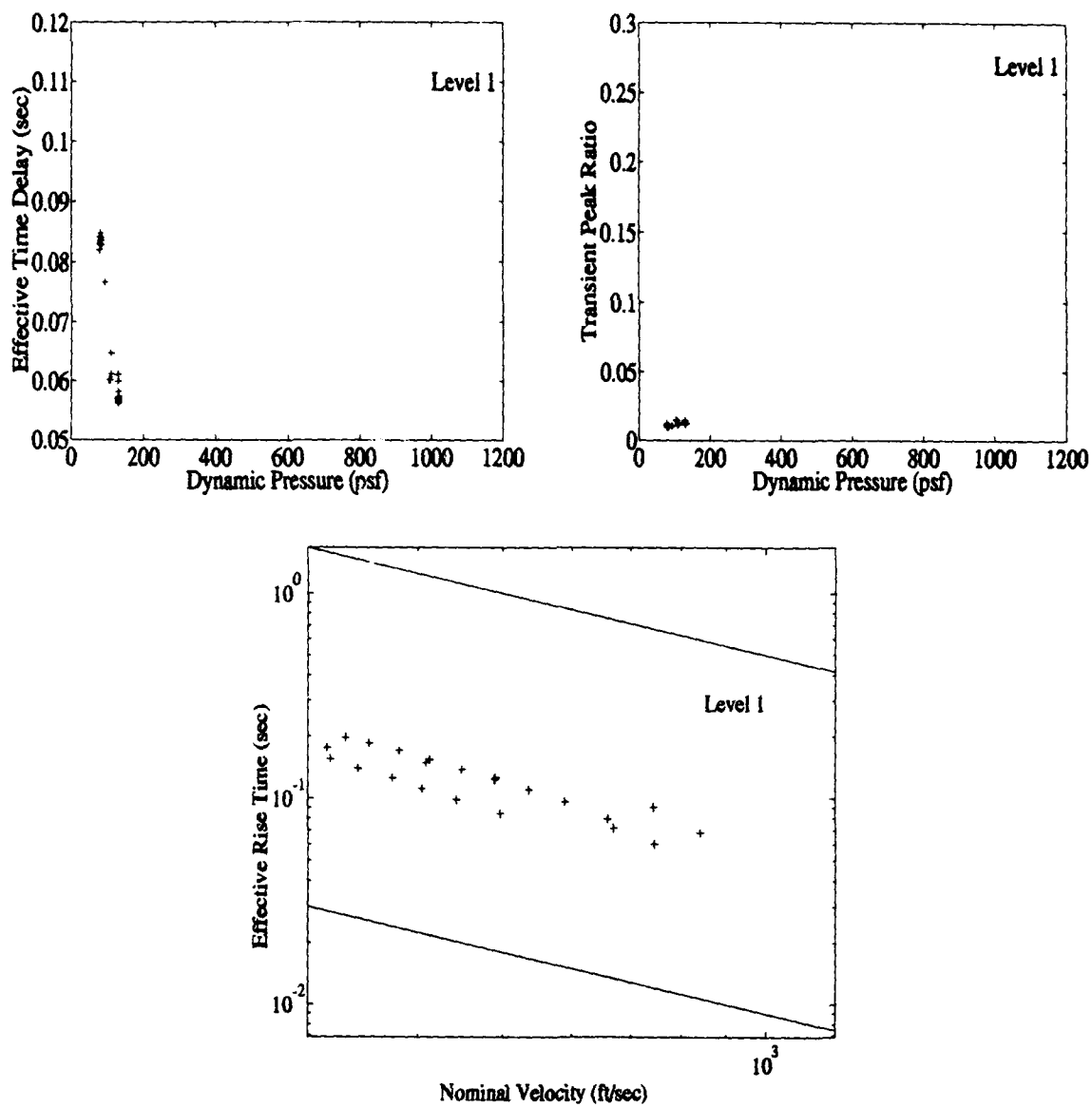


Figure 4.33 Time Domain Specification Results for the  $C^* \alpha$  Design

#### 4.7 Chapter Summary

This chapter illuminates the ability of QFT to design a full envelope flight compensator, but it also demonstrates how the specifications given for full envelope flight control are in conflict with the QFT robust design method.

The  $N_z$  design demonstrates success in that the  $N_z$  frequency responses can all be placed within the specified bounds. Additionally, a Bode plot matching to the second order approximation of the fourth order system in Eq. (4.2) indicates that all specifications are met. However,  $n'$  refers to the normal acceleration of the center of gravity of the aircraft, which is quite different than the normal acceleration at the pilot station. It is quite difficult to use QFT to control  $n'$  because it is a nonminimum phase state with a variable zero. Therefore  $N_z$  is used, and it introduces an anti-resonance to the system that causes several problems.

The  $N_z$  design has problems in the amount of elevator authority required, both in magnitude and rate. The uncanceled resonant poles in the  $q$  response also cause the system to fall short of Level 1 specifications. The  $C^*$  design uses much less elevator, but perfect tracking in  $N_z$  is lost. The  $\alpha$  designs are very robust, as evidenced by the tight grouping of the time responses. This should allow the  $\alpha$  design to work in the shaved off boundary layer or beyond.

## V. Useful Insights Gained From the Longitudinal Design

### 5.1 Introduction

The initial longitudinal compensator design, although incorrect in many ways, led to many useful insights that are used in the lateral design. This chapter describes the initial design and explains each of the lessons learned for the benefit of future designers.

### 5.2 Description of the Initial Design

**5.2.1 Inner Loop Design.** The only bound used in this portion of the design is the stability bound, which is set to a  $1^\circ$  phase margin angle just to insure robust stability. One integrator is added to increase the system type and to insure zero steady state disturbance response. Also, this design uses a first order actuator model, so only one zero is needed to pull the nominal loop around the stability bounds. Therefore, the initial inner loop compensator is just a PI compensator given by

$$G_q(s) = \frac{-1(s+7)}{s} \quad (5.1)$$

The initial zero and gain choice are fortunate in that they cause the disturbance rejection of the system to be above the 30 dB rejection discussed in section 3.6. As in the final design, this compensator stabilizes all the plants except one, but again, the unstable pole's dynamics are outside the time period of interest. This design also reduces the size of the outer loop templates similar to the final design.

#### 5.2.2 Outer Loop $N_z$ Command Design.

**Bounds.** For the  $N_z$  portion of the design, there is a problem in that there is no one valid  $\omega_{sp}$  over the entire range of  $N_z/\alpha$ . The design proceeds using an  $\omega_{sp}$  of 4.5 rad/sec to examine how far the actual responses fall outside the bounds. The upper bound starts with the minimum  $\zeta_{sp} = 0.35$  and adds a zero at  $-9$ . The natural frequency and damping of the original poles are modified slightly to match the same Bode plot peak

as the unmodified bounds:

$$T_{RU}(s) = \frac{2.0544s + 18.49}{s^2 + 3.182s + 18.49} = \frac{2.0544(s + 9)}{s + 1.591 \pm j3.995} \quad (5.2)$$

The lower bound starts with the maximum  $\zeta_{sp} = 1.30$  and a pole is added at  $-10$ . The damping is adjusted to try to maintain the lower frequency match with the final result

$$T_{RL}(s) = \frac{202.5}{s^3 + 20.8s^2 + 128.25s + 202.5} = \frac{202.5}{(s + 2.415)(s + 8.385)(s + 10)} \quad (5.3)$$

These bounds are shown in Fig. 5.1. The original bounds are shown as dotted lines while the bounds modified for use with QFT are solid. The  $-12$  dB line is also shown indicating that the tracking bounds need be met only to a frequency of around 15 rad/sec.

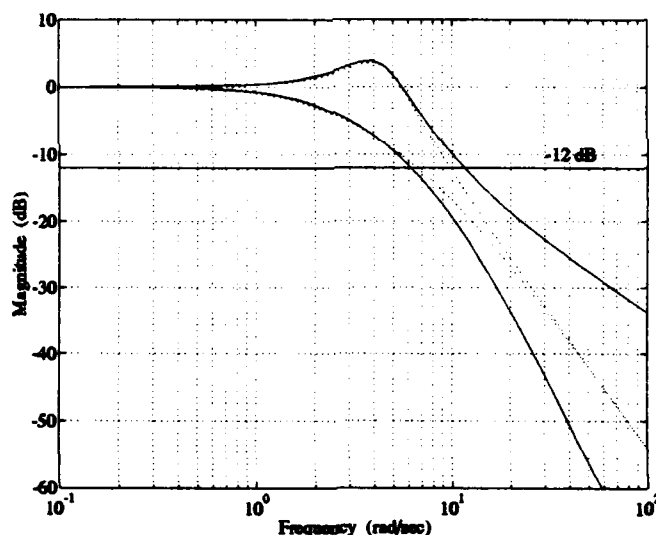


Figure 5.1 Original  $N_z$  Outer Loop Tracking Bounds

*Compensator Design.* As seen in Fig. 5.2, a "loop" exists in the plot of the nominal loop transmission. This feature is retained because it brings the  $L_m L_o(j\omega)$  above the tracking bound at that frequency. Again, because the first order actuator model is used, a simpler compensator is realizable because the extra phase lag added by the fourth

order model is not present. The final compensator is

$$G_n(s) = \frac{-6407.62(s + 0.3)(s + 3.5)(s + 50)}{s(s + 3.48 \pm j4.64)(s + 200)} \quad (5.4)$$

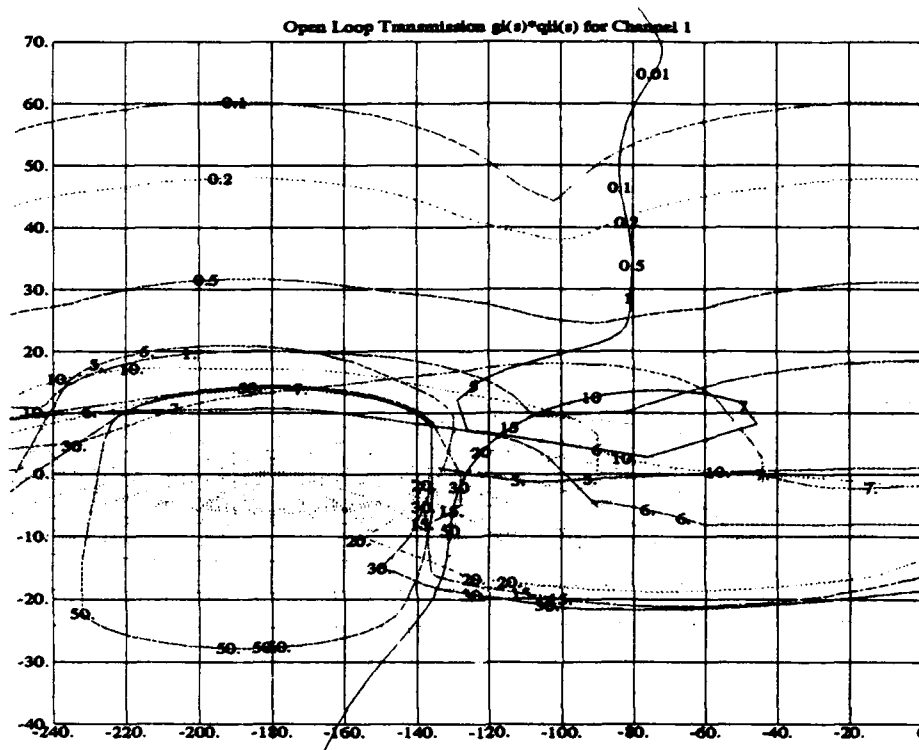


Figure 5.2 Initial  $N_s$  Loop Shaping

**Prefilter Design.** A starting point for the prefilter design is obtained using the QFT CAD package, and the filter is adjusted in the time domain simulations until the desired time response is achieved. The final prefilter is

$$F_n(s) = \frac{25}{s + 3.75 \pm j3.307} \quad (5.5)$$

**Time Domain Results.** The plant time responses to a step  $N_s$  command of 1  $g$  are shown in Fig. 5.3. It is a highly robust system with a second order type response. When a second order conversion, such as the one explained in the references [10], is performed on the  $N_s$  time responses, the natural frequency of the responses all fall

within flying qualities specifications as displayed in Fig 5.4. The problem predicted by the lack of a valid  $\omega_{sp}$  does not occur because the plants with a lower  $N_z/\alpha$  ratio respond with a natural frequency that is slightly lower than the higher  $N_z/\alpha$  plants. This slower response allows all the plants to fit within the given specifications.

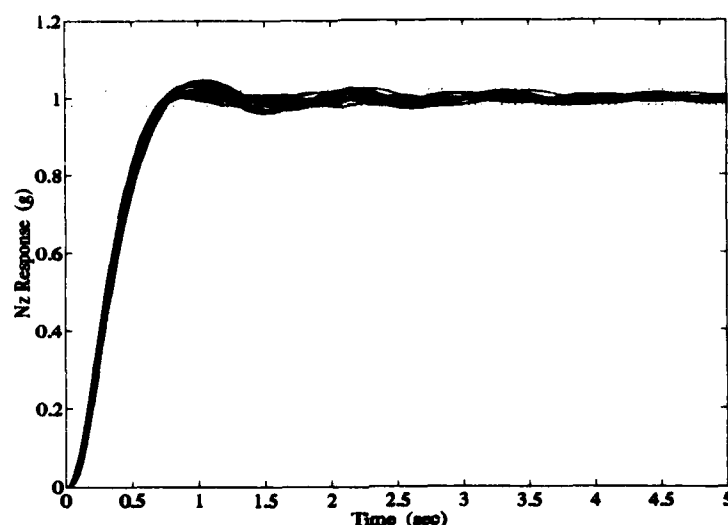


Figure 5.3  $N_z$  Time Response to a Step Input

### 5.2.3 Outer Loop $\alpha$ Command Design.

**Bounds.** The stability bounds for this initial  $\alpha$  design use a  $45^\circ$  phase margin angle, rather than the value of  $35^\circ$  used in the final design. This is originally done to keep the overshoot to a minimum, but proves to be unnecessary in the final design.

**Compensator Design.** As in the final design, the tracking bounds are not very restrictive at higher frequencies, allowing a compensator with a low bandwidth to be designed. However, the low frequency tracking bounds are very high, and are violated below 0.2 rad/sec. This  $\alpha$  loop compensator is given by

$$G_a(s) = \frac{600(s + 0.5)(s + 7.2 \pm j3.487)}{s(s + 54 \pm j26.153)} \quad (5.6)$$



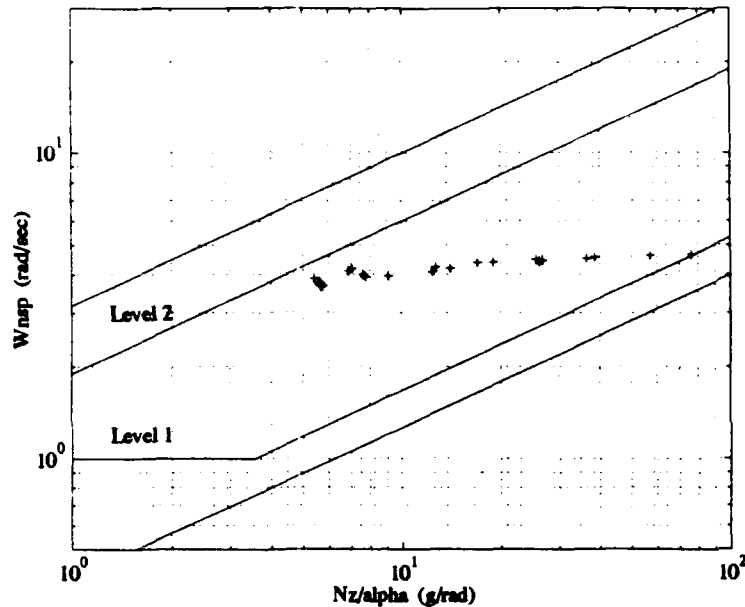


Figure 5.4  $\omega_{nap}$  Results from Second Order Time Response Conversion

The tracking bounds could have been met with a second order compensator, but the low frequency stability bounds would have been violated by some of the plants. This design has the same problem with unstable closed loop plants as the final design, but the time constants associated with these unstable poles are so high that their dynamics are outside the time period of interest.

*Prefilter Design.* Again, the QFT CAD package is used to find a starting point for the prefilter design. The prefilter is adjusted until the desired time response is obtained. This prefilter is

$$F_a(s) \frac{4}{s + 1.5 \pm j1.323} \quad (5.7)$$

*Time Domain Results.* The time domain responses of  $\alpha$  to a step command of  $1^\circ$  are identical to those obtained with the final design, right down to the second order conversions.

### 5.3 Problems with the Initial Design

**5.3.1 Control Surface Requirements.** As seen in Fig. 5.5, the elevator requirements for the type of response in Fig. 5.3 are much too large for the limited range of the actual elevator ability. An attempt is made to reduce the control surface requirements by adding additional disturbance rejection to the inner loop, but it is unsuccessful. The control surface requirements are a result of the desired response of the aircraft: the faster the aircraft must respond, the more elevator deflection required. The low speed plants are being asked to respond quicker than is physically possible.

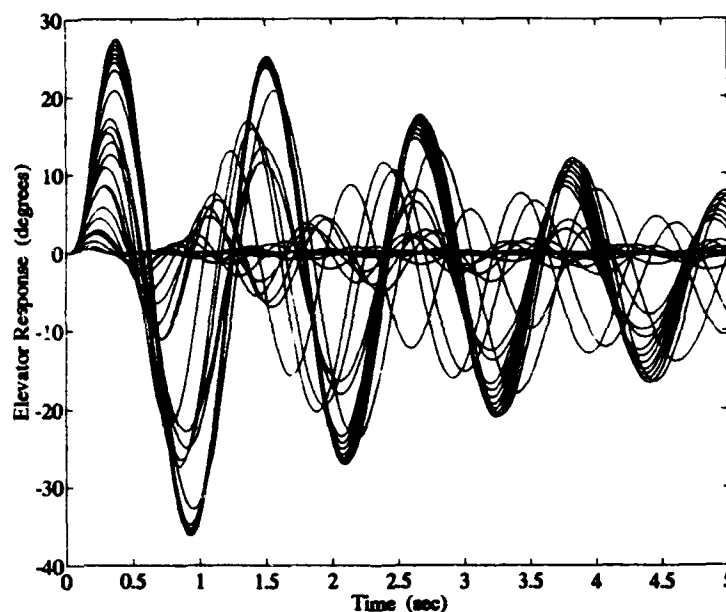


Figure 5.5 Elevator Response to Step Command

The proposed solution to this problem is gain scheduling using dynamic pressure, since the specifications are based on a value proportional to  $\bar{q}$ . The aircraft response can be adjusted by varying the natural frequency and damping of the prefilter poles. If the natural frequency is decreased, the aircraft response slows down, and the elevator requirements are not as great. However, future designs eliminate the extreme elevator requirements present in this design.

**5.3.2 Bandwidth of the Compensator.** The bandwidth of the  $N_1$  outer loop compensated system is around 120 rad/sec, which is much too high for a FCS. Although the nominal loop has an  $\omega_\phi$  less than 30 rad/sec, the choice of the original nominal plant on the bottom of the template causes the remaining plants to have  $\omega_\phi$ 's above that frequency. Both the inner loop and outer loop  $\alpha$  systems have a bandwidth of around 30 rad/sec.

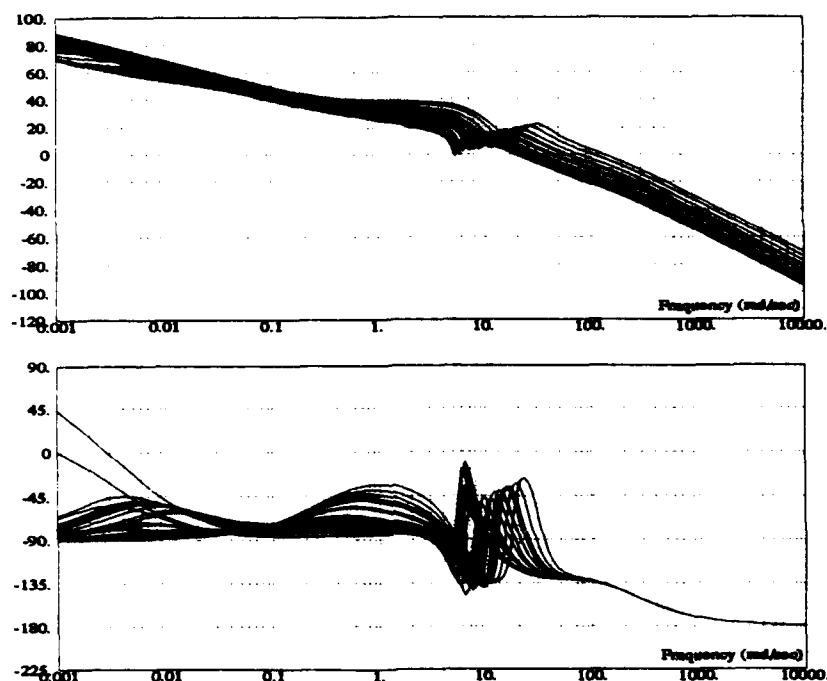


Figure 5.6 Open Loop Bode Plots for the Initial  $N_1$  Design

When a plant at the bottom of the template is chosen, the 30 rad/sec bound moves above the 0 dB line on the Nichols chart (Fig. D.3), making a proper bandwidth compensator impossible. An attempt is made to lower the tracking bounds by decreasing the bandwidth of the inner loop compensator to 20 rad/sec by moving the zero out to  $-15$ , but the gains made here are lost in an increase in the width of the outer loop templates and the resulting upward shift in the tracking bounds. An attempt is also made by decreasing the disturbance rejection to 20 dB by lowering the gain of  $G_c$  to  $-0.15$ , but here again the templates not only become wider, but also taller. The only options left are to gain schedule the inner compensator or modify the tracking bounds to lower the bounds on the Nichols chart.

#### 5.4 Results of Modifying Tracking Bounds

Because the lower  $\bar{q}$  plants respond with a slightly lower  $\omega_p$  in the previous design, it is decided to modify the lower tracking bound to see if the low  $\bar{q}$  natural frequencies will decrease while maintaining the higher  $\omega_p$  of the higher  $\bar{q}$  plants. The upper bound is left as before, but the natural frequency of the original lower bound is changed to 2.5, and the additional pole is moved to  $-6$ . This change makes the difference in the bounds much greater than it was before (Fig. 4.14). The final lower tracking bound is

$$T_{RL}(s) = \frac{37.5}{s^3 + 12s^2 + 42.25s + 37.5} = \frac{37.5}{(s + 1.342)(s + 4.658)(s + 6)} \quad (5.8)$$

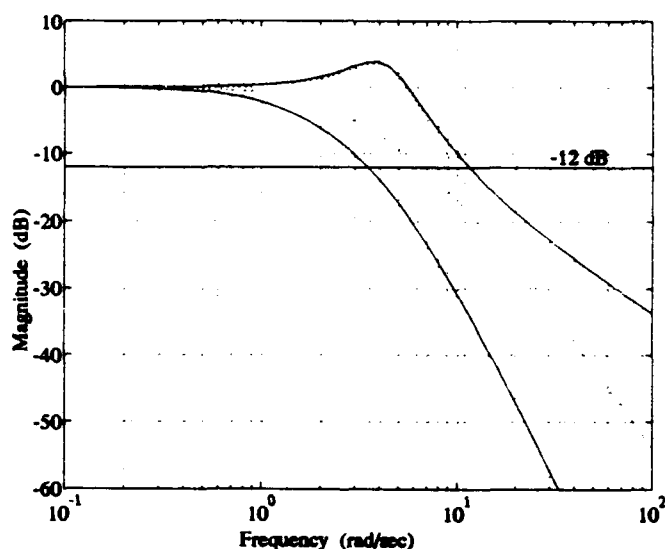


Figure 5.7 Modified  $N_s$  Loop Tracking Bounds

**Compensator Design.** The compensator is designed to have the lowest cutoff frequency for the given bounds, and a choice is made not to meet the tracking bounds below 0.5 rad/sec. The cutoff frequency is below 30 rad/sec for all but two plants: those corresponding to Mach 0.9 at 1,000 and 10,000 ft. The final compensator is actually of lesser order than the previous one and is given by

$$G_n(s) = \frac{-240(s + 0.7)(s + 5)}{s(s + 5.6 \pm j4.2)} \quad (5.9)$$

*Prefilter Design.* Again, the prefilter is adjusted from the QFT CAD starting point until the desired response is achieved. The final prefilter is

$$F_n(s) = \frac{2}{s + 2} \quad (5.10)$$

*Time Domain Results.* The time responses of normal acceleration to a step command of 1 g for each plant are shown in Fig. 5.8. It is a relatively overdamped system, and the second order conversions show that the response's  $\omega_{np}$  all fall within the specifications as shown in Fig 5.9.

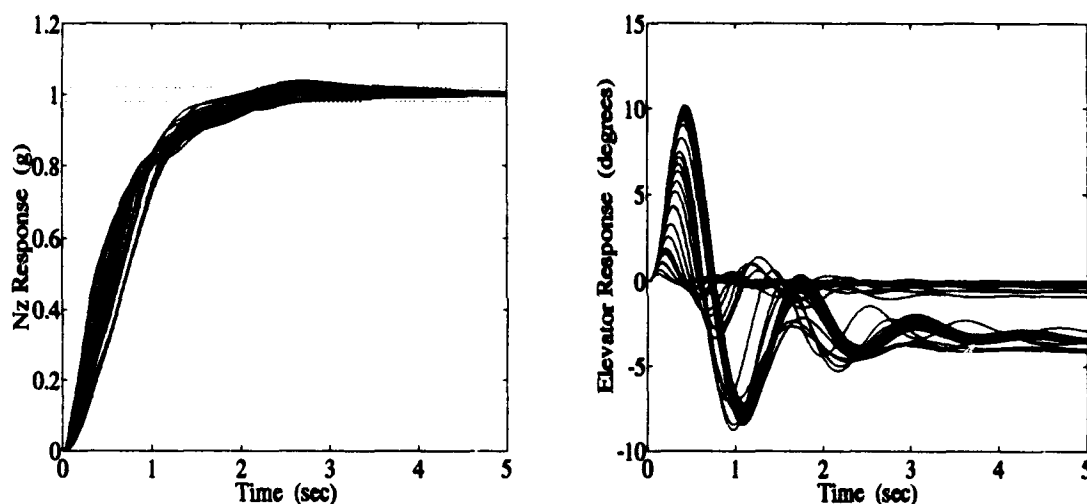


Figure 5.8  $N_z$  and Elevator Time Response to a Step Input

## 5.5 Useful Lessons of Initial Design

*5.5.1 Nominal Plant Choice.* Choosing a plant on the bottom of the template may produce the traditional stability trash can of QFT, but it is not a prudent choice if one is concerned with the bandwidth of the system. During the initial design, a plant on the bottom of the template is chosen as the nominal plant, and a compensator is designed using that nominal loop. If the cutoff frequency of the nominal loop is 30 rad/sec, the nominal plant choice guarantees that all the other plants will have a cutoff frequency greater than 30 rad/sec. If system bandwidth is of concern, then a plant on the top of the templates

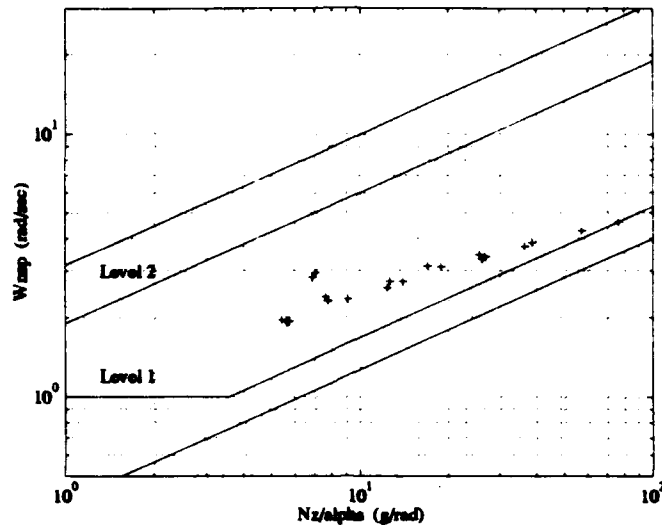


Figure 5.9  $\omega_{sp}$  Results from Time Response Matching

in the cutoff frequency region should be chosen as the nominal plant. This allows one to design with the nominal loop and be assured that the cutoff frequencies of the other plants are below that of the nominal plant.

**5.5.2 Control Surface Requirements.** Although a 1  $g$  maneuver does not require excessive elevator deflection, the VISTA is capable of pulling more than 2  $g$ 's at many flight conditions. Because the plants are linear, if the commanded maneuver is doubled, all values throughout the system will double. This provides an easy way to check how much elevator will be needed at each flight condition. The maximum sustainable  $g$ 's multiplied by the elevator required at one  $g$  gives the maximum elevator required at each flight condition. In this system, the control surface requirements do not exceed the availability for maximum sustainable  $g$ 's.

If a quicker time response is required, the prefilter time constant can be reduced. However, the control surface requirements then become too great for the low  $\bar{q}$  - high  $g$  flight conditions. The prefilter can be scheduled to provide the quickest response at the different flight conditions without exceeding elevator requirements.

**5.5.3 Actuator Model.** For simplicity, this initial design uses the first order actuator model in Eq. (2.3). This approximation proves to be unacceptable for robust compensator design. This is due to the fact that the fourth order model adds an additional  $50^\circ$  of phase lag to the system at the cutoff frequency. This extra phase lag presents a genuine problem in QFT robust control design, where the open loop transfer functions are designed to have a certain phase margin angle at the phase margin (cutoff) frequency. If a FCS is designed for  $\omega_\phi = 30$  rad/sec and a  $\gamma = 45^\circ$  using the first-order actuator approximation, then the system becomes unstable when the fourth-order actuator model is used. This is illustrated by Fig. 5.10, where the left plot is the stability plot of the initial inner loop design with the first-order approximation, and the right plot demonstrates the effect of the fourth-order model. The system is now unstable for several plants and marginally stable for many others. This defeats the purpose of the inner design, which is to stabilize the plants. For this reason, the higher order actuator models should always be used for QFT design.

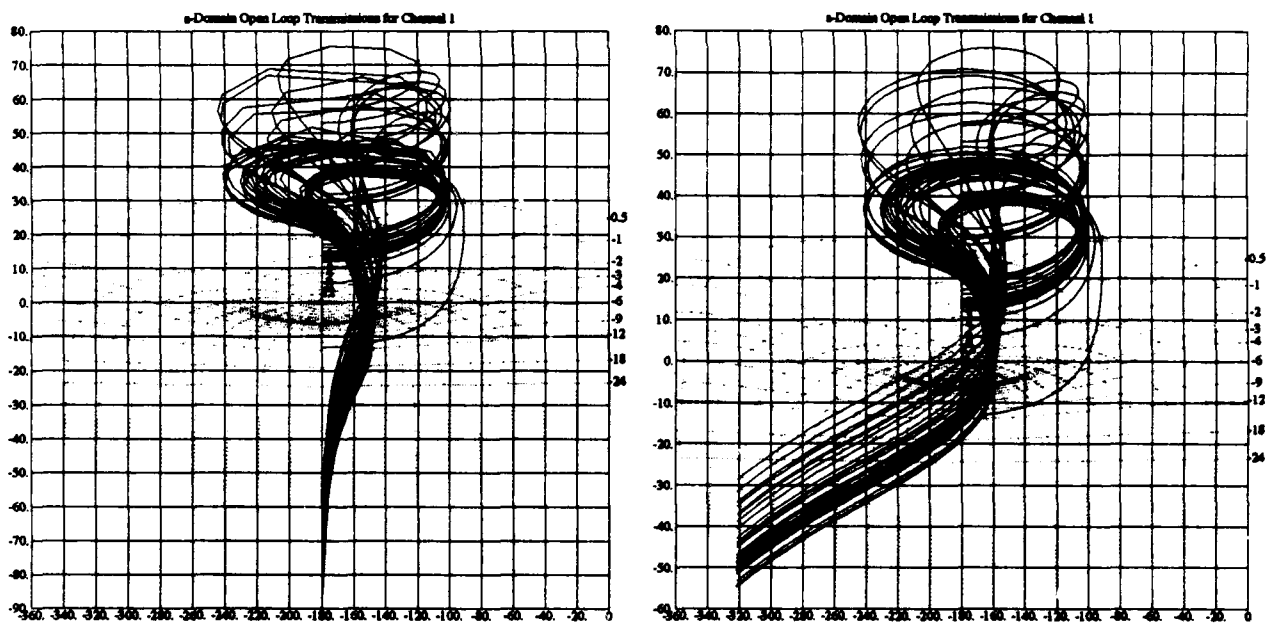


Figure 5.10 Initial Design (left) and Effect of Fourth Actuator Order Model (right)

## VI. Lateral/Directional Compensator Design

The  $2 \times 2$  lateral channel of Fig. 6.1 is designed using MIMO QFT methods, but it incorporates some of the dual loop concepts of the longitudinal channel. Both body axis roll rate ( $p$ ) and stability axis roll rate ( $p_{stab}$ ) designs are examined, with sideslip angle ( $\beta$ ) as the secondary control variable. This chapter contains the specifications for the lateral/directional channel and a description of each of the designs and their results.

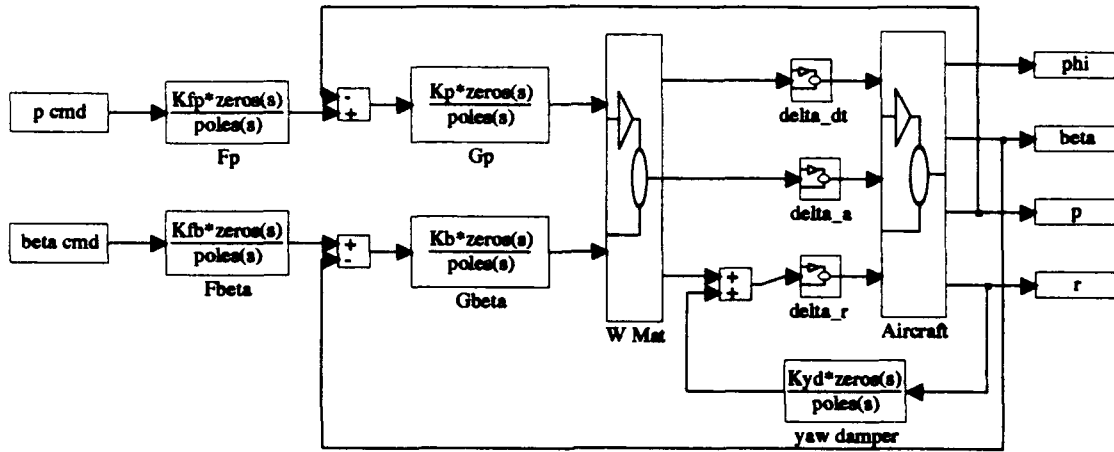


Figure 6.1 Lateral/Directional System

### 6.1 Flying Qualities Specifications

Mil-Std 1797A for flying qualities is also used to define the lateral/directional FCS performance specifications. Here again, the specifications are given in both time and frequency domain representations.

**6.1.1 Frequency Domain Specifications.** For the lateral/directional channel, the flying qualities specifications apply to simultaneously matching the Bode plots of the final system to those of the equivalent fourth order transfer functions given by

$$\frac{\phi(s)}{\delta_{stab}(s)} = \frac{K_{\phi}(s^2 + 2\zeta_{\phi}\omega_{\phi}s + \omega_{\phi}^2) \exp^{-\tau_{\phi}s}}{(s + 1/T_R)(s + 1/T_S)(s^2 + 2\zeta_d\omega_d s + \omega_d^2)} \quad (6.1)$$



and

$$\frac{\beta(s)}{\delta_{rud}(s)} = \frac{(A_3 s^3 + A_2 s^2 + A_1 s + A_0) \exp^{-\tau_{ep}s}}{(s + 1/T_R)(s + 1/T_S)(s^2 + 2\zeta_d \omega_d s + \omega_d^2)} \quad (6.2)$$

where  $T_R$  is the Roll Mode time constant,  $T_S$  is the spiral mode time constant,  $\zeta_d$  is the Dutch Roll Mode damping,  $\omega_d$  is the Dutch Roll Mode natural frequency, and  $\tau_{ep}$  is the roll rate time delay. The fighter aircraft flying qualities specifications are given in Table 6.1, where  $T_2$  is the time to double of the spiral mode given by  $T_2 = -\ln(2)(T_S)$

Table 6.1 Frequency Domain Lateral/Directional Specifications

Parameter	Level 1	Level 2	Level 3
$T_R$ max	1.0 sec	1.4 sec	10 sec
$\zeta_d$ min	0.40	0.02	0
$\omega_d$ min	1 rad/sec	0.4 rad/sec	0.4 rad/sec
$\tau_{ep}$ max	0.1 sec	0.2 sec	0.25 sec
$T_2$ min	12 sec	8 sec	4 sec

Additionally, the phase margin angle and gain margin requirements are identical to the longitudinal channel:  $\gamma = 30^\circ$  and  $a = 6$  dB. The phase margin frequency of the open loop system must also be less than 30 rad/sec as in the longitudinal channel.

**6.1.2 Additional Time Domain Specifications.** The additional time domain specifications apply to the performance requirements of the aircraft. There is a specification on the time to roll through a certain bank angle that is based on aircraft speed. For the majority of the applicable flight envelope, the aircraft must be able to roll through  $90^\circ$  in 1.0 sec and through  $360^\circ$  in 2.8 sec [11]. There is also a requirement that a sustained  $10^\circ$  sideslip will use less than 75% of the available roll axis power (aileron). There is also a complicated specification for the amount of  $\beta$  allowed for a particular roll angle. If one simplifies the requirements in a conservative fashion over the majority of the flight envelope, a roll command of 1 deg should result in less than  $0.022^\circ$  of  $\beta$ , but at low speeds  $\beta$  is allowed to increase to  $0.067^\circ$ . The maximum  $\beta$  allowed in any roll command is  $6^\circ$ . There is also a specification on the amount of roll rate oscillation allowed. For Level 1 flying qualities, the magnitude of the first minimum after the peak must be of the same sign

and not less than 60% of the magnitude of the maximum. Mil-Std 1797A also states that meeting the minimum  $\zeta_d$  requirement should eliminate the need for this last specification.

## 6.2 Lateral Design Bounds

The (1,1) channel involves  $p$  command to  $p$  response. The only frequency domain specification given for this channel is the maximum roll mode time constant of 1 sec. This specification could be used to define a lower bound, but there is no upper bound specification. The (2,2) channel involves  $\beta$  command to  $\beta$  response. There is a lower bound on  $\omega_d$  and  $\zeta_d$ , but no upper bounds. This makes it impossible to define either an upper or lower QFT tracking bound without choosing arbitrary values for the upper bound's  $\omega_d$  and the lower bound's  $\zeta_d$ .

The cross-coupling disturbance requirement for the (1,2) channel is based on the amount of aileron authority used, so it cannot be quantified to  $p$ . The low speed (2,1) disturbance bound could use the  $0.067^\circ$   $\beta$  limitation, but this would not guarantee that the high speed plants would meet the  $0.022^\circ$  requirement. Conversely, setting the bound to the  $0.022^\circ$  requirement places unnecessary restrictions on the low speed plants.

Because there are no upper bounds in any of the channels, and because the  $0.067^\circ$  bound does not apply to all plants, it is decided to design each of the channels for stability bounds only. This design method insures the highest cross coupling rejection and robustness while still meeting the  $30^\circ$  phase margin angle and 6 dB gain margin requirements. To insure that the required  $\gamma = 30^\circ$  is met, slightly conservative stability bounds corresponding to  $\gamma = 35^\circ$  are used in each of the diagonal channels. The stability bounds for each of the lateral/directional designs are shown in Appendix D.

## 6.3 Initial Lateral Design Attempt

**6.3.1 Weighting Matrix.** Although the lateral/directional channel has three inputs and two outputs, the standard VISTA coupling of the differential tail and aileron commands is used to create a  $2 \times 2$  MIMO plant where the primary inputs are "generalized"

aileron and rudder with control variables of  $p$  and  $\beta$  as follows [15]:

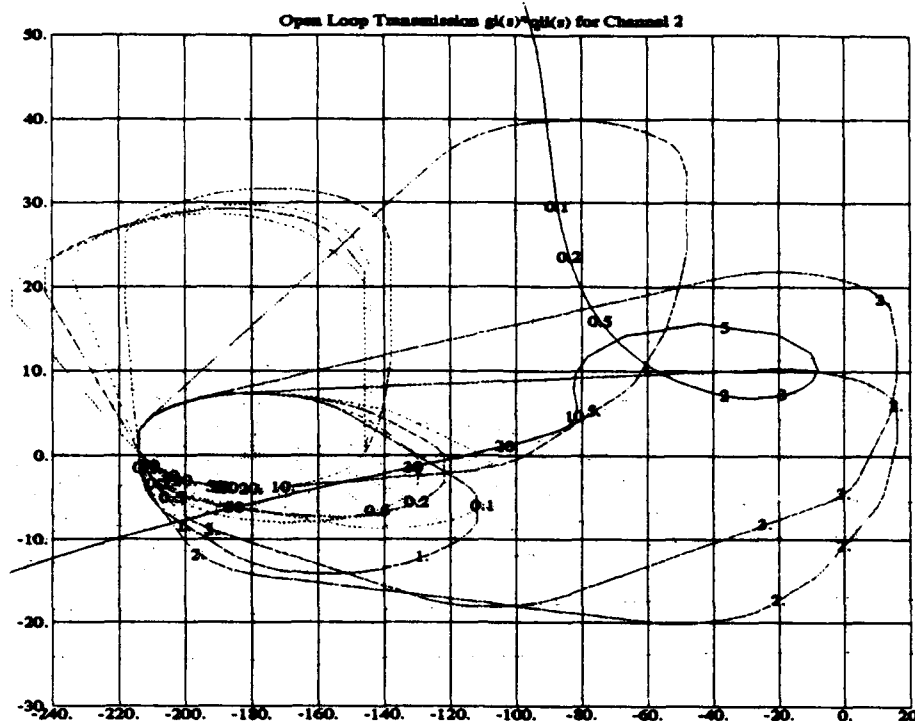
$$\begin{bmatrix} \delta_{dt_{cmd}} \\ \delta_{a_{cmd}} \\ \delta_{r_{cmd}} \end{bmatrix} = \mathbf{W} \begin{bmatrix} p_{cmd} \\ \beta_{cmd} \end{bmatrix} \quad \mathbf{W} = \mathbf{W}_1 = \begin{bmatrix} 0.294 & 0 \\ 1.0 & 0 \\ 0 & 1.0 \end{bmatrix} \quad (6.3)$$

A second weighting matrix design is then attempted to decrease the magnitude of the off-diagonal  $q_{ij}$  matrices to ease the cross-coupling disturbance bounds. An aileron-rudder interconnect of  $-0.42$  and a rudder-aileron interconnect of  $-0.5$  remove all the nonminimum phase from the effective plants, significantly reduce the  $q_{21}$  magnitudes, and maintain all minimum phase  $q_{ii}$ 's.

$$\mathbf{W} = \mathbf{W}_1 \mathbf{W}_2 \quad \mathbf{W}_2 = \begin{bmatrix} 1.0 & -0.50 \\ -0.42 & 1.0 \end{bmatrix} \quad (6.4)$$

After the second weighting matrix is designed, a third weighting matrix design is attempted to try to further diagonalize the effective plants. This attempt is unsuccessful because it reintroduces the nonminimum phase eliminated by the second weighting matrix.

**6.3.2 Compensator Design.** The (2,2) channel ( $\beta/\beta_{cmd}$ ) is the first channel designed because it has the widest templates and gives the best indication of whether the design is achievable. This choice is also motivated by physical considerations. As shown in the loop shaping of Fig. 6.2, a third order compensator does not provide enough lead to the system to meet the stability bounds, because the points  $L_o(j2)$  and  $L_o(j3)$  fall directly inside the stability bounds for these frequencies. Adding gain to move the loop above the bounds requires violating the  $\omega_\phi = 30$  rad/sec requirement and causes instability if additional lead is not added. Lowering the gain to move the loop below the bounds eliminates much of the robustness. At least one more zero is needed to provide the additional  $60^\circ$  of lead required to move the nominal loop outside the 2 rad/sec stability bound. The extra zero also requires a reduction in compensator gain because of the gain added by zeros at higher frequencies, and this would also decrease the robustness.



### 6.4 Implementation of a Yaw Damper

The initial attempt to design a lateral/directional compensator is unsuccessful because of the size of the templates at the Dutch Roll frequencies, which is caused by the underdamped nature of the Dutch Roll mode. Therefore, QFT is used to design a yaw damper to robustly increase the damping of the Dutch Roll mode. Because the goal of the yaw damper is to increase the damping of the system, the closed loop poles are of primary interest, while the zeros are of no concern because they remain unchanged for the final design. This aspect of the design allows the use of QFT, because although the damper is placed in the feedback path and not in cascade, the QFT design method is still valid because it uses the open loop transmissions, which are the same irregardless of feedback or cascade design.

**6.4.1 Yaw Damper Design.** The fastest variable (yaw rate) is chosen as the feedback variable to the rudder command. Stability bounds corresponding to  $\gamma = 60^\circ$  are

chosen to introduce as much robust damping to the system as possible. A differentiator is added to the compensator because the purpose of the yaw damper is to eliminate the fast transient oscillations while allowing for acceptable pilot control authority [2]. A pole is then added to pull the nominal loop under the stability bounds, and the gain is adjusted until the nominal loop is just touching the high frequency stability bounds (Fig. 6.3). In flight control parlance, a robust washout filter is designed.

$$YD(s) = \frac{-s}{s + 0.3} \quad (6.5)$$

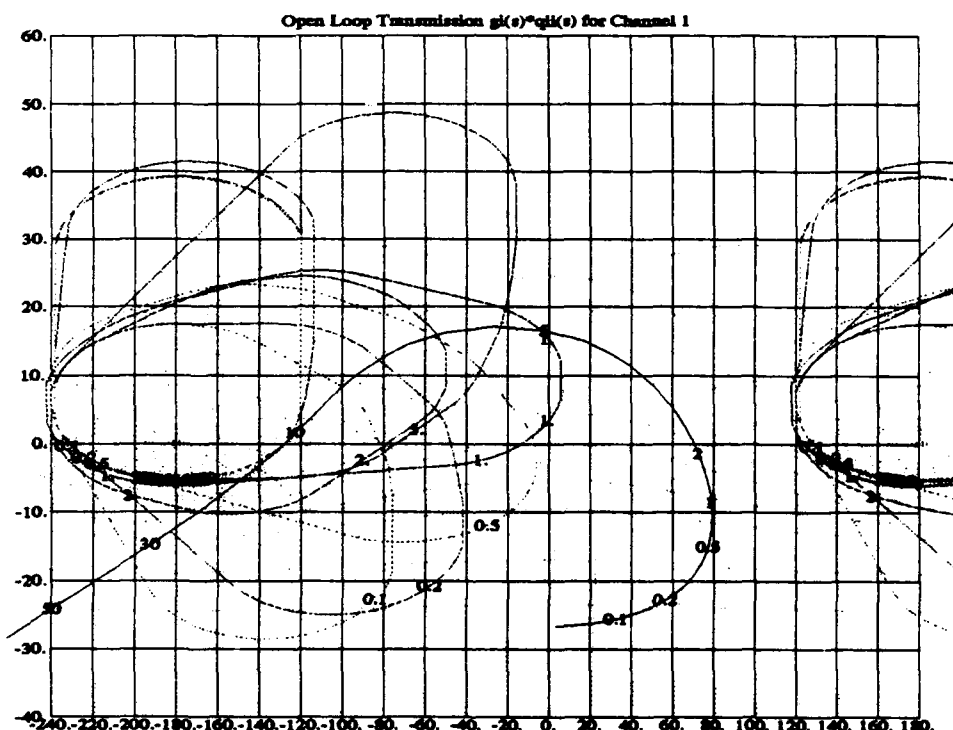


Figure 6.3 Yaw Damper Loop Shaping

**6.4.2 Results of Yaw Damper Implementation.** The effects of the yaw damper are immediately visible in the (2,2) channel. The height of the templates is reduced, but more importantly, the maximum width is reduced by approximately 60°. The  $q_{22}$  Bode plots before and after yaw damper implementation are shown in Fig 6.4.

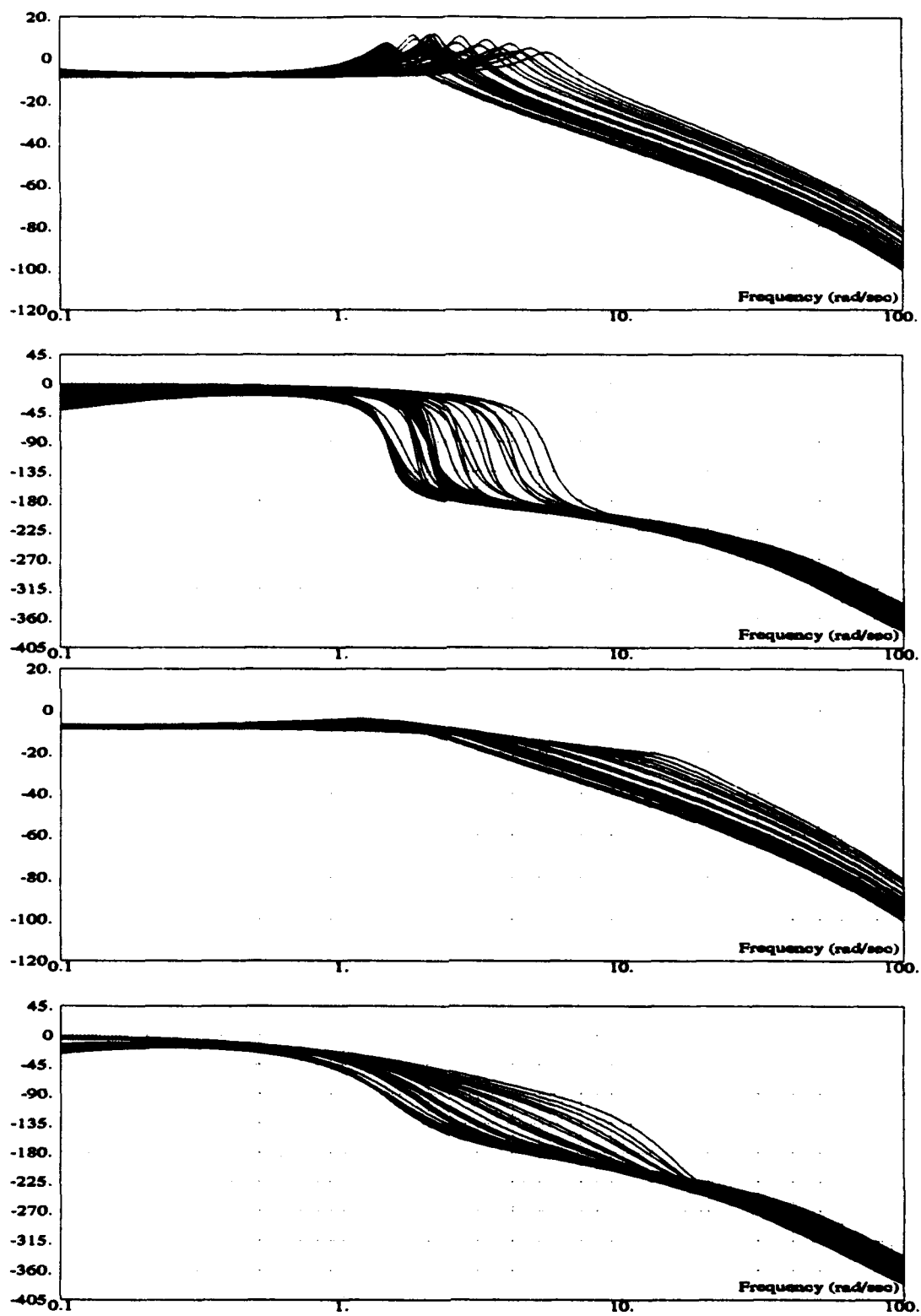


Figure 6.4 Channel (2,2) Bode Plots Before (top) and After (bottom) Yaw Damper Implementation

## 6.5 Second Lateral Design Attempt

**6.5.1 Weighting Matrix.** As in the previous design attempt, a second weighting matrix is designed to decrease the magnitude of the off diagonal  $q_{ii}$ 's. A 1.5 aileron-rudder interconnect and a 0.1 rudder-aileron interconnect significantly decrease the off diagonal magnitudes without severely affecting the diagonal template size. These connections also maintain the required minimum phase  $q_{ii}$  transfer functions. This weighting matrix is placed in series with the first as in Eq. (6.4).

$$\mathbf{W}_2 = \begin{bmatrix} 1.0 & 0.1 \\ 1.5 & 1.0 \end{bmatrix} \quad (6.6)$$

### 6.5.2 Compensator Design.

**Channel (2,2).** Plant number 5 is chosen as the nominal plant because it is on the top of the 30 rad/sec template. The loop shaping plots for the remainder of the chapter are contained in Appendix E. Figure E.13 shows that the primary difficulty in this portion of the design is meeting the stability bound at 5 rad/sec. An integrator is added for robustness, and three zeros are then needed to pull the nominal loop around the stability bounds. Two high frequency poles are then added to make an equal order compensator.

$$G_b(s) = \frac{655(s+1)(s+8.05 \pm j8.2126)}{s(s+50 \pm j86.603)} \quad (6.7)$$

**Channel (1,1).** Plant number 5 is again chosen as the nominal plant because it is still on the top of the 30 rad/sec template. As shown in the loop shaping of Fig. E.16, the limiting factor in this design is the 6 dB gain margin requirement in conjunction with the 5 rad/sec stability bound. Again, a pole is added at zero for robustness and disturbance rejection, and three zeros are then needed to pull the nominal loop around the stability bounds. Two high frequency poles are then added to make an equal order compensator.

$$G_p(s) = \frac{-6.5(s+4.8)(s+18 \pm j24)}{s(s+100)(s+100)} \quad (6.8)$$

**6.5.3 Time Domain Results.** As shown in Figs. E.14, E.15, E.17, and E.18, the design is successful in meeting all of the frequency domain specifications. The time domain responses are acceptable for the low  $\bar{q}$  plants, but there is considerable ringing in some of the high  $\bar{q}$  plants (Fig. 6.5). The time response of the high speed plant literally falls within the time domain thumbprint, but this sort of oscillation is not acceptable, particularly when the control surface responses are examined. Figure 6.6 shows the actuator activity for plant #5. This response is for a 1 deg/sec  $p$  command, but if a high roll rate is commanded, the actuators would be forced to move from one side to the other in a very quick and sustained manner, causing excessive stress or possibly rate saturations.

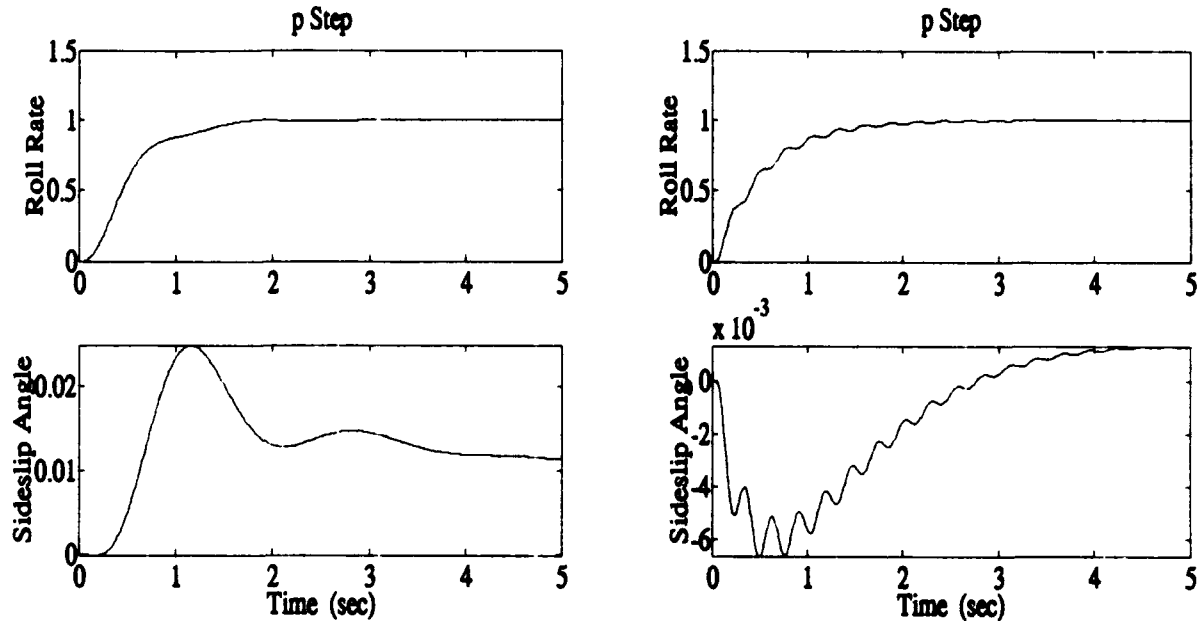


Figure 6.5 Plant #1 (left) and Plant #5 (right) Time Responses with Interconnects

However, it is discovered through experimentation that the elimination of the aileron and rudder interconnects also eliminates the ringing problem (Fig. 6.7), but the compensator design for the (2,2) channel now violates the  $\gamma$  specifications as shown in Fig. E.19. It is decided to modify the compensators without using the interconnects to meet the stability requirements and eliminate the ringing problem.



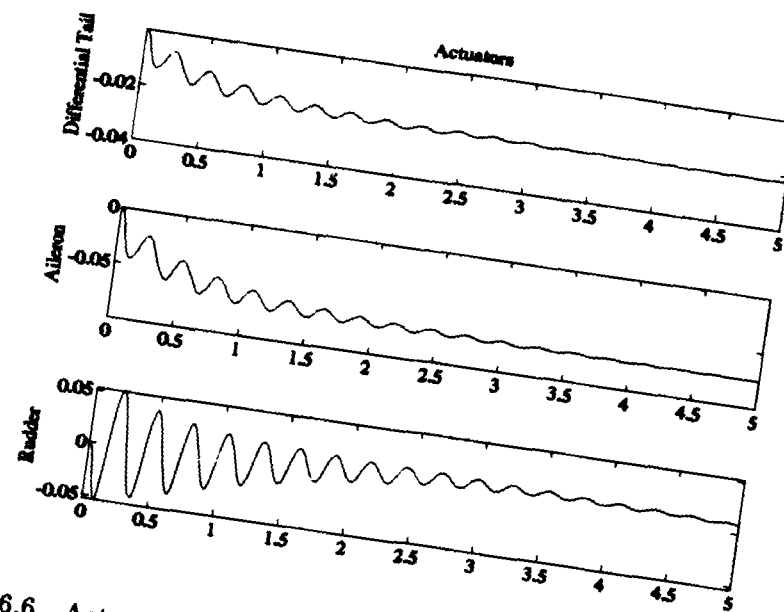


Figure 6.6 Actuator Time Responses for High  $\bar{q}$  Plant with Interconnects

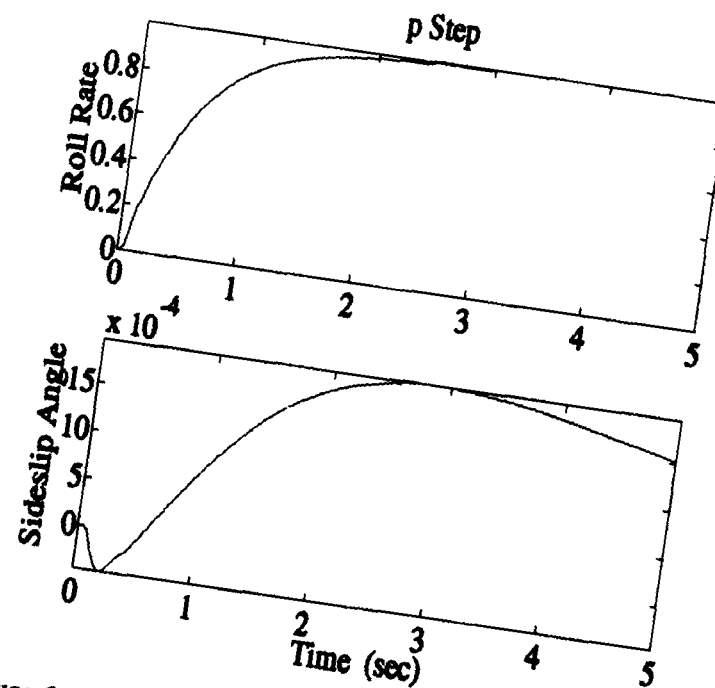


Figure 6.7 Plant #5 Time Response without Interconnects

## 6.6 Final Body Axis Design

**6.6.1 Compensator Design.** The third order compensators designed in the previous attempt are modified for this design. The zeros and gain are adjusted until all the stability bounds are met, while still maintaining the  $\omega_\phi = 30$  rad/sec and  $a = 6$  dB requirements for all plants. The third order compensators are given below.

$$G_b(s) = \frac{700(s+1)(s+5)(s+20)}{s(s+50 \pm j86.603)} \quad (6.9)$$

$$G_p(s) = \frac{-5.1(s+5.2)(s+19.8 \pm j26.4)}{s(s+100)(s+100)} \quad (6.10)$$

It is then discovered that the order of  $G_p$  can be reduced by one and still meet all the stability bounds, but this requires sacrificing some of the disturbance rejection gained with the third order compensator. However, the only specification on this cross-coupling disturbance is that a sideslip angle of  $10^\circ$  must not require more than 75% of the aileron authority. This specification is met as shown in Fig. 6.8. The third order compensator time response is shown as solid lines while the second order is dotted. The second order compensator allows approximately  $5^\circ$  more bank angle after 5 sec, but they both use basically the same amount of elevator authority ( $\approx 60\%$ ). Because both meet specifications, the second order compensator is chosen because it is lower order, and even produces a slightly smoother  $p$  step response.

$$G_p(s) = \frac{-1.6(s+7.6)(s+10)}{s(s+100)} \quad (6.11)$$

The final loop shaping plots for both channels are given in Figs. E.20 and E.26. The  $\omega_\phi$  requirement verification plots are contained in Figs. E.21 and E.27, and the stability margin verifications are shown in Figs. E.22 and E.28.

**6.6.2 Time Domain and Specification Results.** Because there are no tracking bounds in this design, the QFT CAD package cannot be used to find a starting point for the prefilter. In the interest of simplicity, first order prefilters are added to both channels, and the time responses are examined to determine how the prefilters should be adjusted.

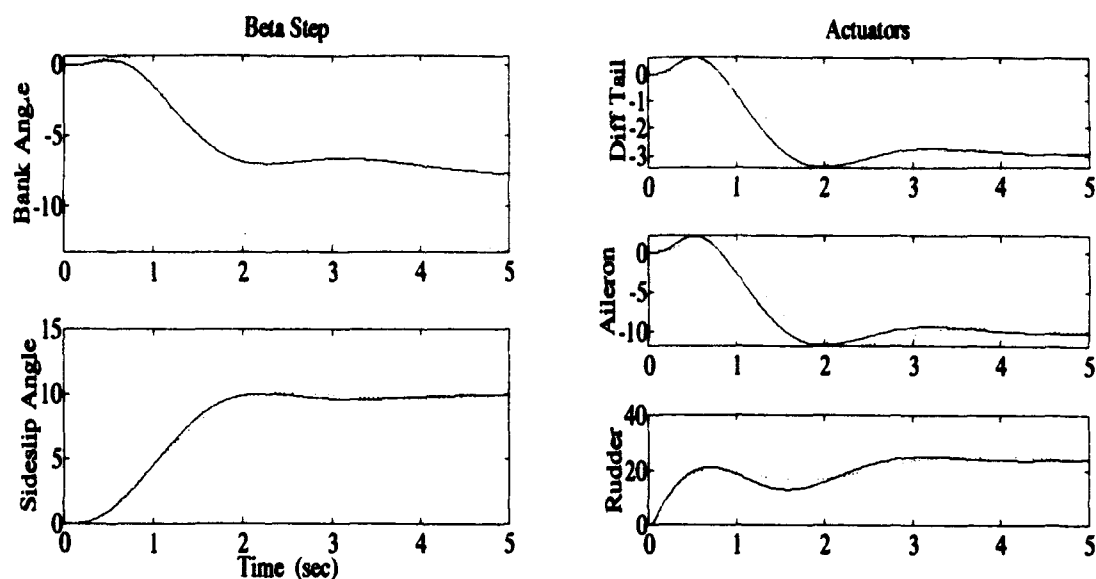


Figure 6.8 Comparison of Third (solid) and Second (dotted) Order Compensator Time Responses

The (1,1) prefilter commands the  $p$  response, and the placement of the prefilter pole affects the speed with which  $p$  responds. A pole at  $-2$  places the Roll Mode time constants in the center of Level 1 flying qualities without excessive actuator requirements. Therefore the following prefilter is implemented, producing the  $p$  responses in Fig. 6.9:

$$F_p(s) = \frac{2}{s + 2} \quad (6.12)$$

The first order prefilter in the (2,2) channel causes too quick a response in  $\beta$ , because the rudder is required to respond at a very high rate, and practically saturates for a  $10^\circ$   $\beta$  command. Therefore, a second-order prefilter is used to slow down the initial response. The choice of damping and natural frequency has a profound affect on the Bode plot matching, so the prefilter is adjusted until Level 1 flying qualities are met. The final choice is given below for the  $\beta$  responses in Fig. 6.9.

$$F_b(s) = \frac{4}{s + 1.6 \pm j1.2} \quad (6.13)$$

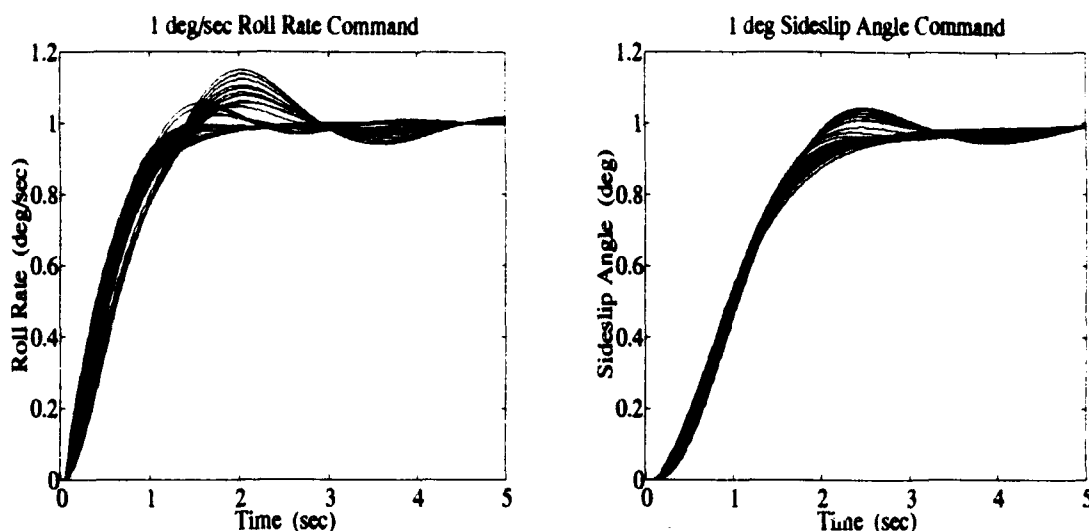


Figure 6.9 Time Responses for Step Commands to  $p$  and  $\beta$

The time responses for  $p$  and  $\beta$  are very similar, probably due to the robustness of the system and the similarity of the prefilters. Both use a frequency of 2 rad/sec, but  $F_\beta$  is second-order while  $F_p$  is first. This difference manifests itself in the initial response; the  $p$  response begins quicker than the  $\beta$  response. The  $p$  oscillation requirement is obviously met because the minimums are all greater than 60% of  $1.2 = 0.7$ . Figure 6.10 shows that the cross-coupling specifications are also met. The  $\beta$  response for a 1 deg/sec  $p_{cmd}$  is below  $0.067^\circ$  for all the plants and below  $0.022^\circ$  for the high speed plants. The actuator responses for a  $10^\circ \beta_{cmd}$  are also shown, and the aileron requirements are all below the 75% of maximum specified.

The bode plots of  $\phi/p_{cmd}$  and  $\beta/\beta_{cmd}$  are now matched to the fourth-order systems in Eq. (6.1) and (6.2) between 0.1 and 10 rad/sec. The results of this matching are given in Appendix F. All of the plants meet Level 1 flying qualities as outlined in Mil-Std 1797A, as is graphically shown in Fig 6.11. The small roll mode time constants in the low  $\bar{q}$  plants match the underdamped time responses in these plants. This indicates that the Dutch Roll mode is more dominant at these flight conditions, preventing the traditional overdamped  $p$  response.

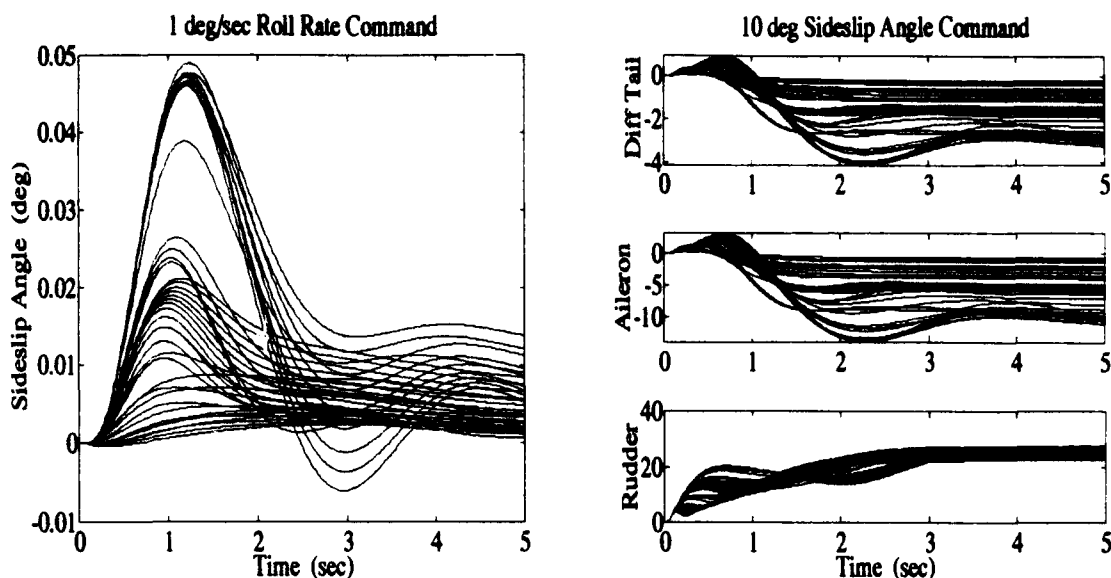


Figure 6.10 Off Diagonal Responses for Step Commands to  $p$  (left) and  $\beta$  (right)

### 6.7 Stability Axis Roll Rate Design

It is then suggested that the pilot actually desires roll about the stability axes. While a body axis roll revolves about the nose of the aircraft, a stability axis roll revolves around the direction of flight. A stability axis roll is preferred because the purpose of a roll is to change the direction in which an aircraft is pointing. After a body axis roll, the aircraft is still pointing in the same direction, and then the pilot must use the longitudinal control to point the nose in the desired direction, but after a stability axis roll, the aircraft is already pointing in the desired direction. This section examines a stability axis roll rate design.

**6.7.1 Compensator Design.** Because the trim  $\alpha$  is small in the majority of the plants,  $p_{stab} \approx p$  because  $\cos(\alpha) \approx 1$  and  $\sin(\alpha)$  is very small (Eq. (2.16)). This implies that the compensators from the body axis design can work in the stability axis. Only slight modifications are necessary to meet all the bounds and specifications.

$$G_b(s) = \frac{850(s + 0.6)(s + 8)(s + 14)}{s(s + 50 \pm j86.603)} \quad (6.14)$$

$$G_p(s) = \frac{-1.7(s + 7.5)(s + 10)}{s(s + 100)} \quad (6.15)$$

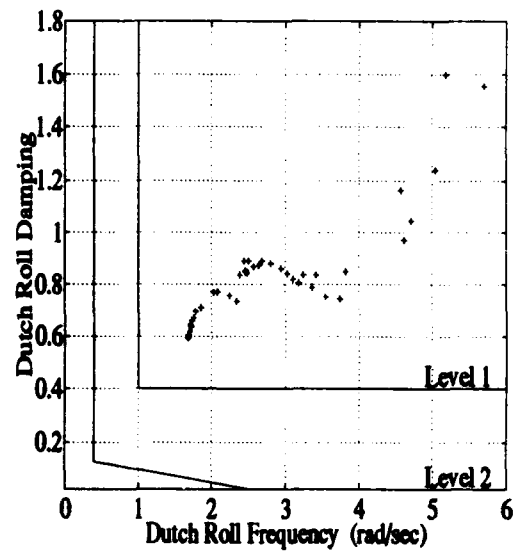
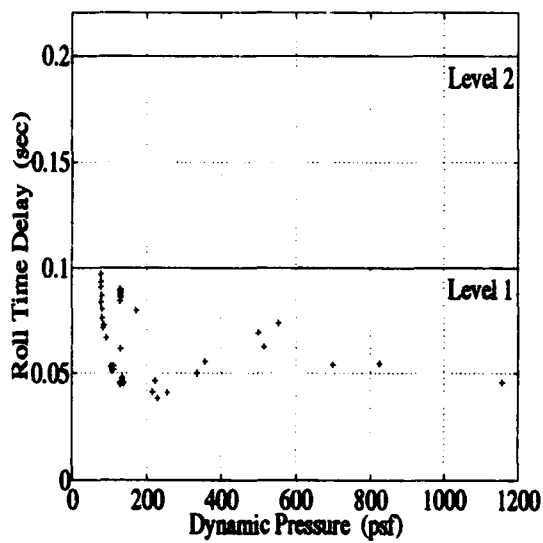
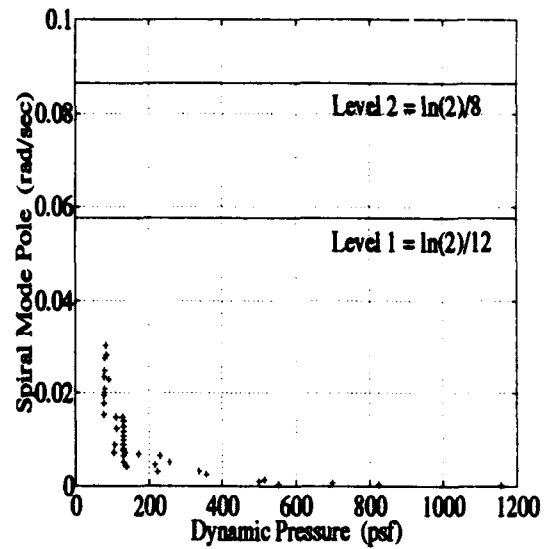
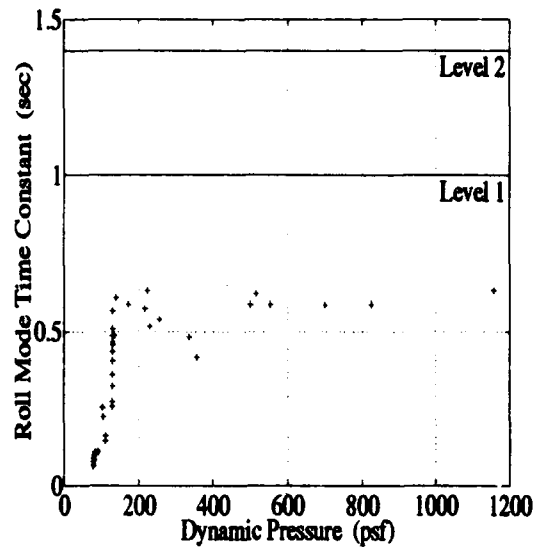


Figure 6.11 Graphical Interpretation of the Lower Order System Matching

The loop shaping plots for both channels are given in Figs. E.29 and E.32. The  $\omega_\phi$  requirement verification plots are contained in Figs. E.30 and E.33, and the stability margin verifications are shown in Figs. E.31 and E.34.

**6.7.2 Time Domain and Flying Qualities Results.** The same prefilters are used as in the body axis design, and they produce very similar results. The time responses to a  $1^\circ$   $p_{stab}$  command and a  $1^\circ$   $\beta$  command are shown in Fig. 6.12, and the off diagonal responses to a  $1^\circ$   $p_{stab}$  command and a  $10^\circ$   $\beta$  command are shown in Fig. 6.13. As before, Level 1 flying qualities are met in both cases.

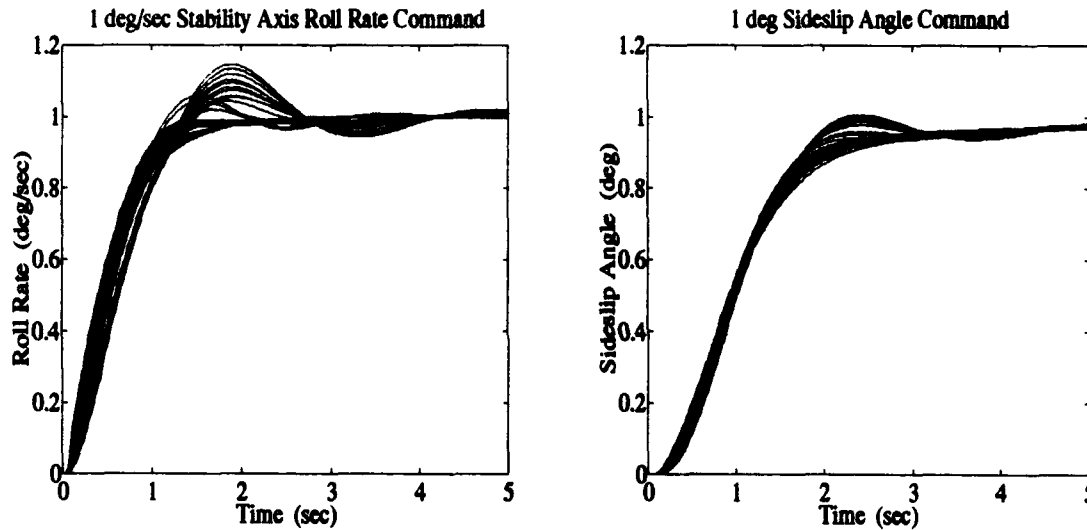


Figure 6.12 Time Responses for Step Commands to  $p$  (left) and  $\beta$  (right)

The bode plots of  $\phi/p_{cmd}$  and  $\beta/\beta_{cmd}$  are again matched to the fourth-order systems of Eqs. (6.1) and (6.2) between 0.1 and 10 rad/sec. The results of this matching are given in Appendix F. All of the plants meet Level 1 flying qualities as outlined in Mil-Std 1797A, and this is shown in Fig 6.14. As in the body axis design, the small roll mode time constants in the low  $\bar{q}$  plants cause the  $p_{stab}$  response to be underdamped.

## 6.8 Chapter Summary

Both the  $p$  and  $p_{stab}$  designs meet Level 1 flying qualities as outlined in Mil-Std 1797A. However, once again the specifications are different for different flight conditions.

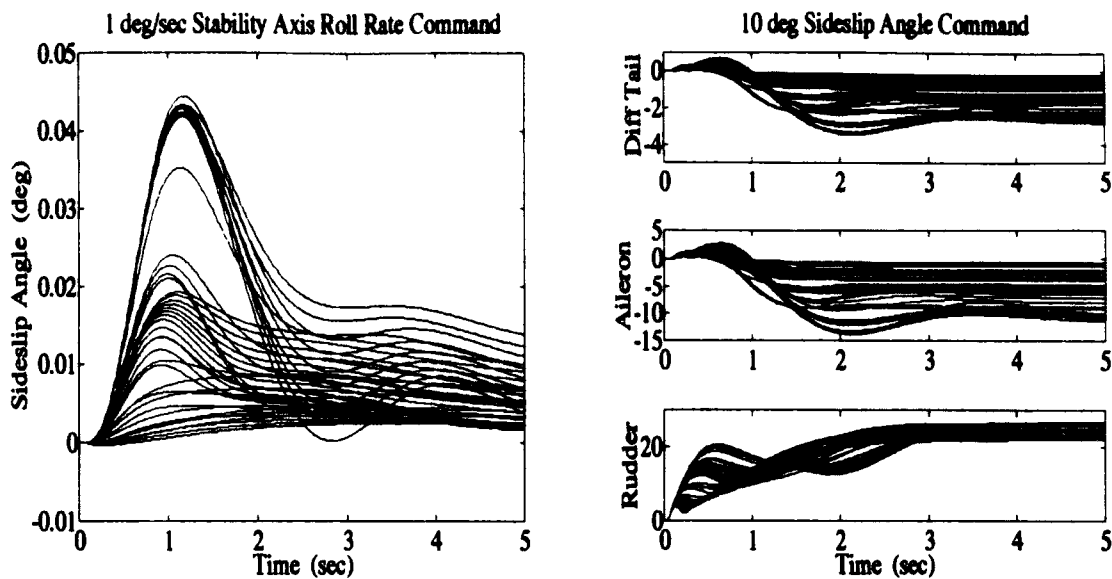


Figure 6.13 Off Diagonal Responses for Step Commands to  $p$  (left) and  $\beta$  (right)

This proves to be a drawback in that quantitative bounds for all the plants cannot be established for QFT design. For instance, the (1,2) channel specifications refer to aileron response, and not roll rate response. In the (2,1) channel, the specifications vary based on the speed at which the aircraft is flying.

Another peculiarity is that the lower order system matching is highly dependent on the choice of  $F_b$ . As  $F_b$  is changed, the roll rate time delay varies even though the  $p$  time response does not change. This illustrates another limitation of the specifications. The characteristics of today's fighter aircraft may no longer match the traditional fourth-order systems of aircraft past.

A double loop has once again proven to be of great use in full envelope design. Although the total order of the compensator is not reduced, placing the additional pole in the yaw damper instead of  $G_b$  allows greater disturbance rejection in the final design. It also eliminates one high frequency pole from the design, easing digital implementation.



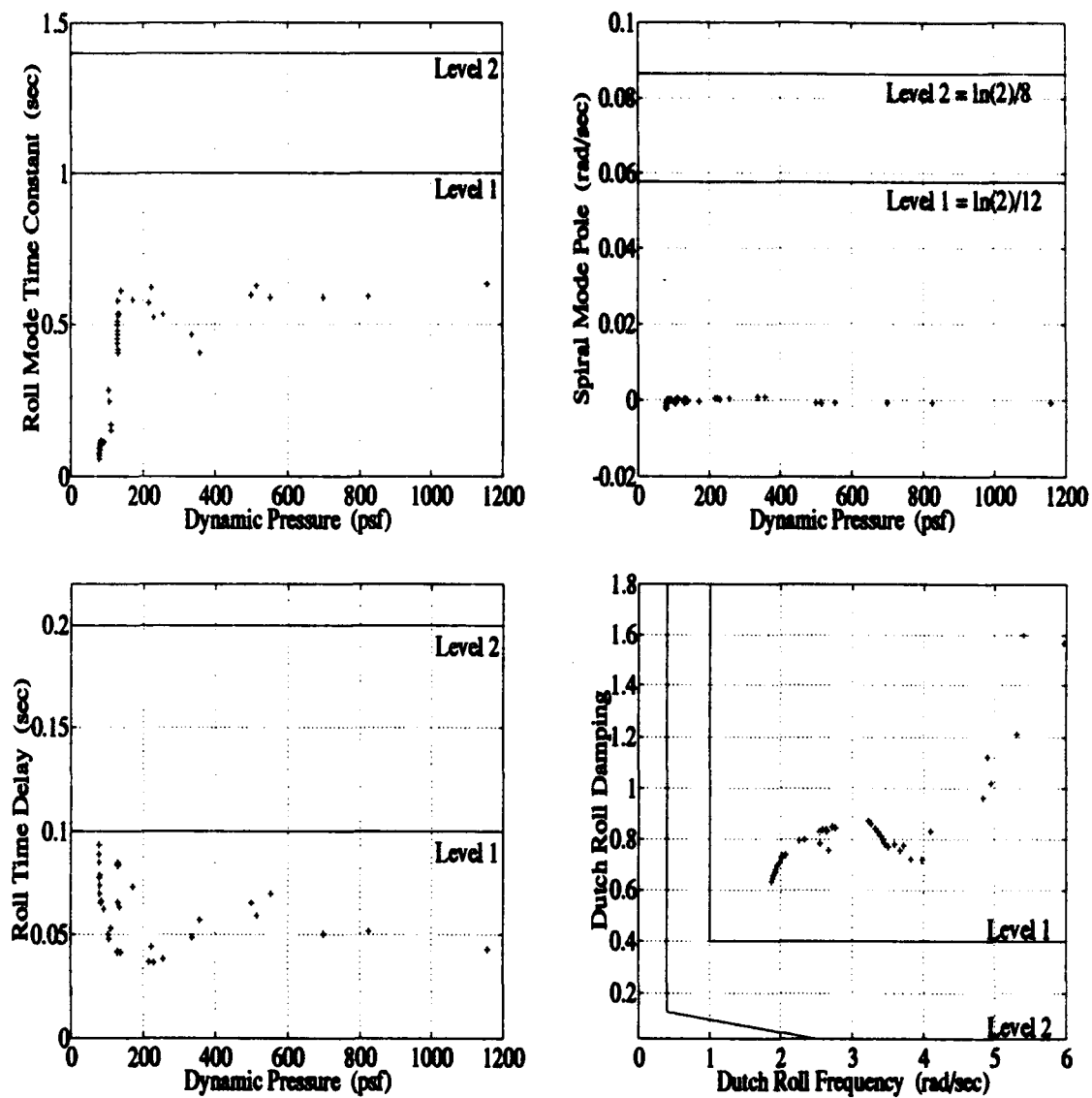


Figure 6.14 Graphical Interpretation of Lower Order Bode Plot Matching

## VII. Conclusions and Recommendations

The objective of this thesis is to demonstrate the benefits of using the robust control method of Quantitative Feedback Theory to design a fixed FCS for the full subsonic envelope of the VISTA F-16. In order to accomplish this, the military flying qualities are explored to establish a set of specifications for the design. The longitudinal design is undertaken first. Pitch rate is used in an initial QFT inner loop design to robustly stabilize the aircraft. This is done in order to accomplish an outer loop design with no gain scheduling. Next, the flight envelope is divided into two sections: a low  $\bar{q}$  region where the pilot flies  $\alpha$  and a high  $\bar{q}$  region where the pilot flies  $N_z$ . This division is not a limitation of QFT, but rather a division based on flying qualities requirements. Outer loop designs using both  $N_z$  and  $C^*$  as control variables are accomplished. Similar to the longitudinal channel, an inner loop yaw damper is implemented in the lateral/directional channel to allow the highest cross-coupling rejection for a given compensator order. Designs using both  $p$  and  $p_{stab}$  are accomplished using  $\beta$  as the secondary control variable.

### 7.1 Longitudinal Channel

The dual loop closure proves to be an effective tool in designing full envelope FCS's. Both the height and width of the outer loop templates are reduced by the inner loop design. The only factor over which the inner loop design has no control is the outer loop transfer function zeros. This proves to be a problem in both the  $N_z$  and  $\alpha$  designs.

In the  $N_z$  design, the highly underdamped zeros of the  $N_z/\delta_e$  transfer function are essentially cancelled by a set of poles in the final system. This leads to an exceptional  $N_z$  response, but in the  $q$  response these resonant poles are not cancelled, and they cause the  $q$  response to oscillate. This oscillation prevents the final system from meeting the  $q$  based specifications. In the frequency domain the applicable specification transfer function is  $q/N_{z_{cmd}}$ , and in the time domain the specifications are based on the  $q$  time response. The frequency domain specifications cannot be used for evaluation because the aircraft response does not correspond to a typical elevator deflection, and therefore the Bode plots are characteristically different. When the time domain specifications are used, the short

period damping is too low, as is predicted by examining the  $q$  time responses. Additionally, the amount of elevator authority required in this design limits the ability of the prefilter to alleviate the specification problems. A slower prefilter can be used to increase the damping, but then the time delays are too long. If the time delays are corrected by adding a prefilter zero, then the elevator requirements become too great without extensive scheduling. QFT is successful in fitting the  $N_z$  responses into the prescribed bounds, but this fit proves to be incompatible with the military specifications.

The solution to this problem is found in state feedback theory, where another state variable is added to shift the design zeros to a better damped position, eliminating the final design resonance. Pitch rate is chosen as the added variable because the specifications are based on  $q$ , and this choice helps the system meet Level 1 flying qualities on all fronts. The elevator requirements are also much less than in the  $N_z$  design. The only drawback to this design is that the final value of  $N_z$  is not equal to the commanded  $N_z$ . This error becomes more pronounced at the lower speeds, but this is not a major problem because the aircraft is not capable of high  $g$  maneuvers at these speeds. Iteration is still required in the prefilter design in order to meet flying qualities, and it may have to be repeated after examining the nonlinear simulations, which include the saturation effects. However, the high degree of robustness imparted to the system by the QFT designed compensator makes this a relatively simple task. In any case, it is easier to modify the prefilter than it is to modify the compensator while still meeting the stability margin and bandwidth requirements. A small bit of prefilter scheduling is necessary to meet flying qualities and remove an unacceptable oscillation in the  $N_z$  response. However, another advantage of prefilter scheduling is that the prefilter is a low energy device, whereas the compensator is a higher energy device.

There is also an antiresonance in the  $\alpha/\delta_e$  transfer functions, but that is not the problem in this design. The problem here is that the zeros for the plants on the left boundary of the envelope are nonminimum phase. This causes the final system to have a pair of unstable poles. However, these poles are practically canceled by the zeros that cause them to migrate to the right-half-plane. Because of this cancellation, and because the time constants of the poles are very large, the time domain contribution of these poles is

negligible in the time period of interest. Additionally, these poles are the Phugoid poles of the system, and are also affected by the throttle commands, which are not incorporated in this thesis. Therefore, this design is successful. Figure 7.1 contains the recommended FCS for the longitudinal channel. Due to time constraints, the method of switching between the different compensators is not explored in this thesis, primarily because it is not related to the QFT design method.

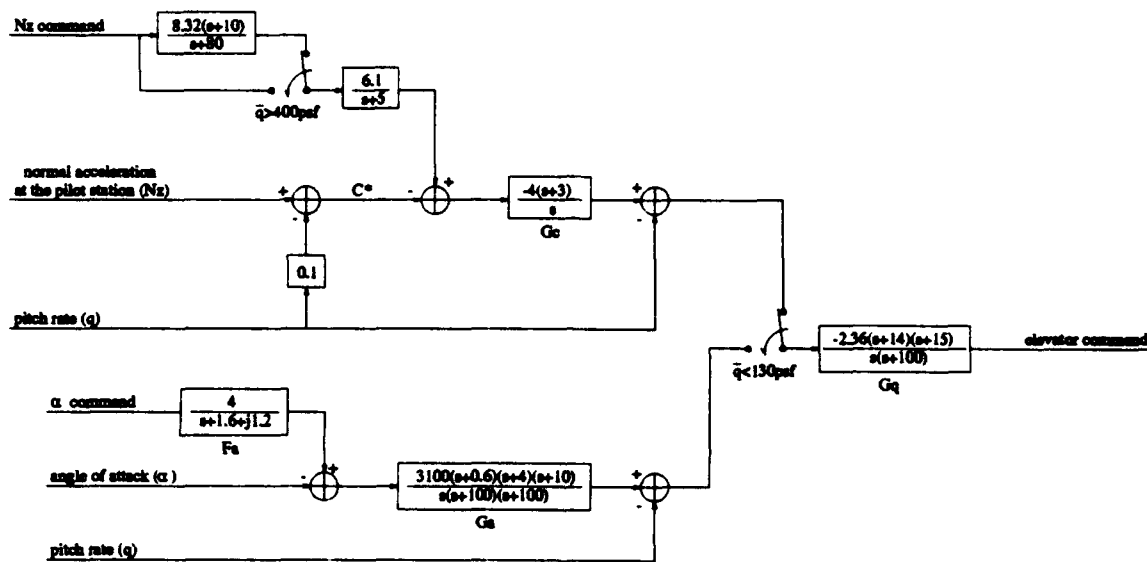


Figure 7.1 Recommended FCS for the Longitudinal Channel

## 7.2 Lateral/Directional Channel

In this channel, an inner loop design proves successful in allowing a full envelope Level 1 FCS to be designed with no gain scheduling and a high degree of cross coupling rejection. Both the  $p$  and  $p_{stab}$  designs easily meet flying qualities specifications. The  $p_{stab}$  design is more in line with what a pilot wants because it points the nose of the aircraft in the proper direction as well as rotating the aircraft to the desired bank angle.

## 7.3 Summary

Robust control QFT design methods are employed for full subsonic envelope flight control, minimizing the need for gain scheduling. One minor prefilter switching/scheduling

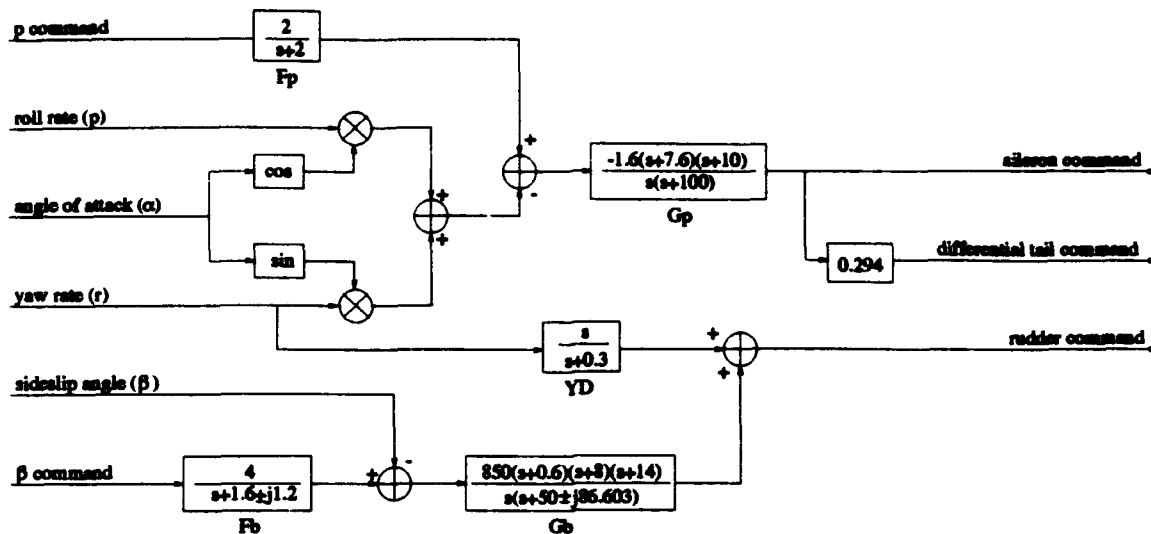


Figure 7.2 Recommended FCS for the Lateral Channel

scheme is necessary in the longitudinal channel to meet Level 1 flying qualities while maintaining smooth  $N_z$  responses. The primary benefit of QFT design seems to be an indication of whether the design is achievable as is. It is not necessary to divide the templates in this thesis, because inner loop closures are used in both channels to improve the feasibility and performance of the outer loop designs. A notable advantage of using QFT for this subsonic envelope design is that it allows one robust compensator to be designed which meets the stability margin and system bandwidth requirements, confining any necessary scheduling to the prefilter. A special effort is made to adapt the QFT design method to full envelope FCS design work, where elaborate military specifications on flying qualities need to be met. A problem arises in applying these specifications to the robust QFT design, because the specifications are not robust. Hence, the QFT robust control design method is employed in innovative ways, but which are still in line with conventional control design methods based on successive loop closures. A subsonic envelope FCS for the VISTA F-16 is designed with Level 1 flying qualities according to Mil-Std 1797A.

#### 7.4 Recommendations

The linear simulations are all successful in meeting Level 1 flying qualities, but the true test will be the performance in the nonlinear simulation, where the saturation effects

are included. The analog FCS should be converted to a digital design for testing on the SRF. There could be two problems with the design. One is the choice of the high frequency poles used to make the compensators equal order and physically realizable. This thesis uses a value of  $-100$ , but this would be easy to change with the help of the MIMO QFT CAD package if it proves necessary due to slower sampling rates. Each of the compensators would require only a lower gain, with the loss of some robustness, to still meet the frequency domain requirements. The designs are extremely robust, and there should not be any problem meeting the time domain specifications, even with a lower gain.

Another problem may arise in the actuators. Some of the initial rates may be too large and may saturate the actuators. However, this is only a problem with very large step commands. The designed system has Level 1 flying qualities for the smaller command signals, but the only to test the actual performance is in the nonlinear simulations. There is no aspect of the linear design that can predict the saturation effects on normal operations. The rate saturations may not even appear, because they are caused by a *step* command, and a pilot cannot input a step command, because there is an inherent physical delay. This could be modelled by a ramped step input, but this would still not be totally accurate, and there are no specifications pertaining to the time delay of the ramp. Even if the saturation problems appear, they can be remedied simply by raising the time constants in the prefilters, but care must be taken to continue meeting the specifications.

Another interesting area of research would be the transonic area of the flight envelope. The characteristics of the aircraft are known to vary greatly in this region due to a shift in the aerodynamic center of the aircraft, and QFT may prove to be a valuable tool for aircraft control in this region. Some of the effects of this region can be seen in the plants corresponding to Mach 0.9 at 1,000 and 10,000 ft. These prove to be difficult plants, especially in the longitudinal design. This is also an indication that *full* envelope flight control is not possible without some gain scheduling.

Although the high degree of robustness in this design will allow for further parameter variation, there are still many flight conditions that are not examined in this design. Different aircraft and weapons configurations are two very difficult problem areas for FCS designers. An effort should be made to transfer as many different configurations and flight

conditions over the *full* envelope onto a QFT template. This will give a frequency domain indication of any flight conditions that should be given special attention.

A final interesting area of research could be the further exploration of the QFT disturbance bound as it relates to the control of nonlinear plants. Although it may not be masters level research, it may prove useful to examine the bound as it relates to both trim input changes and neglected higher order terms.

There are many more applications of QFT to full envelope design, and it will prove to be a very useful design tool, even if it is used only in the initial design phases. It is a powerful visualization design tool.

### Appendix A. Robust Control Attack on Nonlinearity

Consider first the control of a nonlinear system near an equilibrium  $(\bar{X}, \bar{U})$  point, where the system dynamics are described by

$$P: \quad \dot{X} = f(X, U) \quad (\text{A.1})$$

Figure A.1 represents the open loop system where  $P_{\text{non}}$  is the nonlinear plant,  $U$  is the input to the nonlinear plant,  $X_0$  is the initial state of the plant, and  $X$  is the output of the plant.

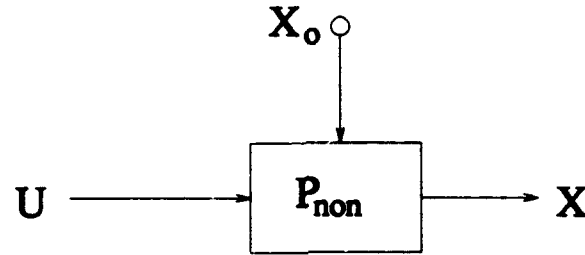


Figure A.1 Open Loop Nonlinear System

At the equilibrium point, the system dynamics are quiescent, that is

$$\dot{X} = f(\bar{X}, \bar{U}) = 0 \quad (\text{A.2})$$

In other words, when  $\bar{U}$  is commanded to the system, then  $\bar{X}$  is the output assuming  $X_0 = \bar{X}$ ,  $P$  is stable, and  $X_0$  is within some region of convergence around  $\bar{X}$ .

On the surface, it may seem that a control system is not needed to regulate or control a system such as this, in other words command  $\bar{U}$  to the system and get  $\bar{X}$  as the output. However, this is not a valid conclusion because one may not know what the particular  $\bar{U}$  is to obtain the desired  $\bar{X}$ , and there are parameter variations and disturbances in any real, nonlinear plant that may cause the output to deviate from the desired point.

Consider now adding state feedback to a system with structured parameter variation for disturbance and parameter variation rejection. Such a system could be represented as



in Fig. A.2 where the reference signal is given by

$$X_r = \bar{X} + x_e \quad (\text{A.3})$$

where  $x_e$  is the desired deviation from the nominal  $\bar{X}$ , and the error signal is given by

$$E = X_r - X \quad (\text{A.4})$$

and  $G$  is the compensator designed to produce the desired response.

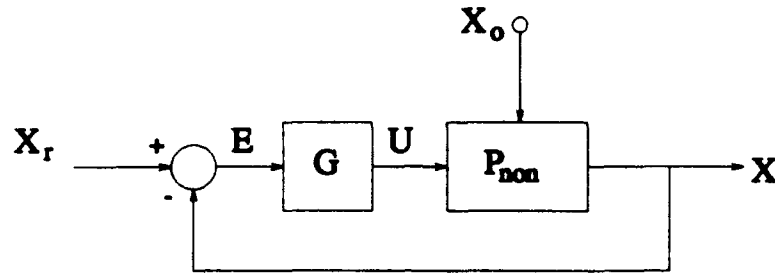


Figure A.2 Nonlinear System with State Feedback

For a regulator,  $X_r$  is chosen as  $\bar{X}$  and  $X_0$  is assumed to be  $\bar{X}$  (initially quiescent). This indicates that  $U$  must be equal to  $\bar{U}$  assuming that for all  $X$ , there is a unique  $U$  such that  $f(X, U) = 0$ . Solving for  $G = f(E) = f(\bar{X} - X)$  such that  $G(\bar{X} - X) = \bar{U}$ , it can be seen that when  $X = \bar{X}$ , the following equation must be true:

$$G(0) = \bar{U} \quad (\text{A.5})$$

Furthermore, Fig. A.2 is equivalent to Fig. A.3. In flight control, the  $\bar{X}$  input is the trim input supplied by the thumbwheel and  $x_r$  comes from the stick. Thus, if  $X_0 = \bar{X}$  and  $x_r = 0$ , then  $X = \bar{X}$  and the FCS is quiescent. In general,  $X$  approaches  $\bar{X} + x_r$  irrespective of  $X_0$ .

There is no established method for designing  $G(E)$  in a nonlinear manner, therefore designers retreat to a linear perturbation method of control system design. In linearization,  $X = \bar{X} + x$ ,  $U = \bar{U} + u$ , and  $X_r = \bar{X} + x_r$ . Differentiating the first equation yields  $\dot{X} = \dot{x}$

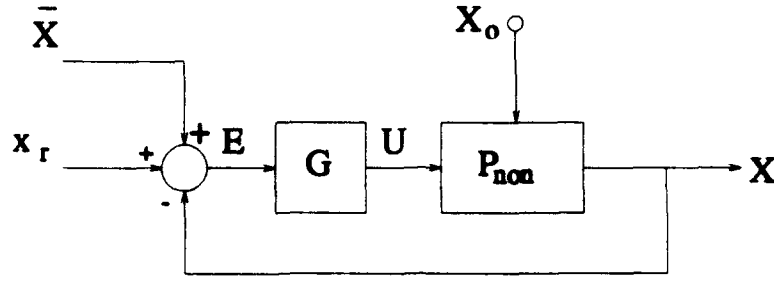


Figure A.3 Nonlinear State Feedback System with Trim Input

since  $\dot{\bar{X}} = 0$ . Performing a Taylor series expansion yields

$$\dot{x} = \dot{X} = f(X, U) = f(\bar{X}, \bar{U}) + Ax + Bu + H.O.T. \quad (A.6)$$

which leads to

$$\dot{x} = Ax + Bu + HOT \quad (A.7)$$

since  $f(\bar{X}, \bar{U})$  is equal to zero by definition.

Equation (A.7) leads to the following block diagram for linear design, where  $x_r$  is the desired perturbation,  $x$  is the actual perturbation,  $u$  is the perturbation command, and the  $H.O.T.$  are equivalent to a disturbance at the plant output.

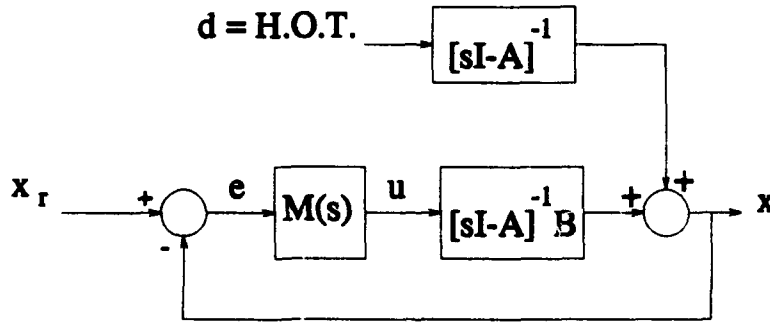


Figure A.4 Linear State Feedback System

The following equations result from Fig. A.4:

$$e(s) = x_r - x$$

$$u(s) = M(s)e(s)$$

$$\begin{aligned}
&= M(s)(x_r - x) \\
&= M(s)((X_r - \bar{X}) - (X - \bar{X})) \\
&= M(s)(X_r - X)
\end{aligned} \tag{A.8}$$

Combining Eq. (A.8) with the perturbation equation  $U = \bar{U} + u$  leads to

$$U = M(s)(X_r - X) + \bar{U} \tag{A.9}$$

which is a valid control law for the nonlinear system since it is a function of  $E(X_r - X)$ , and it is equal to  $\bar{U}$  when  $X = X_r$ , satisfying Eq. (A.5).

If the  $M(s)$  compensator is designed to guarantee that  $x$  approaches  $x_r$  for any reference  $x_r$  and any disturbance  $d$ , then  $X$  will approach  $\bar{X} + x_r = X_r$ . Obviously,  $M(s)$  must employ integral control for robustness and disturbance rejection unless the linearized plant contains integrators. When employed in the nonlinear system, the control law given in Eq. (A.9) is guaranteed only to work for  $x_r$  sufficiently small so that  $X$  stays in the "region of attraction" of the equilibrium point under consideration  $(\bar{X}, \bar{U})$ . In this case,  $d = H.O.T.$  is indeed small. In addition, robust tracking and disturbance rejection come hand in hand. Hence, when the control law given in Eq. (A.9) is added to the nonlinear system, as shown in Fig. A.5, the given control system will work in the region of attraction of  $(\bar{X}, \bar{U})$ .

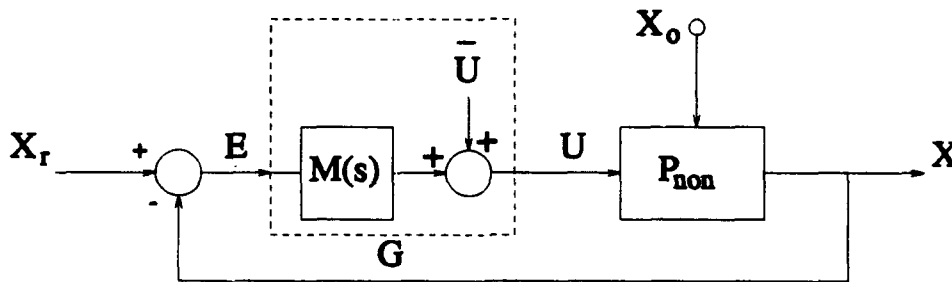


Figure A.5 Nonlinear State Feedback System with Linear Control Law

However, a common practice when evaluating nonlinear systems with linearly designed controllers, which assume perturbation measurements and perturbation control, is to use a method depicted in Fig. A.6.

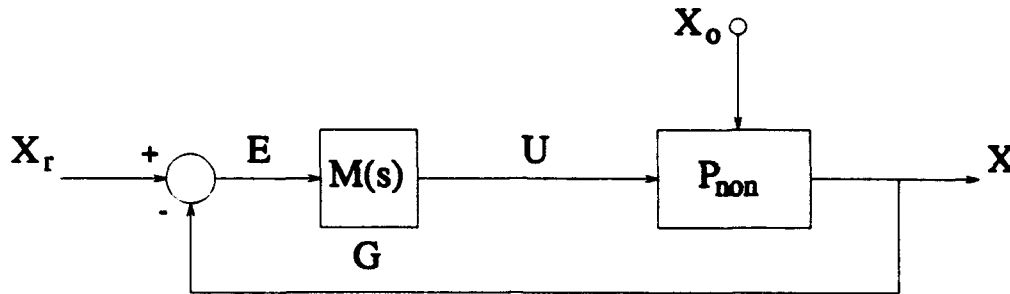


Figure A.6 Commonly Used Nonlinear State Feedback System with Linear Control Law

One may ask why the system in Fig. A.6 gives valid results. The answer lies in Fig. A.7 where a disturbance of  $-\bar{U}$  has been added to the system making the systems in Figs. A.6 and A.7 equivalent.

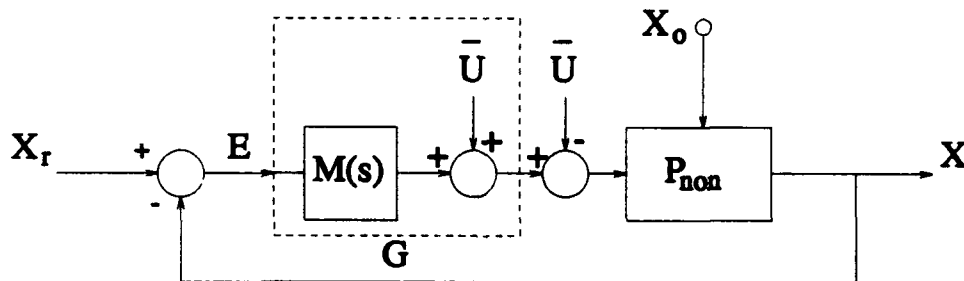


Figure A.7 Nonlinear State Feedback System with Linear Control Law and Disturbance

Now the compensator  $M(s)$ , which is synthesized to reject the disturbance (*H.O.T.*) in the linear system, also rejects the disturbance ( $\bar{U}$ ) in the nonlinear system.

The interest in this examination comes from the fact that the compensator, although designed for the linearized system, does not, in reality, operate on perturbation measurements, but rather on total measurement variables.

As an alternative point of view, reconsider Fig. A.6. Now, the nonlinear plant can be approximated as follows:

$$\begin{aligned}
 \dot{X} &= f(X, U) \\
 &= f(\bar{X}, \bar{U}) + Ax + Bu + HOT \\
 &= A(X - \bar{X}) + B(U - \bar{U}) + HOT \\
 &= Ax + Bu - (A\bar{X} + B\bar{U}) + H.O.T.
 \end{aligned}$$

By construction, the control system in Fig A.4 is known to work, but now the disturbance in Fig A.4 is replaced by:

$$d' = H.O.T. - (A\bar{X} + B\bar{U}) \quad (A.10)$$

The only difference between the two systems is the strength of the disturbance. Hence, the disturbance rejection property caused by the robustness of the  $M(s)$  compensator is the reason why, although the linearized compensators are designed with perturbations in mind, they work when applied in practice with total measurements and outputs.

In conclusion, LTI robustness is essential for the attack on nonlinearity. The more disturbance rejection capability is built into  $M(s)$ , the more the "region of attraction" premise is correct.

### *Appendix B. Plant Information*

This appendix contains the trim information and the stability derivatives for all forty plants. The table contains the trim information, and the others contains the terms for the **A** and **B** matrices as follows.

$$\mathbf{A\_VISTA} = \begin{bmatrix} 0.0 & 0.0 & 0.0 & 1.0 & 0.0 & 0.0 & 0.0 & 0.0 \\ X_{\theta} & X_u & X_{\alpha} & X_q & 0.0 & 0.0 & 0.0 & 0.0 \\ Z_{\theta} & Z_u & Z_{\alpha} & Z_q & 0.0 & 0.0 & 0.0 & 0.0 \\ M_{\theta} & M_u & M_{\alpha} & M_q & 0.0 & 0.0 & 0.0 & 0.0 \\ 0.0 & 0.0 & 0.0 & 0.0 & 0.0 & 0.0 & 1.0 & \phi_r \\ 0.0 & 0.0 & 0.0 & 0.0 & Y_{\phi} & Y_{\beta} & Y_p & Y_r \\ 0.0 & 0.0 & 0.0 & 0.0 & 0.0 & L_{\beta} & L_p & L_r \\ 0.0 & 0.0 & 0.0 & 0.0 & 0.0 & N_{\beta} & N_p & N_r \end{bmatrix}$$

$$\mathbf{B\_VISTA} = \begin{bmatrix} 0.0 & 0.0 & 0.0 & 0.0 & 0.0 \\ X_{\delta_a} & 0.0 & X_{\delta_r} & 0.0 & 0.0 \\ Z_{\delta_a} & 0.0 & Z_{\delta_r} & 0.0 & 0.0 \\ M_{\delta_a} & 0.0 & M_{\delta_r} & 0.0 & 0.0 \\ 0.0 & 0.0 & 0.0 & 0.0 & 0.0 \\ 0.0 & Y_{\delta_{a1}} & 0.0 & Y_{\delta_a} & Y_{\delta_r} \\ 0.0 & L_{\delta_{a1}} & 0.0 & L_{\delta_a} & L_{\delta_r} \\ 0.0 & N_{\delta_{a1}} & 0.0 & N_{\delta_a} & N_{\delta_r} \end{bmatrix}$$

Table B.1 Plant Parameters

Plant	Mach	Altitude	$U$	$\bar{q}$	Elevator Trim	$\alpha_{trim}$
1	0.240	1000	258.96	82.28	-0.932	14.21
2	0.400	1000	443.75	228.56	-1.976	4.68
3	0.600	1000	667.39	514.25	-1.834	2.14
4	0.700	1000	778.89	699.95	-1.896	1.52
5	0.900	1000	1001.64	1157.07	-3.136	0.96
6	0.260	5000	276.80	83.32	-1.019	14.08
7	0.280	10000	292.04	79.88	-0.801	14.61
8	0.300	10000	315.20	91.70	-1.418	12.90
9	0.500	10000	537.50	254.71	-1.910	4.19
10	0.700	10000	754.02	499.24	-1.773	2.08
11	0.900	10000	969.88	825.27	-3.042	1.20
12	0.310	15000	317.75	80.37	-0.408	14.31
13	0.340	20000	341.34	78.75	-0.378	14.59
14	0.400	20000	408.21	109.00	-1.010	10.34
15	0.500	20000	515.65	170.32	-1.584	6.21
16	0.700	20000	725.12	333.82	-1.759	3.07
17	0.900	20000	933.28	551.83	-2.636	1.61
18	0.380	25000	374.09	79.48	-0.417	14.44
19	0.420	30000	404.25	77.75	-0.387	14.75
20	0.500	30000	490.01	110.19	-0.960	10.05
21	0.700	30000	694.41	215.97	-1.744	4.65
22	0.900	30000	895.00	357.02	-2.596	2.36
23	0.470	35000	442.36	77.21	-0.389	14.82
24	0.530	40000	496.41	77.29	-0.371	14.74
25	0.700	40000	672.50	134.83	-1.125	7.27
26	0.900	40000	869.94	222.88	-2.629	3.60
27	0.700	45000	667.97	106.13	-0.675	9.84
28	0.780	50000	744.60	103.74	-0.558	9.72
29	0.900	50000	866.96	138.11	-2.668	5.95
30	0.301	1000	331.09	129.42	-1.669	8.80
31	0.324	5000	351.50	129.38	-1.526	8.72
32	0.357	10000	380.50	129.85	-1.359	8.57
33	0.394	15000	412.23	129.83	-1.256	8.48
34	0.437	20000	448.51	130.10	-1.226	8.37
35	0.486	25000	488.89	130.01	-1.178	8.28
36	0.543	30000	534.96	129.96	-1.108	8.16
37	0.610	35000	588.11	130.07	-1.024	7.99
38	0.686	40000	658.46	129.49	-1.050	7.66
39	0.774	45000	743.57	129.75	-1.059	7.29
40	0.873	50000	839.77	129.95	-2.158	6.68

Table B.2  $\dot{u}$  Longitudinal Stability Derivatives

Plant	$X_\theta$	$X_u$	$X_\alpha$	$X_q$	$X_{\dot{\alpha}}$	$X_{\dot{q}}$
1	-31.2141	-5.29722e-03	25.6644	-64.1725	1.36802	-0.634507
2	-32.0926	-1.02650e-02	44.1175	-35.9929	5.58467	-1.671580
3	-32.1775	-1.38611e-02	56.2269	-24.7609	15.30320	-4.364180
4	-32.1886	-1.59766e-02	47.8820	-20.5185	22.17290	-4.612690
5	-32.1955	-2.40202e-02	18.7719	-16.5991	46.31090	-7.796340
6	-31.2331	-4.67356e-03	24.9647	-67.9272	1.38840	-0.628677
7	-31.1583	-5.67714e-03	26.1363	-74.4449	1.30902	-0.655388
8	-31.3873	-2.56428e-04	19.7416	-70.8308	1.61068	-0.573269
9	-32.1140	-8.71998e-03	38.2505	-39.0657	7.09560	-1.887850
10	-32.1788	-1.18851e-02	51.1469	-27.1735	15.85710	-4.274780
11	-32.1930	-1.78849e-02	26.7723	-20.1388	32.95250	-6.027290
12	-31.2011	-8.39799e-04	21.9930	-79.2995	1.32032	-0.631892
13	-31.1616	-1.58706e-03	22.4789	-86.8867	1.26949	-0.648894
14	-31.6771	2.43115e-03	16.3530	-73.4589	2.08784	-0.542584
15	-32.0112	-5.16937e-03	28.7884	-55.6568	4.34126	-1.090700
16	-32.1536	-6.90603e-03	15.9745	-38.7360	10.57670	-2.597590
17	-32.1873	-1.18833e-02	33.4767	-26.0592	21.66000	-4.977320
18	-31.1832	-7.71469e-04	21.0947	-94.2213	1.27839	-0.640072
19	-31.1394	-1.34468e-03	21.4141	-104.0210	1.20620	-0.656131
20	-31.7059	3.87767e-03	10.9369	-85.7719	2.34375	-0.534296
21	-32.0942	-6.26478e-03	37.1338	-56.1297	6.76856	-1.579760
22	-32.1727	-8.37097e-03	43.0983	-36.6954	13.84540	-2.935970
23	-31.1291	-1.13417e-03	20.6185	-114.3890	1.16985	-0.659890
24	-31.1403	-4.77684e-04	18.8096	-127.6880	1.15293	-0.650885
25	-31.9408	-4.14983e-03	31.1088	-85.2190	3.77481	-0.792291
26	-32.1366	-4.72257e-03	9.7068	-54.4722	8.27701	-1.689630
27	-31.7261	-3.06262e-03	29.3778	-114.5950	2.42427	-0.518227
28	-31.7381	-2.27070e-03	24.4479	-126.1220	2.33955	-0.511643
29	-32.0267	-2.51049e-03	9.6314	-89.8623	4.64228	-0.906366
30	-31.8208	-6.21675e-03	32.3022	-50.5634	2.20793	-0.687108
31	-31.8279	-5.47339e-03	31.2373	-53.2059	2.28743	-0.690458
32	-31.8404	-4.50592e-03	29.1776	-56.6622	2.41797	-0.699594
33	-31.8482	-3.92789e-03	28.1228	-60.7477	2.56116	-0.704075
34	-31.8569	-3.60817e-03	27.7392	-65.3141	2.74006	-0.709878
35	-31.8641	-3.30062e-03	27.4693	-70.4817	2.93895	-0.714227
36	-31.8736	-2.93536e-03	27.0442	-76.0497	3.18453	-0.720146
37	-31.8873	-2.55863e-03	25.5177	-81.8557	3.45645	-0.728603
38	-31.9127	-1.50991e-03	18.7305	-87.8733	3.53311	-0.741461
39	-31.9400	-3.59111e-03	29.3690	-94.3980	3.66637	-0.762463
40	-31.9815	-3.02269e-03	17.7765	-97.7453	4.08987	-0.797675



Table B.3  $\alpha$  Longitudinal Stability Derivatives

Plant	$Z_0$	$Z_u$	$Z_w$	$Z_\delta$	$Z_{\delta_r}$	$Z_{\delta_a}$
1	-3.05331e-02	-4.19285e-04	-0.583872	0.998865	-0.0861032	-0.0396283
2	-5.92266e-03	-1.60652e-04	-0.907097	0.992663	-0.1347810	-0.0719470
3	-1.80311e-03	-7.36040e-05	-1.268190	0.992528	-0.2078660	-0.1147490
4	-1.09803e-03	-5.44363e-05	-1.517170	0.991707	-0.2389300	-0.1790610
5	-5.38026e-04	-2.30771e-05	-2.460180	0.990132	-0.2966700	-0.2587790
6	-2.82938e-02	-3.69042e-04	-0.549095	0.998866	-0.0811602	-0.0376452
7	-2.78180e-02	-3.34315e-04	-0.499479	0.999453	-0.0748765	-0.0338127
8	-2.28069e-02	-2.89196e-04	-0.517095	0.998103	-0.0757602	-0.0372404
9	-4.37475e-03	-1.07929e-04	-0.848239	0.994400	-0.1261100	-0.0672749
10	-1.54841e-03	-5.79756e-05	-1.150910	0.993709	-0.1775160	-0.0984933
11	-6.94541e-04	-2.73017e-05	-1.908370	0.992496	-0.2194280	-0.1884890
12	-2.50454e-02	-2.93027e-04	-0.454934	0.999328	-0.0685085	-0.0314342
13	-2.37642e-02	-2.56359e-04	-0.412692	0.999592	-0.0628252	-0.0284894
14	-1.41578e-02	-1.95975e-04	-0.440414	0.997196	-0.0684394	-0.0337867
15	-6.75244e-03	-1.20899e-04	-0.581751	0.996229	-0.0867622	-0.0435902
16	-2.38182e-03	-5.98105e-05	-0.848612	0.995479	-0.1244930	-0.0677453
17	-9.68497e-04	-3.35493e-05	-1.343290	0.994584	-0.1523890	-0.0895460
18	-2.14602e-02	-2.17619e-04	-0.374309	0.999583	-0.0574754	-0.0263180
19	-2.02753e-02	-1.88685e-04	-0.336112	0.999777	-0.0521672	-0.0236747
20	-1.14679e-02	-1.37644e-04	-0.372490	0.997916	-0.0580365	-0.0283869
21	-3.75591e-03	-6.45474e-05	-0.593611	0.996843	-0.0847186	-0.0435037
22	-1.48032e-03	-3.79065e-05	-0.925160	0.996194	-0.1037290	-0.0596465
23	-1.86170e-02	-1.60848e-04	-0.300258	0.999839	-0.0471820	-0.0214281
24	-1.65038e-02	-1.31318e-04	-0.262145	0.999851	-0.0417852	-0.0191640
25	-6.06268e-03	-7.08768e-05	-0.383021	0.998127	-0.0527614	-0.0253291
26	-2.32200e-03	-3.92951e-05	-0.636603	0.997492	-0.0672052	-0.0370770
27	-8.24003e-03	-8.66777e-05	-0.230418	0.998708	-0.0407982	-0.0200418
28	-7.29828e-03	-7.22741e-05	-0.198306	0.998858	-0.0354386	-0.0175674
29	-3.84868e-03	-5.34410e-05	-0.272346	0.998492	-0.0422786	-0.0212406
30	-1.48823e-02	-3.21772e-04	-0.583050	0.994100	-0.0997477	-0.0490995
31	-1.38862e-02	-2.89258e-04	-0.545615	0.994737	-0.0941042	-0.0462237
32	-1.26127e-02	-2.50784e-04	-0.502441	0.995448	-0.0875454	-0.0428593
33	-1.15143e-02	-2.16022e-04	-0.461928	0.996097	-0.0810456	-0.0395418
34	-1.04529e-02	-1.84056e-04	-0.424963	0.996673	-0.0749311	-0.0364091
35	-9.48927e-03	-1.56404e-04	-0.389067	0.997185	-0.0689465	-0.0333696
36	-8.54817e-03	-1.32174e-04	-0.354764	0.997632	-0.0632686	-0.0304737
37	-7.61127e-03	-1.11484e-04	-0.320735	0.997987	-0.0578512	-0.0277288
38	-6.51844e-03	-9.29282e-05	-0.278835	0.998194	-0.0515032	-0.0246335
39	-5.49169e-03	-5.88901e-05	-0.340624	0.998395	-0.0459876	-0.0220354
40	-4.45940e-03	-5.37084e-05	-0.274699	0.998567	-0.0411295	-0.0200474

Table B.4  $\dot{q}$  Longitudinal Stability Derivatives

Plant	$M_\theta$	$M_u$	$M_w$	$M_q$	$M_{\dot{\theta}}$	$M_{\dot{u}}$
1	3.24104e-04	-2.12406e-03	1.005050	-0.602391	-2.62313	0.134451
2	7.37049e-04	-7.59253e-04	1.230700	-1.035590	-7.66968	0.218051
3	3.64510e-04	-5.07737e-04	3.043320	-1.563560	-18.78070	0.214610
4	2.84188e-04	-4.77784e-04	5.681860	-1.716010	-27.31980	0.669585
5	2.86254e-04	-3.23850e-04	6.392300	-2.062760	-51.22420	-2.478030
6	3.52705e-04	-1.96509e-03	0.993000	-0.572453	-2.66677	0.136391
7	1.79109e-04	-1.85192e-03	0.926228	-0.517550	-2.55828	0.129688
8	6.01509e-04	-1.62317e-03	0.984142	-0.562333	-2.97157	0.155920
9	5.16257e-04	-6.81382e-04	1.750650	-0.956317	-8.84708	0.205157
10	2.94913e-04	-4.81700e-04	3.724070	-1.265880	-19.50350	0.211559
11	2.68968e-04	-2.88469e-04	2.680610	-1.517770	-36.59260	-1.225830
12	2.48241e-04	-1.50690e-03	0.712481	-0.481369	-2.59064	0.133082
13	1.81989e-04	-1.38814e-03	0.672597	-0.438722	-2.54743	0.130040
14	6.42121e-04	-1.34645e-03	1.525120	-0.526916	-3.64478	0.285675
15	5.17768e-04	-1.08870e-03	2.854660	-0.663550	-5.81785	0.287442
16	3.09665e-04	-5.54865e-04	3.088920	-0.879750	-13.00790	0.161706
17	2.55268e-04	-2.85733e-04	1.291490	-1.052130	-24.32820	0.236211
18	2.01991e-04	-1.21741e-03	0.612286	-0.405861	-2.58985	0.131333
19	1.55306e-04	-1.10603e-03	0.559403	-0.367459	-2.54518	0.128093
20	4.81243e-04	-1.16017e-03	1.672290	-0.446565	-3.75734	0.301586
21	3.13886e-04	-5.68574e-04	1.826070	-0.592087	-8.35104	0.198684
22	2.53102e-04	-2.98647e-04	0.722257	-0.706244	-15.71970	0.126182
23	1.47021e-04	-9.69717e-04	0.486184	-0.334625	-2.54650	0.127030
24	1.45886e-04	-8.19412e-04	0.406054	-0.300093	-2.57434	0.127422
25	2.91640e-04	-8.56982e-04	2.473650	-0.380152	-5.08415	0.305409
26	2.33279e-04	-2.93566e-04	0.148186	-0.447547	-9.88464	0.139447
27	2.77215e-04	-8.03426e-04	1.518650	-0.300330	-3.94293	0.288811
28	2.26906e-04	-7.62486e-04	1.720160	-0.251471	-4.06227	0.279959
29	1.94633e-04	-6.83501e-04	3.201320	-0.270880	-6.19941	0.212269
30	1.08722e-03	-1.43963e-03	1.415110	-0.773146	-4.22204	0.337996
31	9.71098e-04	-1.36274e-03	1.437400	-0.729050	-4.23901	0.335533
32	8.38331e-04	-1.26079e-03	1.461280	-0.677312	-4.27997	0.333145
33	7.21985e-04	-1.16456e-03	1.474030	-0.626288	-4.31022	0.330642
34	6.18606e-04	-1.06992e-03	1.485070	-0.578136	-4.35622	0.328944
35	5.27750e-04	-9.80703e-04	1.492610	-0.531259	-4.39585	0.326624
36	4.46986e-04	-8.94698e-04	1.505020	-0.486660	-4.44394	0.323884
37	3.75309e-04	-8.18433e-04	1.555530	-0.441788	-4.53609	0.320513
38	3.00324e-04	-7.62016e-04	1.780040	-0.375887	-4.81222	0.312554
39	2.36968e-04	-7.78755e-04	2.485440	-0.315802	-5.18772	0.294545
40	1.95710e-04	-7.06406e-04	2.840240	-0.264930	-5.69814	0.251440

Table B.5  $\beta$  Lateral Stability Derivatives

Plant	$Y_\phi$	$Y_\beta$	$Y_p$	$Y_r$	$Y_{\delta_a}$	$Y_{\delta_r}$	$Y_{\delta_s}$
1	0.1205350	-0.125678	0.248441	-0.995187	1.60166e-03	0.0178196	0.0246049
2	0.0723211	-0.216088	0.082353	-0.996289	4.21511e-03	0.0272424	0.0323999
3	0.0482141	-0.323310	0.037728	-0.996355	1.00626e-02	0.0418114	0.0497382
4	0.0413264	-0.369592	0.026790	-0.996334	9.60254e-03	0.0447727	0.0567339
5	0.0321427	-0.481253	0.016898	-0.996273	7.81900e-03	0.0446168	0.0540850
6	0.1128360	-0.119496	0.245996	-0.995754	1.34823e-03	0.0167282	0.0227491
7	0.1066910	-0.109244	0.255252	-0.996329	1.03210e-03	0.0151383	0.0205398
8	0.0995786	-0.116244	0.225513	-0.996472	1.06598e-03	0.0158793	0.0205347
9	0.0597472	-0.202815	0.073533	-0.997212	4.32381e-03	0.0266637	0.0301492
10	0.0426766	-0.280849	0.036498	-0.997234	7.32738e-03	0.0354687	0.0445503
11	0.0331929	-0.367059	0.021073	-0.997183	6.66843e-03	0.0380671	0.0477913
12	0.0981936	-0.101604	0.249915	-0.996904	7.44681e-04	0.0138411	0.0183001
13	0.0912931	-0.093332	0.254770	-0.997373	4.39531e-04	0.0125252	0.0163109
14	0.0775991	-0.109880	0.180844	-0.997627	5.69506e-04	0.0137713	0.0169586
15	0.0620793	-0.142120	0.108758	-0.997908	1.76761e-03	0.0187523	0.0204912
16	0.0443423	-0.201980	0.053902	-0.998011	4.78156e-03	0.0255941	0.0316682
17	0.0344885	-0.263339	0.028221	-0.997988	5.52063e-03	0.0279925	0.0377028
18	0.0833575	-0.086697	0.252066	-0.997809	1.57037e-04	0.0114031	0.0143709
19	0.0770298	-0.079119	0.257419	-0.998167	-1.49334e-04	0.0102305	0.0125456
20	0.0647050	-0.095739	0.175686	-0.998373	1.07214e-04	0.0120180	0.0136867
21	0.0462179	-0.140733	0.081333	-0.998592	2.31454e-03	0.0178611	0.0206142
22	0.0359472	-0.182867	0.041308	-0.998612	3.71197e-03	0.0200217	0.0276091
23	0.0703705	-0.072515	0.258649	-0.998488	-4.26571e-04	0.0091764	0.0107761
24	0.0627305	-0.065504	0.257263	-0.998810	-6.65871e-04	0.0080850	0.0089557
25	0.0474960	-0.091465	0.127160	-0.999019	2.66720e-04	0.0111662	0.0122215
26	0.0369413	-0.120937	0.062911	-0.999096	2.03166e-03	0.0134786	0.0189094
27	0.0474960	-0.071849	0.171902	-0.999176	-3.64546e-04	0.0082333	0.0092356
28	0.0426246	-0.064413	0.169664	-0.999354	-4.56120e-04	0.0068168	0.0081295
29	0.0369413	-0.078248	0.103908	-0.999437	5.98656e-04	0.0084451	0.0118629
30	0.0961078	-0.156008	0.154409	-0.995785	1.48425e-03	0.0197581	0.0255327
31	0.0905475	-0.148090	0.152867	-0.996283	1.30353e-03	0.0187951	0.0237907
32	0.0836795	-0.138922	0.150198	-0.996844	1.09536e-03	0.0177490	0.0217805
33	0.0772589	-0.129870	0.148458	-0.997333	8.91369e-04	0.0166550	0.0198140
34	0.0710289	-0.121434	0.146551	-0.997762	7.00342e-04	0.0156716	0.0179924
35	0.0651766	-0.113206	0.144946	-0.998135	5.13257e-04	0.0147008	0.0162501
36	0.0595811	-0.105450	0.142809	-0.998460	3.44246e-04	0.0138213	0.0146331
37	0.0542199	-0.098090	0.139725	-0.998740	2.08977e-04	0.0128871	0.0131236
38	0.0484653	-0.089305	0.133896	-0.999009	1.34828e-04	0.0109640	0.0118305
39	0.0429550	-0.081344	0.127310	-0.999231	1.19861e-04	0.0092689	0.0108495
40	0.0380838	-0.075428	0.116661	-0.999424	3.24604e-04	0.0081104	0.0107617

Table B.6  $\dot{\phi}$  and  $\dot{p}$  Lateral Stability Derivatives

Plant	$\phi_r$	$L_\beta$	$L_p$	$L_r$	$L_{\dot{\beta}}$	$L_{\dot{p}}$	$L_{\dot{r}}$
1	0.253312	-15.6431	-1.46912	0.1989140	-9.5748	-6.4348	1.68185
2	0.081894	-23.6201	-3.11101	-0.0077133	-27.7078	-18.3377	5.97589
3	0.037398	-40.5076	-4.67125	-0.0500673	-55.0688	-40.7879	12.69900
4	0.026570	-47.3741	-5.44911	-0.0801037	-64.5642	-48.9191	16.45290
5	0.016739	-65.3913	-7.00556	-0.1251770	-72.6455	-65.0340	21.80190
6	0.250751	-15.4654	-1.40622	0.1819530	-9.6162	-6.5141	1.76773
7	0.260733	-14.9870	-1.22653	0.1890040	-9.0641	-6.2842	1.68251
8	0.229034	-15.7957	-1.47974	0.1252840	-10.6498	-7.2247	2.19850
9	0.073221	-26.9084	-2.86516	-0.0115901	-30.4425	-22.2978	6.46491
10	0.036283	-39.9148	-4.01372	-0.0548366	-49.7217	-37.7488	11.87080
11	0.020924	-56.0872	-5.16038	-0.0939599	-62.2980	-50.6759	18.31270
12	0.255061	-16.3795	-1.16094	0.1623410	-9.0532	-6.3156	1.80229
13	0.260307	-15.9532	-1.03626	0.1587140	-8.7130	-6.1813	1.81654
14	0.182448	-18.5276	-1.55588	0.0413477	-12.4072	-8.9904	2.86294
15	0.108771	-21.7879	-1.98717	0.0077785	-20.4750	-15.0615	4.50004
16	0.053714	-31.7649	-2.78830	-0.0325008	-35.6371	-26.1397	8.02139
17	0.028082	-44.3875	-3.58565	-0.0670880	-46.5164	-32.0174	13.69710
18	0.257447	-15.7936	-0.96549	0.1409220	-8.6909	-6.2330	1.95031
19	0.263214	-15.3029	-0.85319	0.1374270	-8.2802	-6.0686	1.99004
20	0.177233	-18.0768	-1.32843	0.0294324	-12.5695	-9.5915	2.96807
21	0.081265	-24.7794	-1.87927	-0.0148505	-24.9657	-18.0597	5.25322
22	0.041180	-35.4107	-2.41835	-0.0468374	-33.0467	-21.1877	9.26877
23	0.264557	-14.9612	-0.76982	0.1269110	-8.0367	-6.0207	2.10726
24	0.263090	-14.6444	-0.69079	0.1112610	-7.9027	-6.0417	2.27757
25	0.127646	-18.3005	-1.17091	0.0055770	-15.5508	-11.3287	3.59942
26	0.062857	-28.2537	-1.55134	-0.0301607	-22.4404	-14.4551	5.54630
27	0.173489	-15.3847	-0.88943	0.0178386	-11.1689	-8.8061	2.96771
28	0.171222	-13.8011	-0.74597	0.0136220	-10.2055	-7.9824	2.94533
29	0.104184	-23.8222	-0.94672	-0.0147678	-15.2126	-10.1715	2.92963
30	0.154850	-20.0718	-2.32864	0.0360930	-14.8661	-10.0078	3.35311
31	0.153359	-19.8955	-2.19365	0.0333025	-14.8503	-10.1923	3.37018
32	0.150726	-19.6971	-2.03517	0.0297265	-14.9341	-10.5547	3.41164
33	0.149035	-19.5566	-1.87896	0.0268066	-14.9440	-10.7719	3.43884
34	0.147165	-19.4700	-1.73145	0.0240573	-15.0264	-11.0618	3.47980
35	0.145593	-19.4041	-1.58792	0.0216011	-15.1044	-11.3508	3.50958
36	0.143471	-19.4314	-1.45137	0.0191483	-15.2531	-11.7013	3.54587
37	0.140378	-19.2790	-1.31777	0.0160583	-15.3421	-11.9769	3.57782
38	0.134497	-17.9450	-1.14664	0.0087698	-14.8930	-11.0305	3.50115
39	0.127847	-17.3521	-0.99879	0.0013243	-14.6038	-10.0821	3.43671
40	0.117094	-22.0925	-0.90397	-0.0096816	-14.4653	-9.8365	2.82153

Table B.7  $\dot{\gamma}$  Lateral Stability Derivatives

Plant	$N_\beta$	$N_p$	$N_r$	$N_{\delta_a}$	$N_{\delta_r}$	$N_{\delta_s}$
1	1.80138	-0.0479147	-0.349715	-0.079213	-0.70114	-0.88657
2	6.11399	-0.0498483	-0.524626	-0.487239	-2.34386	-2.40035
3	12.99470	-0.0489432	-0.781803	-1.142960	-4.60729	-5.19528
4	16.25420	-0.0495443	-0.837733	-1.348100	-5.79858	-7.22962
5	26.25520	-0.0539665	-0.878436	-1.544320	-7.64738	-10.03630
6	1.85593	-0.0457436	-0.330925	-0.078895	-0.70778	-0.89379
7	1.76043	-0.0403231	-0.302073	-0.065347	-0.64642	-0.85801
8	2.17809	-0.0465514	-0.316454	-0.099204	-0.82219	-0.97493
9	6.91909	-0.0428275	-0.482285	-0.552333	-2.55395	-2.70743
10	11.86010	-0.0412056	-0.619667	-1.014500	-4.45239	-5.47685
11	20.03600	-0.0421104	-0.650225	-1.283590	-6.29507	-8.31646
12	1.79613	-0.0379820	-0.278646	-0.065283	-0.65337	-0.86029
13	1.76216	-0.0340942	-0.254788	-0.054607	-0.61805	-0.84404
14	2.83301	-0.0432911	-0.282169	-0.130713	-1.03452	-1.16519
15	4.70229	-0.0381457	-0.340794	-0.311424	-1.70549	-1.84029
16	8.30499	-0.0343059	-0.434228	-0.679959	-3.09516	-3.82803
17	14.05780	-0.0310184	-0.455614	-0.926812	-4.45880	-6.22474
18	1.80715	-0.0317044	-0.234342	-0.051732	-0.61739	-0.85036
19	1.77103	-0.0281821	-0.212686	-0.038507	-0.58029	-0.83289
20	2.98709	-0.0363199	-0.236839	-0.130142	-1.02804	-1.19090
21	5.68822	-0.0289153	-0.297332	-0.408285	-2.06120	-2.52778
22	9.31975	-0.0249032	-0.312110	-0.619851	-3.07548	-4.32622
23	1.77276	-0.0254797	-0.193149	-0.028710	-0.55949	-0.82872
24	1.79342	-0.0228645	-0.172196	-0.021355	-0.54663	-0.83279
25	3.74121	-0.0237543	-0.197665	-0.187044	-1.26088	-1.58625
26	5.87525	-0.0194844	-0.207154	-0.376459	-2.04679	-2.81542
27	2.91727	-0.0225244	-0.157520	-0.096890	-0.91962	-1.24468
28	2.81165	-0.0176760	-0.131346	-0.072458	-0.87060	-1.28716
29	3.74891	-0.0155265	-0.135860	-0.206148	-1.29832	-1.79362
30	3.40014	-0.0573310	-0.409882	-0.178022	-1.32017	-1.36976
31	3.41776	-0.0536071	-0.385904	-0.177816	-1.31219	-1.37010
32	3.47009	-0.0490771	-0.357668	-0.179051	-1.31056	-1.37976
33	3.50136	-0.0449202	-0.330016	-0.180240	-1.29527	-1.38450
34	3.54646	-0.0409955	-0.303908	-0.182929	-1.28251	-1.39666
35	3.58573	-0.0372898	-0.278567	-0.183459	-1.26624	-1.40295
36	3.63314	-0.0337029	-0.254427	-0.184854	-1.25102	-1.41350
37	3.67922	-0.0299457	-0.230269	-0.188289	-1.23226	-1.43773
38	3.61215	-0.0242643	-0.196028	-0.174003	-1.20580	-1.50818
39	3.52061	-0.0194833	-0.164656	-0.159097	-1.19070	-1.61170
40	3.53725	-0.0159920	-0.135962	-0.180124	-1.19742	-1.66598

### *Appendix C. Compensator Design Information*

This appendix contains the initial information required before performing a QFT based design. This includes the bare plant, effective plant, and  $q_{ii}$  Bode plots that are not already included in the body of the thesis.

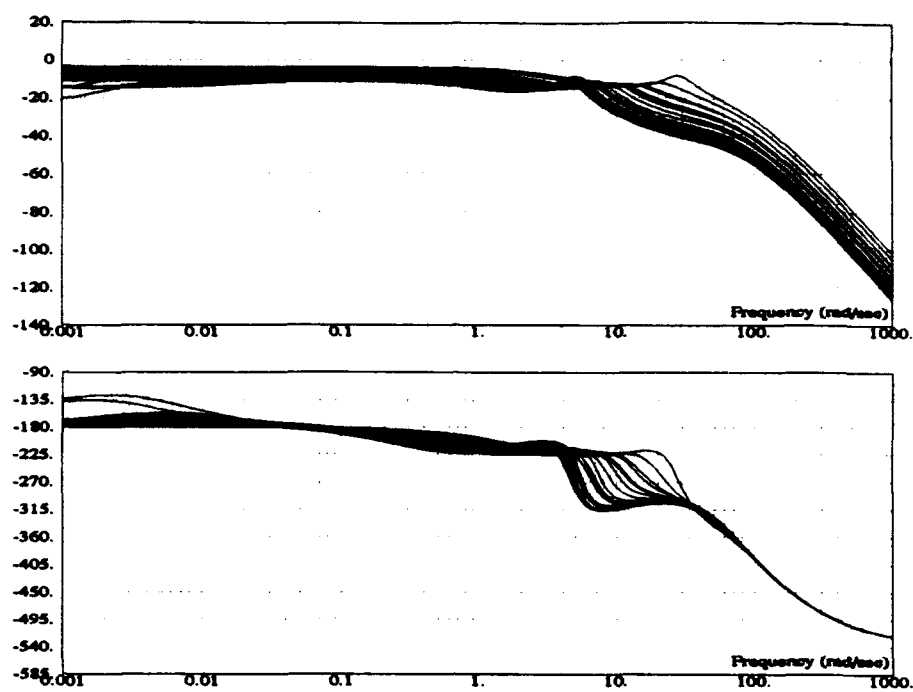


Figure C.1 Longitudinal Outer Loop  $C^*$  Bode Plots

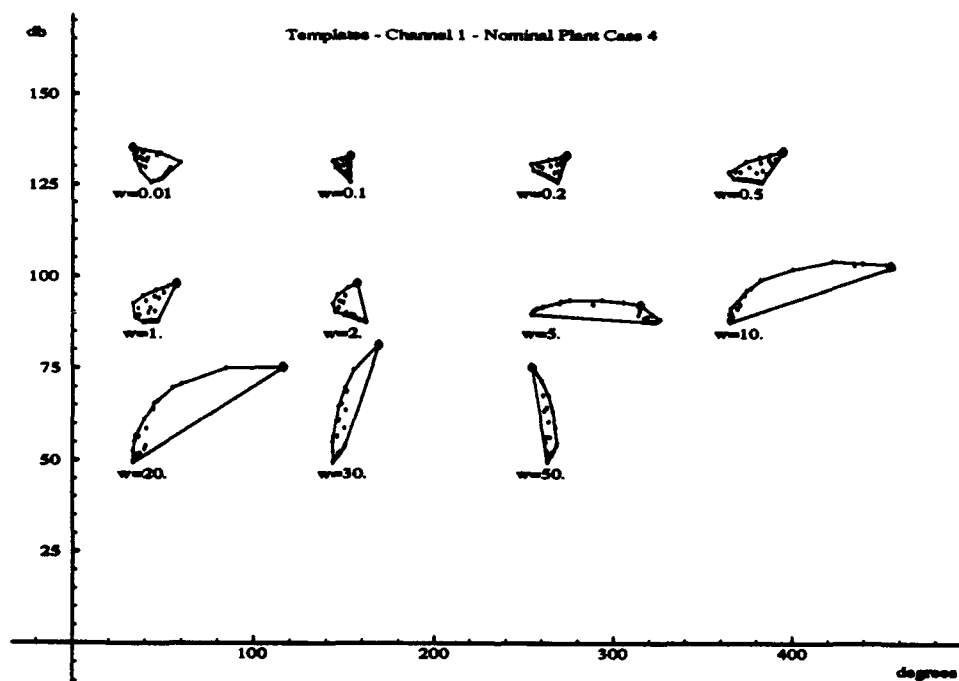


Figure C.2 Longitudinal Outer Loop  $C^*$  Templates

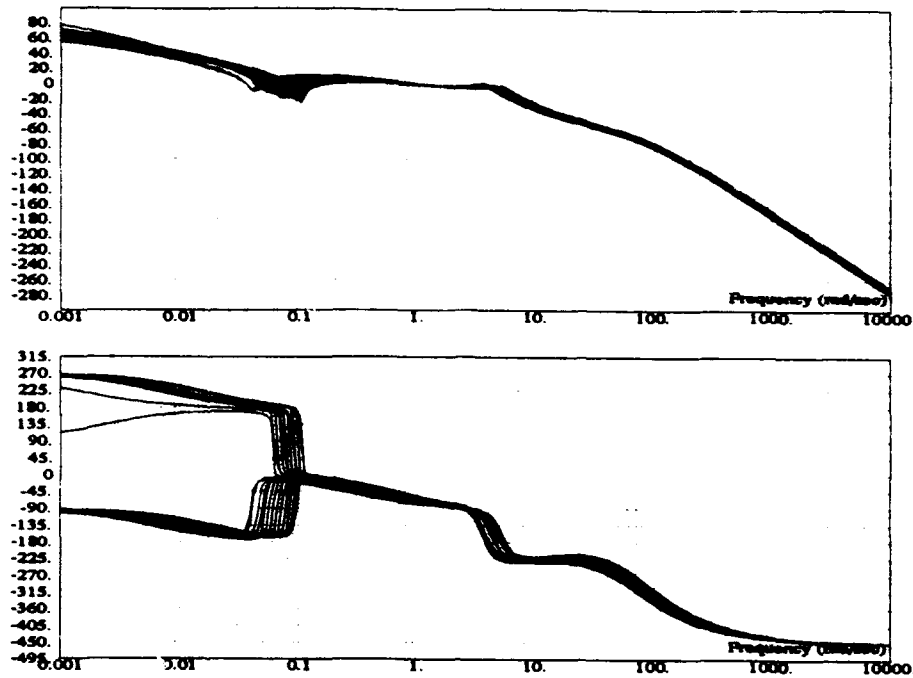


Figure C.3 Longitudinal Outer Loop  $C^* \alpha$  Bode Plots

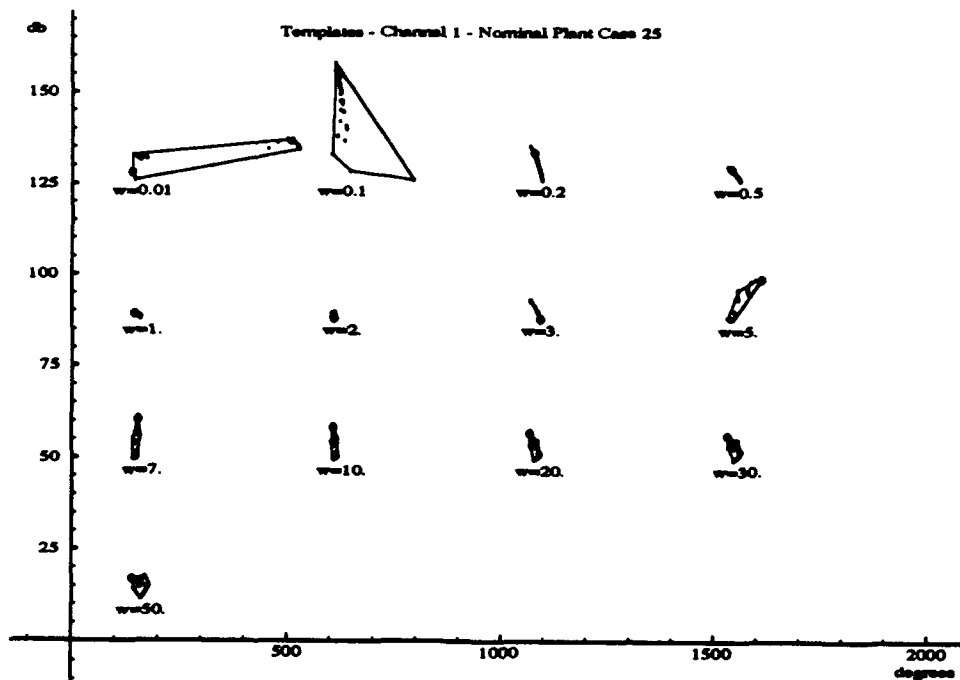


Figure C.4 Longitudinal Outer Loop  $C^* \alpha$  Templates



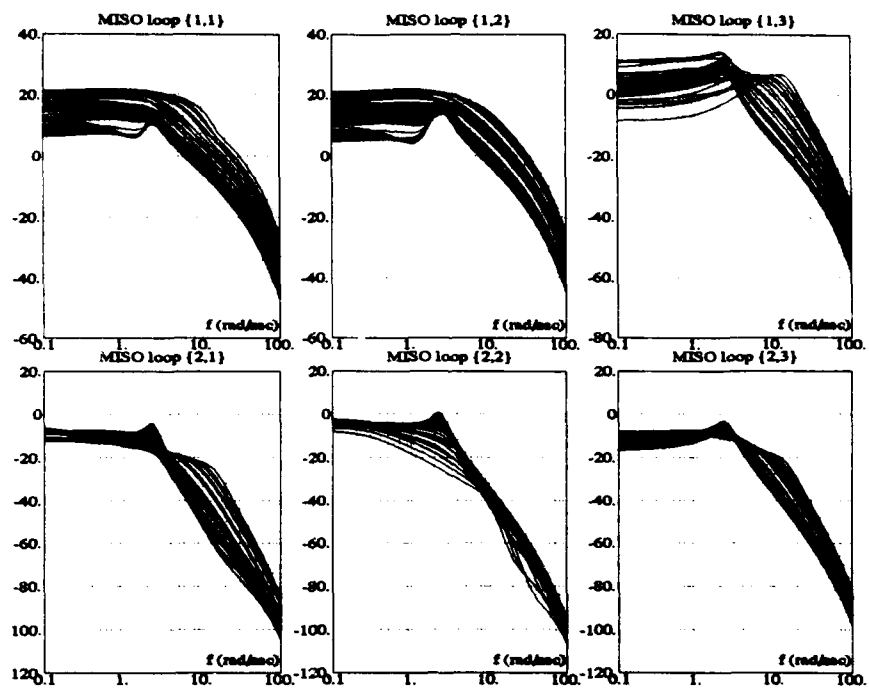


Figure C.5 Bare Plant Bode Plots for the Body Axis Design

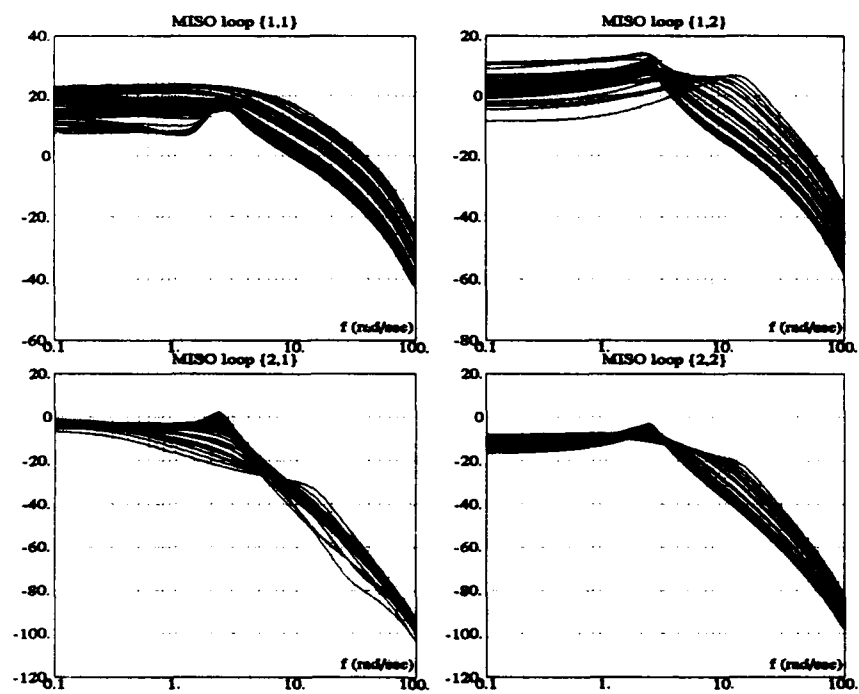


Figure C.6 Body Axis  $P_e$  Bode Plots without Interconnects

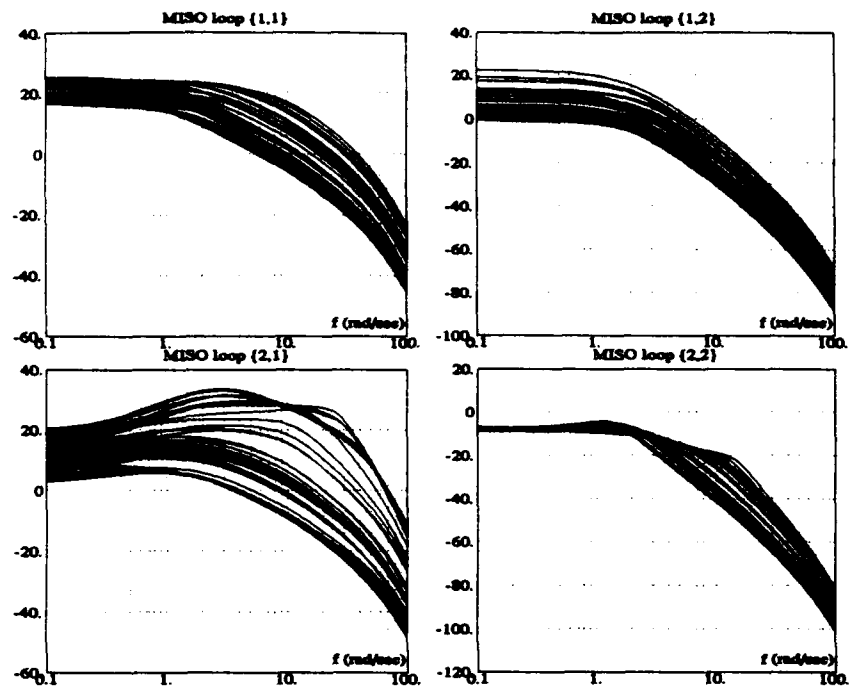


Figure C.7 Body Axis  $q_{ii}$  Bode Plots without Interconnects

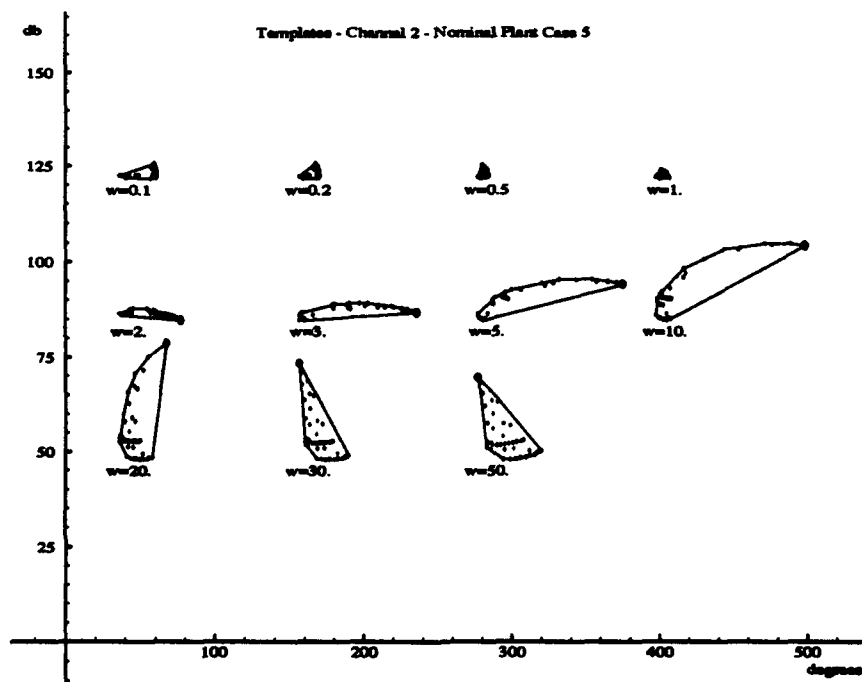


Figure C.8 Body Axis (2,2) Templates without Interconnects

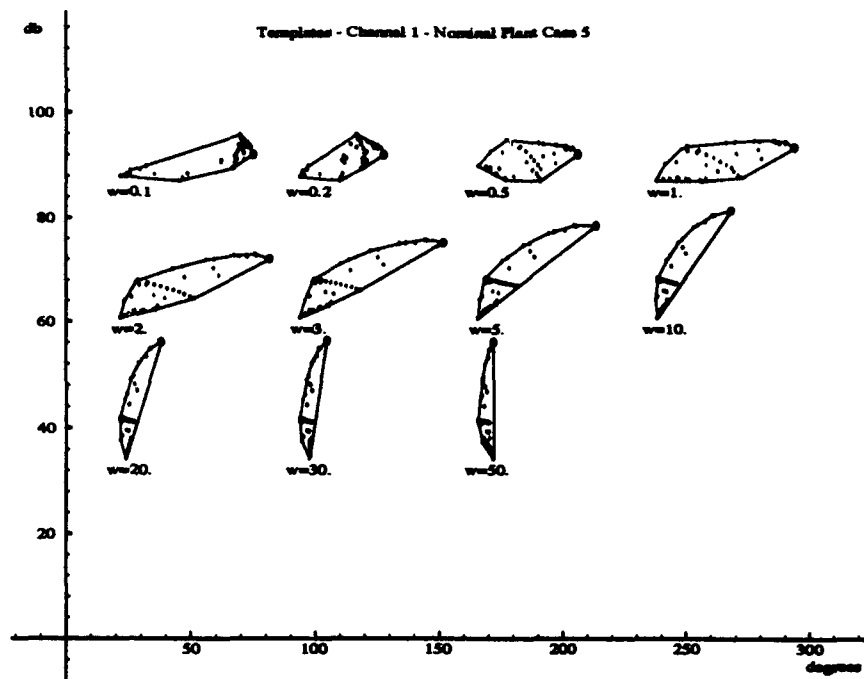


Figure C.9 Body Axis (1,1) Templates without Interconnects

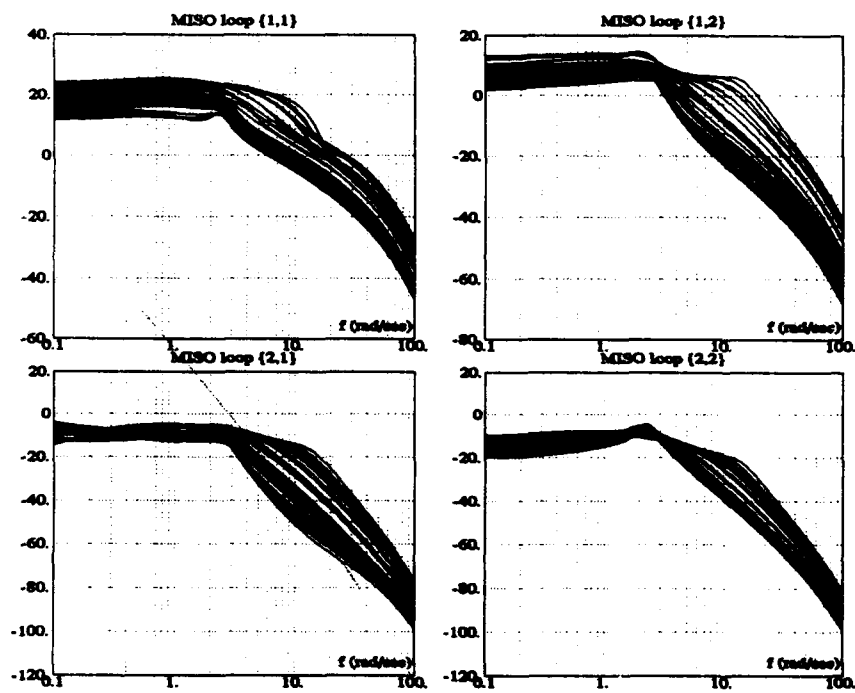


Figure C.10 Body Axis  $P_e$  Bode Plots with Interconnects

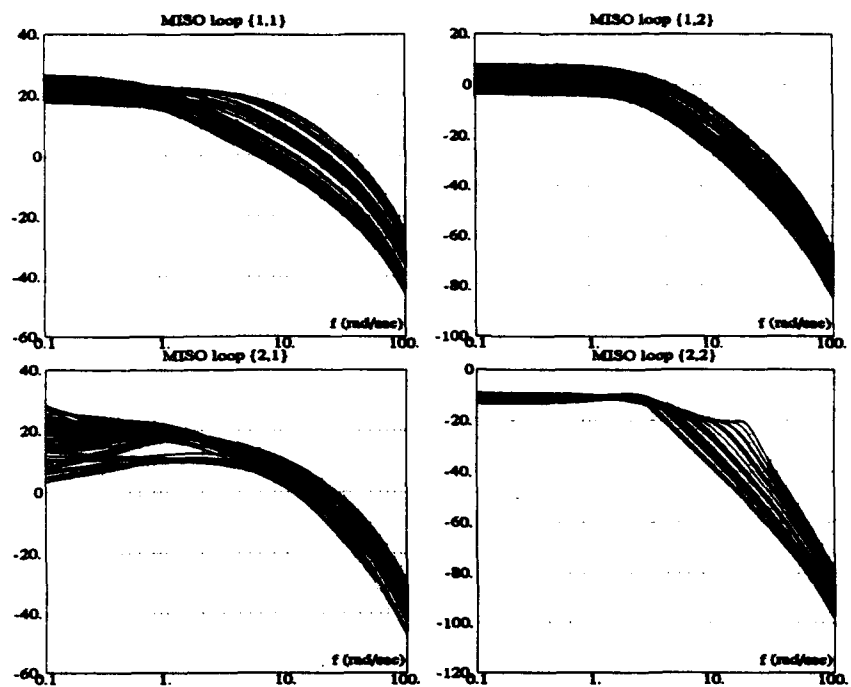


Figure C.11 Body Axis  $q_{ii}$  Bode Plots with Interconnects

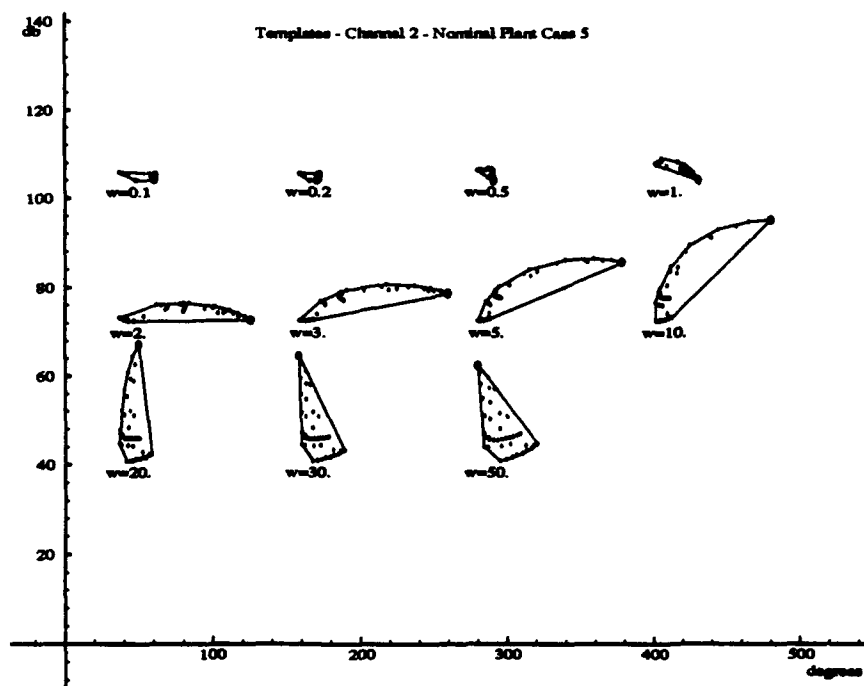


Figure C.12 Body Axis (2,2) Templates with Interconnects

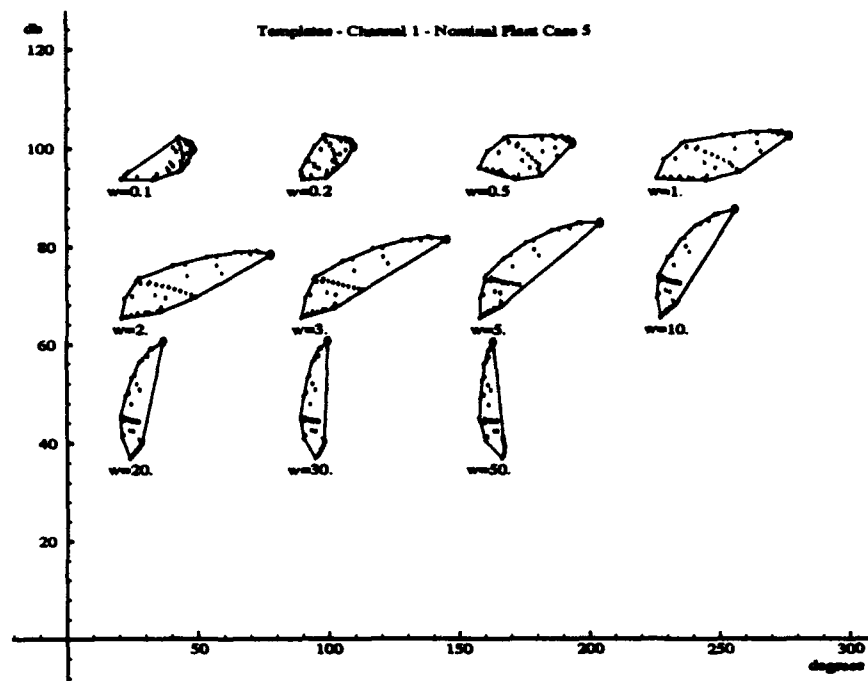


Figure C.13 Body Axis (1,1) Templates with Interconnects

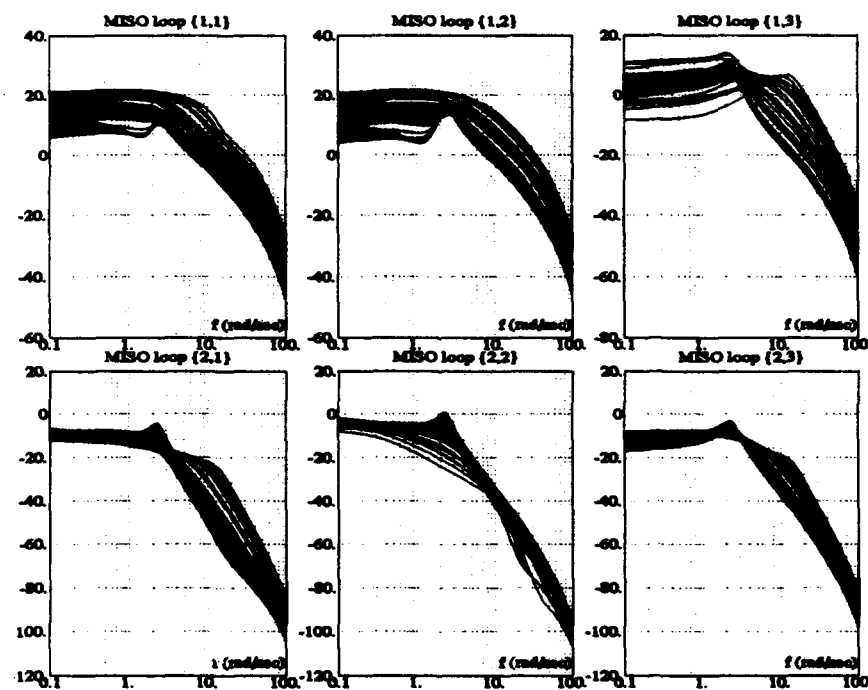


Figure C.14 Bare Plant Bode Plots for the Stability Axis Design

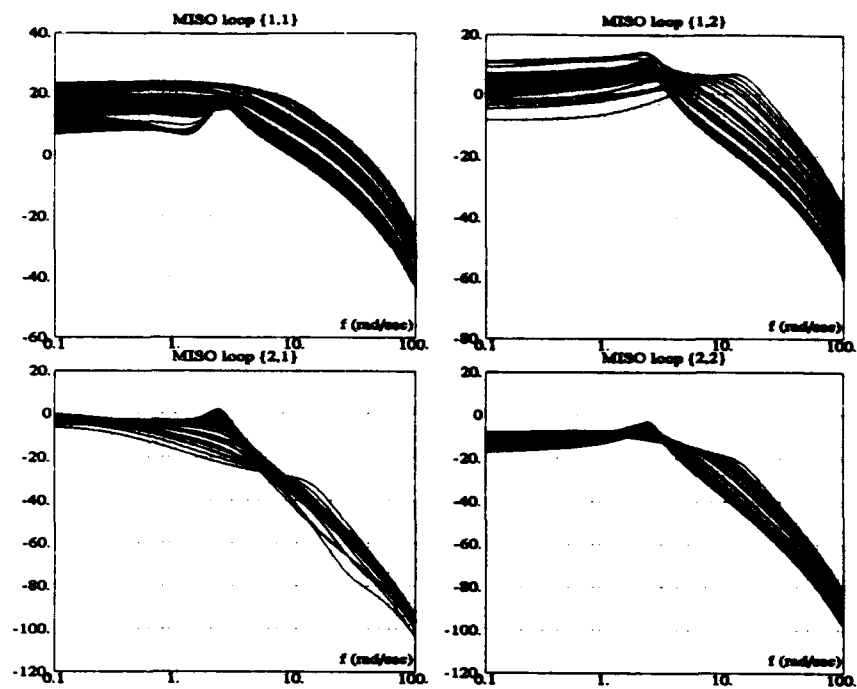


Figure C.15 Stability Axis  $P_e$  Bode Plots

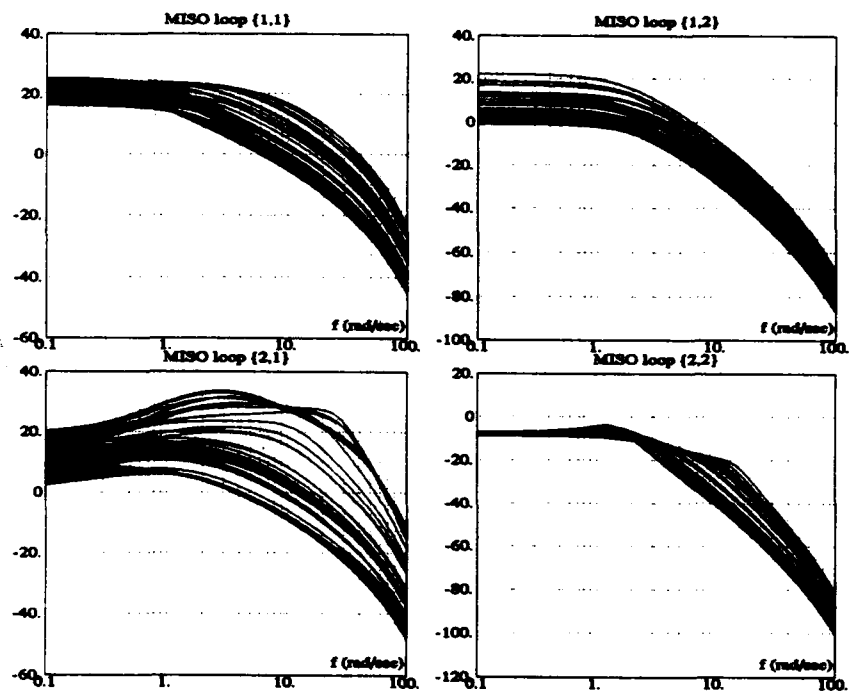


Figure C.16 Stability Axis  $q_{ii}$  Bode Plots without

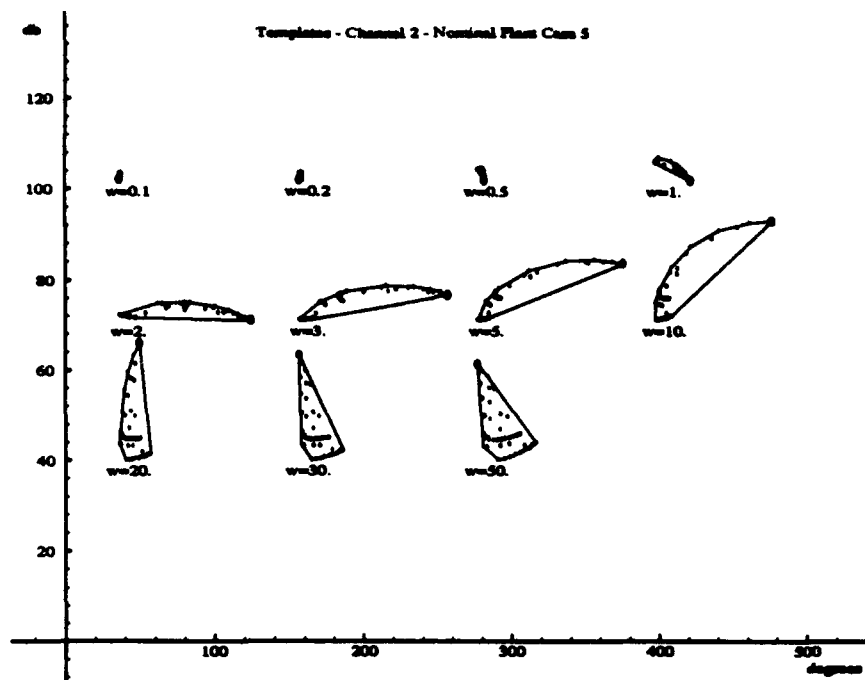


Figure C.17 Stability Axis (2,2) Templates

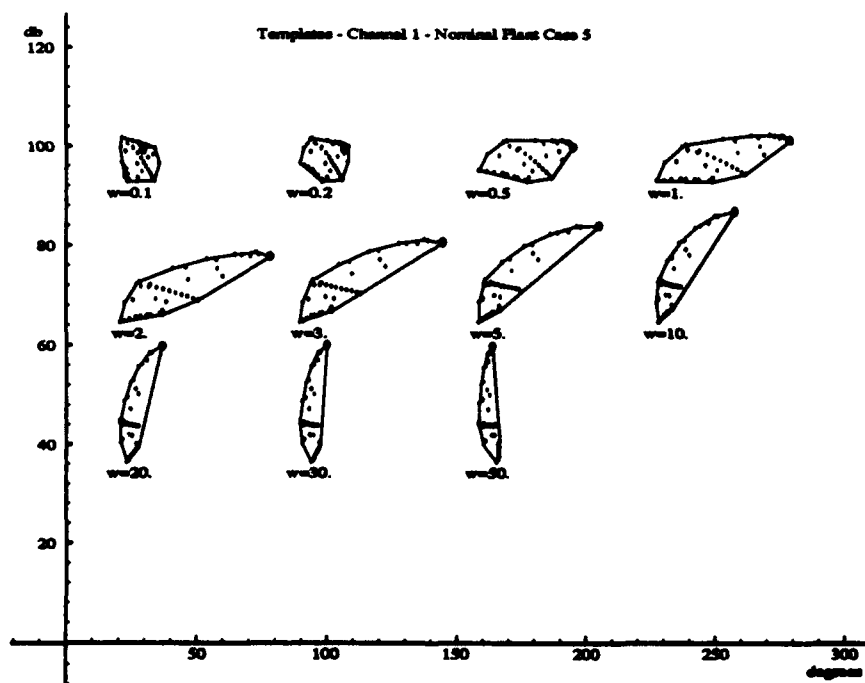


Figure C.18 Stability Axis (1,1) Templates

### *Appendix D. Bound Plots*

**This appendix contains the separate bounds for each of the designs.**



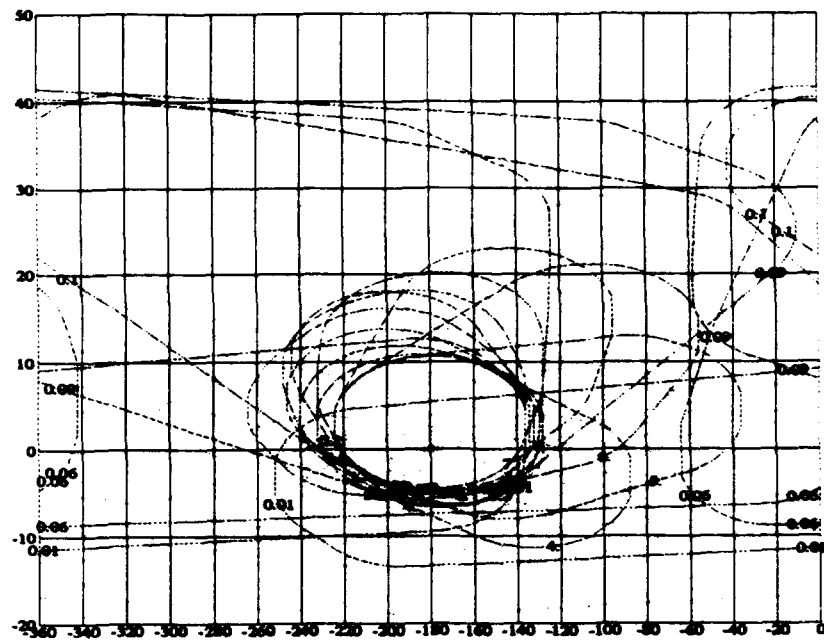


Figure D.1 Alpha Outer Loop Stability Bounds

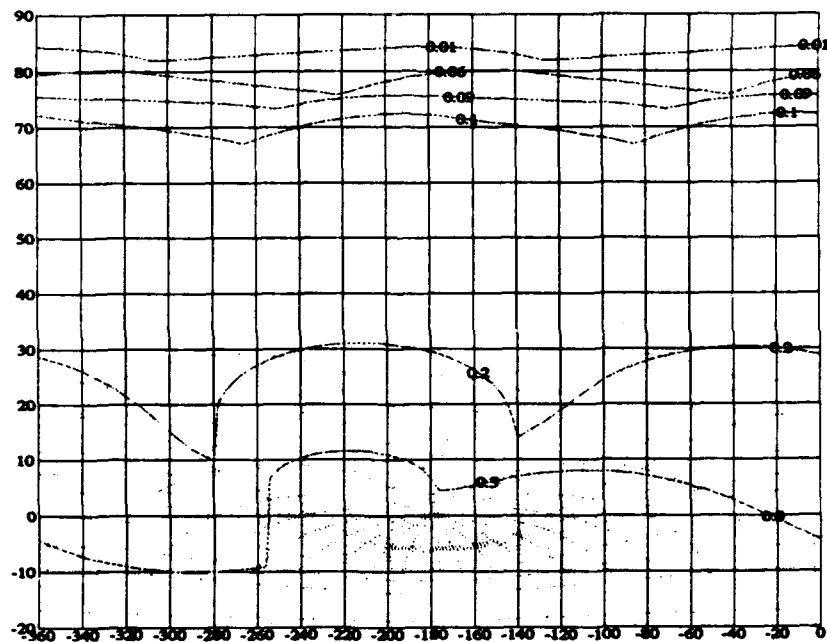


Figure D.2 Alpha Outer Loop Tracking Bounds

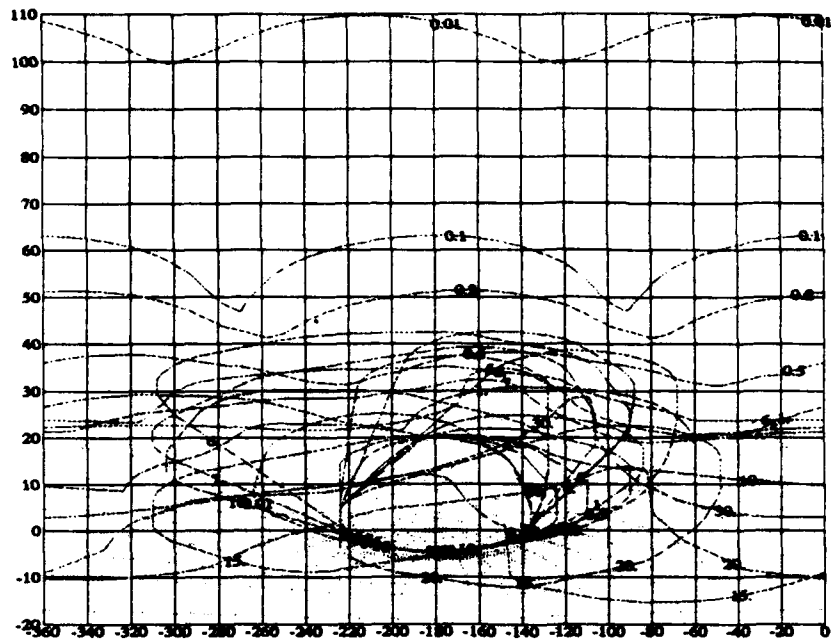


Figure D.3 Initial  $N$ , Outer Loop Tracking Bounds with Low Nominal Plant

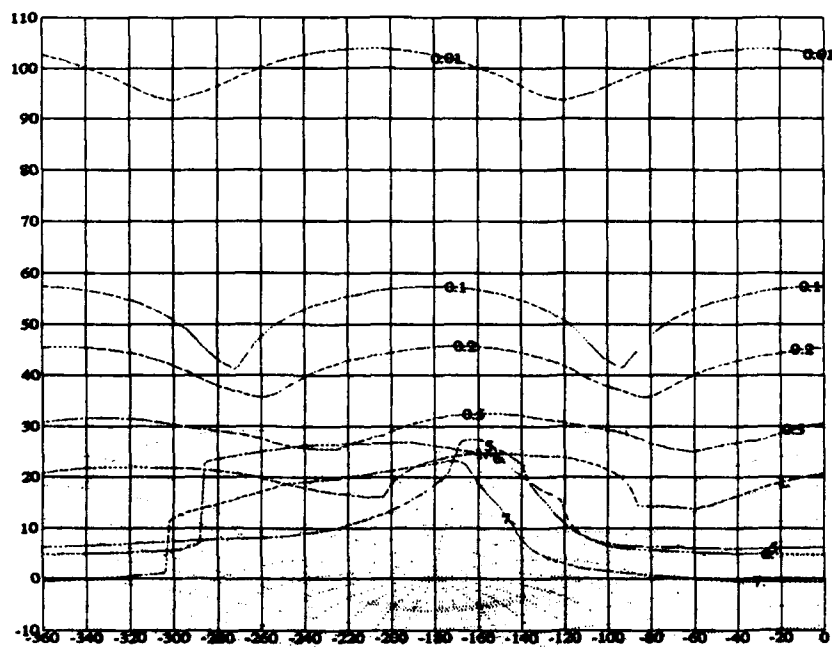


Figure D.4 Final  $N$ , Outer Loop Tracking Bounds

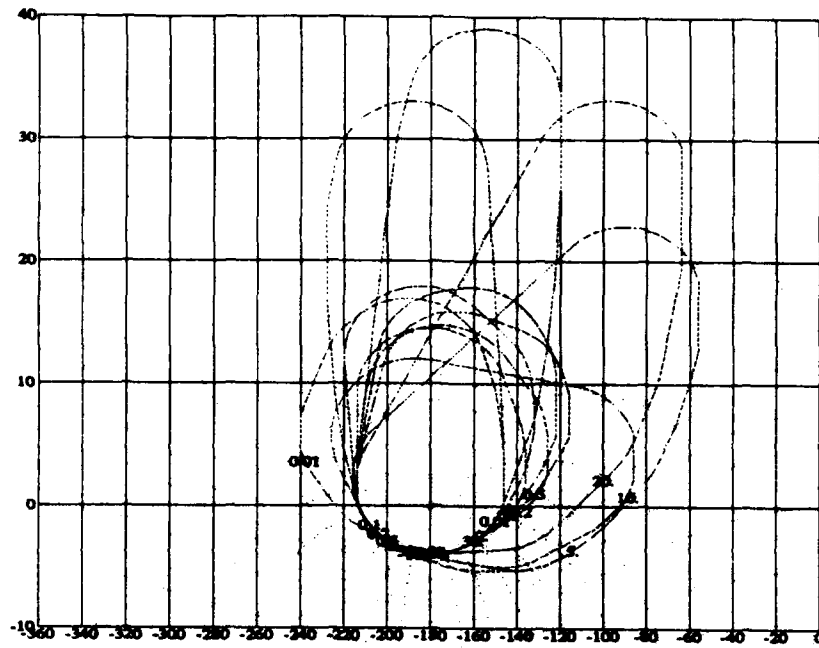


Figure D.5 Final  $C^*$  Outer Loop Stability Bounds

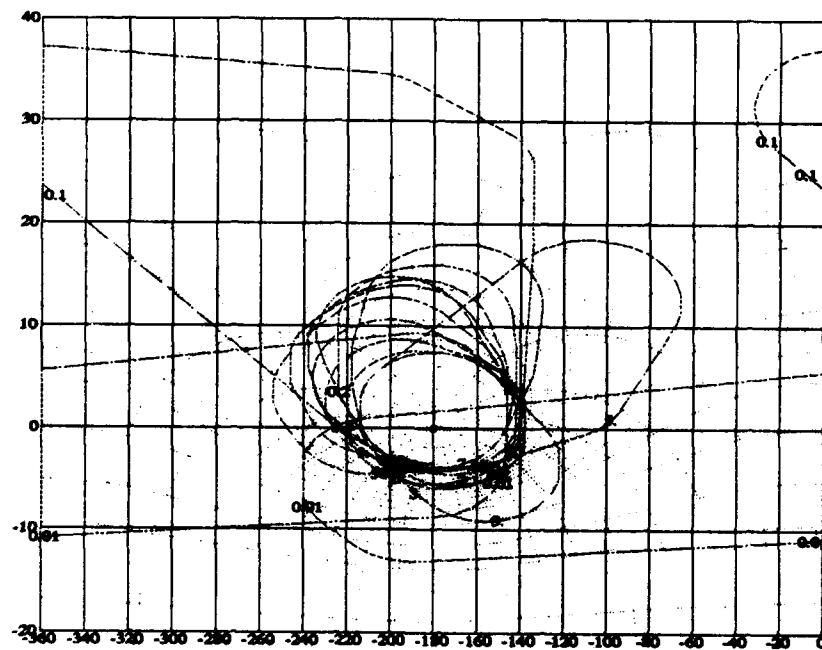


Figure D.6 Final  $\alpha$  Outer Loop Stability Bounds

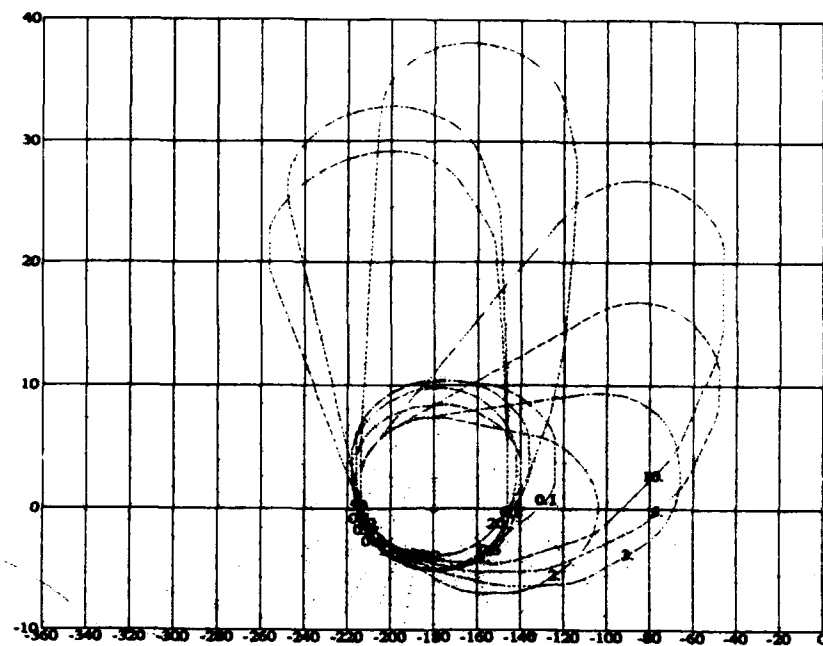


Figure D.7 Body Axis (2,2) Stability Bounds with Interconnects

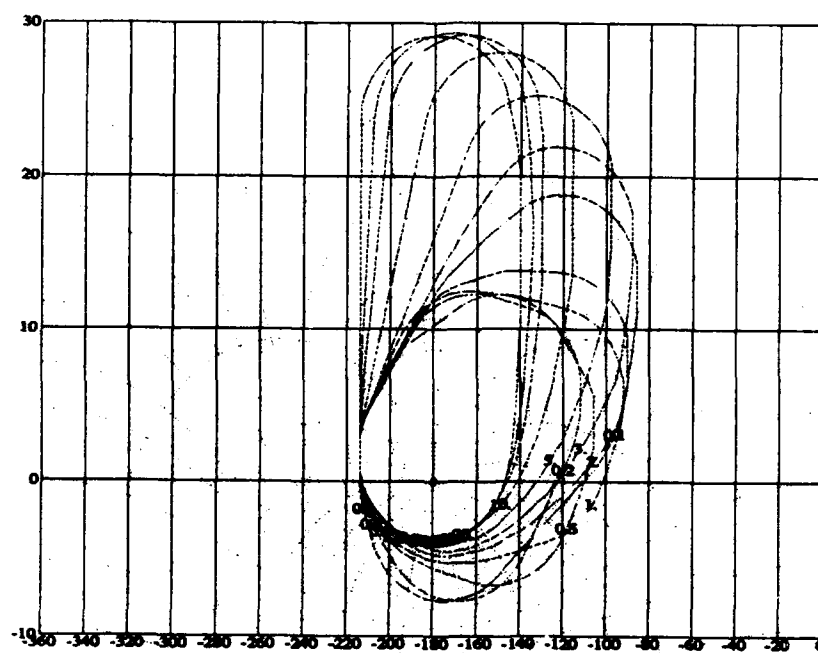


Figure D.8 Body Axis (1,1) Stability Bounds with Interconnects

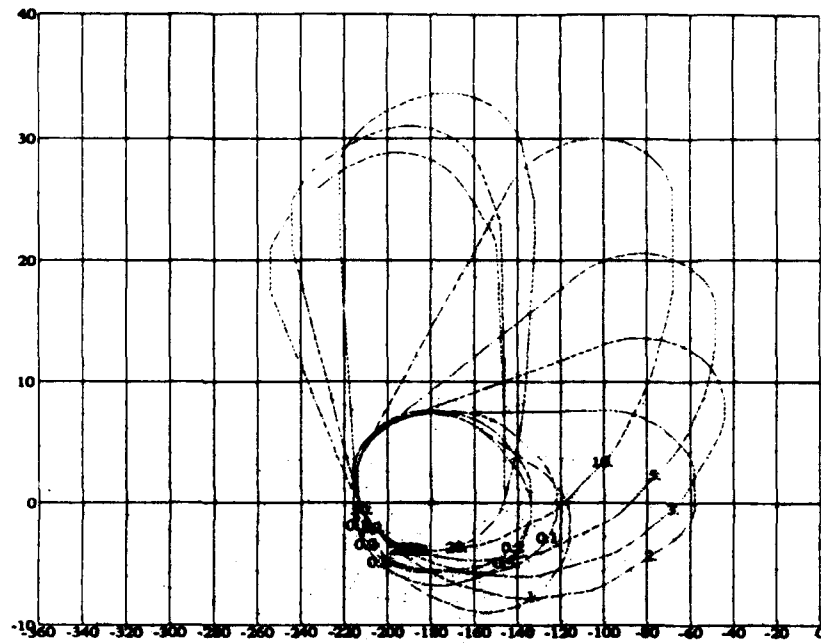


Figure D.9 Body Axis (2,2) Stability Bounds without Interconnects

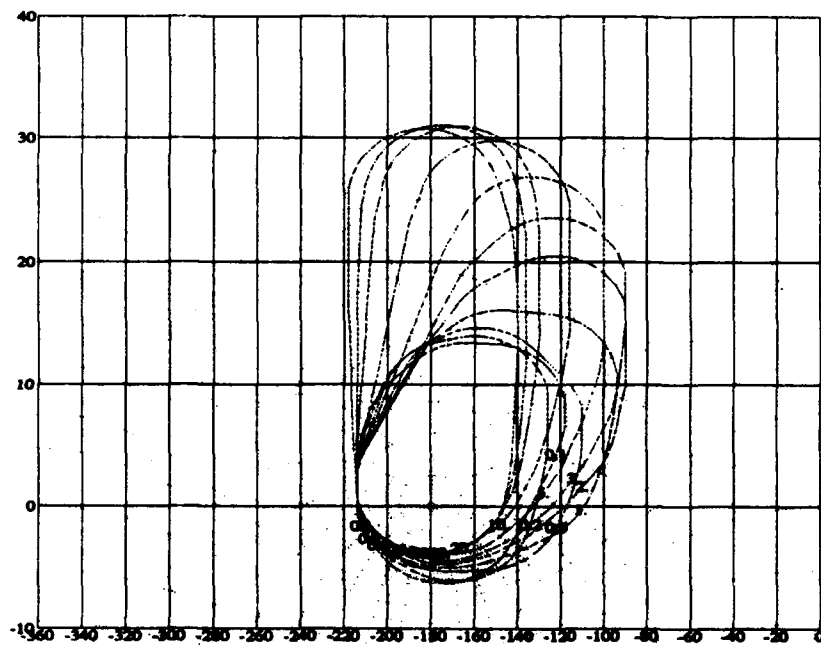


Figure D.10 Body Axis (1,1) Stability Bounds without Interconnects

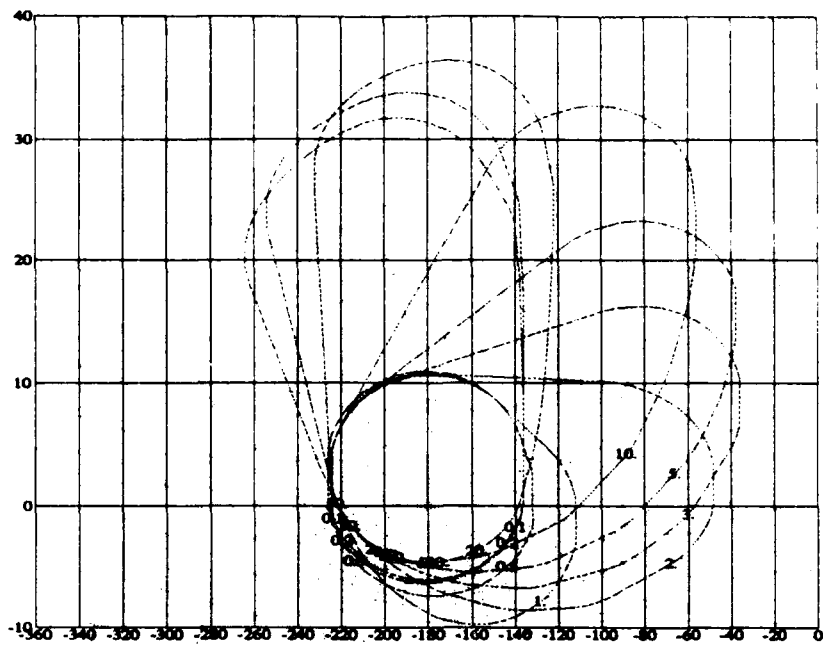


Figure D.11 Stability Axis (2,2) Stability Bounds without Interconnects

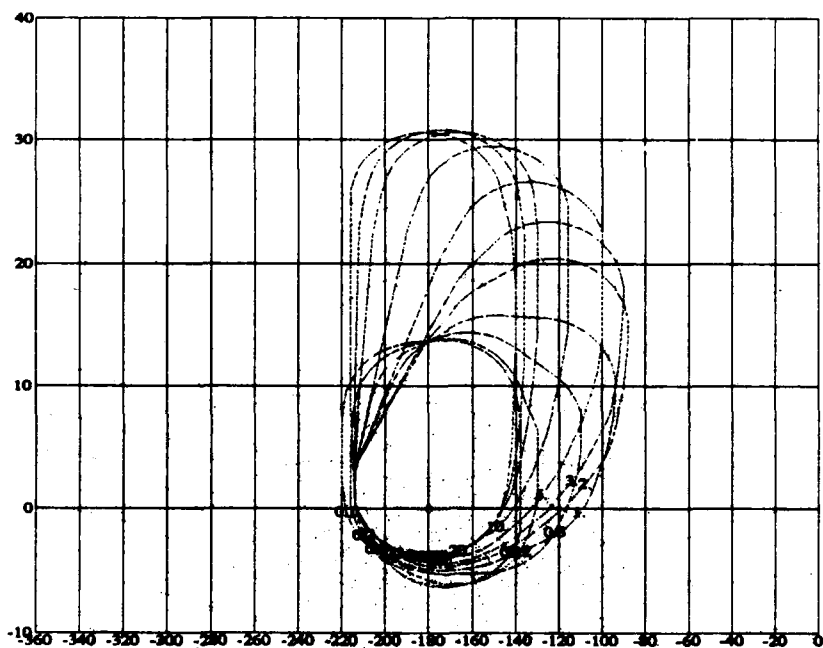


Figure D.12 Stability Axis (1,1) Stability Bounds without Interconnects

## Appendix E. QFT CAD Package Results

This appendix contains

1. the loop shaping plots
2. the open loop Bode plots verifying the cutoff frequencies
3. the Nichols chart plots verifying the phase and gain margins

for each of the designs described in this thesis. The phase and gain margins and the cutoff frequencies are as described in section 4.2.3 and shown in Fig. E.1.

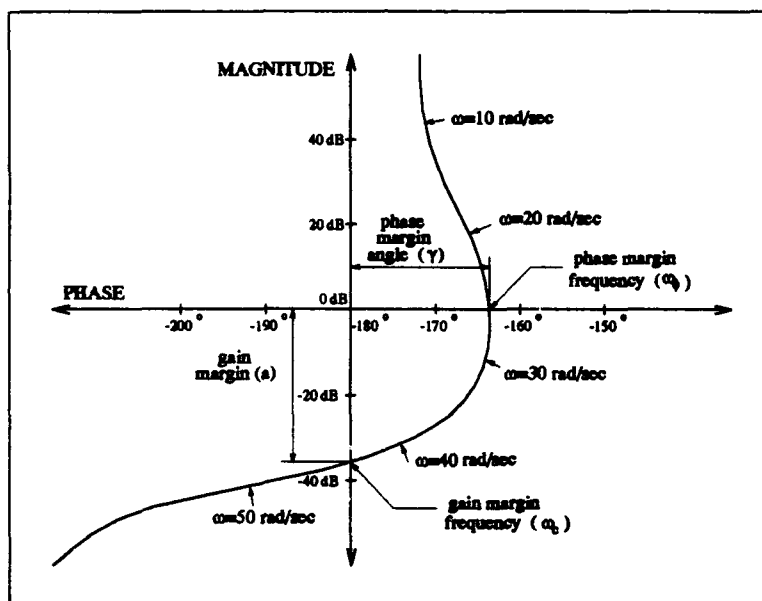


Figure E.1 Representative Nichols Chart Showing Phase and Gain Margins

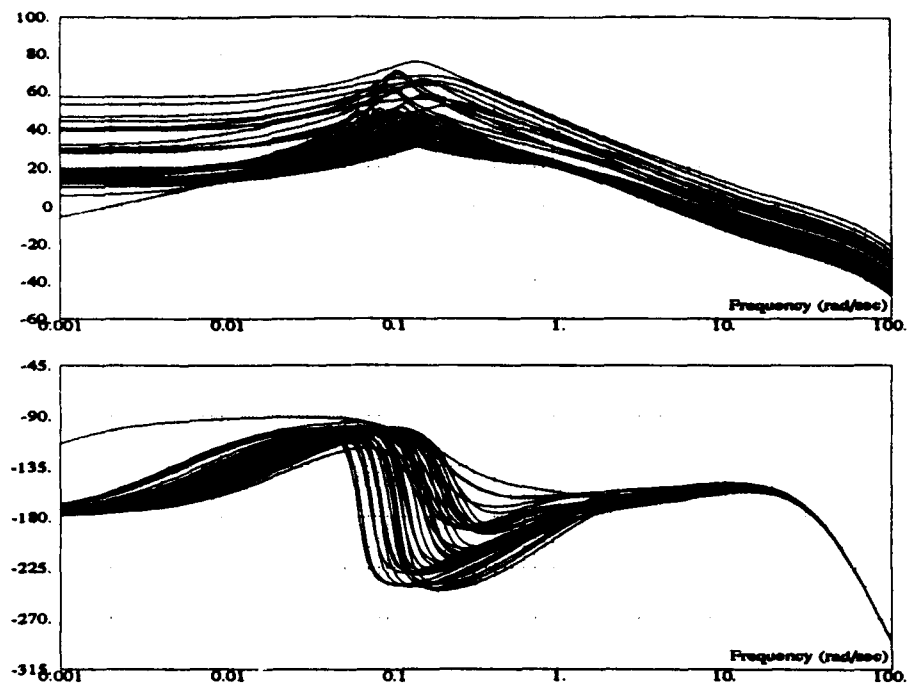


Figure E.2 Cutoff Frequency Verification for the Longitudinal  $N$ , Inner Loop

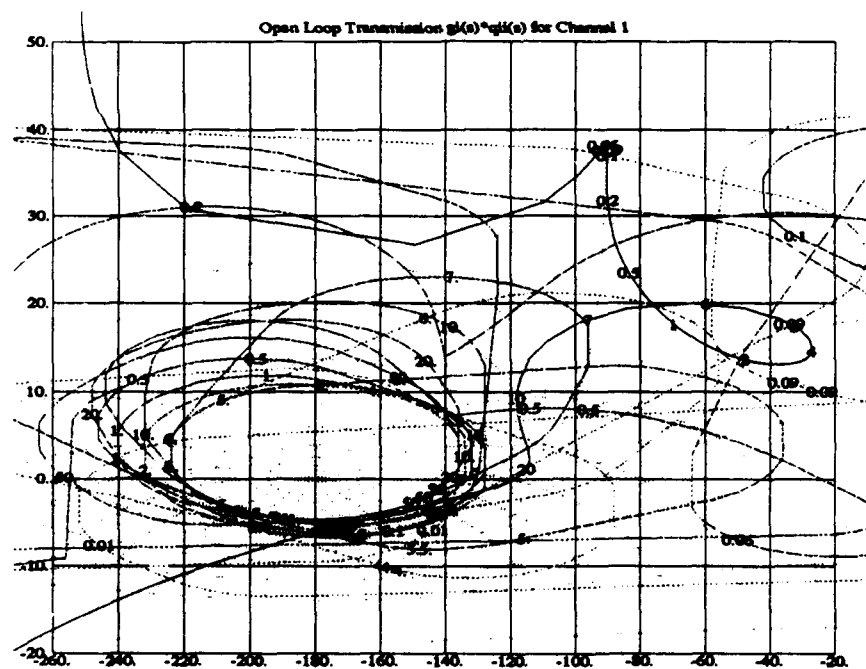


Figure E.3 Loop Shaping for the Longitudinal  $\alpha$  Design





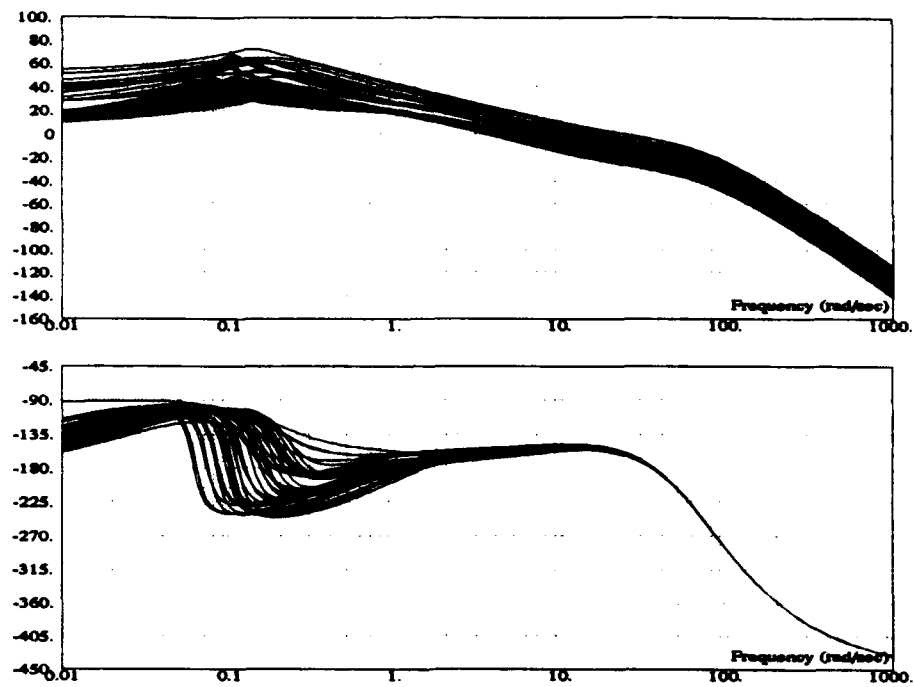


Figure E.6 Cutoff Frequency Verification for the Redesigned  $C^*$  Inner Loop

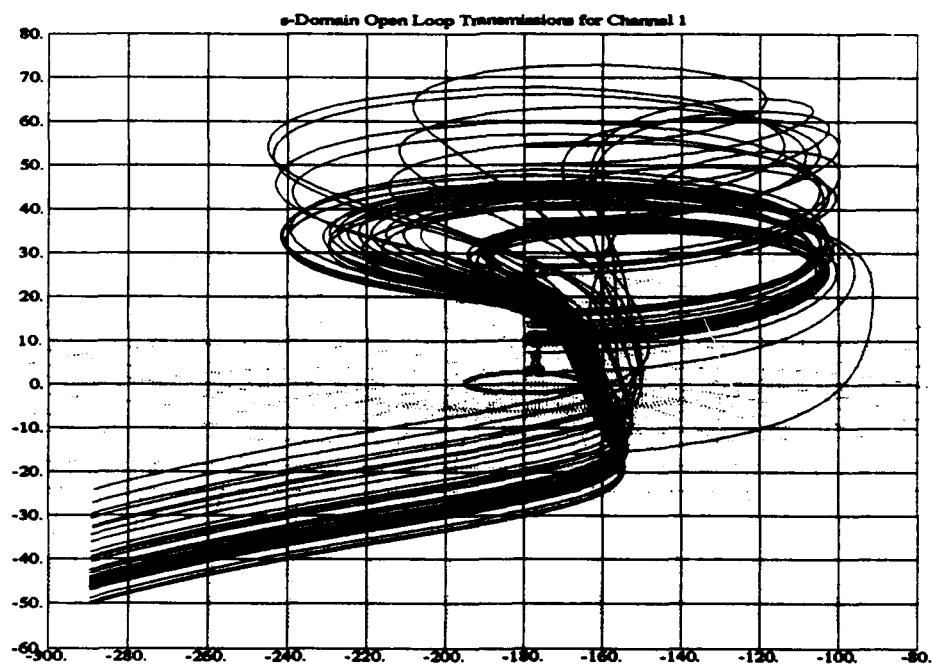


Figure E.7 Stability Verification for the Redesigned  $C^*$  Inner Loop

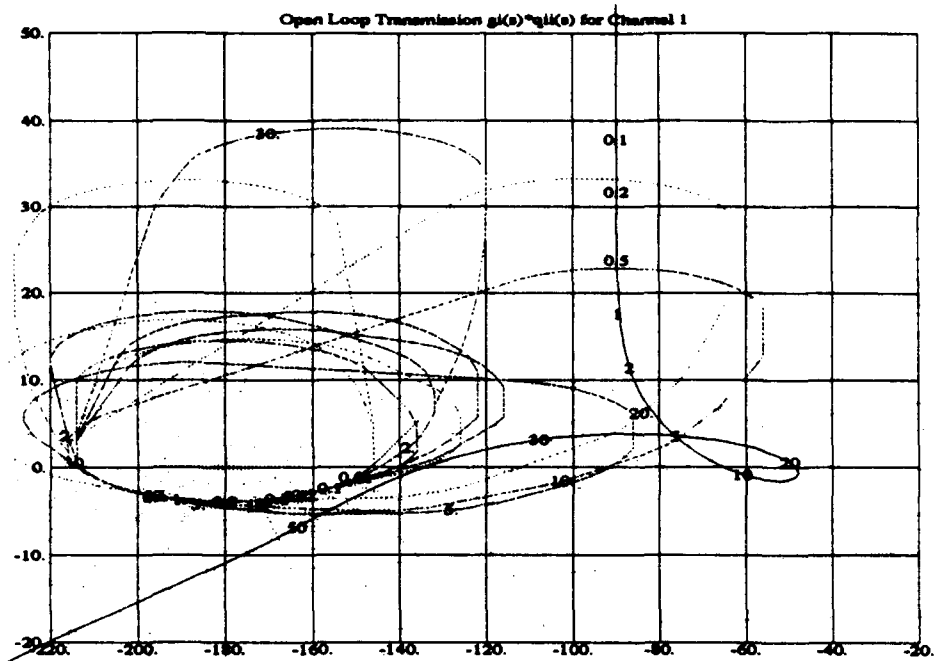


Figure E.8 Loop Shaping for the Longitudinal  $C^*$  Design

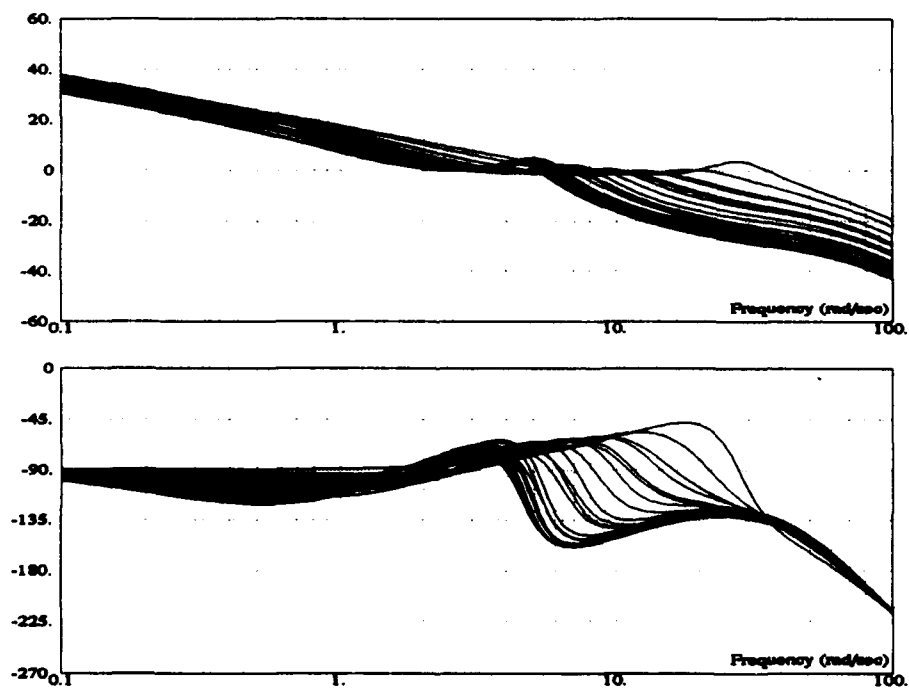


Figure E.9 Cutoff Frequency Verification for the Longitudinal  $C^*$  Design

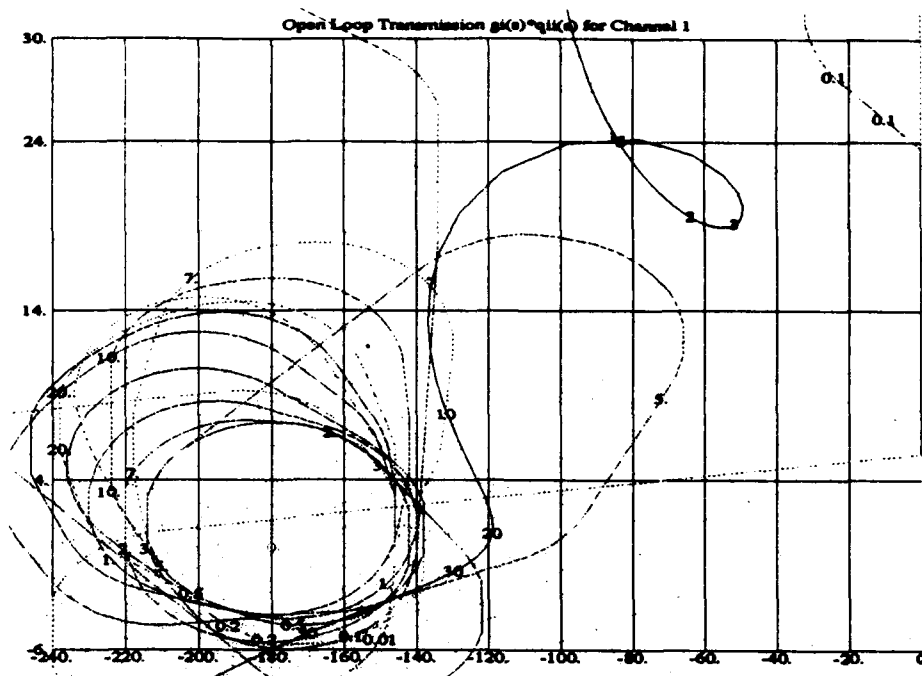


Figure E.10 Loop Shaping for the Longitudinal  $C^* \alpha$  Design

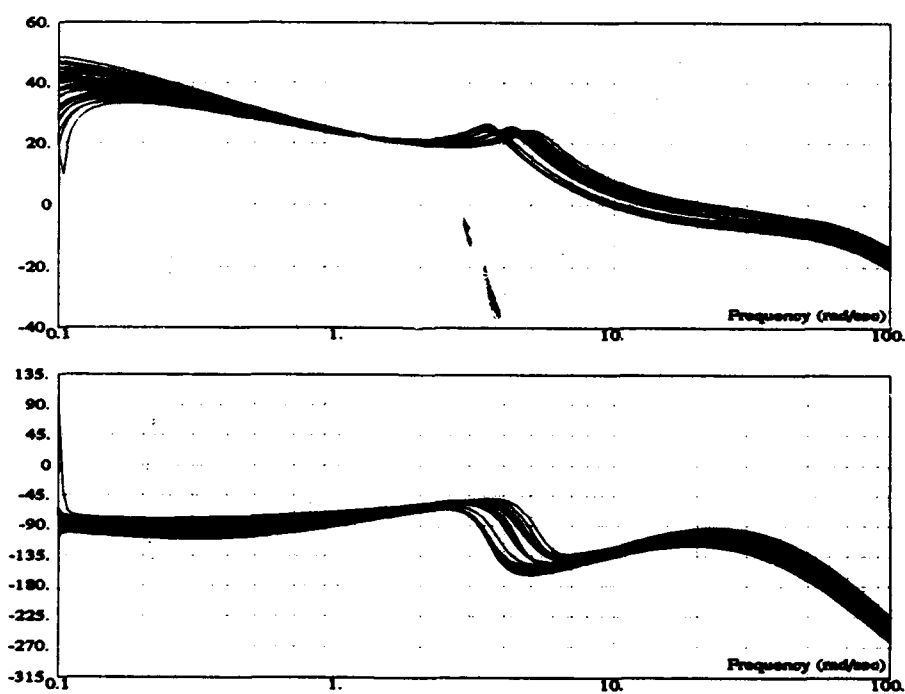


Figure E.11 Cutoff Frequency Verification for the Longitudinal  $C^* \alpha$  Design

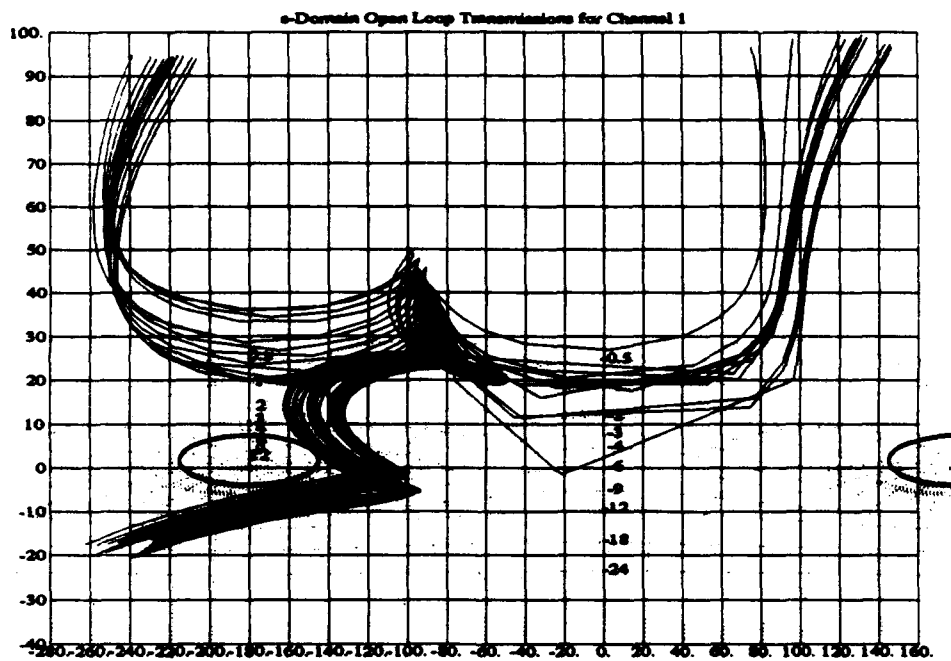


Figure E.12 Stability Verification for the Longitudinal  $C^* \alpha$  Design

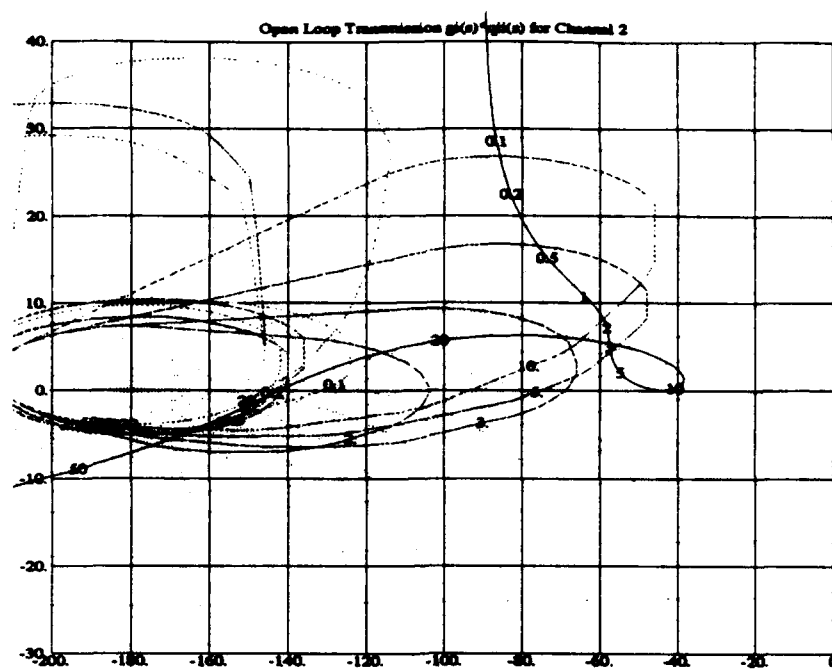


Figure E.13 Initial (2,2) Loop Shaping with Yaw Damper

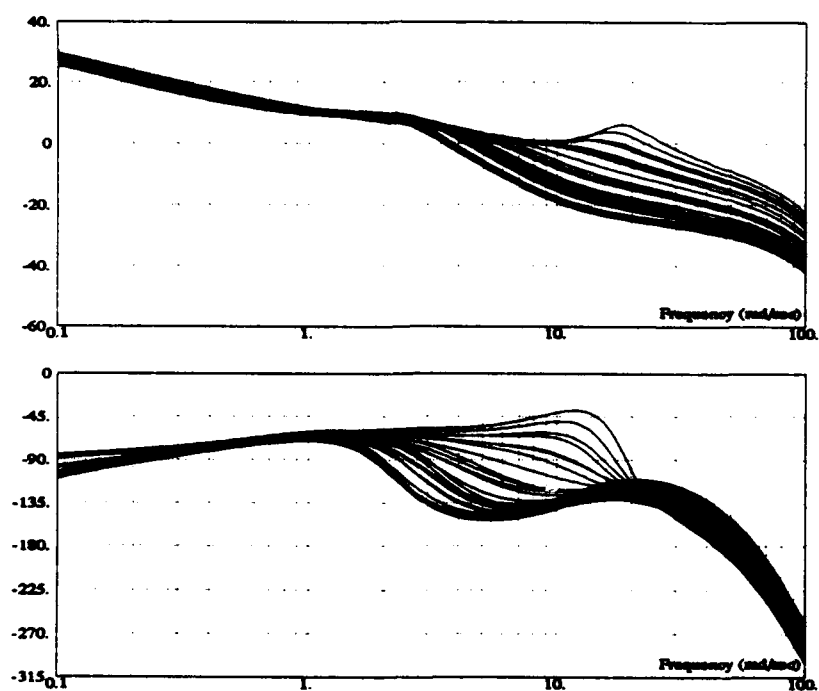


Figure E.14 Cutoff Frequency Verification for Initial Body Axis (2,2) Design

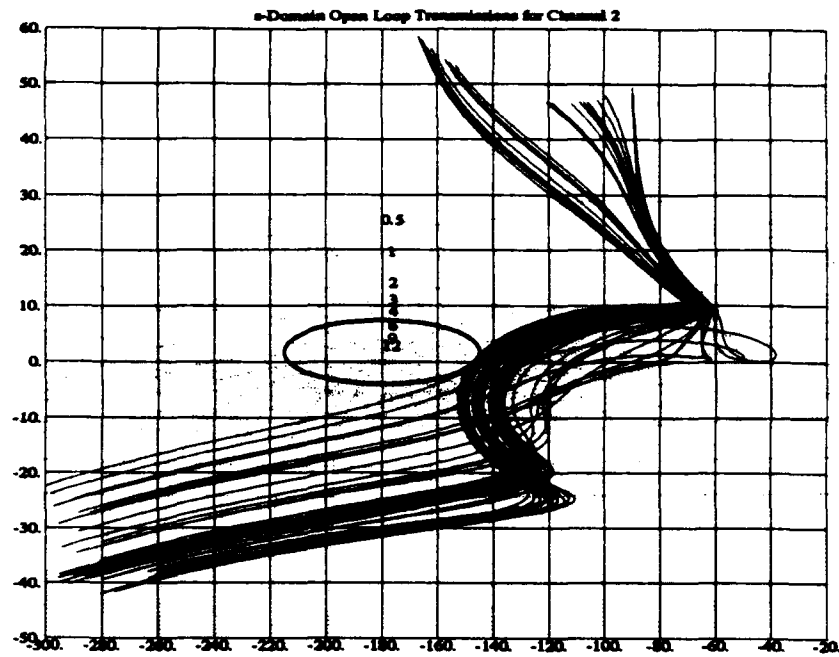


Figure E.15 Stability Verification for Initial Body Axis (2,2) Design

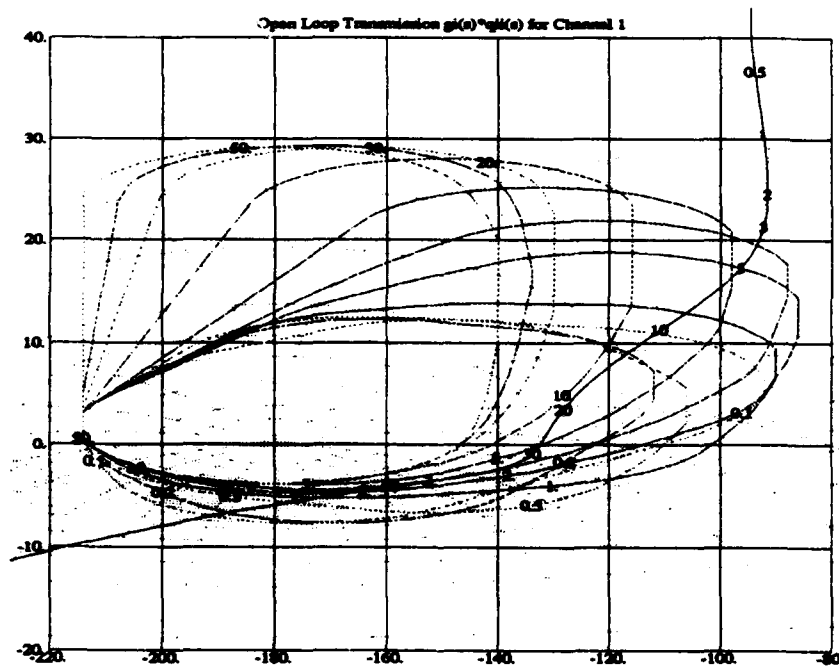


Figure E.16 Initial (1,1) Loop Shaping with Yaw Damper

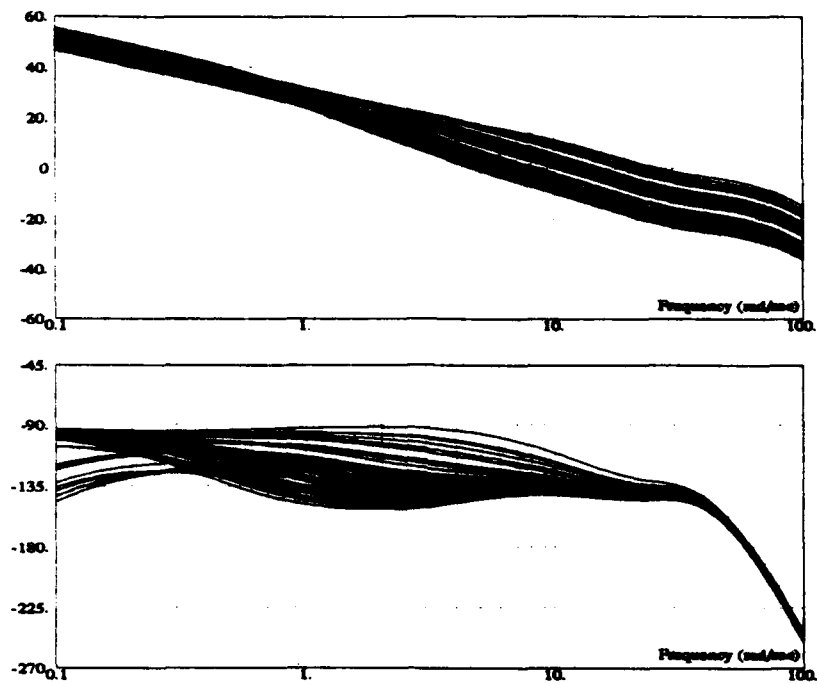


Figure E.17 Cutoff Frequency Verification for Initial Body Axis (1,1) Design

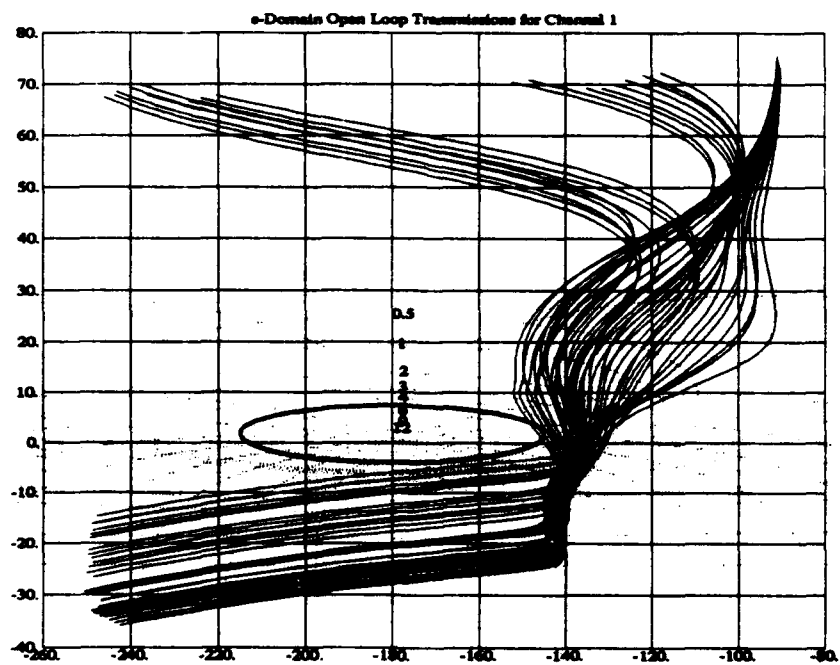


Figure E.18 Stability Verification for Initial Body Axis (1,1) Design



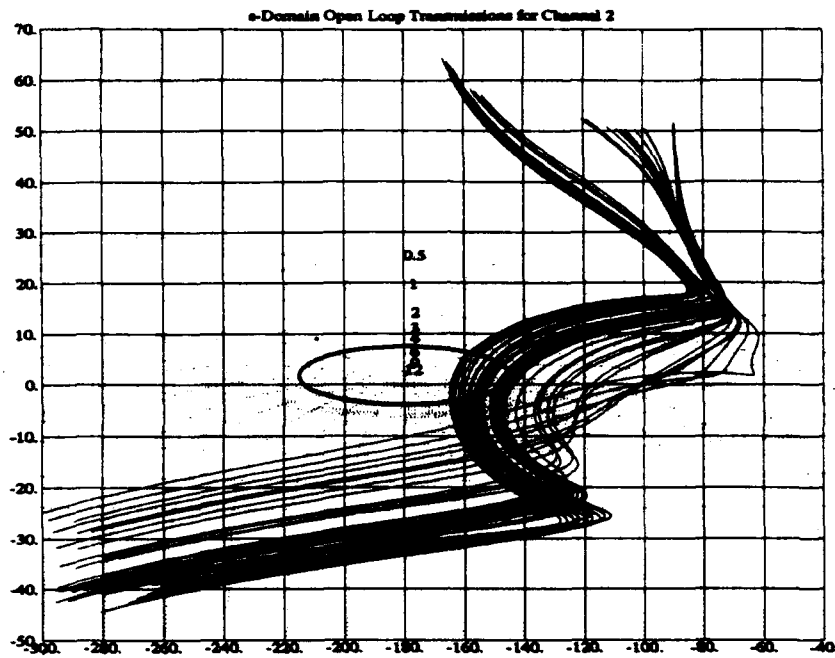


Figure E.19 Stability Plots for Initial Body Axis (2,2) Design Without Interconnects

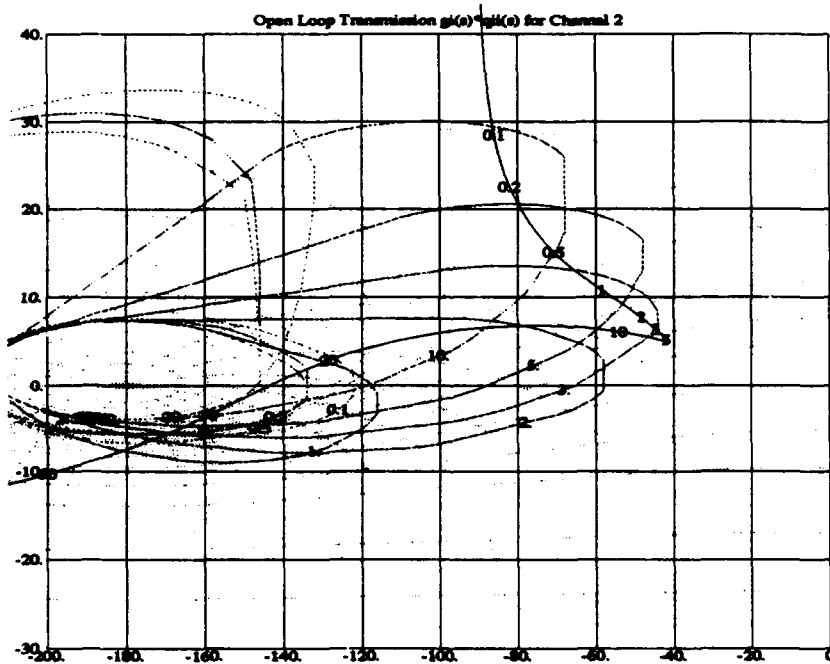


Figure E.20 Final (2,2) Loop Shaping with Yaw Damper

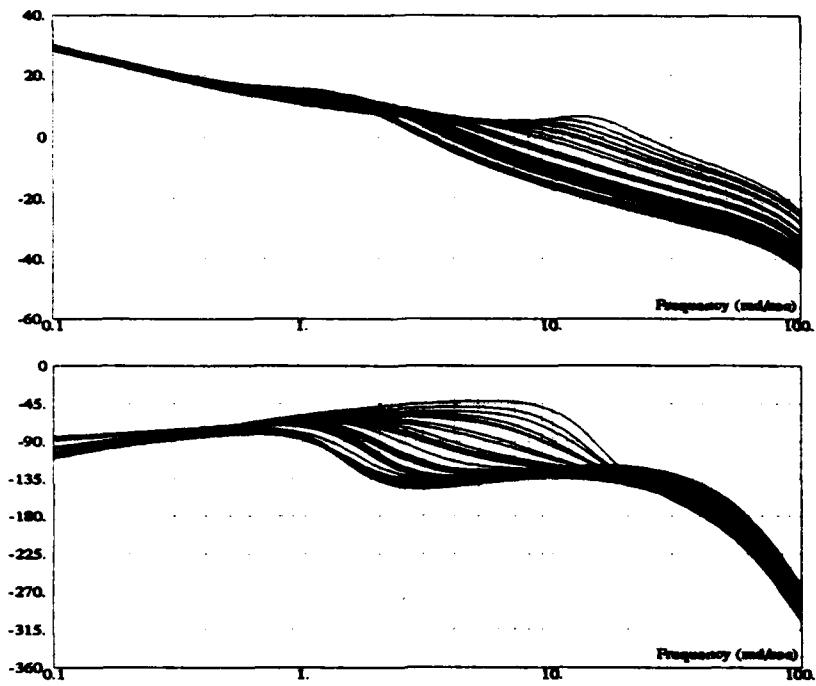


Figure E.21 Cutoff Frequency Verification for Final Body Axis (2,2) Design

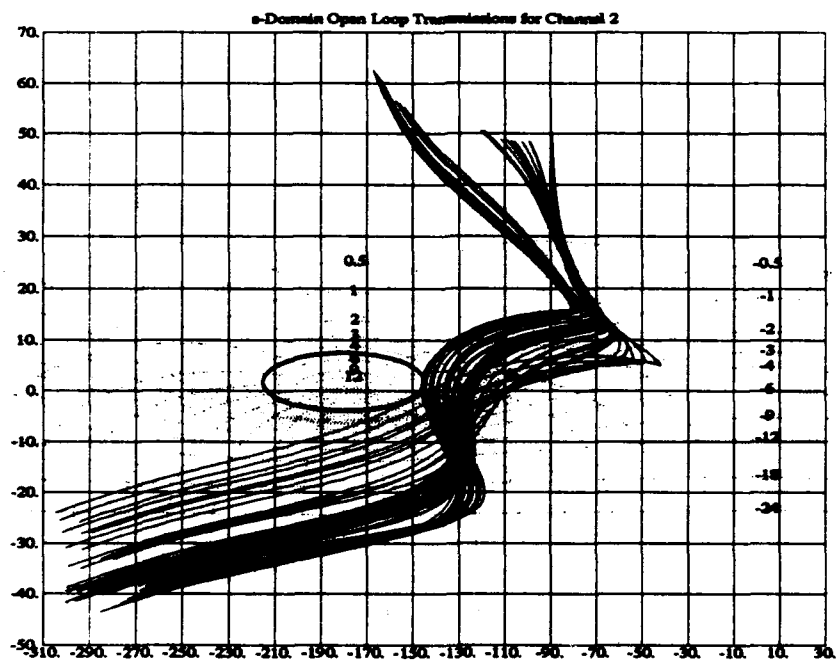


Figure E.22 Stability Verification for Final Body Axis (2,2) Design

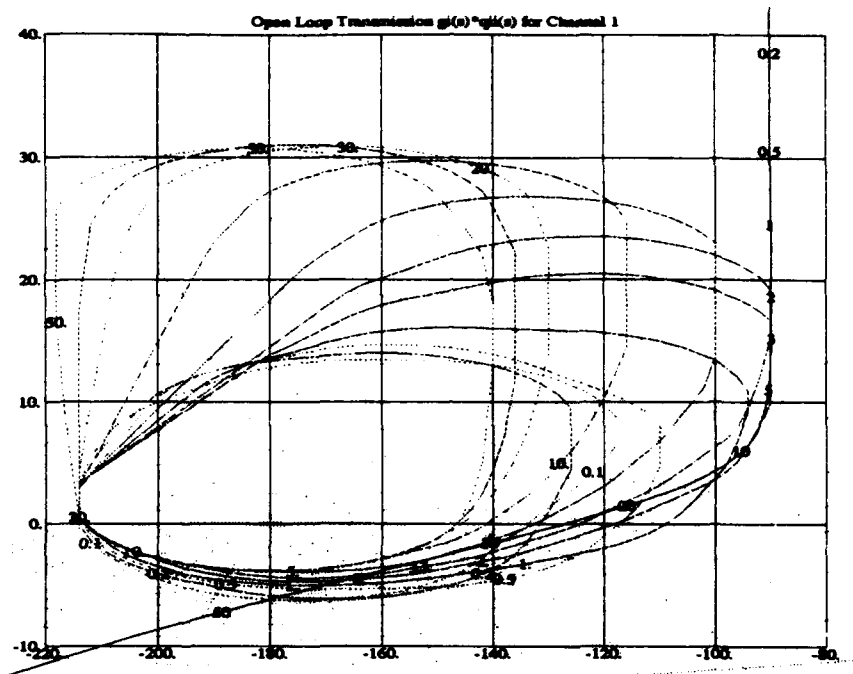


Figure E.23 Third Order (1,1) Loop Shaping with Yaw Damper

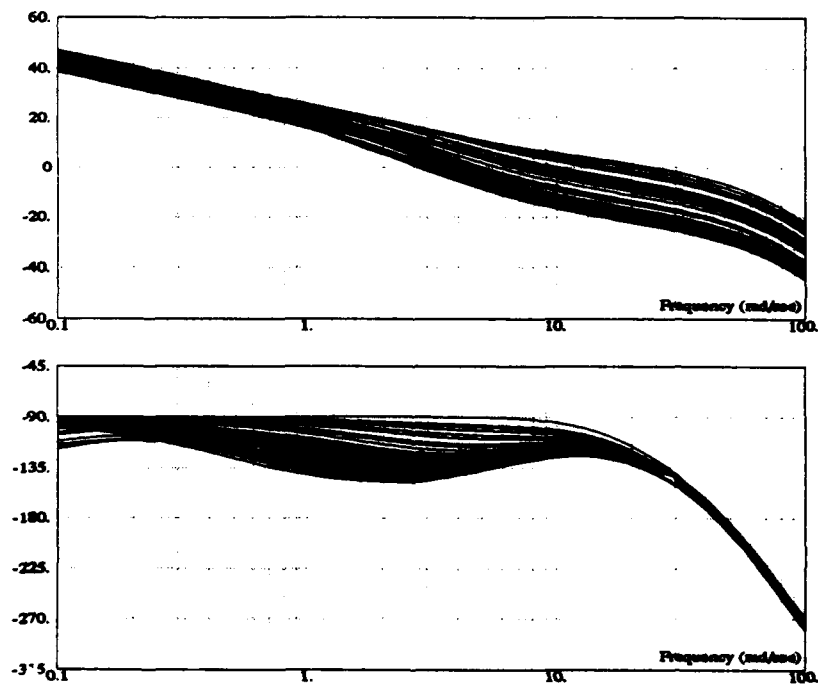


Figure E.24 Cutoff Frequency Verification for Third Order Body Axis (1,1) Design

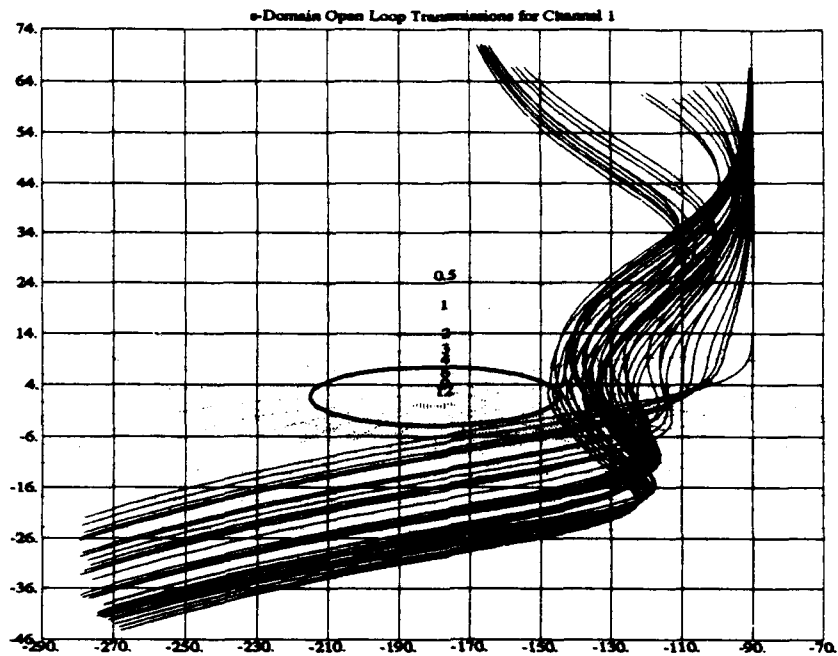


Figure E.25 Stability Verification for Third Order Body Axis (1,1) Design

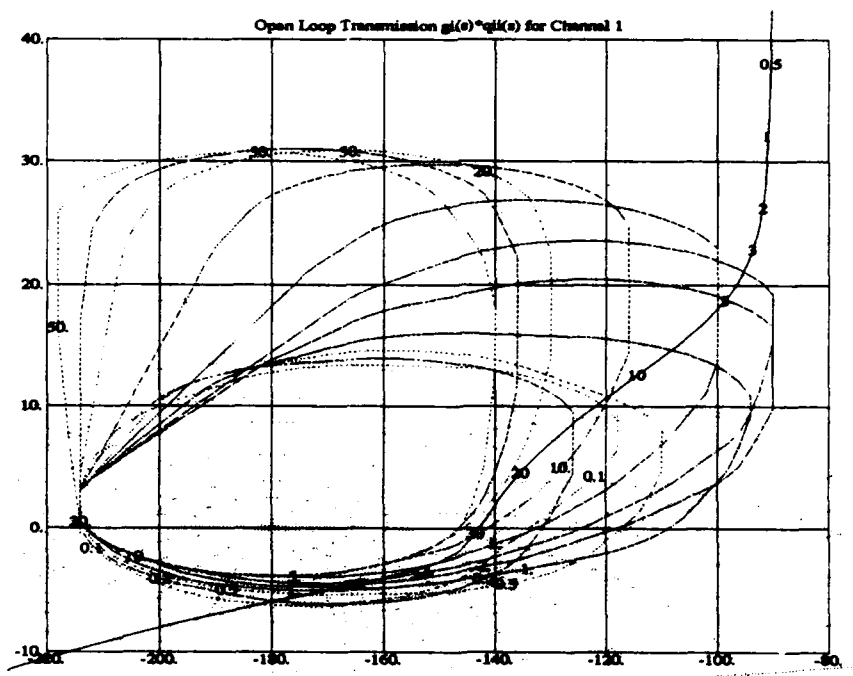


Figure E.26 Final (1,1) Loop Shaping with Yaw Damper

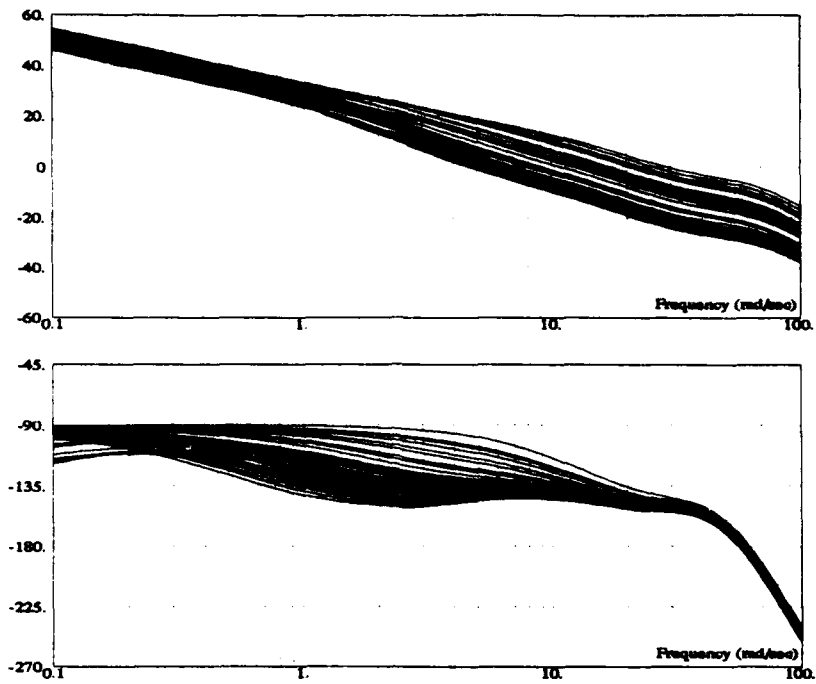


Figure E.27 Cutoff Frequency Verification for Final Body Axis (1,1) Design

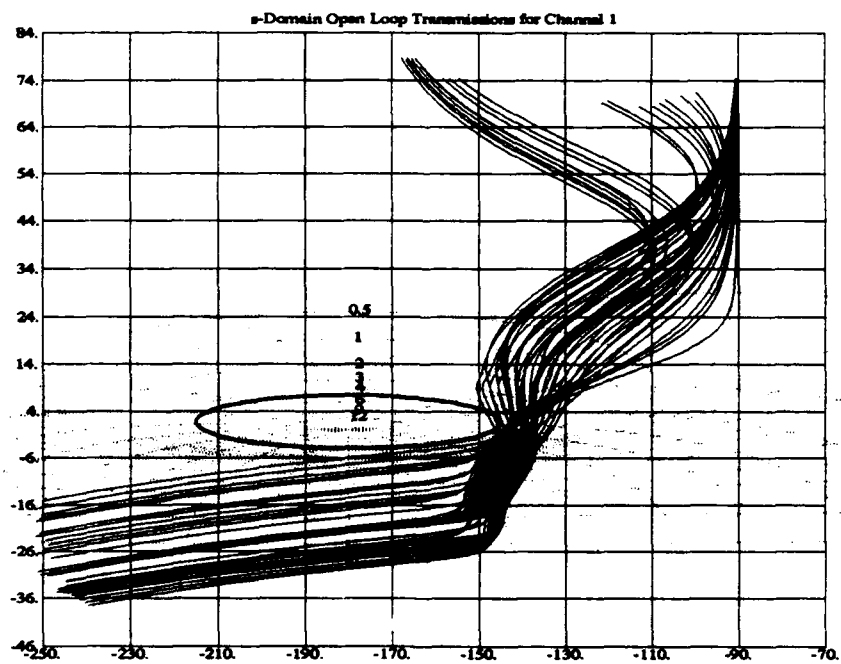


Figure E.28 Stability Verification for Final Body Axis (1,1) Design

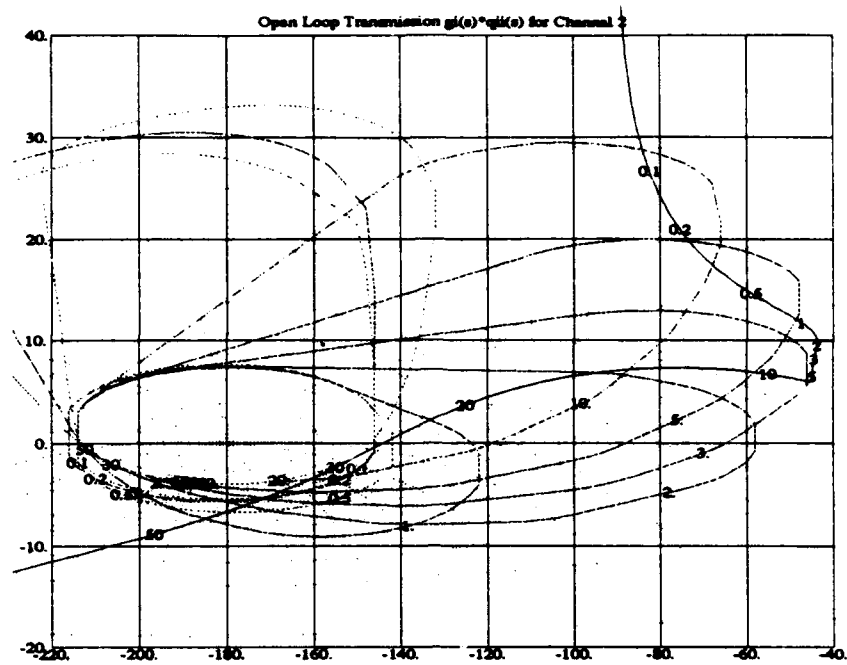


Figure E.29 Stability Axis (2,2) Loop Shaping

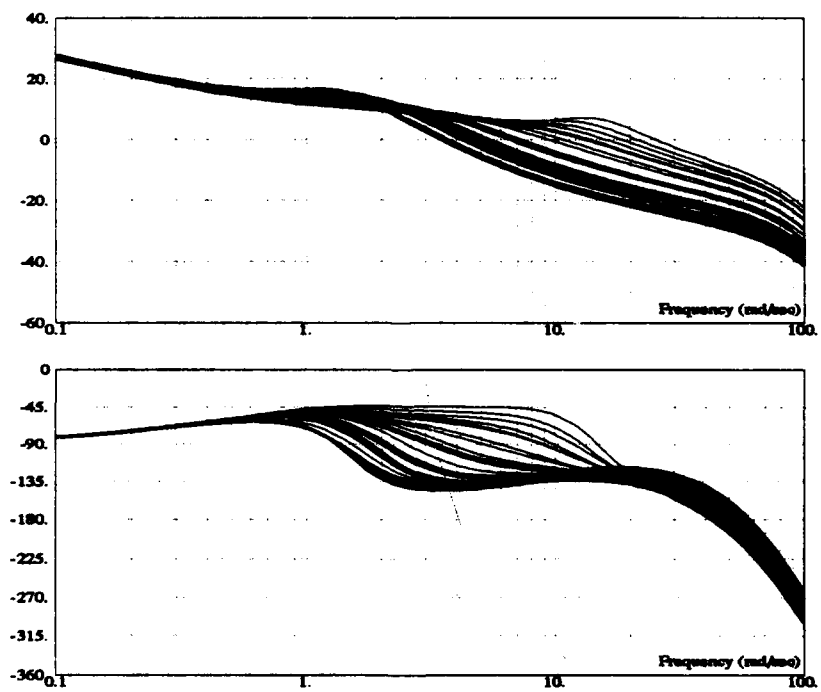


Figure E.30 Cutoff Frequency Verification for Stability Axis (2,2) Design

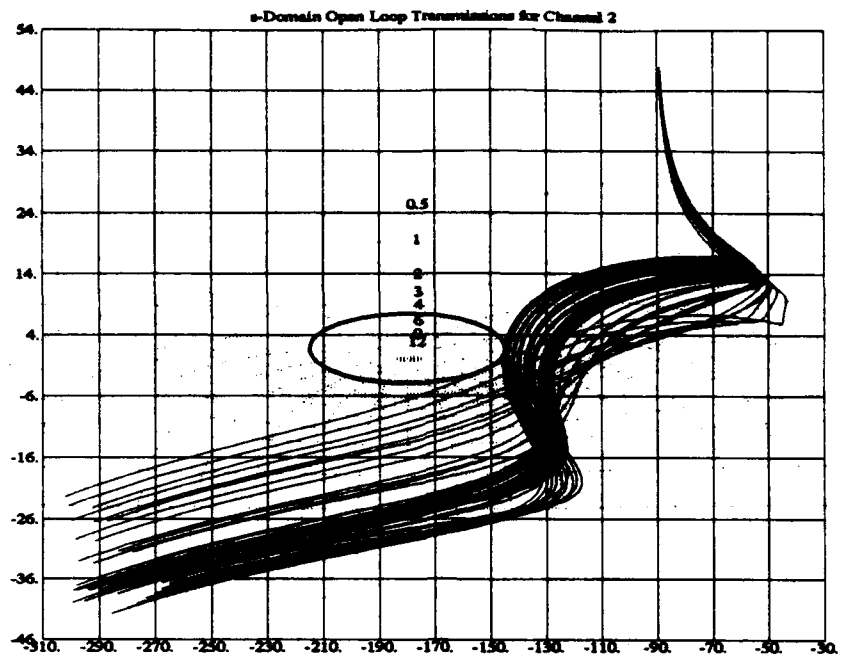


Figure E.31 Stability Verification for Stability Axis (2,2) Design

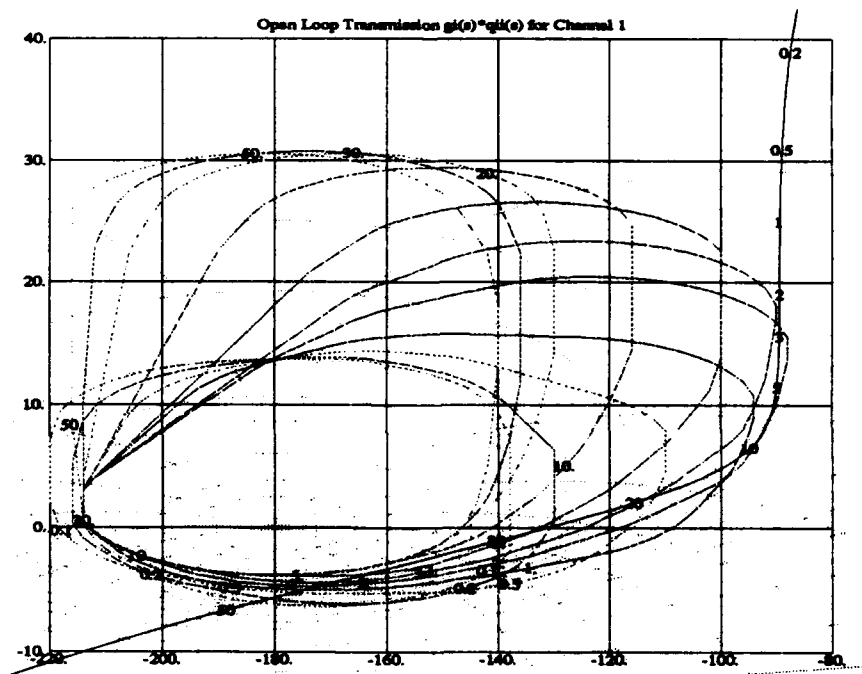


Figure E.32 Stability Axis (1,1) Loop Shaping

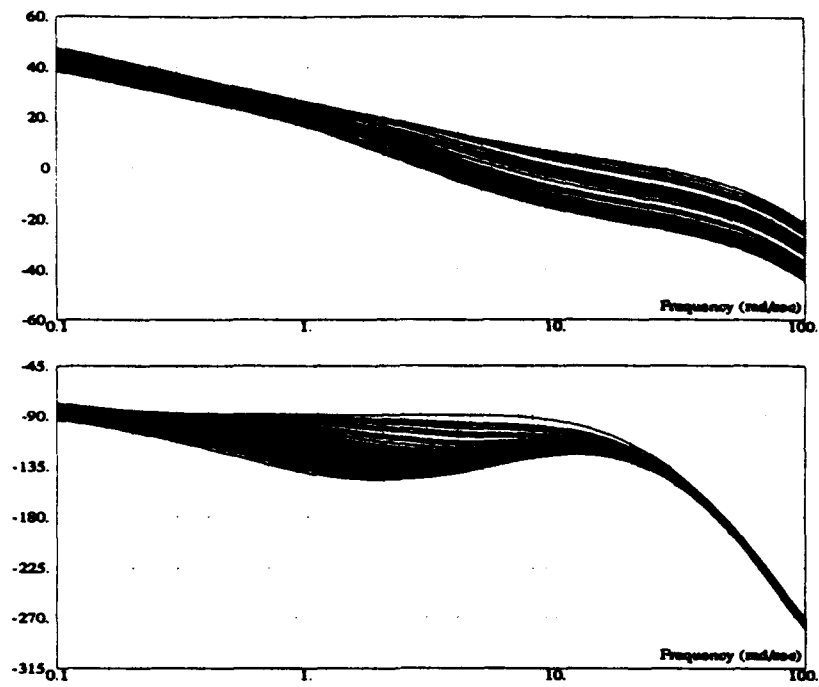


Figure E.33 Cutoff Frequency Verification for Stability Axis (1,1) Design

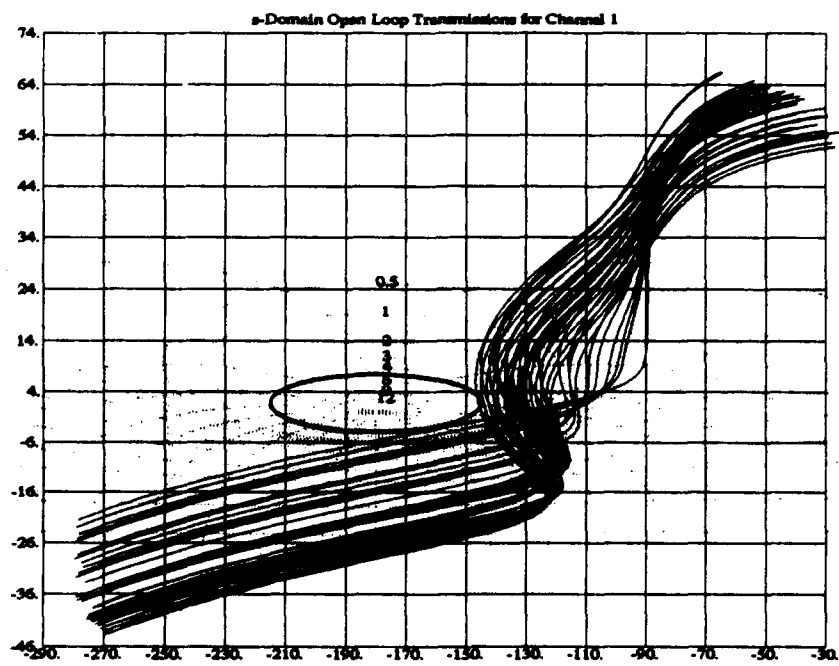


Figure E.34 Stability Verification for Stability Axis (1,1) Design



## Appendix F. Flying Qualities Results

This appendix contains the results of the specification determination for the  $N_z$  and  $C^*$  designs in the longitudinal channel, and the  $p$  and  $p_{stab}$  designs in the lateral/directional channel.

For the longitudinal channel, the specifications are based on the  $q$  response. A typical  $q$  response is given in Fig. F.1. Information on  $t_1$ ,  $t_2$ ,  $\Delta t$ ,  $\Delta q_1$ ,  $\Delta q_2$ , and  $\Delta q_2/\Delta q_1$  for each plant are given in Tables F.1 through F.4.

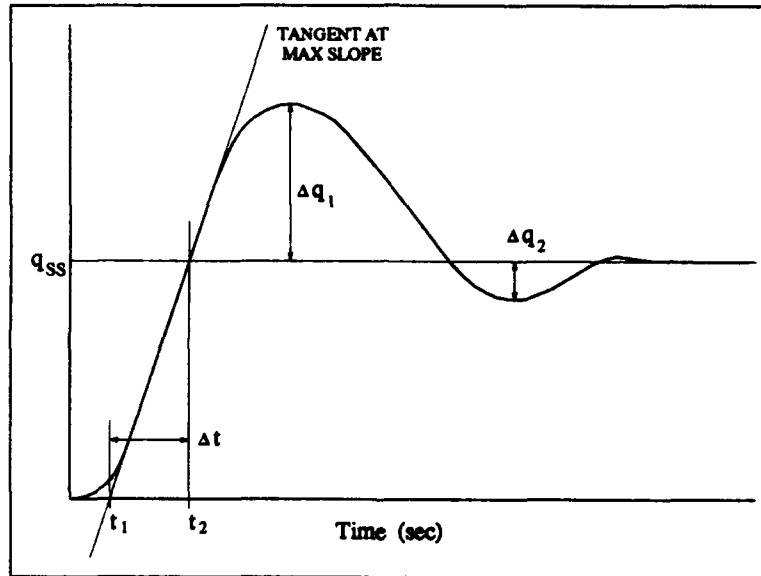


Figure F.1 Second Order Model Pitch Rate Response to Step Controller Deflection

For the lateral directional channel, the specifications are based on converting the Bode plots of the  $\phi/p_{cmd}$  and  $\beta/\beta_{cmd}$  transfer functions to the fourth order systems given in Eqs. (F.1) and (F.2). Each of the terms for both designs are given in Tables F.5 through F.8.

$$\frac{\phi(s)}{\delta_{stk}(s)} = \frac{K_\phi(s^2 + 2\zeta_\phi\omega_\phi s + \omega_\phi^2) \exp^{-\tau_\phi s}}{(s + 1/T_R)(s + 1/T_S)(s^2 + 2\zeta_d\omega_d s + \omega_d^2)} \quad (F.1)$$

and

$$\frac{\beta(s)}{\delta_{rud}(s)} = \frac{(A_3 s^3 + A_2 s^2 + A_1 s + A_0) \exp^{-\tau_\beta s}}{(s + 1/T_R)(s + 1/T_S)(s^2 + 2\zeta_d\omega_d s + \omega_d^2)} \quad (F.2)$$

Table F.1 Results of Time Domain  $q$  Analysis for the  $N_z$  Control Design

Plant	Altitude	Mach	$t_1$	$t_2$	$\Delta t$	$\Delta q_1$	$\Delta q_2$	$\Delta q_2/\Delta q_1$
1	1000	0.400	0.134	0.224	0.090	7.83	3.35	0.428
2	1000	0.600	0.082	0.160	0.078	3.53	1.56	0.440
3	1000	0.700	0.064	0.145	0.080	2.20	1.07	0.487
4	1000	0.900	0.041	0.130	0.088	0.55	0.72	1.325
5	10000	0.500	0.124	0.201	0.077	7.36	3.10	0.422
6	10000	0.700	0.079	0.152	0.072	3.53	1.33	0.377
7	10000	0.900	0.049	0.133	0.084	1.20	0.79	0.654
8	20000	0.500	0.155	0.228	0.073	11.09	5.08	0.458
9	20000	0.700	0.100	0.165	0.066	5.49	1.92	0.349
10	20000	0.900	0.066	0.138	0.072	2.40	0.98	0.408
11	30000	0.700	0.127	0.187	0.060	8.52	2.89	0.339
12	30000	0.900	0.086	0.149	0.063	4.19	1.39	0.333
13	40000	0.700	0.165	0.220	0.055	13.17	5.09	0.387
14	40000	0.900	0.112	0.167	0.056	6.67	2.16	0.324
15	50000	0.900	0.150	0.196	0.046	12.94	2.68	0.207
16	1000	0.301	0.185	0.290	0.105	14.00	4.25	0.303
17	5000	0.324	0.185	0.284	0.098	14.35	4.31	0.300
18	10000	0.357	0.185	0.275	0.091	14.73	4.38	0.297
19	15000	0.394	0.184	0.268	0.083	15.09	4.44	0.294
20	20000	0.437	0.183	0.260	0.077	15.37	4.48	0.292
21	25000	0.486	0.183	0.253	0.070	15.65	4.49	0.287
22	30000	0.543	0.182	0.246	0.064	15.91	4.51	0.283
23	35000	0.610	0.180	0.239	0.059	16.09	4.32	0.268
24	40000	0.686	0.175	0.228	0.054	15.97	3.36	0.210
25	45000	0.774	0.163	0.214	0.051	13.20	4.56	0.346
26	50000	0.873	0.156	0.203	0.046	13.45	3.12	0.232

Table F.2 Results of Time Domain  $q$  Analysis for the First  $\alpha$  Control Design

Plant	Altitude	Mach	$t_1$	$t_2$	$\Delta t$	$\Delta q_1$	$\Delta q_2$	$\Delta q_2/\Delta q_1$
1	1000	0.240	0.082	0.300	0.218	0.46	0.02	0.039
2	5000	0.260	0.081	0.284	0.204	0.48	0.02	0.035
3	10000	0.280	0.083	0.267	0.185	0.53	0.02	0.030
4	10000	0.300	0.075	0.261	0.187	0.49	0.02	0.033
5	15000	0.310	0.081	0.246	0.165	0.56	0.01	0.026
6	20000	0.340	0.082	0.231	0.149	0.60	0.01	0.024
7	20000	0.400	0.063	0.220	0.158	0.52	0.02	0.029
8	25000	0.380	0.081	0.214	0.133	0.63	0.01	0.022
9	30000	0.420	0.081	0.200	0.119	0.66	0.01	0.021
10	30000	0.500	0.059	0.191	0.132	0.57	0.01	0.026
11	35000	0.470	0.081	0.186	0.105	0.69	0.01	0.021
12	40000	0.530	0.080	0.170	0.090	0.72	0.02	0.021
13	45000	0.700	0.060	0.135	0.075	0.67	0.02	0.025
14	50000	0.780	0.060	0.123	0.063	0.69	0.02	0.026
15	1000	0.301	0.059	0.268	0.209	0.42	0.02	0.043
16	5000	0.324	0.056	0.251	0.196	0.45	0.02	0.038
17	10000	0.357	0.056	0.232	0.176	0.47	0.02	0.034
18	15000	0.394	0.056	0.215	0.159	0.50	0.02	0.031
19	20000	0.437	0.056	0.199	0.143	0.52	0.01	0.029
20	25000	0.486	0.057	0.184	0.128	0.55	0.01	0.027
21	30000	0.543	0.057	0.171	0.114	0.57	0.01	0.026
22	35000	0.610	0.057	0.157	0.100	0.59	0.02	0.026
23	40000	0.686	0.057	0.140	0.083	0.62	0.02	0.026
24	45000	0.774	0.057	0.151	0.094	0.58	0.02	0.027
25	50000	0.873	0.056	0.127	0.071	0.62	0.02	0.026

Table F.3 Results of Time Domain  $q$  Analysis for the  $C^*$  Control Design

Plant	Altitude	Mach	$t_1$	$t_2$	$\Delta t$	$\Delta q_1$	$\Delta q_2$	$\Delta q_2/\Delta q_1$
1	1000	0.400	0.077	0.236	0.160	2.94	0.06	0.019
2	1000	0.600	0.080	0.209	0.129	1.27	0.02	0.016
3	1000	0.700	0.069	0.175	0.106	0.86	0.01	0.011
4	1000	0.900	0.056	0.130	0.074	0.40	0.00	0.000
5	10000	0.500	0.070	0.202	0.132	3.11	0.06	0.021
6	10000	0.700	0.079	0.194	0.115	1.44	0.03	0.019
7	10000	0.900	0.062	0.146	0.084	0.62	0.00	0.005
8	20000	0.500	0.096	0.242	0.146	4.45	0.27	0.061
9	20000	0.700	0.059	0.148	0.089	2.93	0.06	0.021
10	20000	0.900	0.071	0.166	0.095	1.23	0.02	0.016
11	30000	0.700	0.074	0.182	0.108	3.94	0.13	0.034
12	30000	0.900	0.055	0.124	0.069	2.76	0.06	0.022
13	40000	0.700	0.107	0.227	0.120	5.58	0.52	0.093
14	40000	0.900	0.066	0.153	0.087	3.72	0.13	0.036
15	50000	0.900	0.093	0.187	0.094	5.68	0.27	0.047
16	1000	0.301	0.119	0.334	0.215	4.19	0.27	0.065
17	5000	0.324	0.119	0.325	0.206	4.38	0.29	0.066
18	10000	0.357	0.119	0.312	0.194	4.62	0.30	0.065
19	15000	0.394	0.118	0.301	0.182	4.85	0.31	0.065
20	20000	0.437	0.118	0.288	0.171	5.07	0.32	0.063
21	25000	0.486	0.117	0.277	0.159	5.29	0.34	0.065
22	30000	0.543	0.117	0.265	0.148	5.51	0.37	0.066
23	35000	0.610	0.115	0.252	0.137	5.71	0.38	0.066
24	40000	0.686	0.111	0.234	0.123	5.85	0.33	0.057
25	45000	0.774	0.105	0.215	0.110	5.76	0.47	0.082
26	50000	0.873	0.099	0.197	0.098	5.85	0.32	0.055

Table F.4 Results of Time Domain  $q$  Analysis for the Second  $\alpha$  Control Design

Plant	Altitude	Mach	$t_1$	$t_2$	$\Delta t$	$\Delta q_1$	$\Delta q_2$	$\Delta q_2/\Delta q_1$
1	1000	0.240	0.084	0.290	0.206	0.47	0.00	0.010
2	5000	0.260	0.083	0.275	0.192	0.49	0.00	0.010
3	10000	0.280	0.085	0.259	0.174	0.54	0.01	0.010
4	10000	0.300	0.077	0.253	0.176	0.50	0.01	0.010
5	15000	0.310	0.084	0.239	0.155	0.58	0.01	0.010
6	20000	0.340	0.084	0.224	0.140	0.62	0.01	0.010
7	20000	0.400	0.065	0.214	0.149	0.52	0.01	0.011
8	25000	0.380	0.083	0.208	0.125	0.64	0.01	0.010
9	30000	0.420	0.083	0.195	0.111	0.68	0.01	0.011
10	30000	0.500	0.061	0.187	0.126	0.57	0.01	0.012
11	35000	0.470	0.083	0.181	0.098	0.71	0.01	0.011
12	40000	0.530	0.082	0.167	0.085	0.74	0.01	0.012
13	45000	0.700	0.060	0.132	0.072	0.67	0.01	0.014
14	50000	0.780	0.060	0.121	0.060	0.69	0.01	0.015
15	1000	0.301	0.061	0.259	0.198	0.41	0.01	0.012
16	5000	0.324	0.060	0.245	0.185	0.43	0.01	0.012
17	10000	0.357	0.058	0.229	0.171	0.46	0.01	0.012
18	15000	0.394	0.056	0.210	0.154	0.49	0.01	0.012
19	20000	0.437	0.057	0.194	0.138	0.51	0.01	0.012
20	25000	0.486	0.057	0.180	0.123	0.54	0.01	0.013
21	30000	0.543	0.057	0.167	0.110	0.56	0.01	0.013
22	35000	0.610	0.057	0.154	0.096	0.58	0.01	0.013
23	40000	0.686	0.057	0.137	0.080	0.61	0.01	0.014
24	45000	0.774	0.057	0.147	0.091	0.56	0.01	0.013
25	50000	0.873	0.056	0.125	0.068	0.61	0.01	0.014

Table F.5 Specification Terms for the Body Axis Design

Plant	Altitude (ft)	Mach	$\tau_{ep}$	$T_R$	$1/T_S$	$\zeta_d$	$\omega_d$
1	1000	0.240	0.072	0.11	3.04e-02	0.70	1.78
2	1000	0.400	0.039	0.52	6.42e-03	1.16	4.58
3	1000	0.600	0.063	0.62	1.28e-03	0.85	2.46
4	1000	0.700	0.054	0.59	7.95e-04	0.85	2.46
5	1000	0.900	0.046	0.63	1.71e-04	0.87	2.64
6	5000	0.260	0.073	0.10	2.83e-02	0.69	1.78
7	10000	0.280	0.077	0.10	2.77e-02	0.67	1.75
8	10000	0.300	0.067	0.11	2.32e-02	0.71	1.85
9	10000	0.500	0.041	0.54	4.93e-03	1.24	5.04
10	10000	0.700	0.069	0.59	1.02e-03	0.84	2.38
11	10000	0.900	0.055	0.59	3.76e-04	0.87	2.57
12	15000	0.310	0.080	0.09	2.49e-02	0.66	1.73
13	20000	0.340	0.084	0.09	2.35e-02	0.65	1.71
14	20000	0.400	0.054	0.14	1.49e-02	0.77	2.03
15	20000	0.500	0.080	0.59	6.77e-03	0.85	3.82
16	20000	0.700	0.050	0.48	3.23e-03	1.56	5.70
17	20000	0.900	0.074	0.59	3.94e-04	0.85	2.49
18	25000	0.380	0.087	0.08	2.09e-02	0.64	1.71
19	30000	0.420	0.091	0.08	1.96e-02	0.62	1.69
20	30000	0.500	0.052	0.16	1.24e-02	0.77	2.09
21	30000	0.700	0.042	0.57	4.48e-03	1.05	4.71
22	30000	0.900	0.056	0.42	2.42e-03	1.60	5.18
23	35000	0.470	0.093	0.07	1.77e-02	0.61	1.68
24	40000	0.530	0.097	0.06	1.54e-02	0.59	1.68
25	40000	0.700	0.048	0.49	7.11e-03	0.84	3.42
26	40000	0.900	0.047	0.63	3.02e-03	0.97	4.62
27	45000	0.700	0.052	0.22	8.82e-03	0.75	2.24
28	50000	0.780	0.053	0.25	7.13e-03	0.73	2.34
29	50000	0.900	0.046	0.61	4.09e-03	0.74	3.74
30	1000	0.301	0.084	0.26	1.48e-02	0.89	2.44
31	5000	0.324	0.084	0.27	1.39e-02	0.89	2.50
32	10000	0.357	0.086	0.32	1.27e-02	0.89	2.68
33	15000	0.394	0.086	0.36	1.17e-02	0.88	2.81
34	20000	0.437	0.087	0.40	1.06e-02	0.86	2.95
35	25000	0.486	0.088	0.43	9.75e-03	0.84	3.03
36	30000	0.543	0.090	0.47	8.83e-03	0.82	3.11
37	35000	0.610	0.089	0.49	8.00e-03	0.81	3.18
38	40000	0.686	0.062	0.46	7.50e-03	0.84	3.24
39	45000	0.774	0.045	0.51	6.47e-03	0.79	3.37
40	50000	0.873	0.046	0.57	4.94e-03	0.75	3.55

Table F.6 Additional Terms for the Body Axis Design

Plant	$K_\phi$	$\zeta_\phi$	$\omega_\phi$	$A_3$	$A_2$	$A_1$	$A_0$	$\tau_{e\beta}$
1	3.02e-03	5.78	32.92	1.84e-02	7.97e-02	3.09	-8.76e-02	0.16
2	1.05e-01	3.47	14.10	6.70e-02	8.82e-01	20.67	-1.02e-01	0.12
3	1.22e+00	0.90	2.23	1.20e-01	2.04e+00	5.93	2.03e-03	0.12
4	1.13e+00	0.88	2.32	1.22e-01	1.83e+00	5.99	3.17e-03	0.10
5	1.16e+00	0.94	2.46	1.26e-01	1.89e+00	6.86	1.14e-02	0.09
6	3.31e-03	5.52	31.54	1.78e-02	7.39e-02	3.10	-8.00e-02	0.15
7	2.33e-03	6.42	36.94	1.64e-02	5.60e-02	2.98	-7.42e-02	0.15
8	3.61e-03	5.53	31.26	1.77e-02	8.03e-02	3.31	-6.51e-02	0.15
9	1.16e-01	3.85	14.77	6.88e-02	1.07e+00	25.09	-9.21e-02	0.12
10	1.19e+00	0.86	2.19	1.22e-01	1.96e+00	5.61	1.18e-03	0.12
11	1.15e+00	0.91	2.40	1.28e-01	1.84e+00	6.50	8.09e-03	0.10
12	2.27e-03	6.41	37.02	1.50e-02	3.68e-02	2.90	-6.26e-02	0.14
13	1.99e-03	6.64	39.07	1.40e-02	1.86e-02	2.83	-5.58e-02	0.14
14	6.89e-03	4.77	24.71	1.75e-02	1.07e-01	3.97	-4.19e-02	0.13
15	5.17e-01	1.44	5.33	2.13e-02	3.78e-01	14.34	-6.97e-02	0.08
16	1.56e-01	3.93	14.38	2.11e-01	2.90e+00	32.42	-1.22e-01	0.17
17	1.22e+00	0.87	2.26	1.39e-01	1.95e+00	6.10	6.09e-03	0.12
18	3.57e-03	4.90	29.23	1.34e-02	3.08e-03	2.83	-4.62e-02	0.13
19	3.04e-03	5.04	31.36	1.27e-02	-1.82e-02	2.75	-4.08e-02	0.12
20	6.71e-03	5.25	25.66	1.50e-02	8.47e-02	4.17	-3.17e-02	0.12
21	5.84e-02	5.10	19.48	6.92e-02	1.14e+00	22.08	-8.96e-02	0.13
22	1.34e-01	3.99	14.06	2.34e-01	2.84e+00	26.76	-8.45e-02	0.18
23	1.80e-03	6.24	40.64	1.23e-02	-3.95e-02	2.71	-3.35e-02	0.12
24	2.14e-03	5.48	37.20	1.22e-02	-6.17e-02	2.69	-2.52e-02	0.11
25	6.95e-02	3.25	12.99	1.84e-02	9.27e-02	11.45	-5.54e-02	0.08
26	1.95e-02	9.39	32.99	7.55e-02	-1.84e+00	21.41	-7.00e-02	-0.04
27	6.17e-03	6.03	28.81	1.33e-02	-2.11e-01	4.83	-1.75e-02	0.03
28	4.46e-03	7.00	35.43	2.02e-02	-3.63e-01	5.24	-8.95e-03	-0.01
29	1.92e-02	6.95	27.04	2.61e-02	-5.81e-01	13.89	-4.19e-02	0.02
30	1.64e-01	1.36	6.07	1.79e-02	1.91e-01	5.78	-6.84e-02	0.11
31	1.74e-01	1.38	6.03	1.74e-02	1.83e-01	6.07	-6.57e-02	0.10
32	2.14e-01	1.38	5.83	1.63e-02	1.64e-01	6.99	-6.66e-02	0.09
33	2.42e-01	1.39	5.75	1.50e-02	1.21e-01	7.68	-6.47e-02	0.08
34	2.79e-01	1.39	5.61	1.29e-02	2.74e-02	8.46	-6.26e-02	0.07
35	3.10e-01	1.39	5.47	1.22e-02	-1.00e-01	8.94	-5.77e-02	0.05
36	3.50e-01	1.38	5.28	1.37e-02	-2.55e-01	9.40	-5.22e-02	0.03
37	3.60e-01	1.42	5.32	1.55e-02	-3.32e-01	9.86	-4.76e-02	0.02
38	1.37e-01	2.23	8.78	1.54e-02	-3.49e-02	10.29	-4.95e-02	0.06
39	3.56e-02	4.49	17.90	2.31e-02	-5.27e-01	11.18	-5.09e-02	0.01
40	2.20e-02	6.07	24.01	2.26e-02	-4.44e-01	12.49	-4.22e-02	0.03

Table F.7 Specification Terms for the Stability Axis Design

Plant	Altitude (ft)	Mach	$\tau_{ep}$	$T_R$	$1/T_S$	$\zeta_d$	$\omega_d$
1	1000	0.240	0.065	0.12	6.63e-05	0.73	2.00
2	1000	0.400	0.037	0.52	3.23e-04	1.12	4.90
3	1000	0.600	0.059	0.63	-7.04e-04	0.84	2.58
4	1000	0.700	0.051	0.59	-4.57e-04	0.84	2.63
5	1000	0.900	0.043	0.63	-6.47e-04	0.84	2.76
6	5000	0.260	0.066	0.11	4.04e-06	0.73	2.01
7	10000	0.280	0.070	0.11	-2.77e-04	0.71	1.98
8	10000	0.300	0.062	0.11	1.52e-04	0.74	2.06
9	10000	0.500	0.039	0.53	4.29e-04	1.21	5.31
10	10000	0.700	0.065	0.59	-6.24e-04	0.83	2.54
11	10000	0.900	0.051	0.59	-5.05e-04	0.85	2.72
12	15000	0.310	0.074	0.10	-4.71e-04	0.70	1.94
13	20000	0.340	0.078	0.09	-7.70e-04	0.68	1.92
14	20000	0.400	0.053	0.15	2.86e-04	0.80	2.25
15	20000	0.500	0.073	0.58	-2.18e-04	0.83	4.10
16	20000	0.700	0.049	0.47	8.00e-04	1.57	5.97
17	20000	0.900	0.070	0.59	-6.67e-04	0.83	2.64
18	25000	0.380	0.079	0.09	-9.35e-04	0.67	1.92
19	30000	0.420	0.085	0.08	-1.42e-03	0.66	1.89
20	30000	0.500	0.053	0.17	4.13e-04	0.80	2.33
21	30000	0.700	0.037	0.57	5.67e-04	1.02	4.94
22	30000	0.900	0.057	0.41	8.78e-04	1.60	5.40
23	35000	0.470	0.089	0.07	-1.83e-03	0.65	1.88
24	40000	0.530	0.093	0.06	-2.17e-03	0.63	1.87
25	40000	0.700	0.063	0.54	3.06e-04	0.77	3.72
26	40000	0.900	0.044	0.62	5.02e-04	0.96	4.83
27	45000	0.700	0.048	0.25	-1.00e-04	0.78	2.54
28	50000	0.780	0.050	0.28	-9.35e-04	0.75	2.67
29	50000	0.900	0.042	0.61	-2.62e-04	0.72	3.98
30	1000	0.301	0.085	0.41	-4.59e-04	0.87	3.23
31	5000	0.324	0.084	0.42	-4.19e-04	0.86	3.26
32	10000	0.357	0.084	0.44	-3.81e-04	0.84	3.33
33	15000	0.394	0.084	0.45	-3.21e-04	0.83	3.36
34	20000	0.437	0.084	0.47	-2.67e-04	0.81	3.39
35	25000	0.486	0.084	0.48	-2.22e-04	0.80	3.42
36	30000	0.543	0.085	0.50	-1.80e-04	0.78	3.46
37	35000	0.610	0.083	0.51	-8.66e-05	0.77	3.51
38	40000	0.686	0.066	0.51	3.08e-04	0.78	3.60
39	45000	0.774	0.042	0.53	4.00e-04	0.76	3.67
40	50000	0.873	0.042	0.58	-7.94e-05	0.72	3.82



Table F.8 Additional Terms for the Stability Axis Design

Plant	$K_\phi$	$\zeta_\phi$	$\omega_\phi$	$A_3$	$A_2$	$A_1$	$A_0$	$\tau_{e\beta}$
1	3.35e-03	5.25	35.00	2.55e-02	1.04e-01	3.84	1.90e-02	0.17
2	1.17e-01	3.22	14.31	6.01e-02	6.12e-01	23.14	9.01e-02	0.10
3	1.22e+00	0.89	2.34	1.13e-01	2.15e+00	6.44	3.13e-02	0.11
4	1.14e+00	0.88	2.47	1.19e-01	1.93e+00	6.71	2.73e-02	0.10
5	1.15e+00	0.92	2.58	1.21e-01	1.94e+00	7.34	3.88e-02	0.08
6	3.73e-03	4.95	33.22	2.48e-02	9.76e-02	3.84	2.12e-02	0.16
7	2.77e-03	5.58	37.94	2.35e-02	8.27e-02	3.72	2.21e-02	0.16
8	4.67e-03	4.60	30.41	2.39e-02	9.90e-02	4.02	2.64e-02	0.16
9	1.20e-01	3.65	15.34	5.41e-02	6.17e-01	27.26	9.67e-02	0.09
10	1.20e+00	0.86	2.32	1.18e-01	2.07e+00	6.25	2.51e-02	0.11
11	1.15e+00	0.89	2.54	1.25e-01	1.92e+00	7.17	3.31e-02	0.09
12	2.54e-03	5.68	39.01	2.16e-02	6.32e-02	3.58	2.43e-02	0.16
13	2.28e-03	5.78	40.78	2.05e-02	4.75e-02	3.50	2.60e-02	0.16
14	1.33e-02	3.31	19.63	2.29e-02	1.16e-01	4.77	3.46e-02	0.13
15	4.82e-01	1.44	5.91	2.50e-02	1.15e-01	16.15	7.94e-02	0.07
16	1.62e-01	3.75	14.77	1.96e-01	2.87e+00	34.92	3.72e-02	0.16
17	1.22e+00	0.87	2.40	1.35e-01	2.05e+00	6.75	2.91e-02	0.11
18	1.58e-03	6.75	48.86	1.95e-02	3.30e-02	3.47	2.87e-02	0.15
19	2.41e-03	5.15	39.12	1.85e-02	1.39e-02	3.37	3.09e-02	0.15
20	1.94e-02	3.04	16.76	2.02e-02	8.87e-02	5.07	3.80e-02	0.12
21	4.48e-02	5.64	23.29	3.90e-02	4.79e-01	23.78	5.39e-02	0.09
22	1.92e-01	3.25	12.28	2.28e-01	2.89e+00	28.60	2.07e-02	0.17
23	2.20e-03	5.08	40.68	1.76e-02	-6.34e-03	3.30	3.34e-02	0.14
24	1.90e-03	5.18	43.53	1.69e-02	-2.87e-02	3.26	3.61e-02	0.14
25	2.17e-01	1.89	8.00	2.39e-02	-3.35e-01	13.33	5.90e-02	0.04
26	2.23e-02	8.49	32.29	8.86e-02	-2.01e+00	22.98	3.44e-02	-0.04
27	9.29e-03	4.90	26.51	1.75e-02	-2.25e-01	6.07	4.88e-02	0.04
28	8.83e-03	5.00	28.61	2.51e-02	-4.19e-01	6.67	5.98e-02	0.00
29	1.43e-02	7.74	33.38	3.72e-02	-7.52e-01	15.43	5.68e-02	0.01
30	2.90e-01	1.23	6.02	2.71e-02	1.95e-01	9.91	6.53e-02	0.09
31	2.96e-01	1.25	6.02	2.60e-02	1.65e-01	10.10	6.66e-02	0.09
32	3.15e-01	1.27	5.95	2.40e-02	1.09e-01	10.51	6.91e-02	0.08
33	3.21e-01	1.29	5.94	2.23e-02	4.67e-02	10.70	7.00e-02	0.07
34	3.34e-01	1.31	5.89	2.06e-02	-5.08e-02	10.95	7.08e-02	0.06
35	3.50e-01	1.33	5.80	1.92e-02	-1.45e-01	11.13	7.15e-02	0.05
36	3.72e-01	1.33	5.68	2.01e-02	-2.46e-01	11.35	7.20e-02	0.04
37	3.74e-01	1.37	5.75	2.13e-02	-3.21e-01	11.71	7.10e-02	0.03
38	2.12e-01	1.82	7.83	2.33e-02	-3.06e-01	12.40	6.08e-02	0.04
39	3.86e-02	4.22	18.69	3.18e-02	-6.47e-01	13.00	4.97e-02	0.01
40	1.86e-02	6.39	28.11	3.25e-02	-5.92e-01	14.14	5.65e-02	0.02

### Bibliography

1. Adams, Richard J., Andrew G. Sparks and Siva S. Banda, "Full Envelope Multivariable Control Law Synthesis for a High Performance Test Aircraft." Proceedings of the 1993 AIAA Guidance, Navigation, and Control Conference, Monterey, CA.
2. Blakelock, John H. *Automatic Control of Aircraft and Missiles* (2nd Edition). John Wiley & Sons, Inc, 1991.
3. D'Azzo, John J. and Constantine H. Houpis. *Linear Control System Analysis and Design* (3rd Edition). McGraw-Hill, 1988.
4. *Flying Qualities of Piloted Aircraft*. Military Standard 1797A, ASA/ENES, Wright-Patterson AFB, OH 45433-6503, January 1990.
5. Horowitz, Isaac. "Quantitative Feedback Theory," *Proceedings of the IEE*, 129D(6):215-226 (November 1982).
6. Houpis, C. H. *Quantitative Feedback Theory (QFT) - Technique for Designing Multivariable Control Systems*. Technical Report AFWAL-TR-86-3107, Flight Dynamics Laboratory AFWAL/FIGL, Wright-Patterson AFB, OH 45433-6553, January 1987.
7. Lacey, Donald J. *A Robust Digital Flight Control System for an Unmanned Research Vehicle Using Discrete Quantitative Feedback Theory*. MS thesis, Air Force Institute of Technology, December 1991.
8. "Matlab." The MathWorks, Inc., 24 Prime Park Way, Natick, MA 01760, December 1992. Version 4.0a, Copyright 1984-92.
9. Nelson, Robert C. *Flight Stability and Automatic Control*. McGraw-Hill, 1989.
10. Pachter, M., J. J. D'Azzo and L. E. Buzogany. "Second-Order System Models of High-Order Plants." To Appear in the International Journal of Systems.
11. Pachter, Meir. Class Notes, EENG641, Automatic Flight Control II, December 1991.
12. Pachter, Meir. Professor of Electrical Engineering, AFIT, WPAFB, OH 45433. Personal Interview, November 1993.
13. "MIMO/QFT CAD Program." Air Force Institute of Technology, Department of Electrical and Computer Engineering, Wright-Patterson Air Force Base, Ohio 45433, May 1993. Version 2.
14. Rasmussen, S. J. *Application of Non-linear QFT to Flight Control Design for High Angle of Attack Maneuvers with Thrust Vectoring*. MS thesis, Air Force Institute of Technology, December 1991.
15. Sheldon, Stuart N. Capt, Flight Control Systems Engineer, WL/FIGS, WPAFB, OH 45433. Personal Interview, November 1993.
16. "Simulation/Rapid-Prototyping Facility." Century Computing, Inc., 4141 Colonel Glen Hwy., Dayton, OH 45431-1662, October 1992. Draft Sun/Unix Version.
17. Trosen, Dennis. *Development of an Air-to-Air Refueling Automatic Flight Control System Using Quantitative Feedback Theory*. MS thesis, Air Force Institute of Technology, June 1993.

### *Vita*

Odell R. Reynolds was born 18 November 1968 in Marshall, Minnesota. He grew up in Russell but graduated from Marshall Senior High School in 1987. From there he attended North Dakota State University, graduating with honors with a BS in Electrical and Electronics Engineering in May 1991. He received his commission through the Reserve Officer Training Corps, Det 610, and reported for active duty in May 1992. From May 1992 to December 1993, he pursued his Masters of Science in Electrical Engineering at the Air Force Institute of Technology. He married Stacey Olson in September of 1993. His academic career is scheduled to continue at AFIT in the pursuit of a PhD.

Permanent address: PO Box 142  
Russell, Minnesota 56169

REPORT DOCUMENTATION PAGE			Form Approved OMB No. 0704-0188	
Public reporting burden for this collection of information is estimated to average 1 hour per response, including the time for reviewing instructions, searching existing data sources, gathering and maintaining the data needed, and completing and reviewing the collection of information. Send comments regarding this burden estimate or any other aspect of this collection of information, including suggestions for reducing this burden, to Washington Headquarters Services, Directorate for Information Operations and Reports, 1215 Jefferson Davis Highway, Suite 1204, Arlington, VA 22202-4302, and to the Office of Management and Budget, Paperwork Reduction Project (0704-0188), Washington, DC 20503.				
1. AGENCY USE ONLY (Leave blank)	2. REPORT DATE December 1993	3. REPORT TYPE AND DATES COVERED Master's Thesis		
4. TITLE AND SUBTITLE DESIGN OF A SUBSONIC ENVELOPE FLIGHT CONTROL SYSTEM FOR THE VISTA F-16 USING QUANTITATIVE FEEDBACK THEORY			5. FUNDING NUMBERS	
6. AUTHOR(S) Odell R. Reynolds First Lieutenant, USAF				
7. PERFORMING ORGANIZATION NAME(S) AND ADDRESS(ES) Air Force Institute of Technology, WPAFB OH 45433-6583			8. PERFORMING ORGANIZATION REPORT NUMBER AFIT/GE/ENG/93D-34	
9. SPONSORING/MONITORING AGENCY NAME(S) AND ADDRESS(ES) Capt Stuart Sheldon WL/FIGS 2210 Eighth St STE 11 WPAFB, OH 45433-7521			10. SPONSORING/MONITORING AGENCY REPORT NUMBER	
11. SUPPLEMENTARY NOTES				
12a. DISTRIBUTION/AVAILABILITY STATEMENT Approved for public release; Distribution Unlimited			12b. DISTRIBUTION CODE	
13. ABSTRACT (Maximum 200 words) A controlled plant's characteristics can vary widely throughout its operational envelope. This is a major problem in nominal plant-based control system design. Hence, gain scheduling is often used for full envelope design. In this paper, it is proposed to address the plant's variability using robust control design concepts. In particular, the frequency domain based Quantitative Feedback Theory Multiple-Input Multiple-Output robust control design method is employed for the synthesis of a full envelope flight control system for an F-16 derivative. Compensators for the aircraft's pitch and lateral directional channels are designed, and the designs are validated using linear simulations.				
14. SUBJECT TERMS Quantitative Feedback Theory, Flight Control System, Subsonic Envelope, VISTA			15. NUMBER OF PAGES 180	
			16. PRICE CODE	
17. SECURITY CLASSIFICATION OF REPORT UNCLASSIFIED	18. SECURITY CLASSIFICATION OF THIS PAGE UNCLASSIFIED	19. SECURITY CLASSIFICATION OF ABSTRACT UNCLASSIFIED	20. LIMITATION OF ABSTRACT UL	